Author:
Bracho Garcia, Diego

Title:
Study and design of colour correction optical filters

STUDY AND DESIGN OF COLOUR CORRECTION OPTICAL FILTERS

DIEGO BRACHO GARCÍA

A dissertation submitted to the University of Bristol in accordance with the requirements for award of the degree of Doctor of Philosophy in the Faculty of Engineering

August 2023

ABSTRACT

The aim of this work is to assess the potential use of frequency selective optical filters as wearable devices for colour correction in human visual perception, establishing computational design methods based on numerical optimization for the design of these devices, and fabricating some of these using well established deposition techniques.

Computational colour appearance models based on physiological cone sensitivity functions were implemented, and red-green anomalous trichromacy was simulated according to the photopigment replacement model. Using numerical optimization, a set of ideal optical properties was computed by minimizing the average total colour and chroma differences between the perception of normal and anomalous trichromats provided with a frequency selective filter. It was found that while some enhancement in colour perception can be achieved by blocking light in the overlap region between the cone sensitivity functions, the difference is imperceptible to most observers. Optimizing for the average square, and higher powers, it was found that wider stopbands in the cone overlap region can improve the discrimination of colours whose anomalous perception is further away from the normal response (such as red, green, and orange). While the total number of discernible colours is reduced by the effect of the designed optical filters, caused majorly by the reduction in the luminance value, there is a significant increase in colour saturation. Optical filter design methods based on refinement of an initial solution, needle synthesis (NS) methodology, and genetic algorithm (GA) synthesis. While NS can provide high precision and computation efficiency, GA is a flexible and robust alternative for optical filter design. Silica/silicon nitride multilayers designed by these methods were fabricated using plasma enhanced chemical vapour deposition (PECVD), and compared to well-known optical devices, such as notch filters, and dielectric mirrors. Spectral characterization of the fabricated devices is in good agreement with expectations, both for normal and oblique incidence. Other photonic structures, such as colloidal crystals and inverse opals, fabricated by colloidal self-assembly, were also considered for this application. The results from this work support the idea of using optical filters for passive assistance in red-green anomalous trichromacy. The trade-off between the improvement and detriment in the perception of different colours, and the correlation between optical power and manufacturing costs, makes the design of these types of optical filters an open-ended question.

AUTHOR’S DECLARATION

I declare that the work in this dissertation was carried out in accordance with the requirements of the University's Regulations and Code of Practice for Research Degree Programmes and that it has not been submitted for any other academic award. Except where indicated by specific reference in the text, the work is the candidate's own work. Work done in collaboration with, or with the assistance of, others, is indicated as such. Any views expressed in the dissertation are those of the author.

SIGNED: Diego Bracho García. DATE: 25 August 2023

ACKNOWLEDGEMENTS

I want to thank my supervisors, Annela Seddon and Ian Hamerton, for their continuous support and guidance. For pushing me to challenge my own limits, for giving me the liberty to do my own research and make my own mistakes, and for their continuous help in all academic and non-academic matters.

To the International Iberian Nanotechnology Laboratory (INL), for their cooperation and support in the fabrication and characterization of multilayer devices. To Martin Lopez and the photonics group, for welcoming me into their lab and making my time in Portugal unforgettable. To William Wardley, for his efforts and cooperation in the fabrication of multilayer devices.

Special thanks to Alan Champneys for his great disposition, and help working the math for the linearized optimisation problem.

Thanks to Paul Weaver and Flavia De Luca for their support and encouragement.

To CONICYT- Becas Chile, for financial support.

To the ACCIS staff members and academics, for their teachings and continuous support; none of this would be possible without every single one of you.

To my colleagues and classmates, for helping each other out, for their friendship, and for making ACCIS such a great group of people.

To my father, for inspiring me to dream big and work hard. You are my role model.

To my mother, for her immeasurable care, love, and support.

To my wife, Marcela, for travelling across the globe with me, for her unconditional love and continuous support.

To my daughter, Sofía, for giving me purpose and inspiration, and for making my day every day with her smile.

LIST OF CONTENTS

LIST OF FIGURES

LIST OF TABLES

CHAPTER 1: BACKGROUND AND INTRODUCTION

1.1 ABSTRACT

To study and assess the potential role and impact of wavelength selective optical filters in colour perception, and their potential use for chromatic enhancement and colour correction, we need to understand how the human visual system works from the perspective of the different relevant sciences and disciplines, such as anatomy, biochemistry, genetics, and optics.

This chapter presents an introduction to the concepts of human colour vision, colour vision deficiency (CVD), colorimetry, optics, and electromagnetism in mixed dielectric media. These serve as a knowledge base of the physical, biological, and mathematical concepts in human vision and optics, which will be used in the following chapters of this work to study and design colour correction optical filters.

1.2 AIMS AND OBJECTIVES

The general aim of this thesis work is to study and assess the potential application of frequency-selective optical filters for chromatic enhancement and colour correction in human visual perception, including potential materials and manufacturing processes capable of producing such filters.

To achieve this, the current understanding of visual and colour perception will be studied and presented, in terms of the anatomy, molecular biology, genetics, psychophysics, physical chemistry, optics, and mathematics.

Models of human colour appearance and colour vision deficiency will be studied, and a numerical implementation of these will be used to analyse the effect of frequency selective optical filters in the perception of colour.

Using these numerical tools, frequency selective optical filters will be designed based on thin multilayer optical systems. These devices will be fabricated using deposition techniques, and characterized in terms of structure, optical properties, and colour correcting capabilities.

1.3 MOTIVATION

In humans, approximately 8% of the male and 0.5% of the female population display some form of colour vision deficiency (CVD). A CVD condition, even in a moderate form, can have a real impact on a person’s daily and professional life, and can constitute a competitive disadvantage when performing colour related tasks. Some examples associated with hindering due to CVD conditions are shown in Figure 1-1, such as interpreting maps or other colour coded information, or visually detecting obstacles which might be more easily confused with the background. As a result of this handicap, people with CVD are generally excluded from certain occupations, such as airline pilot, air traffic controller, train driver, *etc*., in which failure to discern differences in colour might present a hazard either to themselves or others.

Over the past few years, a series of home- and professionally-made videos have become viral on social media and other online platforms, where colour correction glasses made by different companies are given to colour vision deficient individuals, and their initial reactions and personal impressions on the effectiveness of these glasses are recorded. Their reactions are, in many cases, very emotional, as people in the videos claim to be able to see colours that they were not able to recognize without such glasses, and many of them even end-up crying as they are overwhelmed by the “colourfulness” of their surroundings.

Manufacturing companies, such as EnChroma, claim their product is capable of improving colour vision for red-green CVD individuals by “selectively filtering out wavelengths of light at the precise point where confusion or excessive overlap of colour sensitivity occurs” [1]. However, little research has been published on the subject, and clinical testing is scarce.

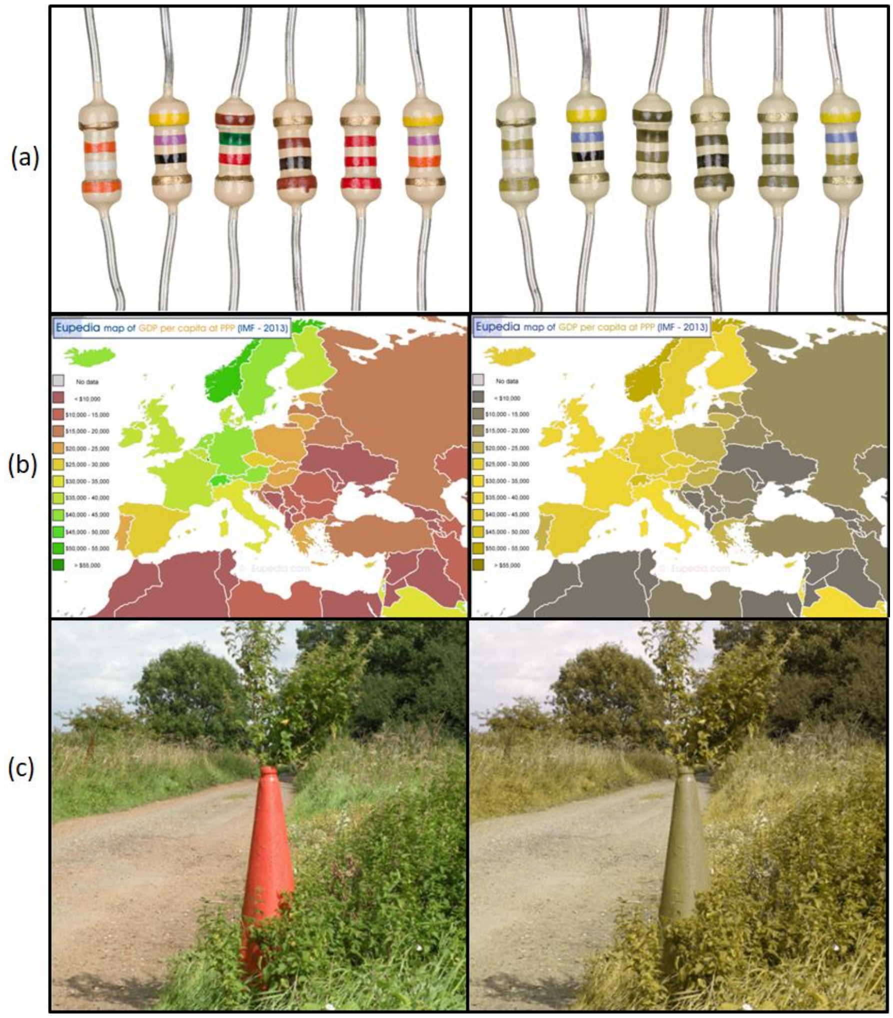

Figure 1-1: Examples of colour related tasks affected by colour vision deficiency. On the left are the original images, and on the right are simulations of the same images as seen by a dichromat observer (protan). (a) An image of assorted electric resistors, where the resistance of each device is indicated *via* colour coded strips. (b) Map of Europe's gross domestic product (GDP) *per capita* (2013). (c) An image of a traffic cone on a countryside road. Left original images (a) and (c) from [2]; (b) from [3]. Right images simulated *via* [4], for dichromatic red-blind/protanopia.

The development of these technologies has been driven by the continuous advances in the understanding of human and animal vision, the development of more generalized and thorough models of visual perception based on the physiology, physical chemistry, and optics of the visual system. Additionally, manufacturing of finely tuned optical devices is possible thanks to the development of a wide range of nano-fabrication techniques, including chemical and physical vapour deposition, spin coating, sol-gel driven fabrication, nanolithography, *etc*.

In this work, a study is presented on the theorical and mathematical basis on the possible mechanisms of action by which these products may work, as well as the development of numerical design tools for similar colour correction optical filters. Finally, the fabrication of optical devices based on multilayer and other optical systems is studied and carried out as a proof of concept and for future testing and analysis.

1.4 PHYSIOLOGICAL ASPECTS OF HUMAN VISION

Visual perception is the process by which the human brain interprets the surrounding world as seen through the eyes, by measuring incoming light in a specific region of the electromagnetic spectrum, known as the **visible spectrum** [5].

The process of visual perception begins with light entering the visual system through the eye, wherein a series of optic elements are set to form and focus an image in an area in the back of the eye called the retina. The latter contains a set of photosensitive cells, which are activated, and the information is then processed and transmitted to the brain.

1.4.1 The Human Eye

To understand the different optical elements and their function in the visual perception process we need to study the anatomy of the eye. The following section provides a brief description of the anatomic structure of the human eye. Figure 1-2 shows a cross-sectional diagram of the human eye, with marked areas of the relevant optical and anatomical structures described in this section.

The **cornea** is the curved and transparent outermost layer of the eye, which covers the anterior chamber, pupil, iris, and lens. It is the first optical element of the eye which transmits light into the rest of the optical components, and its interface with air corresponds to the highest refractive index change within the optic system, meaning that it is responsible for most of the image forming and focussing power of the eye.

While most of the refraction takes place in the cornea, it is the **lens** that is responsible for adjusting the focus point, depending on the proximity between observer and observed object. It is a layered, flexible structure that makes for a gradient-index optical element (refractive index is higher at the centre than the edges) and is shaped by the actuation of the ciliary muscles adjusting the focal point. The lens becomes thicker when viewing nearby objects, increasing the optical power as required to focus on the near object, and becomes thinner and flat for distant objects, reducing the optical power of the lens to increase the focus of distant objects.

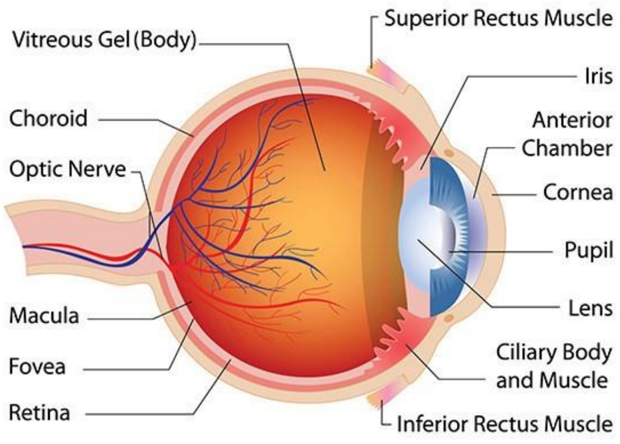

Figure 1-2: Cross-sectional diagram of the anatomy of the human eye (reproduced from [6]).

The **anterior chamber** is a small space, between the cornea and the iris, filled with a watery fluid known as aqueous humour. Deeper in the eye, between the lens and the retina lies a much larger chamber filled with a gelatinous, viscous fluid called **vitreous humour** (vitreous gel/body). Both the aqueous and vitreous humours are kept at elevated pressures, which helps the flexible structure of the eyeball to retain its spherical shape and resist injury, by providing a counterforce to inward deformation, and shape memory of the structure after small deformations (similar to an air-filled rubber balloon that becomes spherical again after being “squeezed”).

The **iris** is a sphincter muscle that controls the aperture size of a small hole in the centre of the eye, called the pupil, regulating the total amount of light that enters the eye. The colour of the iris (usually just referred to as eye colour) is determined by the concentration and distribution of melanin pigments in the iris and has no effect in the visual process.

The **retina** corresponds to a light sensitive thin layer in the innermost section in the back of the eye. It is in the retina where an image is formed by the previous optical elements (mainly the cornea and lens), and it is transduced into chemical and electrical signals by photosensitive cells (photoreceptors). This signal is then processed and transmitted by neurons into latter stages of the visual and nervous system.

The **retinal pigmented epithelium (RPE)** is a dark pigmented layer situated behind the retina, which serves to absorb any light that might not be captured at first in the retinal photoreceptors, preventing it from being scattered back though the retina and improving the visual quality of the image.

The **fovea** is a small pit in the rear of the retina, about 1.5 mm in diameter, and it is the area where we have best colour and spatial vision. This sharp central vision, also known as foveal vision, is possible due to the fact that in the foveal region lies the highest concentration of cone photoreceptors (Figure 1-3), and approximately half of the nerve fibres in the optic nerve carry information from the fovea, while the other half carries information from the rest of the retina. It covers an area of the retina that represents approximately 2° of visual angle in the central field of vision, and it is composed only of cone cells (no rods).

Figure 1-3 shows the packing density of photoreceptors in the human retina. It displays the high cone concentration and lack of rod cells in the foveal region (eccentricity 0°). In the rest of the retina, beyond the fovea, cones are present in much smaller quantities while rods are well distributed in the entire visual field.

The **macula** is an oval-shaped pigmented area near the centre of the retina, which protects the fovea from intense short-wave energy, and helps to reduce effects of chromatic aberration for short wavelength images. Unlike the lens, there is no yellowing of the macula over time, however, there are significant differences in the optical density of the macula between observers (and even between the two eyes of the same observer in some cases).

The **optic nerve** consists of a cable-like bundle of nerve fibres (retinal ganglion cell axons) that transmit the visual information, in the form of action potential, from the retina to the different areas in the brain concerned with visual processing.

This information is collected and transmitted by intermediate neurons called **bipolar cells**. In this stage, information is compressed, as multiple photoreceptors serve as input for a single bipolar cell, and multiple bipolar cells to a single ganglion cell. In fact, the information obtained by approximately 130 million photoreceptors is carried out by 1 million fibres into higher stages of visual processing. Besides compression, other complex operations take place at this stage, as **horizontal cells** connect multiple bipolar and photoreceptor cells, and **amacrine cells** connect multiple bipolar and ganglion cells (Figure 1-4-b). These connections serve as a first stage in neurological image processing, as the synapse in these neural networks can effectively perform a mathematical operation on the electrochemical information of the input signals (add, subtract, divide, *etc*.), in addition to amplification, gain control, and other nonlinearities that can occur within neural cells [5].

Note that the optic nerve layer is situated before the retinal photoreceptor cell layer (Figure 1-4-a), and light passes through this neural "wiring" before reaching the photoreceptors. Although these cells are mostly transparent and in fixed position, thus having little impact on visual performance, the ganglion cells' axons converge and leave the eye through an area in the retina known as the **optic disk**, where no overlying rod or cone cells are present (see Figure 1-3). This lack of photoreceptors causes a "**blind spot**" in the visual field located 12-15° from the fovea, where no visual information is received by eye. The reason we do not normally "see" this hole in our visual field is that out brain makes up for this missing information by interpolating information from the surrounding field.

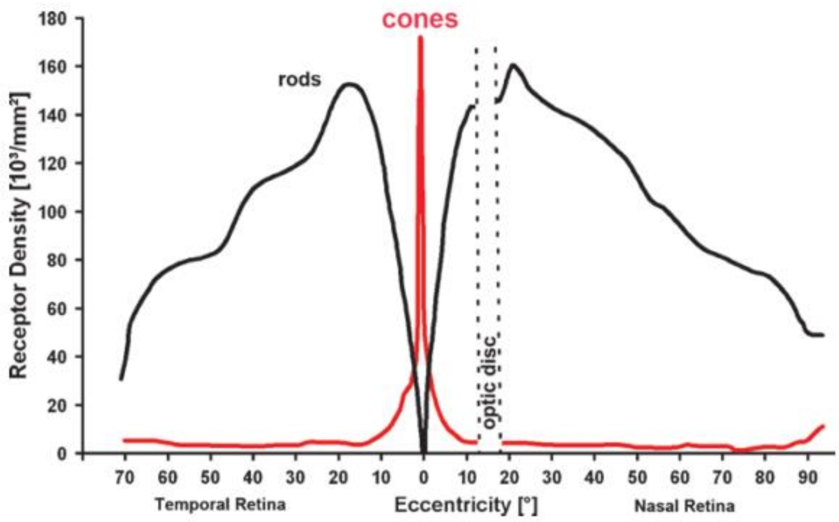

Figure 1-3: Cone and rod packing densities across the horizontal meridian of the visual field in a normal human retina. Reproduced from [7].

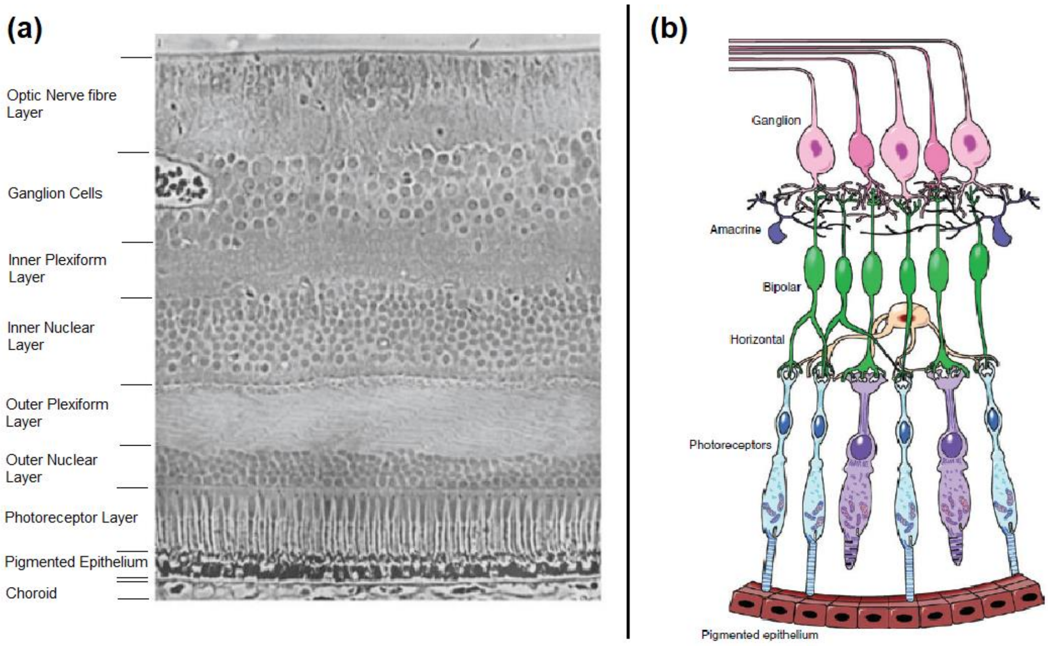

Figure 1-4: (a) Electron micrography of a cross section of the human retina (total thickness ~400μm) [8], and (b) schematic diagram showing the "wiring" of cells in the retina [5]. Light travels from top to bottom in both images.

1.4.2 Photoreceptors: Rods and Cones

As previously mentioned, the process of human vision starts when light enters the eye and is detected by two different types of photoreceptors: rods and cones. These are specialized types of neuroepithelial cells that lie in the back of the retina and can capture light and converting it into electrical signals, in a process known as **visual phototransduction**. Visual pigments in these cells consist of a group of proteins called opsins bound to a universal chromophore 11-*cis*-retinal. Photons of specific energy cause the excitation and photoisomerization of the chromophore (Figure 1-5), triggering a series of enzymatic reactions, that collectively result in phototransduction. The continuous photoisomerization and regeneration of the prosthetic group 11-*cis*-retinal through the **visual cycle** (Figure 1-6) is the electrochemical equivalent of the retina to the thermodynamic cycle in a heat engine.

In vertebrates there are five evolutionary distinct classes of visual pigments: rhodopsin (Rh1), LWS, MWS (or Rh2), SWS1, and SWS2 [9]. The contribution of a sixth class, melanopsin, is still a topic of research. All these however bind to the universal chromophore 11-*cis* retinal *via* a Schiff base (*i.e.*, a compound with the general structure $R_2C{=}NR'$ ($R' \neq H$)). They can be considered a sub-class of imines, being either secondary ketimines or secondary aldimines depending on their structure, thus the difference in the absorption of visual pigments originates from the different opsin proteins.

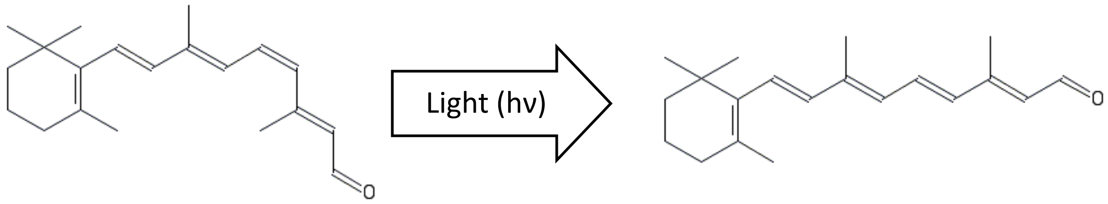

Figure 1-5: The photoisomerization of 11-*cis*-retinal into all-*trans*-retinal through a series of enzymatic processes is responsible for light detention and phototransduction in rods and cones.

Photoactivation by a single photon leads to the excitation of the chromophore and subsequent photoisomerization of 11-*cis*-retinal to all-*trans*-retinal. The interactions of the retinoid chromophore with its local environment and bound opsin protein determine the activation energy of this isomerization, in other words, it determines which wavelengths of light can activate the process of visual phototransduction. These interactions, which determine the electrochemical potential of the chromophore and its isomers, constitute the basis for spectral tuning of visual pigments [9]. The same retinal chromophore is capable of absorbing light from a wide range of the spectrum (UV-visible-IR).

A schematic showing the proposed mechanism of the visual cycle is presented below in Figure 1-6. Current understanding of the visual cycle is largely based on studies on rod photoreceptors, which has derived in the so called “classical visual cycle”. Photons are absorbed in the rod outer segment by visual pigment molecules, isomerizing 11-*cis*-retinal to all-*trans*-retinal, detaching from the activated opsin. It is then reduced by RDH8 (retinol dehydrogenase 8), in presence of NADPH (nicotinamide adenine dinucleotide phosphate), into all-*trans*-retinol, which is transferred to the RPE (retinal pigment epithelium), where the all-*trans*-form is isomerized and oxidized to 11-*cis*-retinal. The cycle is closed when the 11-*cis*-retinal is transferred back to the rod outer segment, to regenerate the visual pigment.

While the classical visual cycle, associated with the rod outer segment and the RPE, is well studied in rods, the visual cycle in cones is still a topic of research, and there is no consensus in the proposed biological and electrochemical mechanisms. It is generally agreed however that the classical visual cycle applies to cones, however, there are unique visual cycle pathways involving the cone photoreceptors and the Müller glia cells [10], [11].

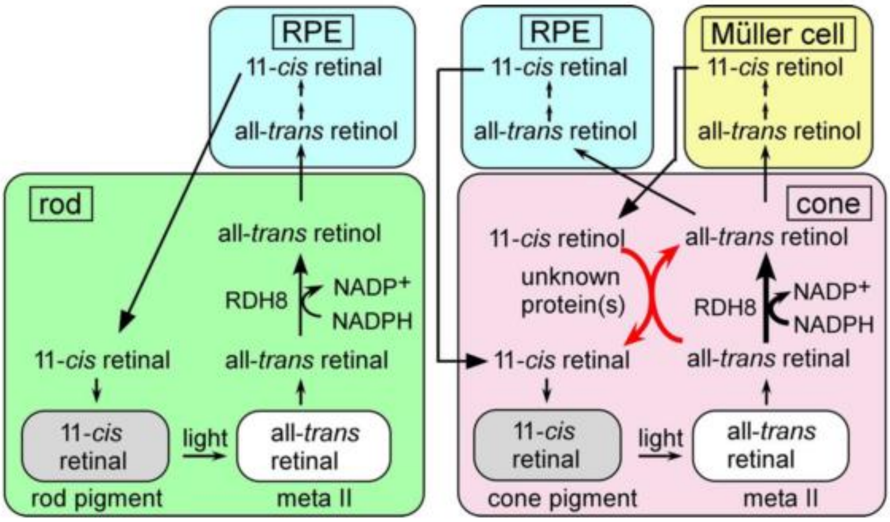

Figure 1-6: Proposed mechanisms for rod (left) and cone (right) visual cycles [11]

1.5 COLOUR VISION DEFICIENCY

Colour vision deficiency (CVD) refers to a group of conditions affecting the perception of colour. These conditions can be inherited or acquired, and broadly categorized into three types according to the number of affected cones, and its severity: anomalous trichromats, dichromats, and monochromats.

Anomalous trichromats present all three kinds of cone photoreceptors, but the spectral sensitivity of at least one of them is shifted with respect to normal trichromats. Depending on whether the red, green, or blue cone photoreceptors are affected, the conditions are named protanomaly, deuteranomaly, or tritanomaly respectively.

Dichromats lack one of the three distinguishable cone photoreceptors, and the conditions are named in the same way as anomalous trichromacy, depending on the missing photoreceptor: protanopia (missing red cones), deuteranopia (missing green), or tritanopia (missing blue).

The term colour blindness is often used to describe these conditions; however, it is important to note that individuals with these conditions are not necessarily “blind” to colour, but rather have a decreased ability to see some differences in colour, and the term colour blind is strictly only applicable to the rarer conditions of monochromacy and achromatopsia.

Anomalous trichromacy is the most common form of colour vision deficiency, followed by dichromacy (Table 1-1). Within these categories, conditions affecting the green cones (deuteranopia/deuteranomaly) are the most prevalent and is more commonly present in male individuals. The reason that these conditions are more frequent in males is that the most common CVD types (protan/deutan) are genetic conditions linked to sex chromosomes: the genes for the red and green photoreceptors are located in the X chromosome; for females (XX) to exhibit the condition, both X chromosomes must have the same or very similar deficiency; while for males (XY) it is sufficient that their sole X chromosome presents this condition.

Table 1-1: Prevalence of different types of colour vision deficiency [5]

	Type	*Male %*	*Female %*
Monochromacy	Cone Monochromatism	~ 0	~ 0
	Rod Monochromatism	0.003	0.002
Dichromacy	Protanopia (L-cone absent)	1.0	0.02
	Deuteranopia (M-cone absent)	1.1	0.01
	Tritanopia (S-cone absent)	0.002	0.001
Anomalous Trichromacy	Protanomaly	1.0	0.02
	Deuteranomaly	4.9	0.38
	Tritanomaly	~ 0	~ 0
	Total	8.0	0.4

1.5.1 Molecular genetics of human colour vision and colour vision defects

The relation between colour vision genotype and phenotype is still a contentious topic of research. Over the past two decades, researchers have continuously extended and redefined the genetic models and hypothesis on human colour perception, combining results from molecular genetics with physiologic and psychophysical test results. It has been long understood that the organization of genes encoding colour vision would have to be complex enough to accommodate for the existence of three different opsin types in the three spectral classes of cones. However, the molecular genetics of colour vision has turned out to be much more complex than predicted, partly because of the fact that red (L) and green (M) opsin genes are adjacent and almost identical (about 98% similarity) [12].

Genes encoding the red (OPN1LW) and green (OP1MW) opsins are arranged in a head-to-tail tandem array on the long arm of the X-chromosome, at location Xq28, starting with a single L-pigment gene and one or more M-pigment genes, composed of six exons each [13]. The S-pigment (OPN1SW) gene, on the other hand, is located on chromosome 7 and is coded by five exons. Figure 1-7 shows a diagram of the L and M-pigment genes. Note that while there are multiple M pigment genes, only the first one in the sequence is expressed. The expression of the L/M gene array is controlled by the locus control region (LCR), a non-coding DNA sequence, known as a *cis*-regulatory element, which regulates the transcription of neighbouring genes, and are vital components of the genetic regulatory networks. Much of the difference between the spectral absorbance coded by the L- and M-pigment genes has been found to be associated to different amino acids at specific locations within exons 3 (180) and 5 (277 and 285).

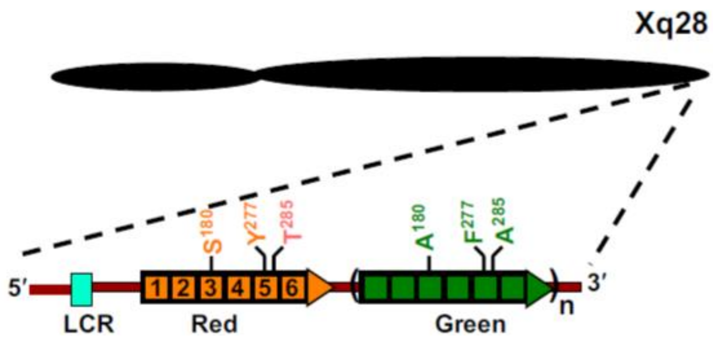

Figure 1-7: Diagram showing red and green gene arrays. Rectangles represent exons 1-6, and connecting lines represent introns. LCR is the locus control region. Amino acid differences in specific locations exons 3 and 5 contribute the major difference in the spectral absorbance of the encoded pigments [14].

It was originally thought that all people with normal trichromatic vision would share the same L and M pigment. However, owing to the recombination and high homology of the L and M opsin genes, there are variations in the amino acid sequences of both L and M opsins among normal trichromats, resulting in different spectral peaks [12], [15], [16] (Figure 1-8). In fact, some individuals which are considered dichromats by the psychophysical analysis are in fact strong anomalous trichromats, with three distinguishable photopigments encoded by different opsin genes, however, the high overlap in two of the photopigments absorbance curves results in a form of vision that is closer to dichromacy.

Current understanding on the molecular basis of X-linked red/green colour vision deficiency is that various types of deficiencies are a result of unequal homologous crossover or recombination between red and green pigment genes, facilitated by the high degree of homology between these given that both genes are almost identical. This results in the deletion of one of the red or green pigment genes, and/or the formation of red-green hybrid genes (Figure 1-9).

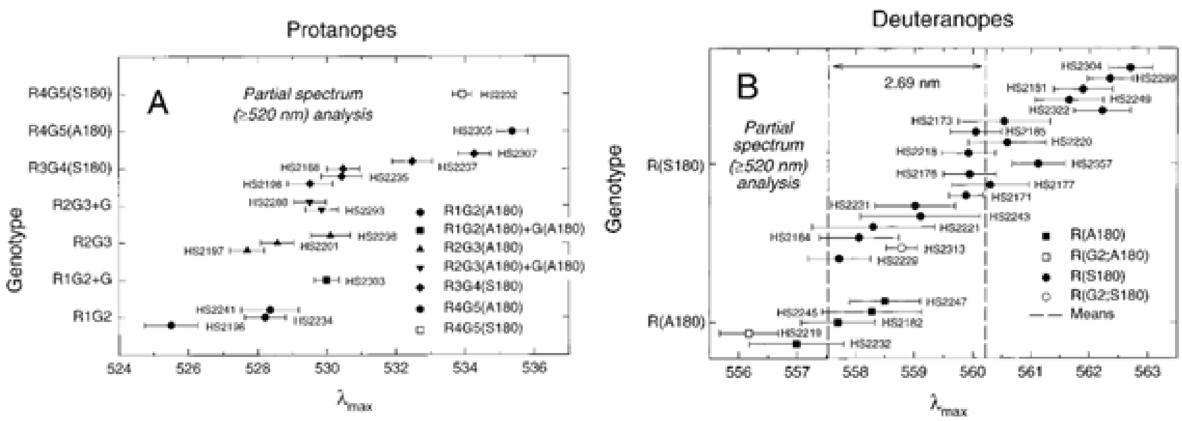

Figure 1-8: λ_{max} values for red, green, or red-green hybrid pigments for individual dichromats grouped by genotypic class. **(A)** Protanopes; **(B)** Deuteranopes. The vertical dashed lines represent the mean λ_{max} estimates for R(A180) and R(G2;A180) observers (left line, 557.53 nm) and R(S180) and R(G2; S180) observers (right line, 560.22 nm). The spectral difference between the two means is 2.69 nm. [16]

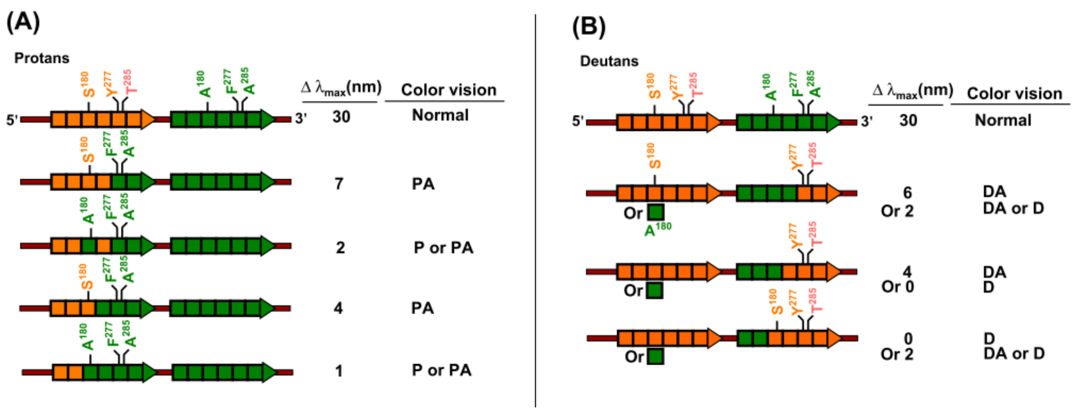

Figure 1-9: Genotype-phenotype relationships in men with red/green colour vision deficiency. Rectangles represent exons 1-6 of the red and green pigment genes, and connecting lines represent introns. $\Delta\lambda_{max}$ is the difference between maximum spectral absorbances of the red and green photopigments [14]. P, D correspond to protan and deutan dichromacy, while PA, DA are protanomaly and deuteranomaly respectively.

1.5.2 Treatment and management of colour vision deficiency

Several methods have been utilized in the past with the intention of 'correcting' CVD, or aiding CVD individuals for better colour discrimination in certain specific tasks, many of which are still utilized in the present. However, none of these methods has proven to be a definitive answer to the question of enabling normal colour discrimination for CVD individuals, and many of these have been and are still being disputed on the basis of their effectiveness. Even though visual aids can be beneficial for CVD individuals, there is currently no effective treatment for CVD in humans [17].

Formerly, during the late 1800s, it was generally thought that colour discrimination difficulties were a result of poor education on the subject of colours and learning disabilities. Thus, people who were unable to correctly name or differentiate certain colours were deemed as 'colour ignorant' and given 'training' in the subject. These ideas were put aside as research and awareness on colour vision deficiency became widespread during the 20th century. Counselling and career advice are common among CVD individuals, as the reduced colour discrimination capabilities can be an important handicap for certain tasks and occupations, particularly those requiring good visual capabilities, such as piloting and driving passenger and cargo vehicles, and other occupation which require visual inspection and good colour discrimination, such as sorting fruits or vegetables by ripeness.

A classification of techniques and devices aimed towards aiding CVD can be made depending on whether the device is actively performing a task, such as digital re-mapping of colour spaces, re-colouring of an image, high contrasts overlays, *etc*., or whether the device is working passively such as colour tinted lenses or other optical devices aimed towards better colour discrimination.

Active tools to aid people with CVD include recolouring techniques for colour coded information on digital platforms [18], recolouring and high contrast overlays for live feed video and images in mobile cameras, and smart glasses [19]. For example, searching in Google Play Store for Android devices it is possible to find a number of different mobile apps for these purposes, such as "Color Blind Pal" by Vincent Fiorentini, "Color Blindness Correction" by NGHS.fr, "NowYouSee" by Martin Douděra, *etc*. Whilst these techniques can be very helpful to convey specific information to the user, they have limited usability, as they require the visual information to be processed in digital form, meaning the user is compelled to take the extra time required to turn-on and launch the application on the device, as well as setting up for the specific task at hand. Additionally, recolouring and overlay techniques will set a trade-off between conveying useful information to the user at the exchange naturalness of the scene. Examples of these techniques are shown in Figure 1-10.

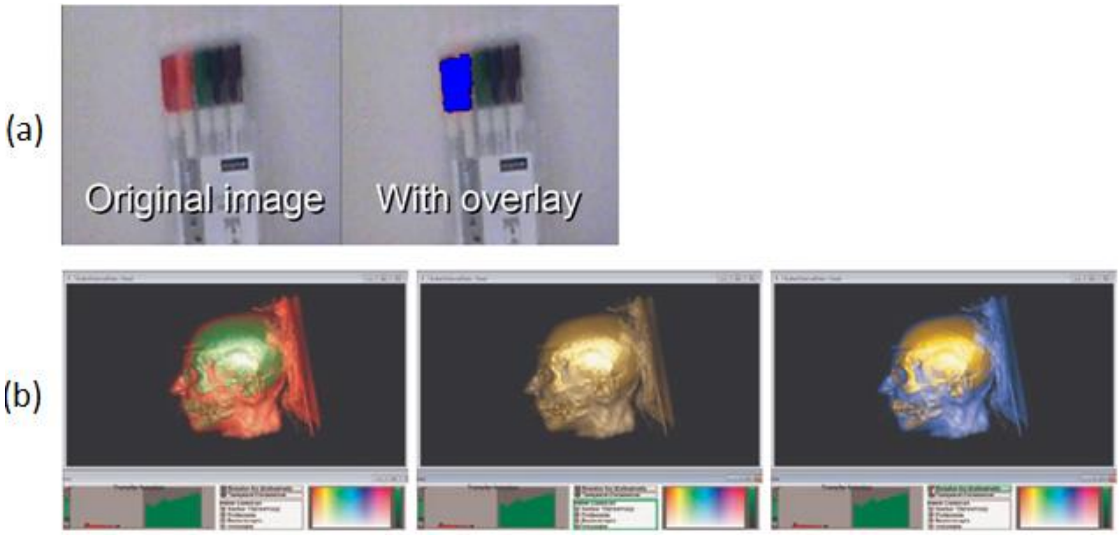

Figure 1-10: Examples of overlay and re-colouring techniques to achieve better colour discrimination for CVD on digital colour coded information. (a) Overlay for colour identification in problematic colours highlighted by high contrast overlay [19]. (b) Re-colouring techniques to achieve better colour discrimination for CVD on digital colour coded information. (Left) Reference image as perceived by a normal trichromat, (centre) simulation of perception by a deuteranope dichromat, (right) re-coloured image as seen by deuteranope, using re-colouring techniques for better colour discrimination. [18]

Of the passive tools for CVD correction and colour discrimination aid, wearable tinted spectacles and lenses have been widely tested and used in the past, dating back to some of the first studies on colour science, such as works by J.C. Maxwell [20]. Although these colour filters have proven to be useful for aiding CVD individuals in colour discrimination for colours in the areas of confusion, they have been criticized for reducing perception and discrimination on other non-problematic colours [19]. Such lenses are usually worn monocularly, allowing the wearer to obtain additional information on the spectral properties of the object being observed by means of comparison. For example, a red tinted lens would make red colours appear darker, and the comparison with an un-tinted lens worn on the other eye, a deuteranope individual can obtain information that can help differentiate those red colours affected by the tinted lens with green, which is less affected by the tinted lens. Empirical evidence suggests that monocular lenses can improve colour discrimination in dichromats, even though normal colour discrimination cannot be fully achieved [17], [19], [21].

Another strategy to achieve better colour discrimination is the use of selective band-pass and band-stop filters, in other to artificially separate the effective peak sensitivities of the photoreceptor absorbance sensitivities. This strategy is found in some of today's available glasses in the market aimed towards CVD correction and colour discrimination improvements, such as EnChroma glasses [1]. Even though these wearable devices have attracted a lot of attention lately with viral videos on social and other digital media, and there are claims by users that colour discrimination is subjectively improved, clinical trials and simulation results have generally yielded negative results [17], [22].

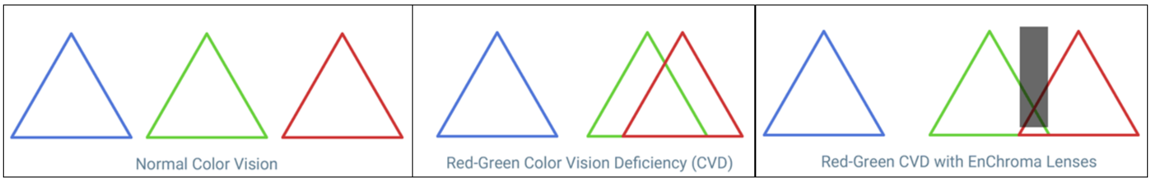

Figure 1-11: Schematic on the principle of improved colour discrimination by wearable frequency selective filters, as proposed by EnChroma's website [1]. Triangles represent the spectral sensitivity of the three different cone photoreceptors in the human eye, and the dark rectangle represents a photonic stopband.

Possibly the most promising definitive solution for congenital CVD is in the field of gene therapy, which has been successfully tested on non-human primates and mice [23], [24]. However, this technique is still very experimental and the ethics of testing on human subjects is the subject of open debate, so is not likely to lead to therapeutic applications in the near future.

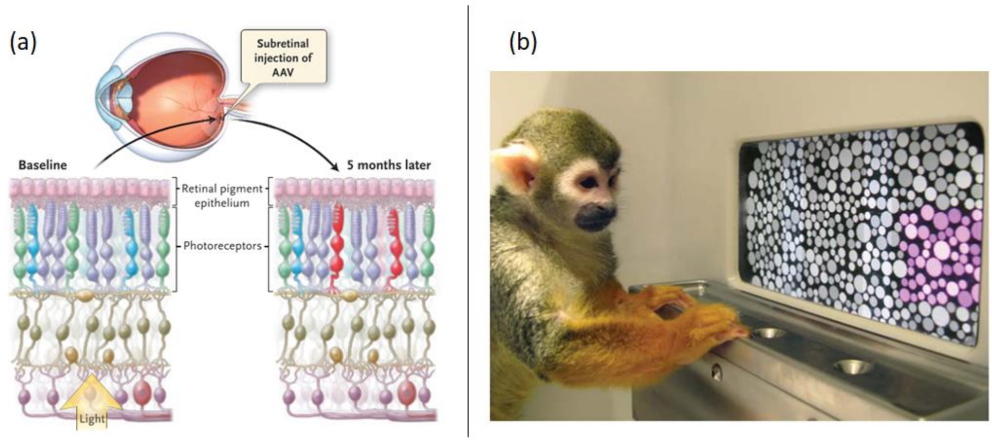

Figure 1-12: (a) Gene therapy approach used by [23] in which they delivered the wild-type human L-opsin gene to cone photoreceptors through subretinal injection of a recombinant, replication-defective adeno-associated virus (AAV) [25]. (b) Colour vision test adapted for use with animals, utilized for testing gene therapy as treatment for CVD [24].

1.6 COLORIMETRY

Colorimetry is the science of the study and measurement of light and colour according to the human visual perception. It incorporates the properties of human colour vision system into the measurement of light intensity and wavelength. It is a tool that allow us to make predictions on the visual perception of a light stimuli, depending on the viewing conditions such as illumination, surroundings, size, *etc*.

Several practical applications make use of the principles of colorimetry, such as colour display devices (television sets, computers, *etc*.). In physical chemistry, a colorimeter is a commonly used instrument to calculate the concentration of a known solute in a solution, by measuring light absorbance at a specific wavelength, and by the application of the Beer-Lambert law.

1.6.1 Photometry and radiometry

Radiometry is the science of measuring light, in terms of absolute power, in any portion of the electromagnetic spectrum. It is a physical measurement of the properties of electromagnetic radiation. Intensity of light, **Irradiance**, is measured in units of Watts per square metre (W/m^2).

Photometry is the science of measuring visible light and its effects on the human visual system. Units of measurement are weighted according to the sensitivity of the human eye, and it is a quantitative science based on a statistical model of human visual response to light. Photometric measurements of light, called **Illuminance**, is measured in Lux (lx), which corresponds to Lumens per square metre ($lx = lm/m^2$).

In photometry, the radiant power at each wavelength is weighted by a luminosity function, which models the sensitivity of the human visual system to brightness. This luminosity function (V(λ)) represents the achromatic channel response of the human visual system and, depending on the level of illumination, can be mediated by different photoreceptors (Figure 1-13).

Table 1-2: Radiometric and photometric units of light intensity and power (W = = J/s; sr = square radian).

Quantity	***Radiometric***	***Photometric***
Power	W	$Lumen\ (lm)\ =\ cd * sr$
Power per unit area	$\frac{W}{m^2}$	$Lux\ (lx) = \frac{cd * sr}{m^2} = \frac{lm}{m^2}$
Power per unit solid angle	$\frac{W}{sr}$	$Candela\ (cd)$
Power per unit area per unit solid angle	$\frac{W}{m^2 * sr}$	$\frac{cd}{m^2} = \frac{lm}{m^2 * sr}$

Conversion from radiometric to photometric units is performed by integrating the product of the spectral power distribution of the light stimuli ($\Phi_E(\lambda)$) and the luminous efficiency function ($V(\lambda)$) over the range of visible wavelengths (380-780 nm).

$$\Phi_V = K_m \int_{\lambda} \Phi_E(\lambda)\, V(\lambda)\, d\lambda \qquad \text{Eq. 1-1}$$

where Φ_V is the photometric power, measured in lumen, of a light stimulus with a spectral power distribution Φ_E (in Watts); K_m is a scaling factor, equal to 683 lm/W (by definition of the candela unit, there are 683 lumens per Watt at 555 nm); and $V(\lambda)$ is the photopic spectral luminous efficiency.

Under well-lit conditions (luminance 10-10^8 cd/m^2) vision is mediated by cone cells, with a maximum efficiency around 555 nm. Under low levels of illumination (10^{-6} – $10^{-3.5}$ cd/m^2), cone cells are non-functional, and vision is mediated exclusively by rod photoreceptors. The maximum efficiency in scotopic conditions occurs around 510 nm. This change in relative spectral sensitivity towards the blue end of the spectrum at low levels of illumination is referred to as the **Purkinje effect**, which explains why at low levels of illumination, blue colours tend to look brighter than, for example, red colours. A third regime of vision is known as mesopic vision, which occurs in intermediate light conditions (10^{-3} – $10^{0.5}$ cd/m^2) and corresponds to a combination of both photopic and scotopic vision.

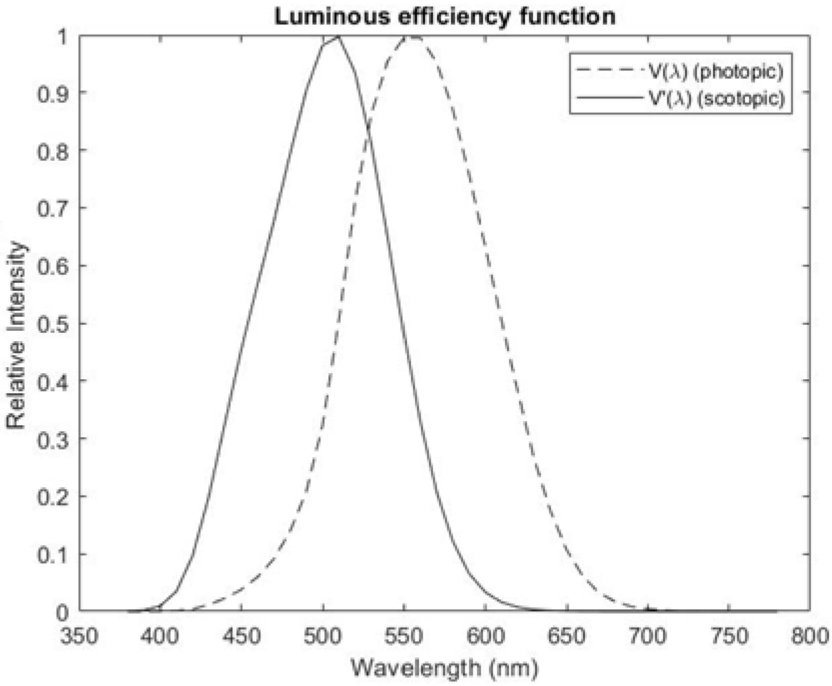

Figure 1-13: Spectral luminous efficiency curves V'(λ), for low levels of illumination (scotopic vision), and V(λ), for high levels of illumination (photopic vision).

1.6.2 Tristimulus and colour matching

Based on human perception, colour measurement relies on a system of three values, indicating the proportions of primary colours (red, green, and blue) which combined appear to "match" the colour of the light stimuli in study. These three colour values are called "tristimulus values" and they can be expressed in different colour systems depending on the spectral properties of the three primaries that make up the colour space.

Results from psychophysical experiments of colour matching are shown in Figure 1-14. Each curve is associated to a primary monochromatic light (blue: 444.5 nm, green: 526.3 nm, and red: 645.2 nm). The graph represents the fraction of each primary light needed to match the colour of a monochromatic stimulus with wavelength λ, according to a human observer. Note that the value for each curve at the corresponding wavelength of that primary is equal to one ($r_{10}(645.2\ nm) = g_{10}(526.3\ nm) = b_{10}(444.5\ nm) = 1$), while the other two values are equal to zero. In other words, each primary matches itself (*i.e.*, has the same light intensity at the same wavelength).

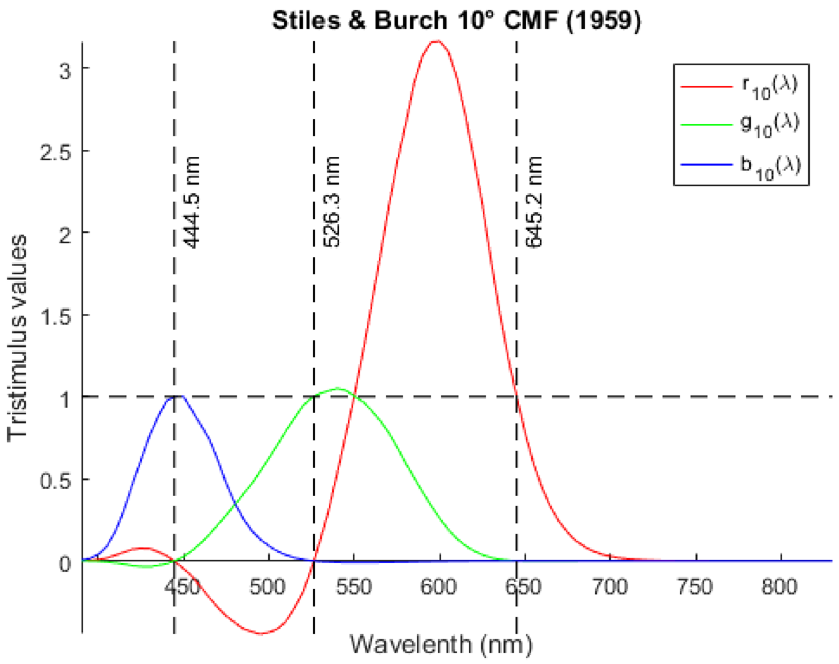

Figure 1-14: Stiles and Burch 10° colour matching functions (1959).

Note also that there are negative values for each curve. While it is not possible to "subtract" light in the additive light mix, these negative values mean that the primary in question has been added to the test light to make a match. Further discussion on the colour matching experiment will be presented in Chapter 2.

1.7 ELECTROMAGNETISM IN MIXED DIELECTRIC MEDIA

Understanding the physiological, psychophysical, and optical aspects of human vision can allow to predict the behaviour of the visual system under different conditions, such as changes in total luminance, chromaticity of the illuminant, background, and surrounding conditions, *etc*. On the other hand, understanding the physics of light, optics, and light-matter interactions, allows for the design of optical elements and tools used in many different applications, ranging from astrophysics, microscopy, ophthalmic devices, and audio-visual display devices, *etc*. This section presents a brief introduction on the physics of light-matter interactions, and particularly where it applies to the field of optics.

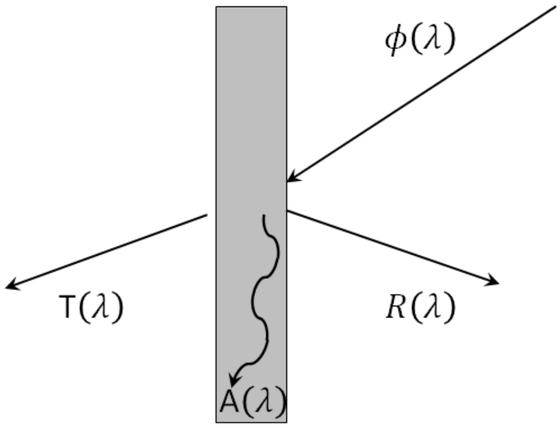

Figure 1-15: Light passing through the interface made up of two materials with different refractive indices. Incident light ($\phi(\lambda)$) is partially reflected ($R(\lambda)$) and absorbed by the material ($A(\lambda)$), while the remaining fraction is transmitted through the material ($T(\lambda)$).

1.7.1 Classical Electromagnetism and Optics

Classical electromagnetism (or classical electrodynamics) is a branch of physics, studying the interaction of electric charges and electric current, and forces associated with the electric and magnetic fields generated by these. The field of electromagnetism results from the combined study of the interrelated forces of electricity and magnetism, as described by the combined laws and relations deduced and proposed during the 19th century by researchers such as James Clerk Maxwell and Michael Faraday:

Gauss's Law	$\nabla \cdot \vec{D}(t) = \nabla \cdot \left[\varepsilon\, \vec{E}(t)\right] = \rho_r(t)$	Eq. 1-2
No magnetic charge	$\nabla \cdot \vec{B}(t) = \nabla \cdot \left[\mu\, \vec{H}(t)\right] = 0$	Eq. 1-3
Faraday's Law	$\nabla \times \vec{E}(t) = -\dfrac{\partial \vec{B}(t)}{\partial t}$	Eq. 1-4

Ampere's circuit Law	$$\nabla \times \vec{H}(t) = \vec{J}(t) + \frac{\partial \vec{D}(t)}{\partial t}$$	Eq. 1-5

where $\vec{D}$ is the electric flux density (C/m^2), $\vec{E}$ is the electric field density (V/m), ε is the material's permittivity (F/m), ρ_r is the volume charge density (C/m^3), $\vec{B}$ is the magnetic flux density (Wb/m^2), $\vec{H}$ is the magnetic field intensity (A/m), μ is the material's permeability (H/m), $\vec{J}$ is the electric current density (A/m^2).

1.7.2 Snell's Law

The law follows Fermat's principle of least time,

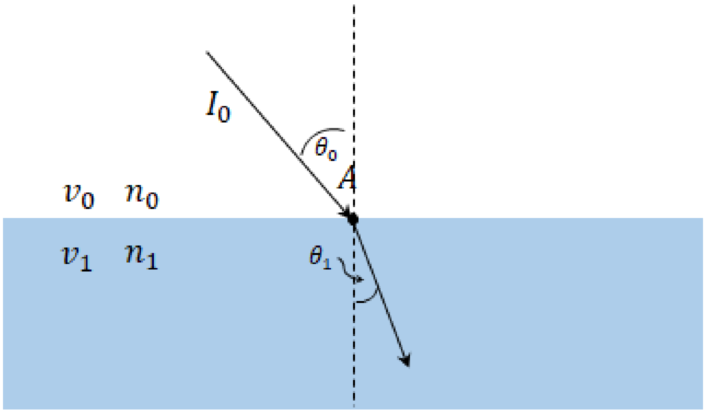

Figure 1-16: Light refraction schematic. Light is refracted in the interface between media of different refractive indices ($n_1 > n_0$). Light is "slowed down" in the higher refractive index media ($v_0 > v_1$), and the angle of refraction is less than the angle of incidence ($\theta_0 > \theta_1$).

The refractive index, n, is defined as a dimensionless number describing the speed of light in a material, v, in relation to the speed of light in vacuum, c. It is a fundamental physical property of matter, which depends on the electric and magnetic properties of the propagating media:

$$n = \frac{c}{v} = \sqrt{\varepsilon_r \mu_r} \qquad \text{Eq. 1-6}$$

$$\frac{\sin\theta_0}{\sin\theta_1} = \frac{v_0}{v_1} = \frac{n_1}{n_0} \qquad \text{Eq. 1-7}$$

1.7.3 Thin film interference and multilayers

Thin film interference is a phenomenon where light is reflected in the lower and upper boundaries of a thin film, enhancing, or reducing the intensity of light by constructive or destructive interference respectively. This physical phenomenon depends mainly on the light bending properties of the thin film, measured in terms of refractive index, the dimensions of the thin film, the frequency of light, and the angle of incidence.

A simple analysis can be applied combining Snell's law of refraction, and Bragg's law of diffraction. From Figure 1-17-a it is possible to deduce the difference in optical path length between the reflected rays R_1 and R_2:

$$G = n_1\left(\overline{AB} + \overline{BC}\right) - n_0\overline{AD} \qquad \text{Eq. 1-8}$$

$$G = 2n_1\overline{AB} - n_0\left(\overline{AC}\sin\theta_0\right) \qquad \text{Eq. 1-9}$$

$$G = 2n_1\left(\frac{d}{\cos\theta_1}\right) - 2d\,(n_0\sin\theta_0)\tan\theta_1 \qquad \text{Eq. 1-10}$$

Using Snell's Law,

$$G = 2n_1\left(\frac{d}{\cos\theta_1}\right) - 2d\,(n_1\sin\theta_1)\tan\theta_1 \qquad \text{Eq. 1-11}$$

Reordering terms,

$$G = 2dn_1\cos\theta_1 \qquad \text{Eq. 1-12}$$

Constructive interference occurs when the optical path difference, G, is equal to an integer multiple of the wavelength, λ, of light being propagated:

$$m\lambda = 2d\,n_1\cos\theta_1 \qquad \text{Eq. 1-13}$$

This effect can be enhanced in multilayer systems. A multilayer device is made-up of a stack of sequential thin film layers with different refractive indexes. The simplest form of multilayer devices consists of alternating layers of high and low refractive index materials with determined thicknesses, as shown in Figure 1-17-b. The optical behaviour of these 1-D systems can be described in a simple form, using the same logic as Eq. 1-8 through Eq. 1-13, leading to Eq. 1-14, for normal incidence and non-absorbing materials:

$$m\lambda_{max} = 2(n_1 d_1 + n_2 d_2) \qquad \text{Eq. 1-14}$$

where λ_{max} is the maximum reflection wavelength, m is the diffraction order, n_1 and n_2 are the refractive indexes of the high and low refractive index materials, and d_1 and d_2 are their respective thicknesses. As the refractive index contrast of the components is increased, selectivity of the transmitted and reflected wavelengths is increased [26]. When the optical path length is equal for each layer ($n_1\, d_1 = n_2\, d_2$), we have an ideal multilayer reflector, also known as Bragg mirror or a quarter-wave stack, and Eq. 1-14 becomes:

$$\frac{\lambda_{max}}{4} = n\, d \qquad \text{Eq. 1-15}$$

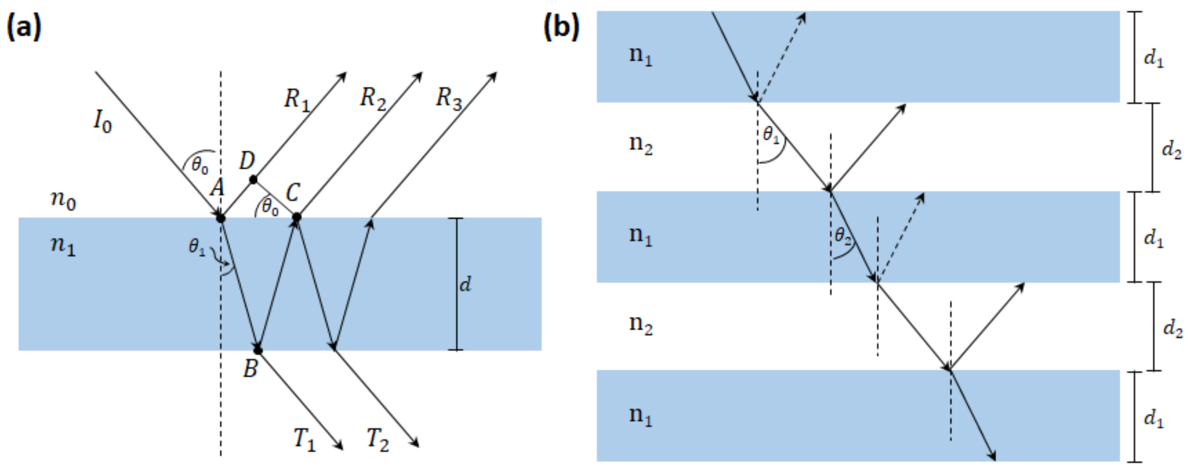

Figure 1-17: Scheme showing the path length difference of optical rays reflected in different surfaces of thin film (a), and alternating multilayer stack (b).

1.7.4 Closed packed colloidal crystals and 3D structures

A similar analysis can be applied to more complex, higher order 3D photonic crystals. Under similar conditions, equation 2 can be utilized as a good approximation, widely employed in literature [27]–[29]:

$$m\lambda = 2d_{hkl}\sqrt{n_{avg}^2 - \sin^2\alpha} \qquad \text{Eq. 1-16}$$

where α is the angle of incidence, d_{hkl} is the spacing between the close-packed planes (h, k, l), and n_{avg} is the average refractive index, which can be calculated from the materials volume fraction, ϕ, and lattice parameter, D:

$$n_{avg} = \phi_1 n_1 + (1 - \phi_1)n_2, \qquad \text{Eq. 1-17}$$

$$d_{hkl} = \frac{D\sqrt{2}}{\sqrt{h^2 + k^2 + l^2}}, \qquad \text{Eq. 1-18}$$

This equation illustrates how the optical properties, particularly the reflected wavelength, are related to the structure's physical parameters such as interplanar spacing (or lattice parameter) and refractive index.

1.7.5 Periodic structures and photonic crystals

Photonic crystals are periodic ordered microstructures, built from dielectric materials or building blocks, with a periodicity in the scale of visible light wavelength (~200-700 nm). Diffraction effects caused by the spatially periodic variation of the refractive index and dielectric function of these materials creates a photonic band gap (PBG) in the visible spectrum, inhibiting or forbidding the propagation of light at certain wavelengths; analogue to the electronic band gap in conventional semiconductors [30]–[32].

The concept of PBG was first proposed by Yablonovich and John in 1987 [33], [34], and has been the subject of extensive research up to this date due to the wide field of possible applications, such as photonics [35], [36], catalysis [37], [38], chemical [39], [40] and biochemical sensing [41], [42], sensors [43], and solar energy harvesting [44], [45].

Photonic band gap structures can be classified according to the structure's periodicity as one-dimensional (1-D), two-dimensional (2-D) and three-dimensional (3-D) as illustrated in Figure 1-18. The simplest form of PBG materials are 1-D thin film stacks, or Bragg reflectors. These consist of alternating thin layers of high and low refractive index materials, and display structural colour due to thin films and multilayer interference. An interesting concept of single-material Bragg reflectors has been developed by some research groups, alternating porous layers of a single material with different porosity, thus alternating the local average refractive index in each layer [46], [47].

2-D PBG structures usually consist of a regular array of dielectric rods, or periodically perforated dielectric slabs. 3-D photonic crystals on the other hand, are more complex structures, usually formed by an ordered array of spheres in a close-packed array (*e.g.*, face-centred cubic or hexagonal close-packed) or stacking of 2-D photonic structures or gratings.

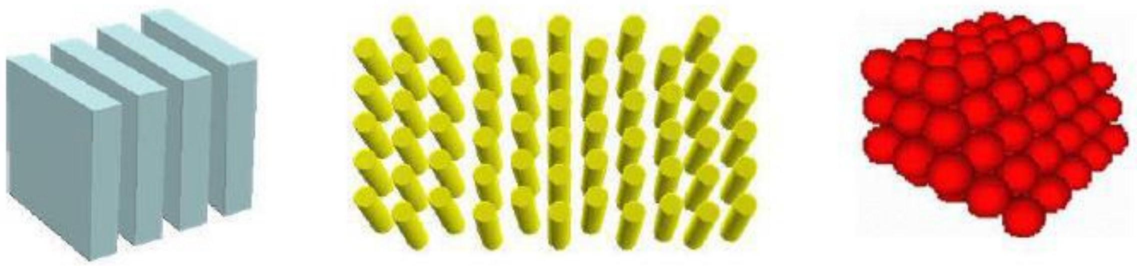

Figure 1-18: Photonic crystal structures: 1-D Bragg reflectors (left), 2-D hexagonal lattice rods (centre), 3-D opal structure (right) [32].

The light-matter interaction in photonic band gap structures can be described in detail using Maxwell's equations (Eq. 1-2 though Eq. 1-5) for electromagnetic waves applying the periodic medium condition (Eq. 1-19).

Periodic boundary condition $\varepsilon(\vec{r} + \overrightarrow{\Lambda_r}) = \varepsilon(\vec{r})$ Eq. 1-19 where $\overrightarrow{\Lambda_r}$ is a vector describing the translational symmetry of the periodic medium (m). A detailed study and expansion of this equations, and the corresponding physics and mathematics can be found elsewhere in literature [32], [36]. An important corollary from Maxwell's equations is that when dimensions of the photonic structure are scaled, the electromagnetic mode is the same, but the mode and frequency are scaled by the same factor. This means that photonic crystals can be, in principle, designed without specifying size, and subsequently fabricated on any scale [32].

Some examples for the photonic band structures of 1D and 3D periodic structures are presented in Figure 1-19, Figure 1-20, and Figure 1-21. A photonic band gap is formed when light within a specific range of frequencies in blocked in every direction by the photonic structure. Partial bands can be also found in a particular direction, or a range of directions, without necessarily forming a complete photonic band gap.

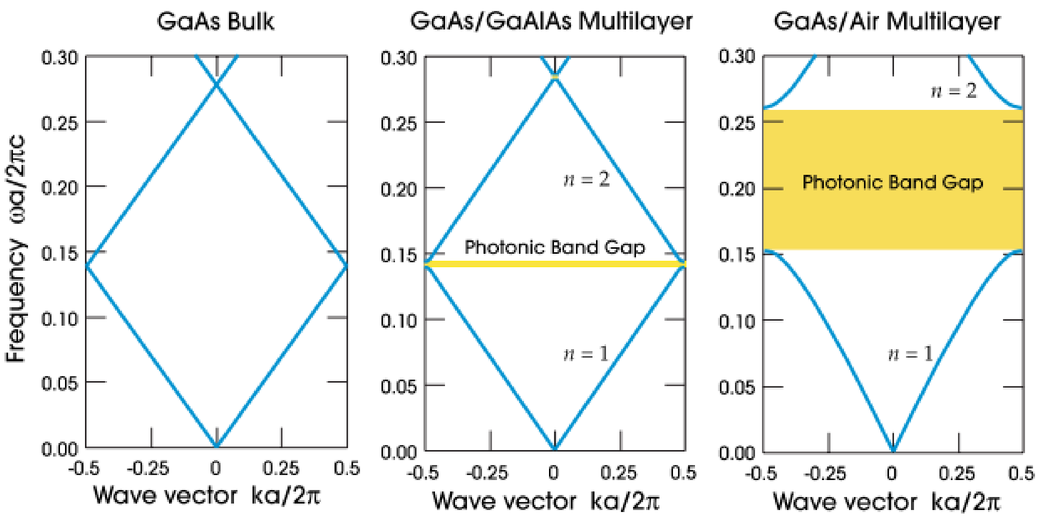

Figure 1-19: Photonic band structures for an on-axis propagations, as computed for three different multilayer film systems. The width of each layer in all three cases is equal to 0.5a. Left: every layer has the same dielectric constant ε=13 (bulk material). Centre: alternate layers ε_1=13 and ε_2=12. Right: alternate layers ε_1=13 and ε_2=11. Figure reproduced from [36].

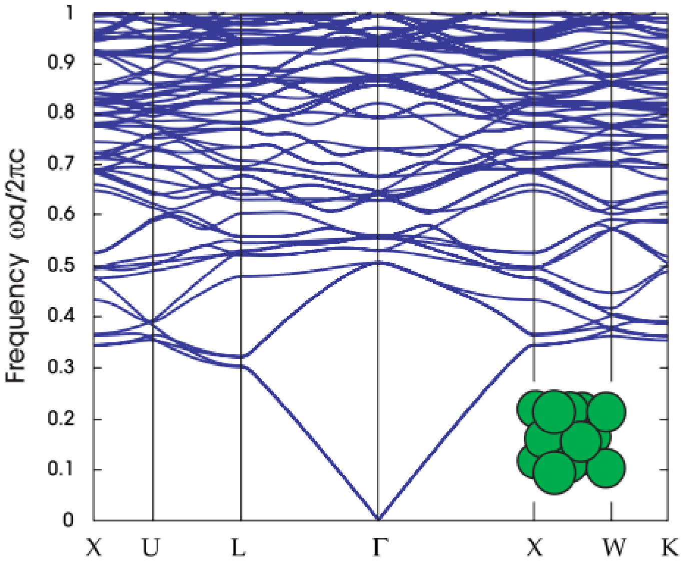

Figure 1-20: Photonic band-structure of a face-centred cubic (FCC) lattice of close-packed dielectric spheres (ε=13) in air (opal). Note the absence of a complete photonic band-gap [36].

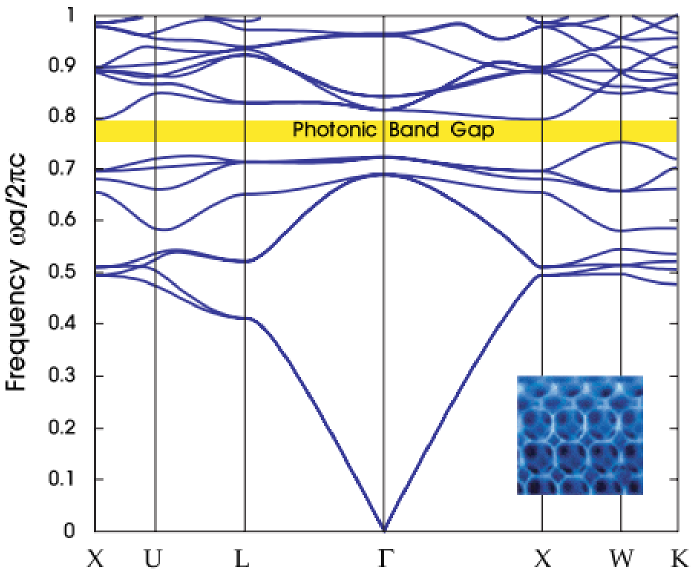

Figure 1-21: Photonic band-structure of an inverse opal structure, consisting of a face-centred cubic (FCC) lattice of close-packed air spheres in a dielectric matrix (ε=13). Note that there is a complete photonic band-gap between the eighth and ninth bands [36].

1.8 SUMMARY AND FINAL REMARKS

Understanding the underlying biological mechanisms in human vision and colour perception and the physics of light-matter interaction in optical devices can allow for the design and fabrication of optical devices that can help improve certain aspects of colour perception.

Colour vision deficiency (CVD) is a prevalent condition affecting over 8% of the male population (0.4% in women), affecting the ability of the individuals to recognize and distinguish between some colours. The most common form of CVD is the red-green type, affecting the long (L) and intermediate (M) wavelength photoreceptors in the human retina. The lack of one of these types of photoreceptors is known as dichromacy, while in anomalous trichromacy all three types of photoreceptors (L, M and S) are present, however, one of these has different spectral sensitivities to normal colour vision. In the case of red-green CVD, the main cause is associated to genetic conditions linked to the X chromosome, where the high degree of homology between the genes encoding the L and M-photopigment facilitates unequal homologous crossover or recombination between the genes, resulting in the deletion of one of these pigment genes or the formation of hybrid genes.

To date, there is no known and definitive solution for the correction of CVD. Different methods have been tested in the past, including active tools such as digital re-mapping of colour spaces, re-colouring of images, high contrast overlays, *etc*. in digital colour display devices, as well as passive tools such as wearable tinted spectacles and frequency selective optical filters. Gene therapy is a promising solution for CVD, successfully tested in mice and non-human primates, however, the technique is still experimental and the ethics and required prior testing makes it unlikely to lead to therapeutic application in human in the near future. Optical wearable devices designed for correction of colour perception in anomalous trichromacy are currently available in the market, however, the effectiveness of these is a contentious topic and scientific evidence supporting the claims made by manufacturers is scarce.

In this work, the potential for colour vision deficiency correction of frequency selective optical devices is evaluated, and numerical design methods are implemented for the fabrication of these devices based on multilayer and photonic structures.

CHAPTER 2: COLOUR APPEARANCE MODELS AND COLOUR VISION DEFICIENCY

2.1 ABSTRACT

This chapter presents an introduction to the concepts of colour appearance, chromatic adaptation, and colour vision deficiency, as well as a description and implementation of current mathematical models of human colour vision describing these phenomena. Red-green colour vision deficiency simulation methods were implemented, based on the spectral-shift, and cone-replacement hypotheses.

2.2 INTRODUCTION

Colorimetry is the science of measuring colour and human perception of colour. The concept of colour can be defined as a function of the human visual system in response to an external light stimulus, which depends on the relative and total amount of light reaching the visual system at different frequencies within the visible spectrum, and how the resulting physiological responses are combined in the neural pathway.

Historical accounts on the development of the concepts and ideas about colour vision and the relation to physical theories on the nature of light can be found in the literature [48]–[50]. The foundation and elaboration of the mathematical concepts of colour vision and colour appearance is presented in-depth in the books by Fairchild [5] and Hunt [51].

The following section provides a brief introduction to the historical context and development of mathematical models and experiments in the field of colorimetry and colour appearance models.

2.2.1 The Colour Matching Experiment

This experiment allows to study colour perception and estimate colour matching functions for a particular individual. It corresponds to a psychophysical test, meaning that it studies the relation between a physical stimulus which can be measured, such as light, and the subjective perceptions or sensations evoked by this stimulus, such as the perception of colour. It consists of matching a specific colour with a combination of two or more primary colours according to the subjective visual evaluation of an individual under study.

This experiment is an integral part on the foundation and basis of colorimetry, colour science, and trichromatic theory, and it is the best tool up to date to study colour perception in terms of the physical measurements of light.

The resulting CMFs and their standardization have allowed for the development and testing of colour theories, image processing techniques, photography, *etc*. These functions differ for different individuals depending on age, genetic conditions, *etc*., so generally CMFs are calculated as an average over a large test group. The colour of a stimulus is represented in the form of a tristimulus value, calculated from the spectral power distribution of the stimuli and a set of CMFs.

Maximum saturation method

This method was used obtain the matching data which form the basis of the CIE 1931 colour-matching functions [52]. In this method, an observer is presented with a half field illuminated by a monochromatic test light of a specific wavelength, and a half-field illuminated by a mixture of primary lights (generally monochromatic). The observer then adjusts the intensities and proportions of primary lights in order to match the colour of both half-fields (Figure 2-1-a), and data is obtained in the form of three different functions, the colour-matching functions (CMFs) $\bar{r}(\lambda)$, $\bar{g}(\lambda)$, and $\bar{b}(\lambda)$, corresponding to the fractions of each primary needed to match the monochromatic stimuli E_λ:

$$E_\lambda \sim \bar{r}(\lambda)\boldsymbol{R} + \bar{g}(\lambda)\boldsymbol{G} + \bar{b}(\lambda)\boldsymbol{B} \qquad \text{Eq. 2-1}$$

Generally, one of the primary lights is admixed to the test half-field, while the other two are mixed in the adjacent mixture half-field. This results from the fact that given the three chosen primaries, not all spectral colours can be formed by additive mixture of these, so in order to make a match there must be 'subtractive' colour mixing, by adding one of the primaries to the test light. This is represented in the CMFs as negative values for the primary being added to the test light.

Maxwell's matching method

Some of the first colour matching experiments were carried out by James Clerk Maxwell, better known for the development of electromagnetic theory. He designed an experiment using a rotating disk, in which three different coloured papers were arranged so that the relative proportions between the area of the different coloured sections could be changed between trials. The disk would be separated into two sections: a circular region in the centre, and an annular section surrounding it. This way, the test subjects should determine a combination of primaries in one on these regions to match an objective colour in the second. Later, Maxwell would design a device for mixing spectral lights, in order to match a white stimulus (Figure 2-1-b).

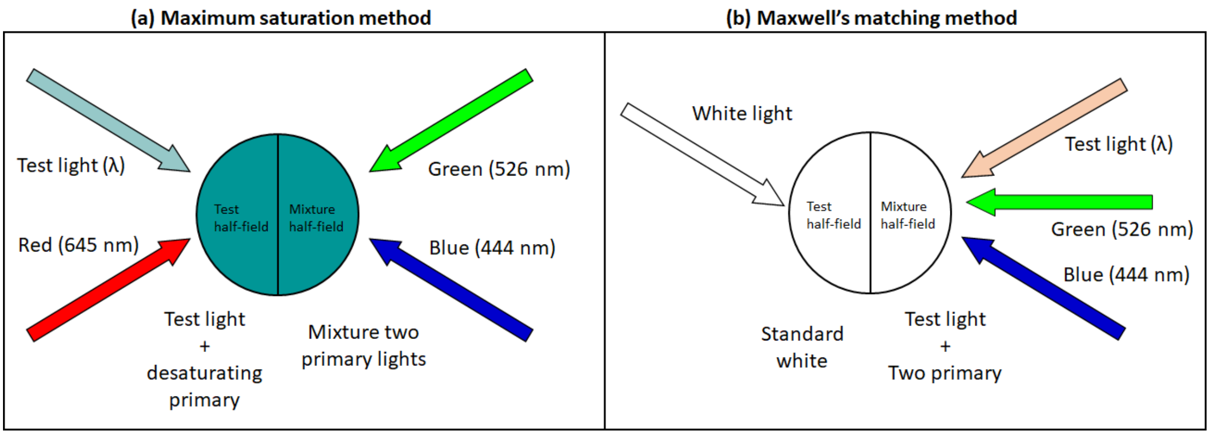

Figure 2-1: Colour-matching experiment: (a) Maximum saturation method, and (b) Maxwell's spectral light mixing method.

2.2.2 Properties of Colour Matching

Grassmann's laws

Named after German linguist and mathematician Hermann Günther Grassmann, who first proposed in 1853 a set of axioms in a 3-dimensional vector formulation, stressing the continuous nature of colour transitions [49], [53]. These laws describe crucial properties of colour matching, and are described with varying degrees of algebraic notations, sometimes expressed as corollaries of the original axioms. One modern interpretation of these four laws is presented below [52]:

1. Symmetry: if a light stimulus A matches stimulus B, then B matches A.

$$A \sim B \Leftrightarrow B \sim A \qquad \text{Eq. 2-2}$$

2. Transitivity: if light stimulus A matches B, and B matches C, then A matches C.

$$(A \sim B) \wedge (B \sim C) \Leftrightarrow (A \sim C) \qquad \text{Eq. 2-3}$$

3. Proportionality: if A matches B, then t*A matches t*B, where t is a constant of proportionality.

$$A \sim B \Leftrightarrow (t * A) \sim (t * B) \qquad \text{Eq. 2-4}$$

4. Additivity: If A matches B, and C matches D, then a combination of A and C matches the same combination of B and D (and a combination of B and C matches A and D).

$$(A \sim B) \wedge (C \sim D) \Leftrightarrow (A \oplus C) \sim (B \oplus D) \qquad \text{Eq. 2-5}$$

Grassmann's laws have been extensively tested and are widely accepted. A consequence of these laws is that colour matching is considered to be approximately linear and additive.

Uniqueness of colour matches

Colour matches are unique, meaning that any light stimulus is matched by a unique weighted combination of the three colour primaries. In other words, there is a single set of tristimulus values that describe the colour match of any given test light, and two lights that match each other will have identical tristimulus values.

Persistence of colour matches

Two matching light stimuli, under one set of viewing conditions, continue to match under different viewing conditions. This phenomenon is explained by the concepts of chromatic adaptation.

Consistency across observers

There should be agreement about colour matches across observers. That is to say that different observers should have the same (or similar) colour matching functions. While there is general agreement that colour matching functions remain mostly the same for most of the population, small individual differences are found, caused by small differences in photopigment sensitivities, as well as macular and optical densities.

As discussed in the previous chapter (Chapter 1: Background and Introduction), photopigments are encoded by genes, and differences can arise depending on the encoded genes, and their location within the gene array. These differences are small across normal trichromat observers but some genetic conditions, such as those generated by unequal homologous crossover or recombination between different pigment genes, can result in large differences in individual pigment absorption.

Abney's Law

The principle according to which the total luminance of light composed of several wavelengths is equal to the sum of luminances of its monochromatic components. Alternatively: "the impression on the eyes of a mixed light is equal to the sum of the impressions of each of the components of the light" [54].

The König Hypothesis

Dichromatic vision is a reduced form of trichromatic vision, where one of the three cones is missing, while the other two remain unchanged with respect to their spectral sensitivity.

2.2.3 Trichromatic Theory

Trichromatic theory states that there are three types of receptors sensitive to different frequencies within the visible spectrum, in the long (L), medium (M), and short (S) wavelength regions of the spectrum, corresponding approximately to red, green, and blue light respectively. It is based extensively on the work and research by Maxwell, Young, and Helmholtz [49].

One of the first scientific formulations of trichromatic theory was postulated by Young, in the Bakerian Lecture, on the theory of light and colours:

"… it is almost impossible to conceive each sensitive point of the retina to contain an infinite number of particles, each capable of vibrating in perfect unison with every possible undulation, it becomes necessary to suppose the number limited, for instance to the three principal colours, red, yellow, and blue, of which the undulations are related in magnitude … each sensitive filament of the nerve may consist of three portions, one for each principal colour" [55].

Later contributions, such as Grassmann's three-dimensional vector formulation on the nature of colour, supported the Young hypothesis and trichromatic theory, and helped Helmholtz to show experimentally that most colours have complementary colours, with the exception of a region within the green portion of the visible spectrum, whose complementary colour is purple (which is made of a mixture of red and blue spectral colours).

Evidence for trichromatic theory comes from psychophysics and colour matching experiments: all colours of the spectrum can be matched by an appropriate additive/subtractive combination of three primaries, in agreement with a triplet sensory system. The colour (or wavelength) of these primaries is not of critical importance, as long as they are independent from each other, in other words, the colour of any of these primaries cannot be matched by a combination of the other two.

While trichromatic theory can explain many aspects of colour perception, such as colour mixing and colour matching, it cannot account for certain phenomena, such as complementary afterimages.

2.2.4 Opponent Colour Theory

This theory was first proposed by Ewald Hering in 1978 [48], based on the analysis of colour sensations, rather than the physical stimuli which results in the sensation of colour. It assumes there are six unique independent colour channels (red, green, blue, yellow, black, and white), which are activated by the absorption of light in the photopigment receptors, resulting in the activation of the visual neural system. This activity however is transmitted in three channels consisting of opposing pairs of colour activity: black-white, red-green, and blue-yellow. The activation of a specific channel will in turn diminish the activity of the opposing colour pair. For example, it has been long pointed out that certain colour combinations, such as “yellowish-blue” or “reddish-green”, are simply inconceivable, while other combinations are much more intuitive (a “reddish-yellow” is orange, and “blueish-green” is turquoise). The simultaneous and equal activation of both colours in an opposing channel cancel out to zero.

This theory provides a model for the perception of colour, supported by empirical evidence and observations, such as the optical illusion in complementary after-images (see Figure 2-2). When staring at an image for a prolonged period, the photopigment receptors become “bleached”, as the chromophores in the photoreceptors undergo photo-isomerization, and the visual system adapts for overstimulation, momentarily losing sensitivity towards that colour (see Section 2.4 Chromatic Adaptation and Colour Appearance). When rapidly changing the visual field to a background white, the areas of the retina which were adapted for overstimulation will perceive a signal corresponding to the opposing colour, as sensitivity towards the original colour is diminished, activating the opposing colour response. This effect is only transient, and the afterimage should start disappearing as the chromophores are regenerated through the retinal cycle, and the visual system is re-adapted.

Trichromatic and opponent colour were thought of as two independent theories, both with their own advantages. However, these theories are complementary, and both help to explain the process of colour vision at different stages of the visual system. Trichromatic theory is applicable at the cone receptor level in the retina, while opponent process theory is concerned to subsequent neural stages of visual processing.

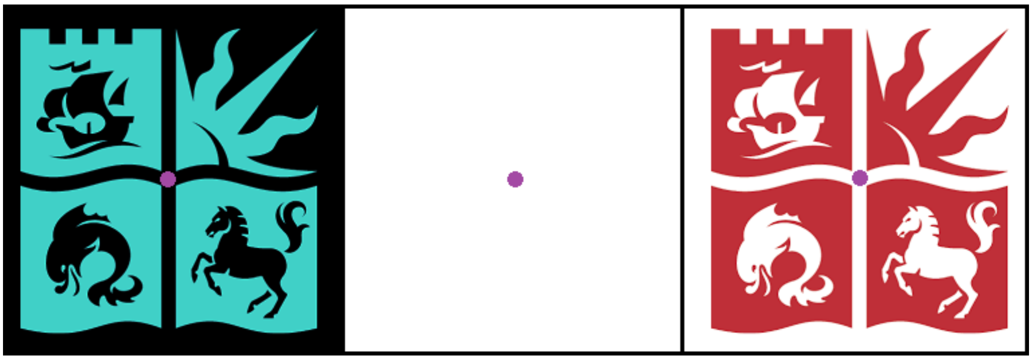

Figure 2-2: Optical illusion: example of complementary (or negative) afterimage effect. Stare and focus on the centre of the left or rightmost image for at least 30-60 seconds, then quickly focus on the point at the centre image. An image should appear, corresponding to the "negative" of the original image.

2.3 CIE COLOUR SPACES

The International Commission on Illumination (CIE, abbreviated from the French, *Commission Internationale de l'Éclairage*) is an organization devoted to the cooperation, dissemination, and exchange of information on matters of light, illumination, and colour.

In 1924, it established the standard photopic observer, defined by the spectral luminous efficiency function $V(\lambda)$, and the standard scotopic observer, defined by $V'(\lambda)$. These functions describe the variation in perceived brightness as a function of wavelength under photopic (mediated by cone photoreceptors) and scotopic (rod-mediated) conditions.

In 1931, the Commission published the formulation of the CIE 1931 XYZ colour space and defined the 1931 2° standard observer and corresponding colour matching functions, with the intention of establishing an international standard on colorimetric specifications. These were based on colour matching experiments conducted independently by Wright and Guild [50]. The CIE 1931 CMFs characterize the colour-matching experiment performed on an "average" or "standard" human observer with normal colour vision. These functions are available in the form of $\bar{r}(\lambda), \bar{g}(\lambda), \bar{b}(\lambda)$, corresponding to the ratio of primaries in the colour matching experiment, and in the form of $\bar{x}(\lambda), \bar{y}(\lambda), \bar{z}(\lambda)$, both of which specify the colour spaces known as CIE RGB and CIE XYZ. The CIE XYZ CMFs correspond to a linear transformation of the original RGB functions, obtained by empirically from colour matching, to a set of CMFs based on a set of "imaginary" colour primaries. The transformation was chosen in order for this new set of CMFs to satisfy some desirable properties:

- All values are to be positive $(\bar{x}(\lambda), \bar{y}(\lambda), \bar{z}(\lambda) \geq 0, \forall\lambda)$, simplifying hand-made calculations done at the time, as well as avoiding the unintuitive negative values in colour specification.
- The $\bar{y}(\lambda)$ function is equal to the photopic luminous efficiency function $\bar{V}(\lambda)$.
- The white point for the equal-energy illuminant has tristimulus values $X = Y = Z = 1$ (chromaticity coordinates, $x = y = z = 1/3$).
- The full gamut of visible colours lies inside the triangle $[x, y] = [1,0], [0,0], [1,0]$ in the xy chromaticity diagram.

In 1964, the CIE released the 10° standard observer, and corresponding CMFs. Based on the empirical colour-matching data collected by Stiles and Burch (1959), and Speranskaya (1959). In 1976, the CIELAB and CIELUV colour spaces were developed.

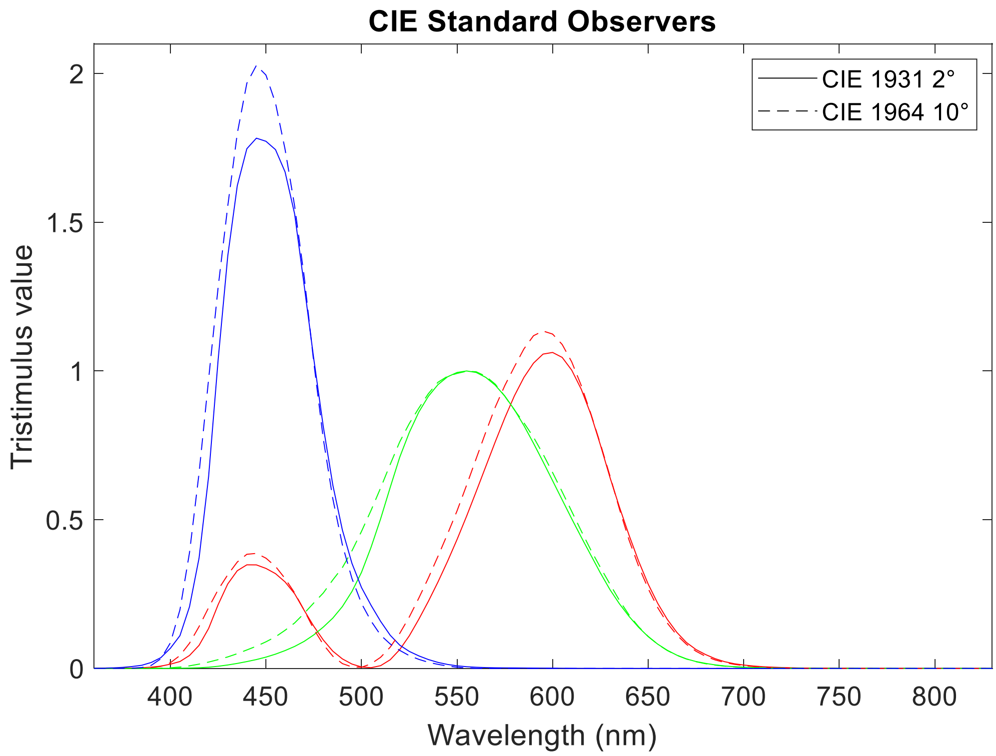

Figure 2-3: The CIE standard colorimetric observer: CIE 1931 2° and CIE 1964 10° colour matching functions.

Tristimulus values defined by the International Commission on Illumination (*Commission Internationale de l'Éclairage*, CIE) [56].

For reflecting surfaces, with spectral reflectance $R(\lambda)$ under an illumination $S(\lambda)$, the tristimulus values are calculated as follows:

$$X = k\int_{\lambda} R(\lambda)S(\lambda)\bar{x}(\lambda)d\lambda \qquad \text{Eq. 2-6}$$

$$Y = k\int_{\lambda} R(\lambda)S(\lambda)\bar{y}(\lambda)d\lambda \qquad \text{Eq. 2-7}$$

$$Z = k\int_{\lambda} R(\lambda)S(\lambda)\bar{z}(\lambda)d\lambda \qquad \text{Eq. 2-8}$$

where k is a normalizing factor, defined by:

$$k = \frac{100}{\int_{\lambda} S(\lambda)\bar{y}(\lambda)d\lambda} \qquad \text{Eq. 2-9}$$

In order to describe the full colour gamut in human vision, a three-dimensional space is required to describe every colour according to all the possible values for the tristimulus coordinates. A chromaticity diagram is a two-dimensional space given by two independent parameters (for example, x and y), which specify the quality of a colour regardless of its luminance. The CIE xy chromaticity diagram is presented in Figure 2-4. The limits of this diagram, also known as the spectral locus, are given by the colour specification for monochromatic light stimuli for each wavelength within the visible spectrum (spectral light). All possible combinations of spectral lights, which describe all possible spectra in the visible spectrum, lie within this diagram. Note that purple is not a spectral colour and is formed by the combination of blue and red spectral lights.

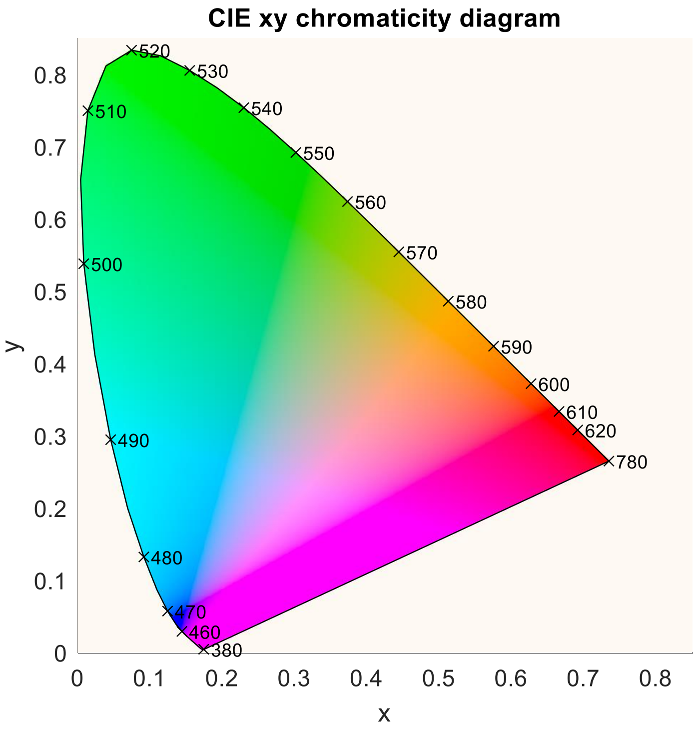

Figure 2-4: The CIE xy chromaticity diagram. Wavelength for spectral colours (monochromatic stimuli) are marked in nanometres.

For the CIE xy diagram, chromaticity coordinates are calculated using:

$$x = \frac{X}{X + Y + Z} \quad \text{Eq. 2-10}$$

$$y = \frac{y}{X + Y + Z} \quad \text{Eq. 2-11}$$

$$z = \frac{z}{X + Y + Z} \quad \text{Eq. 2-12}$$

The CIE xy chromaticity diagram is the most widely used diagram, but it is non-equidistant, or non-uniform, in terms of colour difference perception, meaning that there is a non-linear relation between perceived colour differences and the Euclidian distance between coordinates in the chromaticity diagram. The lack of perceptual uniformity incentivised the exploration of non-linear transformations of the XYZ colour system, resulting in the creation of colour spaces such as the 1976 CIE L*a*b (CIELAB) and CIE L*u*v* (CIELUV).

Figure 2-5 illustrates the perceptual non-uniformity of the xy chromaticity diagram, and the more uniform u’v’ chromaticity diagram. The ellipses show the limits of colour difference perception (scaled by a factor of 10 for visualization). The area of the ellipses in the xy chromaticity diagram vary widely depending on the region within the diagram.

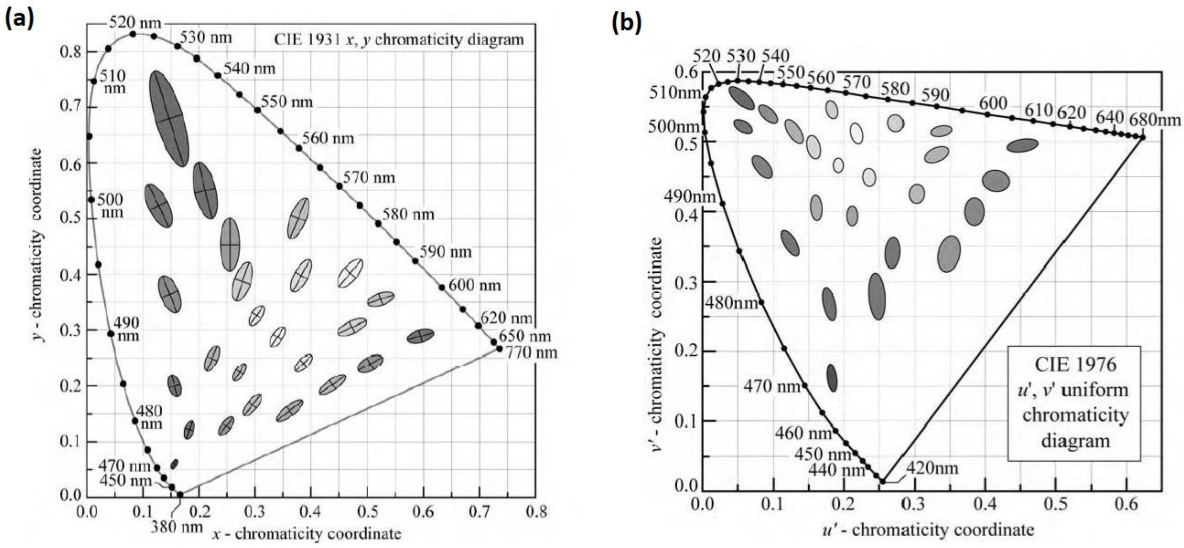

Figure 2-5: MacAdam ellipses (showing barely noticeable colour differences) plotted in the CIE 1931 xy chromaticity diagram (a), and their transformation to uniform 1976 CIE u’v’ chromaticity coordinates (b). For better visualization, the axes of the ellipses are scaled to ten times their actual length (images reproduced from Schubert [57])

The deficiency of the xy chromaticity with respect to perceptual uniformity is strongly reduced, but not eliminated, in the u’v’ chromaticity diagram. In the later, the ellipses areas are more similar, and the colour difference between coordinates within the diagram is approximately proportional to the geometric distance between them [57].

The total number of differentiable chromaticities can be calculated by dividing the total area of the spectral locus by the average area of the MacAdam ellipses, yielding approximately 50,000 distinct chromaticities. When taking into account lightness variations, the number of differentiable colours is estimated around 10^6.

2.3.1 CIELAB

Defined in 1976 by the CIE. It was developed as a colour space to be used for the specification of colour differences. CIELAB defines colour in terms of three values: lightness, L*, ranging from 0 to 100 for black to a diffuse white respectively, and two chromaticity values, a* and b*, corresponding to the red-green and blue-yellow chroma perception respectively. The values of a* and b* can take both positive (red, yellow) and negative values (green, blue), and are equal to zero for achromatic stimuli. The limit values of a* and b* are given by the physical properties of the material and the specific implementation of the model, rather than the equations themselves.

$$L^* = 116[f(Q_Y)] - 16 \qquad \text{Eq. 2-13}$$

$$a^* = 500[f(Q_X) - f(Q_Y)] \qquad \text{Eq. 2-14}$$

$$b^* = 200\left[f\left(Q_y\right) - f(Q_Z)\right] \qquad \text{Eq. 2-15}$$

where,

$$Q_X = \left(\frac{X}{X_n}\right); \qquad Q_Y = \left(\frac{Y}{Y_n}\right); \qquad Q_Z = \left(\frac{Z}{Z_n}\right) \qquad \text{Eq. 2-16}$$

$$f(Q_i) = Q_i^{\frac{1}{3}} \qquad \text{If} \qquad Q_i > \left(\frac{6}{29}\right)^3 \qquad \text{Eq. 2-17}$$

$$f(Q_i) = \frac{841}{108}Q_i + \frac{4}{29} \qquad \text{If} \qquad Q_i \leq \left(\frac{6}{29}\right)^3 \qquad \text{Eq. 2-18}$$

CIE 1976 lightness: L^*, as defined in Eq. 2-13 Eq. 2-19

CIE 1976 chroma: $$C^*_{ab} = (a^{*2} + b^{*2})^{\frac{1}{2}} \qquad \text{Eq. 2-20}$$

CIE 1976 hue angle: $$h_{ab} = arctan\left(\frac{b^*}{a^*}\right) \quad \text{Eq. 2-21}$$

To evaluate differences in colour appearance aspects between two different stimuli, the total colour difference and hue differences are defined:

CIE 1976 colour difference $$\Delta E^*_{ab} = [(\Delta L^*)^2 + (\Delta a^*)^2 + (\Delta b^*)^2]^{\frac{1}{2}} \quad \text{Eq. 2-22}$$

CIE 1976 hue difference $$\Delta H^*_{ab} = k[(\Delta E^*_{ab})^2 - (\Delta L^*)^2 - (\Delta C^*_{ab})^2]^{\frac{1}{2}} \quad \text{Eq. 2-23}$$

$k = -1$ if $\Delta h_{ab} < 0$, $k = 1$ elsewhere

With respect to differentiation of colours, a standard observer can differentiate colours as follows [58]:

- $0 < \Delta E < 1$ - observer does not notice the difference;
- $1 < \Delta E < 2$ - only experienced observers can notice the difference;
- $2 < \Delta E < 3.5$ - unexperienced observers also notices the difference;
- $3.5 < \Delta E < 5$ - clear difference in colour is noticed;
- $5 < \Delta E$ - observers notices two different colours.

The CIELAB dimensions can be combined in a three-dimensional cartesian space, or in cylindrical coordinates according to chroma (C^*_{ab}) and hue angle (h_{ab}).

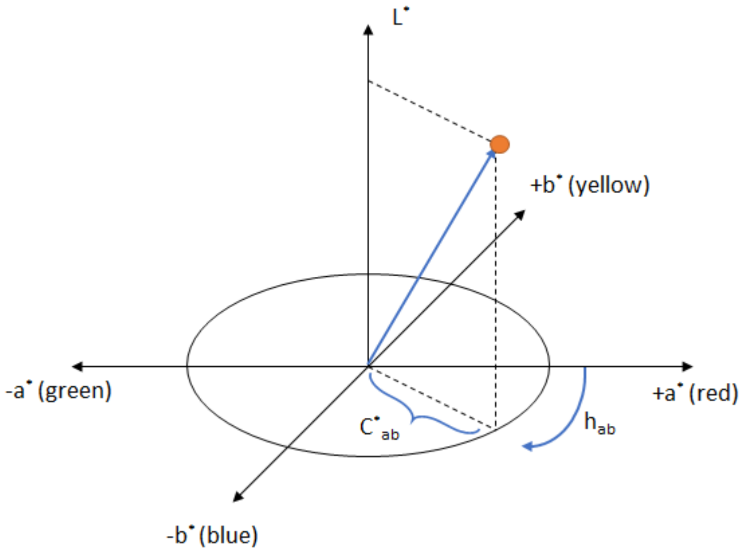

Figure 2-6: Cartesian and polar representation of the CIELAB colour space.

2.3.2 CIELUV

This is an updated version of the CIE 1964 UVW colour space and is an attempt to define a space presenting uniformity in the perception of colour differences.

$$L^* = \begin{cases} \left(\frac{29}{3}\right)^3 \frac{Y}{Y_n}, & \frac{Y}{Y_n} \leq \left(\frac{6}{29}\right)^3 \\ 116\left(\frac{Y}{Y_n}\right)^{\frac{1}{3}} - 16, & \frac{Y}{Y_n} > \left(\frac{6}{29}\right)^3 \end{cases} \qquad \text{Eq. 2-24}$$

$$u^* = 13L^*(u' - u'_n) \qquad \text{Eq. 2-25}$$

$$v^* = 13L^*(v' - v'_n) \qquad \text{Eq. 2-26}$$

$$u' = \frac{4X}{X + 15Y + 3Z} \qquad \text{Eq. 2-27}$$

$$v' = \frac{9Y}{X + 15Y + 3Z} \qquad \text{Eq. 2-28}$$

Chroma, hue, and colour difference formulae are calculated in the same way as for CIELAB (see Eq. 2-20 through Eq. 2-23, replacing the variables and subscripts a^*, b^* for u^*, v^*).

The structure of the CIELUV space is similar to CIELAB, with the exception of the subtractive adaptation transform on CIELUV ($u' - u'_n, v' - v'_n$), rather than the multiplicative normalization of tristimulus values on CIELAB ($X/X_n, Y/Y_n, Z/Z_n$). Both CIELAB and CIELUV were adopted simultaneously by the CIE in 1976.

In 1994, the CIE recommended an updated formula for colour difference based on the CIELAB space, known as ΔE^*_{94}, followed by the CIE DE200 colour difference formula.

2.3.3 Colourspace transformation matrices

The transformation of tristimulus values across different colourspaces is dependent on the primaries that define each space. In the case of linear transformations, the process can be written in terms of the transformation matrix. Consider the transformation between two colourspaces, XYZ to RGB, the coefficients for the linear transformation correspond to the value of the tristimulus values in the destination space, RGB, evaluated for the wavelength of primaries of the XYZ colourspace, e_1, e_2, and e_3:

$$\begin{aligned} R(\lambda) &= R(e_1)X(\lambda) + R(e_2)Y(\lambda) + R(e_3)Z(\lambda) \\ G(\lambda) &= G(e_1)X(\lambda) + G(e_2)Y(\lambda) + G(e_3)Z(\lambda) \\ B(\lambda) &= B(e_1)X(\lambda) + B(e_2)Y(\lambda) + B(e_3)Z(\lambda) \end{aligned} \qquad \text{Eq. 2-29}$$

$$[RGB]^T = (T_{XYZ \to RGB})[XYZ]^T \qquad \text{Eq. 2-30}$$

$$(CMF_{RGB})^T = (T_{XYZ \to RGB})(CMF_{XYZ})^T \qquad \text{Eq. 2-31}$$

$$(T_{XYZ\to RGB}) = (T_{RGB\to XYZ})^{-1} \quad \text{Eq. 2-32}$$

$$(T_{XYZ\to RGB}) = \begin{bmatrix} R(e_1) & G(e_1) & B(e_1) \\ R(e_2) & G(e_2) & B(e_2) \\ R(e_3) & G(e_3) & B(e_3) \end{bmatrix} \quad \text{Eq. 2-33}$$

2.3.4 Physiologically based CMFs: Cone Fundamentals

In 2005, the CIE released a technical report, establishing a fundamental chromaticity diagram with physiologically significant axes [59]. Based on the Stiles and Burch (1959) CMFs, it follows the ideas put forward by Stockman and Sharpe [60] on the application of the König's hypothesis, and using data for spectral sensitivity functions of dichromats in order to derive the spectral sensitivity function of the long (L), medium (M), and short-wave sensitivities (L) of cone photoreceptors. The L, M, and S sensitivity functions are called the "cone fundamentals", and they represent the actual human visual system response light in the visible spectrum.

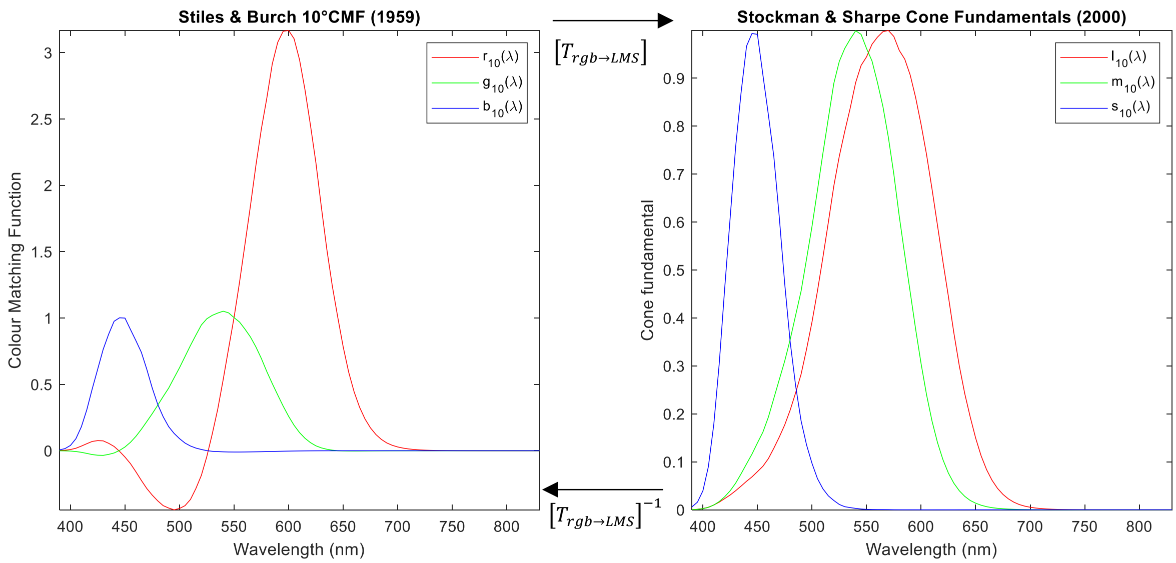

Figure 2-7: (Left) Stiles & Burch 10° CMF; (Right) Stockman & Sharpe cone spectral sensitivities for the long (L), medium (M), and short wavelengths (S).

The cone fundamentals do not correspond directly to the photopigment absorbance, but they result from the combined effect of cone photopigment absorbance along macular and ocular media. These are obtained from the transformation of Stiles and Burch 10° colour matching functions to cone fundamentals:

$$\begin{bmatrix} \bar{l}_{10}(\lambda) \\ \bar{m}_{10}(\lambda) \\ \bar{s}_{10}(\lambda) \end{bmatrix} = \left[T_{rgb\to LMS}\right] \begin{bmatrix} \bar{r}_{10}(\lambda) \\ \bar{g}_{10}(\lambda) \\ \bar{b}_{10}(\lambda) \end{bmatrix} \qquad \text{Eq. 2-34}$$

$$\left[T_{rgb\to LMS}\right] = \begin{bmatrix} 0{,}192325269 & 0{,}749548882 & 0{,}0675726702 \\ 0{,}0192290085 & 0{,}940908496 & 0{,}113830196 \\ 0 & 0{,}0105107859 & 0{,}991427669 \end{bmatrix} \qquad \text{Eq. 2-35}$$

In the same way, the cone fundamentals can be transformed from LMS to CIE XYZ using the transformation (for 2° field, under D65 illumination):

$$[T_{LMS\to XYZ}] = \begin{bmatrix} 1.9474 & -1.4145 & 0.3648 \\ 0.6899 & 0.3483 & 0 \\ 0 & 0 & 1.9349 \end{bmatrix} \qquad \text{Eq. 2-36}$$

The mathematic expansion and sourced psychophysical data is available in the CIE technical reports [59], [61]. However, a summary of the steps used to calculate the photopigment absorption spectra is presented below:

- cone fundamentals are calculated from Stiles and Burch 10° CMFs;
- apply lens pigment and other ocular media optical density, $D_{\tau,ocul}$;
- apply macular pigment optical density (for 10°), $D_{\tau,macula}$;
- cone photopigment optical density (10°), $D_{\tau,L/M/S}$;

- the result is the photopigment low density spectral absorbance ($A_{i,0(L/M/S-pigment)}(\lambda)$), which is independent of field of view, age, and other effects in macular and ocular media (Figure 2-8).

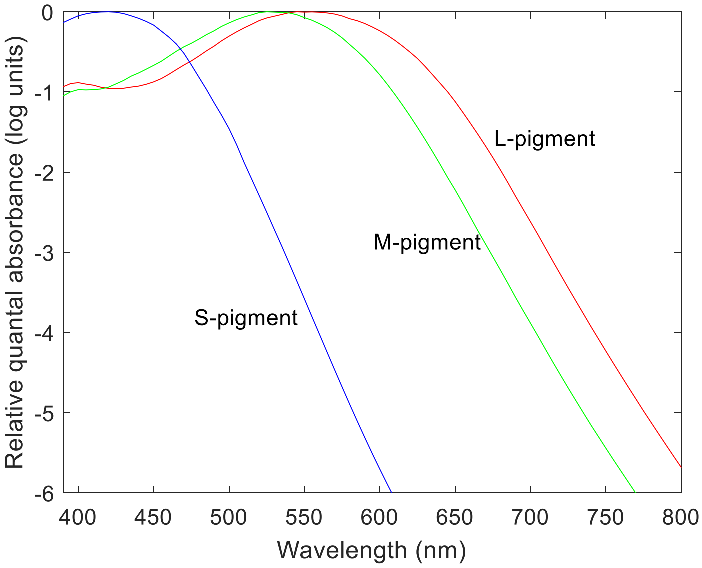

Figure 2-8: Low density absorbance spectra of cone photopigments, $A_{i,0}$.

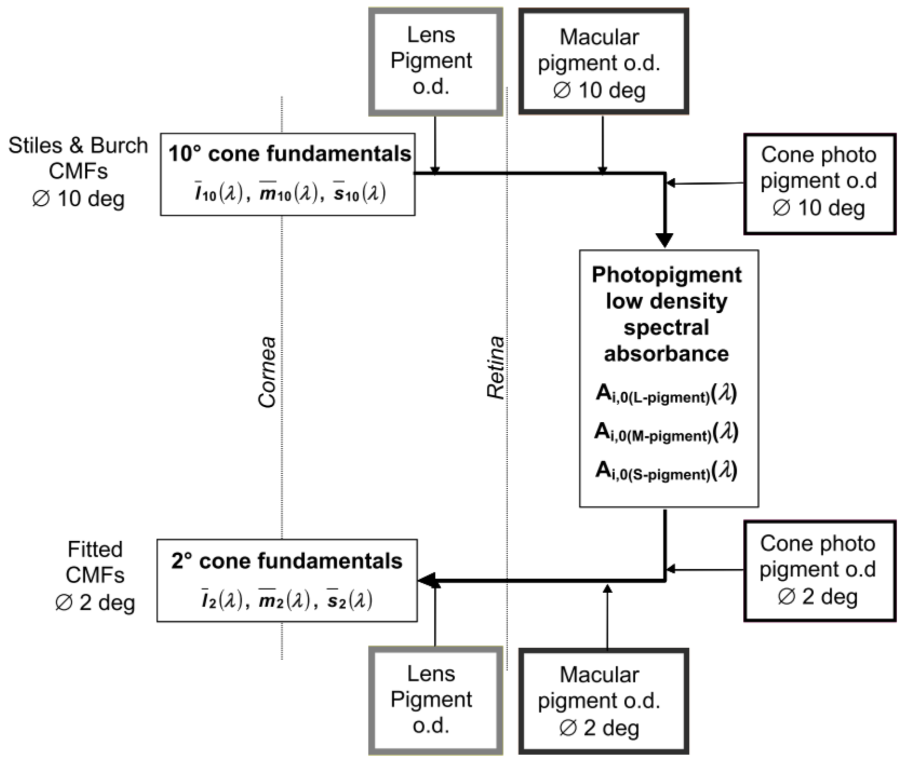

Figure 2-9: Schematic representation of the derivation of the 2° cone fundamentals from the 10° cone fundamentals. Reproduced from [59].

From the photopigment low density absorbance, it is possible to estimate different sets of cone fundamentals, for different conditions, such as different field of view, or changes in the lens optical density due to ageing. An example on how to calculate the 2° cone fundamentals is represented in Figure 2-9.

2.3.5 Calculating cone fundamentals from photopigment spectral absorbance

In this work, the interest is centred on estimating cone fundamentals from the photopigment spectral absorbance, $A_{i,0}$. The mathematical expansion of this operation is summarised below:

1- The optical density template of the macular pigment, $D_{\tau,macula}$, is calculated according to the field of view, fs (2-10°):

$$D_{\tau,macula}^{max} = 0.485 * e^{(-fs/6.132)} \qquad \text{Eq. 2-37}$$

2- Peak densities of the visual pigments, $D_{\tau,(L/M/S-cone)}^{max}$:

$$D_{\tau,(L-cone)}^{max} = 0.38 + 0.54 * e^{(-fs/1.333)} \qquad \text{Eq. 2-38}$$

$$D_{\tau,(M-cone)}^{max} = 0.38 + 0.54 * e^{(-fs/1.333)} \qquad \text{Eq. 2-39}$$

$$D_{\tau,(S-cone)}^{max} = 0.30 + 0.45 * e^{(-fs/1.333)} \qquad \text{Eq. 2-40}$$

This formula yields values of 0.5 and 0.38 at 2° and 10° respectively for the L- and M-cones, and 0.4 and 0.3 for S-cones.

3- The fraction of incident light at the retina level absorbed by the cones, $\alpha_{i,l/m/s}$:

$$\alpha_{i,l}(\lambda) = 1 - 10^{\left[-D_{\tau,(L-cone)}^{max} * A_{i,0(L-pigment)}(\lambda)\right]} \qquad \text{Eq. 2-41}$$

$$\alpha_{i,m}(\lambda) = 1 - 10^{\left[-D^{max}_{\tau,(M-cone)} * A_{i,0(M-pigment)}(\lambda)\right]} \quad \text{Eq. 2-42}$$

$$\alpha_{i,s}(\lambda) = 1 - 10^{\left[-D^{max}_{\tau,(S-cone)} * A_{i,0(S-pigment)}(\lambda)\right]} \quad \text{Eq. 2-43}$$

4- Finally, the LMS cone fundamentals are calculated in terms of the fraction of incident light absorbed by the cones, the optical density of visual pigments:

$$\bar{l}(\lambda) = \alpha_{i,l}(\lambda) * 10^{\left[-D^{max}_{\tau,macula} * D^{relative}_{macula}(\lambda) - D_{\tau,ocul}(\lambda)\right]} \quad \text{Eq. 2-44}$$

$$\bar{m}(\lambda) = \alpha_{i,m}(\lambda) * 10^{\left[-D^{max}_{\tau,macula} * D^{relative}_{macula}(\lambda) - D_{\tau,ocul}(\lambda)\right]} \quad \text{Eq. 2-45}$$

$$\bar{s}(\lambda) = \alpha_{i,s}(\lambda) * 10^{\left[-D^{max}_{\tau,macula} * D^{relative}_{macula}(\lambda) - D_{\tau,ocul}(\lambda)\right]} \quad \text{Eq. 2-46}$$

2.3.6 Luminous Efficiency Function

The luminous efficiency function, $V_F(\lambda)$, represents the average spectral sensitivity of visual perception to a light stimulus. Under photopic vision, perception of light is cone-mediated, and the luminous efficiency function is dependent on the cone spectral sensitivities. Current models for of photopic vision, based on Sharpe *et al.* work [60]–[63] consider the luminous efficiency as a function by the retinal and higher stages of neural processing as a weighted combination of the L and M-cone responses, normalised by a factor to unity peak.

$$V_F(\lambda) = \frac{\alpha \bar{l}(\lambda) + \beta \bar{m}(\lambda)}{C} \quad \text{Eq. 2-47}$$

For 2° field size

$$V_F(\lambda) = \frac{1.98064704\ \bar{l}(\lambda) + \bar{m}(\lambda)}{2.87090767} = 0.68990272\ \bar{l}(\lambda) + 0.34832189\ \bar{m}(\lambda) \quad \text{Eq. 2-48}$$

For 10° field size

$$V_{F,10}(\lambda) = \frac{1.98137697\, \bar{l}_{10}(\lambda) + \bar{m}_{10}(\lambda)}{2.85979294} = 0.69283932\, \bar{l}_{10}(\lambda) + 0.34967567\, \bar{m}_{10}(\lambda) \qquad \text{Eq. 2-49}$$

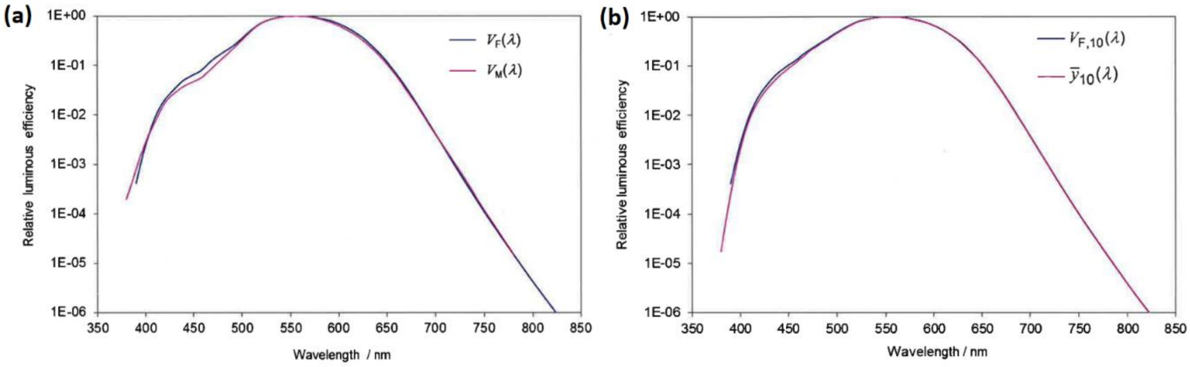

Figure 2-10: Comparison of relative spectral luminous efficiency function in terms of energy (log-scale): (a) 2° cone-fundamental-based, $V_F(\lambda)$, and CIE 1988 spectral luminous efficiency function, $V_M(\lambda)$; (b) 10° cone-fundamental-based, $V_{F,10}(\lambda)$, and CIE 1964 spectral luminous efficiency function, $\bar{y}_{10}(\lambda)$ [61].

2.4 CHROMATIC ADAPTATION AND COLOUR APPEARANCE

Adaptation refers to the ability of the human visual system to adjust according to changes in illumination, preserving the perceived colour of objects despite the wide variation in the spectral power distribution and intensity of different illumination sources.

Chromatic adaptation transforms can be divided into three groups: those that occur as parts of uniform colour spaces; those that depend on normalization of cone responses; and those that form part of a colour appearance model (CAM) [51].

The CIE colour systems, CIELAB and CIELUV, fall within this first category. While these can be utilized as simple colour appearance models, they can only account for chromatic adaptation due to changes in illuminant, and fail to predict the change in appearance due to changes in luminance level, background, or surround [64].

In the second group, we can identify chromatic adaptation transforms such as the Von Kries transform. Although Von Kries-type transforms are useful, they are not always accurate.

In the third group are more elaborated models and formulae, such as the CAT97 and CAT02 transforms. These models include a Von Kries-type chromatic adaptation, with a different set of cone sensitivity functions. Figure 2-11 shows the cone sensitivity functions used in Von Kries transform, CAT02, and the Stockman & Sharpe LMS cone fundamentals.

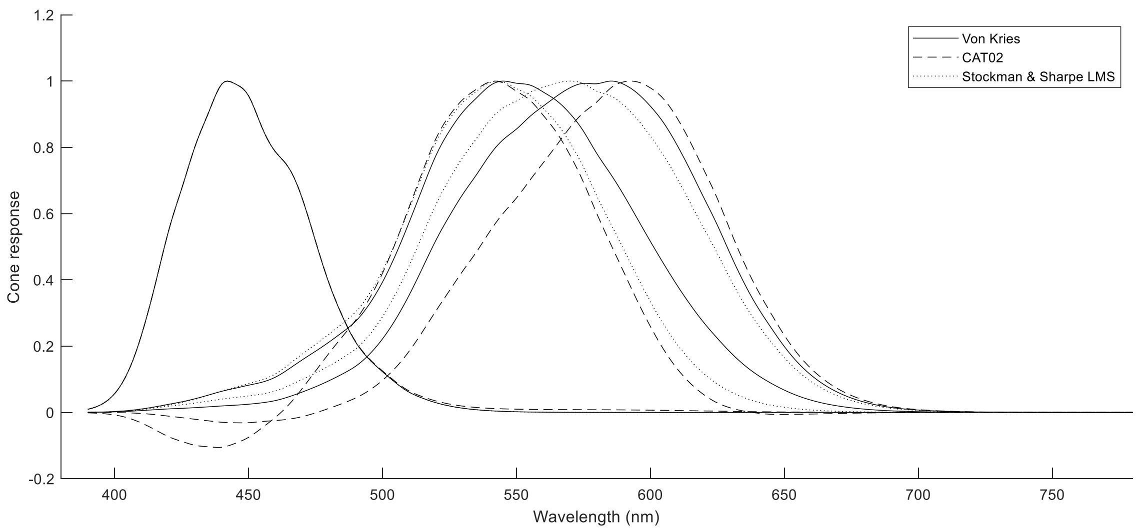

Figure 2-11: Cone sensitivity functions (normalized by unity peak, for equi-energy illumination) as used in chromatic adaptation transforms: Von Kries (full line), CAT02 sharpened RGB (dashed line), and Stockman & Sharpe LMS cone fundamentals (dotted line).

2.4.1 Von Kries

An early chromatic adaptation transform (CAT) was developed by von Kries in 1902, following the Young-Helmholtz theory of trichromatic vision, following the observations of persistence of colour matching[48].

It is based on the assumption that the relative change in sensitivity for the three types of cone photoreceptors [65]

$$\frac{\rho}{\rho_w} = \frac{\rho_c}{\rho_{wr}}; \qquad \frac{\gamma}{\gamma_w} = \frac{\gamma_c}{\gamma_{wr}}; \qquad \frac{\beta}{\beta_w} = \frac{\beta_c}{\beta_{wr}}; \qquad \text{Eq. 2-50}$$

where ρ, γ, β are the cone responses for a light stimulus. Subscripts w, wr, and c correspond to the values of the reference white under the first illuminant, the reference white under the adapted conditions, and the adapted cone responses under the second illuminant.

$$[\rho\ \gamma\ \beta] = M_{VonKries}[X\ Y\ Z] \qquad \text{Eq. 2-51}$$

For quasi-energy illuminant (S_E),

$$M_{VonKries}^{S_E} = \begin{bmatrix} 0.38971 & 0.68898 & 0.07868 \\ -0.22981 & 1.18340 & 0.04641 \\ 0 & 0 & 1 \end{bmatrix} \qquad \text{Eq. 2-52}$$

For D65 illuminant,

$$M_{VonKries}^{D65} = \begin{bmatrix} 0.40024 & 0.70760 & -0.08081 \\ -0.22630 & 1.16532 & 0.04570 \\ 0 & 0 & 0.911822 \end{bmatrix} \qquad \text{Eq. 2-53}$$

Figure 2-12: Visual example of chromatic adaptation. (a) A photograph of different coloured houses, (b) simulation of a red filter applied to one of the houses (marked with an arrow), and (c) same filter as in (b) applied to the entire image. The red filter is simulated by removing the cyan information in the CMYK digital image. Note that the RGB values of the marked house in (b) is the same as in (c), however, chromatic adaptation mechanisms result in different colour appearances.

Figure 2-12 and Figure 2-13 show two examples of optical illusions illustrating the effect of chromatic adaptation. The colour and hue of the boxes and their ribbons from (a) to (c), and (b) to (d), seems to remain mostly the same as their predecessor image. Since the rest of the gift boxes in (c) and (d) correspond to two different transformations of the same image (the only difference in (a) and (b) was the colour of the centre gift box), the colour of these has to be different between (c) and (d), and in fact, the only gift box that can be the same in these two images is the one in the centre.

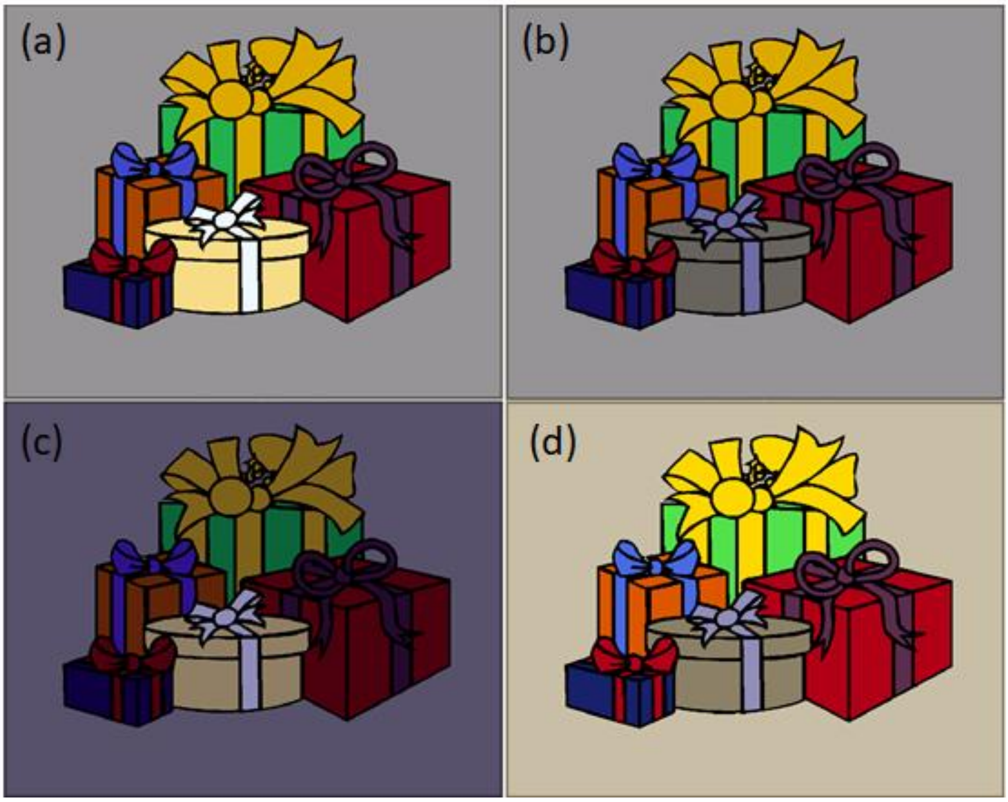

Figure 2-13: An optical illusion caused by chromatic adaptation. (a) A set of differently coloured gift boxes with ribbons*, and (b) an identical image of that in (a), with a different colour only for the central gift box and corresponding ribbon. (c) Von Kries transformation of (a), from xyz = [0.097,0.090,0.154] → [0.289,0.300,0.335]. (d) Von Kries transformation of (b) from xyz = [0.497,0.5247,0.4406] → [0.289,0.300,0.335]. The colour of the central gift box and its ribbon is the same in (c) as it is in (d), while colour of 'the rest of the gift boxes' are different.

* Original black and white image downloaded from http://clipart-library.com/clipart/zTXe88kEc.htm (available 09 Jan 2019), recoloured for this demonstration.

2.4.2 CIE Chromatic Adaptation Transforms (CAT), and Colour Appearance Models

The CIE commission has recommended a set of different chromatic adaptation transforms (CAT) over the years, such as CMCCAT2000, CMCCAT97, CAT02, and CIECAT94 [5], [51], [66], [67].

The CAT02 is a chromatic adaptation transform, proposed by the CIE commission. It differs from the Von Kries transform in using a different set of R, G, B responses. Unlike typical cone responses, such as those used in the Von Kries transform, the R, G, B functions used in CAT02 can take negative values (see Figure 2-11). It has been found that the use of sharpened colour-matching functions, having some negative lobe, provides better prediction of experimental chromatic adaptation results [51]. The CAT02 method, and corresponding equations are presented in Annex 2.

The CAT02 transform forms part of the CIECAM02 colour appearance model. CIECAM02 is the latest published colour appearance model by the CIE commission (2002), and the successor of CIECAM97. This model consists of two major parts: chromatic adaptation transform (CAT02); and the mathematical correlates for six technical variables defining colour appearance (brightness, lightness, colourfulness, chroma, saturation, and hue).

It takes tristimulus values for the stimulus, the adapting white point, adapting background, surround luminance, and degree of adaptation. The model is used to predict these appearance attributes, with forward or reverse implementations for different viewing conditions.

Colour appearance models, such as CIECAM02, are some of the best available tools for prediction of colour appearance under different sets of viewing conditions. However, this work will be focused on simpler models, such as Von-Kries-type transforms, and uniform colour spaces. Future work should be aimed towards the application and evaluation of colour appearance models for CVD observers.

2.5 COLOUR VISION DEFICIENCY (CVD) SIMULATION

Colour vision deficiency (CVD) has been of interest to researchers in the field of colour science since the dawn of this science. Much of what we know about normal trichromatic vision has resulted from the study of CVD conditions, particularly from dichromacy. For example, cone fundamentals, such as those proposed by Stockman & Sharpe, are calculated from psychophysical data corresponding to dichromat observers, under the König hypothesis [16], [59], [60], [68].

Different models and hypothesis have been proposed to model CVD based on the concepts and colour systems used for normal trichromatic vision. While many of these models were originally proposed for cases of dichromacy, some of these can be generalized to anomalous trichromacy. Note that most of the available literature and research is focused on the red-green-type conditions, and are not necessarily consistent with conditions such as tritanopia. In this work, focus will be centred around the red-green type conditions.

Some models which have been proposed for simulation of dichromacy include the empty space model, the empty cones model, and the replacement model [69]:

- The empty space model states that one kind of cones and the corresponding photopigment are lost. This means that there are empty spaces within the cone array, corresponding to the lost cones. Evidence contradicting this has risen from structural studies of the cone foveal array, showing that the mosaic of cone photoreceptors in dichromats is similar to that of normal trichromats [70].
- The empty cones model suggests that all types of cones are present, but one of these is missing the corresponding photopigment.
- The replacement model suggests that all three kinds of cones are present in the cone foveal array, but in of these cone types there has been a replacement of the photopigment by one of the two other photopigments.

On the other hand, simulating anomalous trichromacy is much more complex for many reasons. In general, most CVD models are based on general models and assumptions, hence may not reflect perceptual capabilities of a particular individual [71]. Some factors which difficult the simulation of anomalous trichromacy, as compared to dichromatic simulation are:

- The number of different genotypes and phenotypes in anomalous trichromacy is much larger than in dichromacy, making generalization harder.
- The cone spectral sensitivities in anomalous trichromacy varies significantly, from cases very close to normal trichromacy, only with small differences in one or more cone sensitivities, to cases that fall very close to dichromacy.
- Experimental and psychophysical data on anomalous trichromacy are scarce, compared to the normal trichromat and dichromat cases.

It is desirable that a model for simulating anomalous trichromacy, would apply to the cases of normal trichromacy, and dichromacy. Two different models for anomalous trichromacy simulation will be discussed in this work: the spectral shift, and the replacement model.

2.5.1 Spectral shift

The spectral shift hypothesis states that in anomalous trichromacy, the maximum absorbance of the affected photopigment is "shifted" with respect to the normal photopigment spectra. In the case of protanomalous, the L-cone spectra is shifted towards blue, and for deuteranomalous, the M-cone spectra is shifted towards red. Mathematically, this can be described as [69], [72]:

$$L_{protan}(\lambda) = L(\lambda + \Delta\lambda_L) \qquad \text{Eq. 2-54}$$

$$M_{deutan}(\lambda) = M(\lambda - \Delta\lambda_M) \qquad \text{Eq. 2-55}$$

where $\Delta\lambda_i$ is the shift in wavelength of the maximum absorbance for the photopigment in the i-cone. Note that the difference in the sign associated to $\Delta\lambda$ in Eq. 2-54 and Eq. 2-55 describes the direction of the spectral shift (L_{protan} is shifted to the "left", while M_{deutan} is shifted to the "right-end" of the spectrum). An example for $\Delta\lambda = 10\ nm$ is presented below in Figure 2-14:

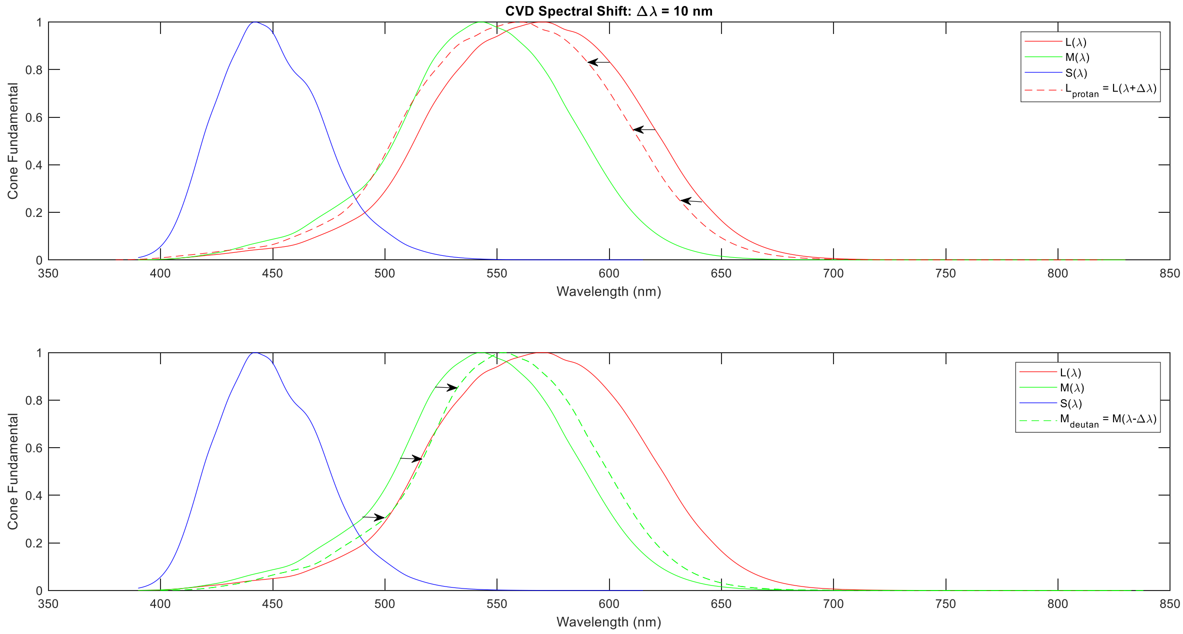

Figure 2-14: Anomalous LMS cone fundamentals estimated by spectral shift hypothesis (Eq. 2-54 and Eq. 2-55) for protanomalous (top) and deuteranomalous (bottom) ($\Delta\lambda = 10\,nm$).

Empirical evidence shows that in red-green anomalous trichromats there is in fact a shift in the maximum absorbance in one of the cones photopigments. This apparent change in the maximum absorption cannot be attributed to a simple shift of the absorption spectra, and the hypothesis of a shifted spectra seems unlikely according to the physiological aspects in human vision. The “shift” in the maximum values for the photopigment spectra is rather a consequence of physiological differences in the genes encoding cone photopigments, which result in an apparent shift in the maximum absorbance value. This apparent shift in the spectra could be explained by the replacement model hypothesis, which will be discussed in the following section.

2.5.2 Replacement model

The replacement model is a comprehensive approach to the construction of anomalous, or hybrid, cone fundamentals. The model assumes that the spectral properties of anomalous cone photopigments can be estimated by some combination of the normal photopigment spectral properties.

As mentioned in previous sections (see Section 1.5.1 Molecular genetics of human colour vision and colour vision defects), the molecular genetics of colour vision is a contentious topic of research. The complex relation between the specific genes encoding visual pigments, their position within the gene array, and their phenotypic expression, is not fully understood, partly because of the high degree of homology and proximity of the L- and M-opsin genes. For this same reasons, unequal homologous recombination of red and green pigment genes is facilitated, creating hybrid red-green pigment genes that determines certain types of anomalous red-green colour vision deficiency [13], [14], [73]. The replacement hypothesis, however, is normally discarded for tritanopia because of the significant differences between the genes that define the pigments of the S cone and the genes for the L and M cones [74].

To implement a model for anomalous trichromacy, based on the replacement model, two options are considered:

- **Photopigment replacement**: Total replacement of photopigment within a fraction of the total number of cone cells in one type of cone photoreceptors. For example, in a protanomalous observer, a fraction of L-cone photopigment is replaced by M-pigment, while the remaining fraction contains the original L-pigment.
- **Hybrid photopigment**: Formation a new photopigment, encoded by a hybrid red-green opsin gene, with spectral properties resulting from some combination of the spectral properties of the original pigments. For example, a protanomalous observer would have all L-cone pigments with the same hybrid red-green pigment.

2.5.3 Photopigment replacement

The first case, photopigment replacement, is probably the most studied case. When there is partial replacement of a photopigment within a certain type of cone, then the psychophysical colour matching curves for the partially replaced cones is calculated as [69], [74], [75].:

$$L_{protan}(\lambda) = (1-\alpha) * L(\lambda) + \alpha * k * \left(\frac{Area_L}{Area_M}\right) * M(\lambda) \qquad \text{Eq. 2-56}$$

$$M_{deutan}(\lambda) = (1-\alpha) * M(\lambda) + \alpha * \frac{1}{k} * \left(\frac{Area_M}{Area_L}\right) * L(\lambda) \qquad \text{Eq. 2-57}$$

$$\alpha \approx \frac{\Delta\lambda}{\Delta\lambda_{max}} = \frac{\Delta\lambda}{(\lambda_L^{max} - \lambda_M^{max})}, \qquad \Delta\lambda \in [0, \Delta\lambda_{max}] \qquad \text{Eq. 2-58}$$

where α is the fraction of cones being replaced ($\alpha = 0$ in normal trichromacy, $\alpha = 1$ for dichromacy), and the terms $(Area_L/Area_M)$ are normalizing factors, such that $L = M = 1$ for the equi-energy illuminant. A scaling factor, k, can be used to partially correct the deviation of the consistent achromatic/blue-yellow channel. Note that the factor α is expressed some times in terms of the shift $\Delta\lambda$ in the maximum absorbance, with respect to the total difference between the maximums of the original L and M cone fundamentals, $\Delta\lambda_{max}$, however, this relation is only an approximation, and the relationship between the spectral shift, $\Delta\lambda$, and the replacement factor, α, in in fact not linear (see Figure 2-18).

The replacement model, expressed in Eq. 2-56, and Eq. 2-57, can be expressed in matrix form, normalizing by area:

$$(L_n, M_n, S_n) = \left(\frac{L}{Area_L}, \frac{M}{Area_M}, \frac{S}{Area_S}\right) \qquad \text{Eq. 2-59}$$

$$(L'_n\ M'_n\ S'_n\ ) = A_i(L_n\ M_n\ S_n\ ) \qquad \text{Eq. 2-60}$$

$$A_{protan} = \begin{bmatrix} (1-\alpha) & \alpha * k & 0 \\ 0 & 1 & 0 \\ 0 & 0 & 1 \end{bmatrix} \qquad \text{Eq. 2-61}$$

$$A_{deutan} = \begin{bmatrix} 1 & 0 & 0 \\ \alpha/k & (1-\alpha) & 0 \\ 0 & 0 & 1 \end{bmatrix} \qquad \text{Eq. 2-62}$$

Figure 2-15 shows an example of anomalous cone fundamentals calculated with the photopigment replacement model (Eq. 2-56, and Eq. 2-57). Note that for a 50% replacement ($\alpha = 0.5,\ k = 1$), the anomalous curve is equivalent for protanomaly and deuteranomaly ($L_{pa}^{\alpha=0.5}(\lambda) = M_{da}^{\alpha=0.5}(\lambda)$).

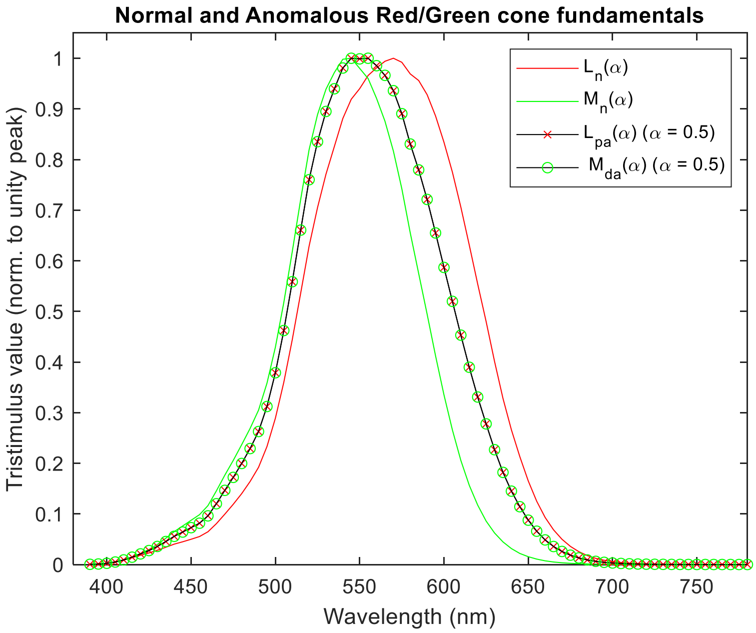

Figure 2-15: Red-green anomalous cone fundamentals calculated using the replacement model (Eq. 2-56, and Eq. 2-57).

Note that the anomalous colour matching functions are estimated from the cone fundamentals, and in this work all simulations will be based on the Stockman and Sharpe cone fundamentals as proposed by the CIE commission [59], [60]. However, this general model can be applied for a different set of cone fundamentals, such as those proposed by Hunt-Pointer-Estevez, or the CAT02 spectral sensitivity functions [5], [51]. The selection of a set of cone fundamentals will depend the specific application and viewing conditions of the experiment, as different sets of colour matching functions have different levels of precision depending on these conditions. However, the use of physiologically based cone fundamentals, such as the LMS, has the advantage of allowing for a direct connection with the physiological aspects of human colour vision, and appear to be the most promising candidate available in the literature to achieve a physiologically based model of CVD.

Variations of the mathematical formulation of the replacement model can be found in the literature. Machado *et al.* compared results from the photopigment substitution model, to current models used for dichromatic simulation [18], [69]. Figure 2-16 shows the comparison of dichromatic perception as calculated by the empty space model, direct photopigment substitution (no normalizing factor), photopigment substitution normalized by area (Scale Ratio, Eq. 2-56, and Eq. 2-57), normalized photopigment substitution with a correction factor (0.96 ratio), and the method by Brettel *et al*. [18], [76]. The so-called Brettel method is a well-studied and tested method, widely used for dichromatic simulation. It is based on the idea of equivalence of the achromatic and blue-yellow channels, between trichromat and dichromat observers. It consists of projecting the Cartesian LMS-tristimulus coordinates of a stimulus, on to the semi-plane formed by the coordinates of the yellow-blue-white-black signals (YBWK). Depending on what cone pigment is affected, the projection is parallel to the Cartesian L- (deutan), or M- axis (protan). The bottom-half of Figure 2-16 shows the comparison between different forms of the replacement model, with the Brettel method. The authors propose using a scaling factor, $k = 0.96$, in the normalised photopigment substitution, to reduce the deviation of the YBWK plane for the dichromatic limit (full cone replacement, $\alpha = 1$).

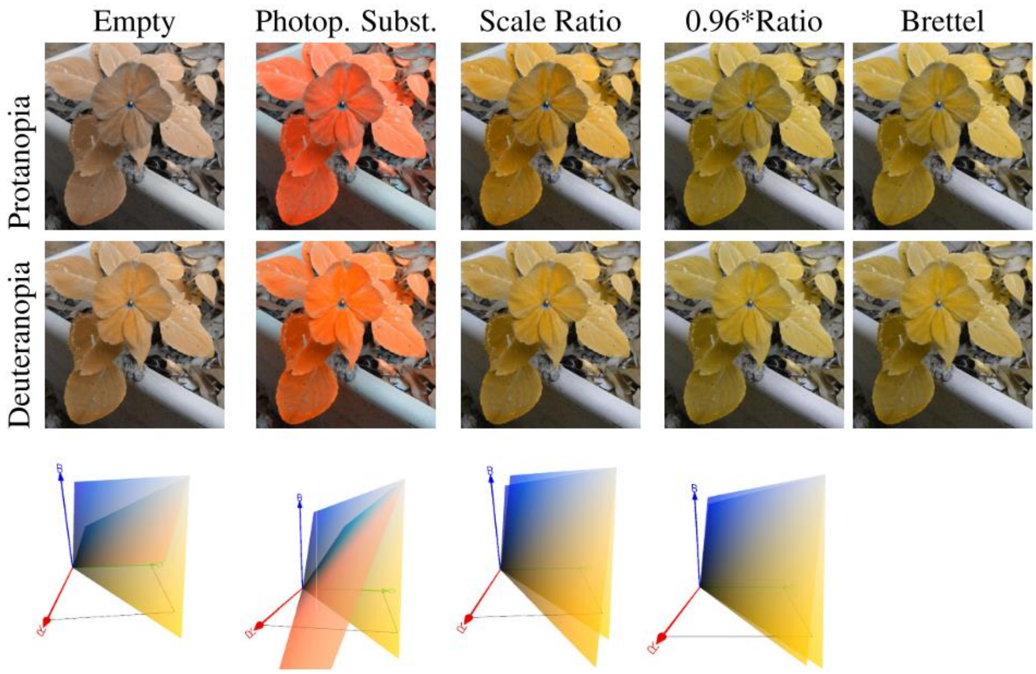

Figure 2-16: **Top**: Simulation of dichromat perception using (a) empty cones model, (b) photopigment substitution, (c) photopigment substitution normalized by area, (d) photopigment substitution normalized by area and scaled by a 0.96 factor, (e) Brettel *et al.* [76]. **Bottom**: Comparison of dichromacy models for protan observer, considering the entire RGB colour space for a CRT monitor. A surface obtained by the Brettel method is shown in all cases for comparison (reproduced from [69]).

2.5.4 Hybrid photopigment

On the other hand, the hybrid photopigment hypothesis assumes that photopigments are not replaced (in a fraction or in the total number of one type cones), but rather there is a new photopigment being formed in all the cones of the affected class, which corresponds to some hybrid form of the original photopigments. To estimate with precision what the spectral properties of this photopigment are, it would be required to have full information on the molecular genetics and dynamics of the expression of the hybrid gene, which is a complex task. However, some assumptions and simplifications allow for a direct estimation of anomalous cone fundamentals, from the photopigment spectral properties proposed by the CIE commission [59].

The universal chromophore 11-*cis*-retinal is responsible for absorbing light in all four types of photoreceptors (rods, and three types of cones), and the difference in spectral absorption originates from the different opsin protein moiety. The ability to tune 11-*cis*-retinal over such a broad range is due to several factors, including the variable protonation state of the retinylidene moiety, the pigments different amino acid residues, their spatial orientation, internal water molecules, counter ions, *etc.* [9]. From this it can be expected that the anomalous cone photopigments present properties from both red and green photopigments, resulting from some combination of the spectral-tuning moieties and factors in the original red and green photopigments. In order to estimate the spectral properties of these hybrid photopigments, one would need the information on what specific spectral-tuning moieties and elements are being expressed from the hybrid gene, from which the spectral absorbance may be calculated through molecular dynamics. Because of this, this approach requires intensive calculations, and an extensive set of experimental data concerning information on the genome and psychophysics for each individual.

In this work, an estimation of hybrid cone photopigment absorbance data is proposed, calculated from normal trichromat photopigment spectral absorbance data. The low-density spectral absorbance, $A_{i,0}$, of the hybrid L and M cones is calculated as a linear combination of the original photopigments:

$$\mathrm{A}_{i,0(\mathrm{L})}^{protan}(\lambda) = (1-\alpha) * A_{i,0(L)}(\lambda) + \alpha * \left(\frac{Area_{A_{i,0(L)}}}{Area_{A_{i,0(M)}}}\right) * A_{i,0(M)}(\lambda) \qquad \text{Eq. 2-63}$$

$$A_{i,0(\mathrm{M})}^{deutan}(\lambda) = (1-\alpha) * A_{i,0(M)}(\lambda) + \alpha * \left(\frac{Area_{A_{i,0(M)}}}{Area_{A_{i,0(L)}}}\right) * A_{i,0(L)}(\lambda) \qquad \text{Eq. 2-64}$$

Note that these equations are equivalent to those of the cone replacement model (Eq. 2-56 through Eq. 2-62), applied for the photopigment density absorbance rather than cone fundamentals. In order to obtain the anomalous cone fundamental from the pigment low density absorbance, Eq. 2-37 through Eq. 2-46 are used to account for the macular and ocular absorption. A comparison between the cone fundamentals obtained by the cone replacement model and hybrid photopigment formation is presented in Figure 2-17.

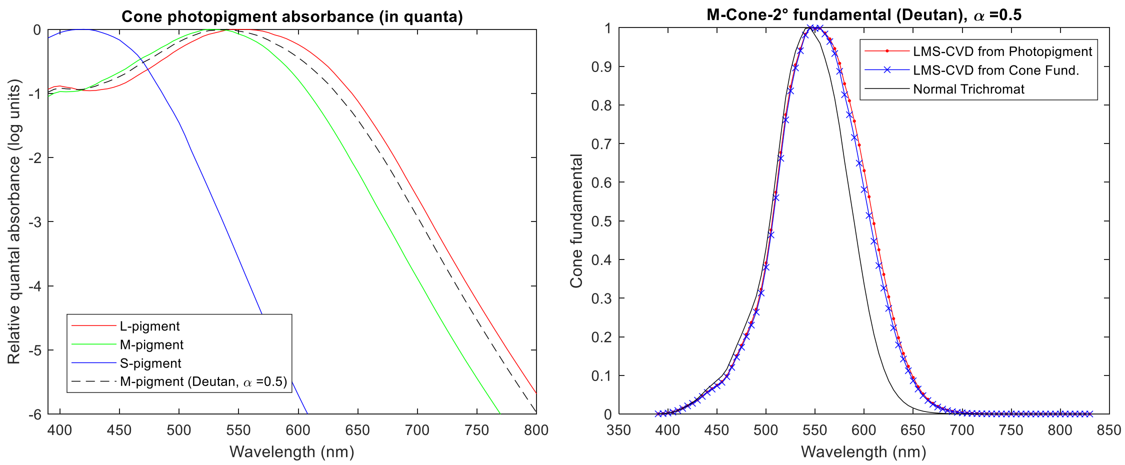

Figure 2-17: Quantal spectral absorbance estimation of hybrid red-green cone photopigment (a), and resulting cone fundamental compared to cone photopigment replacement (b) for a deuteranomalous observer ($\alpha = 0.5$).

Note that when there is no replacement ($\alpha = 0$) or full replacement ($\alpha = 1$), both the cone replacement method and hybrid photopigment will yield the same result, and the largest difference between these methods is observed at a value of $\alpha = 0.5$. The numerical difference between cone fundamentals obtained by these two methods is small, and it falls within the same error margin of individual differences between observers, and experimental variance in psychophysics. It follows that, without more information or further testing of these two methods (such as experimental psychophysical data fitting, which falls out of the scope of this investigation), there is no particular reasons in this work to prefer one method over the other in terms of their accuracy of predictions. From this point onwards, all simulations will be performed using the photopigment replacement hypothesis.

Also note that while Eq. 2-58 gives out an approximation of the cone fundamentals spectral shift in terms of the replacement factor, the relation between these is in fact not linear, which can be observed in Figure 2-18. On the other hand, Figure 2-19 presents the relation between replacement factor and the wavelength for maximum luminous efficiency, presenting similar non-linearities to those observed in Figure 2-18.

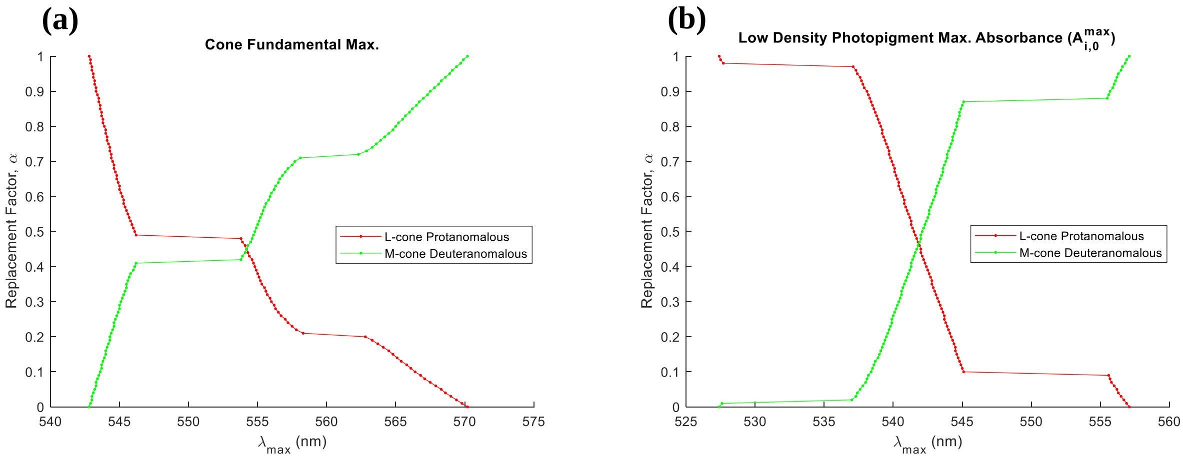

Figure 2-18: **(a)** Maximum absorbance of anomalous cone fundamentals, and **(b)** hybrid cone photopigment as a function of replacement factor, α (normalized to the nearest 0.1 nm).

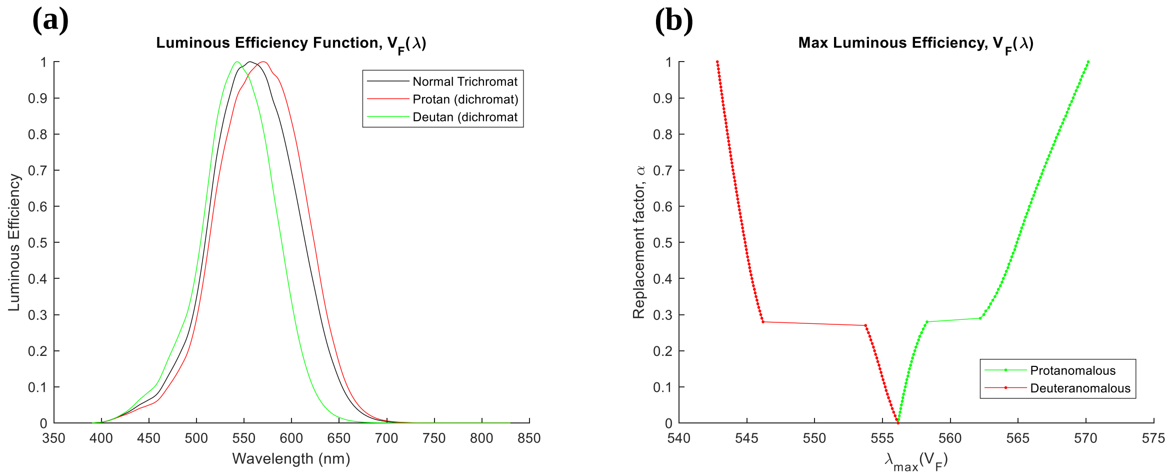

Figure 2-19: **(a)** Luminous efficiency function, $V_F(\lambda)$, for a normal trichromat, and protan and deutan dichromats (normalized to peak unity); and **(b)** Wavelength for the maximum luminous efficiency function $\lambda_{max}(V_F)$ as a function of replacement factor, for anomalous red-green trichromats (normalized to the nearest 0.1 nm, for 2° field).

These graphs were produced by calculating the anomalous CMFs (Eq. 2-56, Eq. 2-57) for various replacement factors, α, and subsequently determining the wavelength at which the L and M-cone responses have their maximum value (λ_{max}). Similarly, Figure 2-19 was produced by calculating the anomalous luminous efficiency function (Eq. 2-47, Eq. 2-48), V_F, for various replacement factors, and subsequently determining the wavelength corresponding to its maximum value.

2.6 RESULTS

2.6.1 Dichromat confusion lines

Dichromat confusion lines, or pseudoisochromatic lines, represent sets of stimuli that are perceived by dichromat observers as having the same chromaticity and hue values, and may only be differentiated by their luminance value. In the standard xy and u'v' chromaticity diagram, these are represented as straight lines converging to a singular copunctal point. The copunctal point represents imaginary stimuli that activates a single type of cone receptor, the L, M, or S-cone receptors for the protan, deutan, and tritan observers respectively.

Under the assumption that dichromacy is a reduced form of trichromacy, these lines can be characterized by standard colorimetry. Figure 2-20 shows the dichromat pseudoisochromes for deutan and protan observers in the xy and u'v' chromaticity diagrams, calculated by the cone replacement model implemented in this work. These were calculated as the straight-line projection connecting the chromaticity coordinates of monochromatic stimuli as perceived by the normal trichromat observer, and the chromaticity values for the same monochromatic stimulus as perceived by the dichromat observer. The copunctal point is then calculated as the intersection of the extrapolated confusion lines, and the calculated values were found consistent with the literature, as shown in Table 2-1.

The lines intersecting all pseudoisochromes within the chromaticity diagrams presented in Figure 2-20 correspond to the dichromat chromaticity gamut, *i.e.*, the chromaticity values for all monochromatic stimuli as perceived by the dichromat observer. For a dichromat, the perceived chromaticity values of any given stimuli will lie within this line, and the 2-D chromaticity space is reduced to a 1-D relation. This is consistent to what is expected, as the "loss" of "full-replacement" of a cone receptor reduces the dimensionality of colour perception by one dimension. Within the dichromat gamut line, the perceived chromaticity for a trichromat will be the same as that of the dichromat observer, consistent with matching experiments for unilateral dichromat observers.

Graphically, dichromat perception can be estimated using standard colorimetry for the normal trichromat observer, the copunctal point, and the dichromat gamut line. For a given stimuli, we first calculate the chromaticity values for the trichromat observer and plot the coordinates in the chromaticity diagram. Connecting this point to the copunctal point gives the corresponding confusion line, and the intersection of this line with the dichromat gamut line gives the dichromatic perception coordinates. This method is analogous to the Brettel method of projecting the tristimulus values in the 3-D LMS colour space on to a 2-D plane.

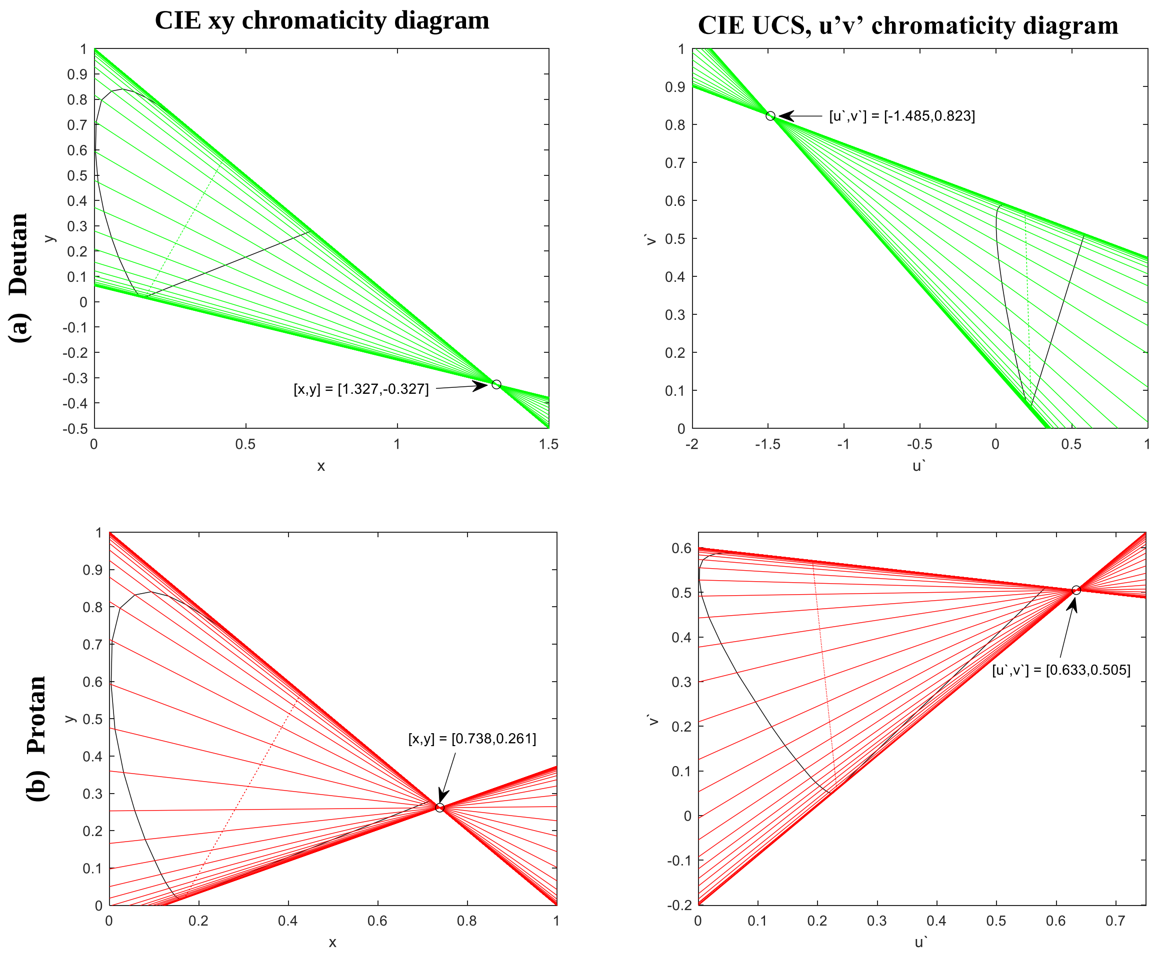

Figure 2-20: Dichromat confusion lines (isochromes), as estimated by replacement model (full replacement, $\alpha = 1$) for deutan **(a)**, and protan **(b)** observers. Isochromes converge to a single point: $(x,y)_{deutan} = (1.327,-0.327)$, $(u',v')_{deutan} = (-1.485,0.823)$; $(x,y)_{protan} = (0.738,0.261)$, $(u',v')_{protan} = (0.633,0.505)$.

Table 2-1: Chromaticity coordinates (cone-fundamental-based) of the protan, deutan and tritan copunctal points for 2° field size [61]

	x_F	y_F	z_F
Protan	0.73840	0.26160	0
Deutan	1.32672	-0.32672	0
Tritan	0.15862	0	0.84138

2.6.2 Chromaticity diagram gamut

The limits of colour perception are given by the tristimulus value for the monochromatic stimuli across the full visible spectrum. Any given colour, as perceived by the observer, can be expressed as a linear combination between two or more monochromatic stimuli. In other words, for any given light stimulus, a metamer can be formed as a linear weighted combination between monochromatic stimuli.

The limits of the colour gamut can be calculated by evaluating the tristimulus values for the monochromatic stimulus (Eq. 2-6 through Eq. 2-9) across the entire visible spectrum, and subsequently transforming to the appropriate chromaticity coordinate system (Eq. 2-24 though Eq. 2-28). The same process can be applied to the anomalous trichromat observer, utilizing the corresponding anomalous colour matching functions (Eq. 2-56, Eq. 2-57, and the transformation in Eq. 2-36), and subsequently applying the transformation to the chromaticity coordinate system. Note that the same transformation is performed for both normal and anomalous observers, from tristimulus values to the chromaticity coordinate system.

Figure 2-21 and Figure 2-22 show the limits of the colour gamut as a function of the replacement coefficient, α, for deuteranomalous and protanomalous observers respectively. The value for α is colour coded, and chromaticity diagrams are presented as colour-scaled contour map. The relative area of the chromaticity diagram is reduced, as the severity of the condition increases, to the limit of dichromatic vision ($\alpha = 1 \rightarrow rel.area = 0$).

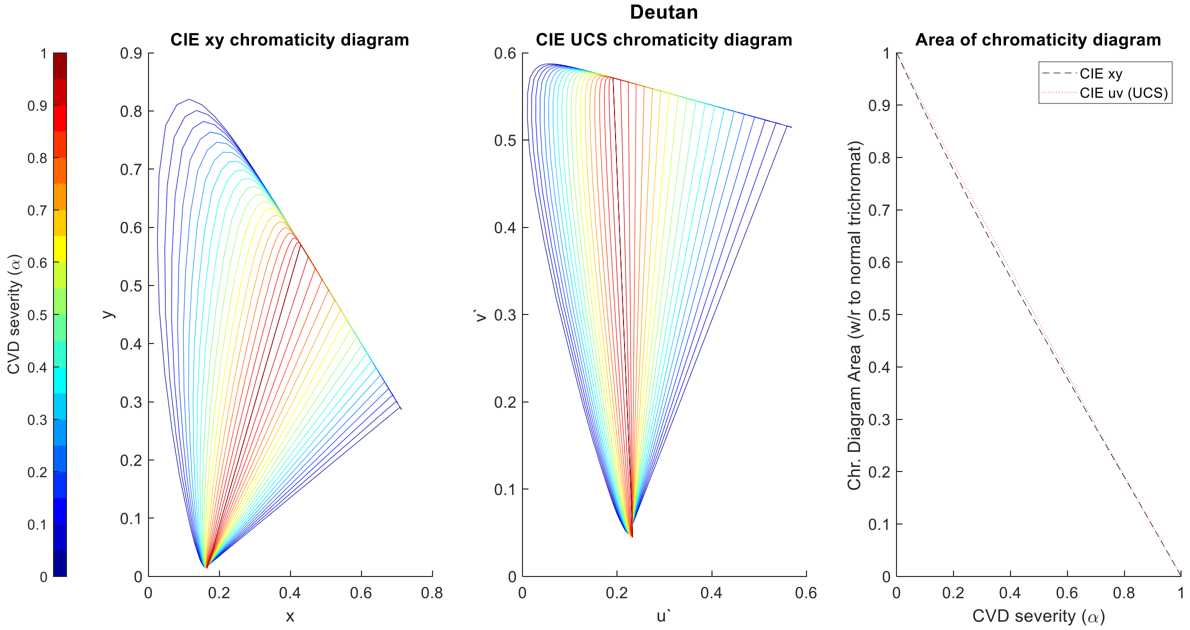

Figure 2-21: Chromaticity diagram reduction in deuteranomalous for various severity conditions (alpha = 0-1). CIE xy chromaticity diagram (left); CIE UCS chromaticity diagram (centre); reduction of chromaticity diagram inner area at various alpha values.

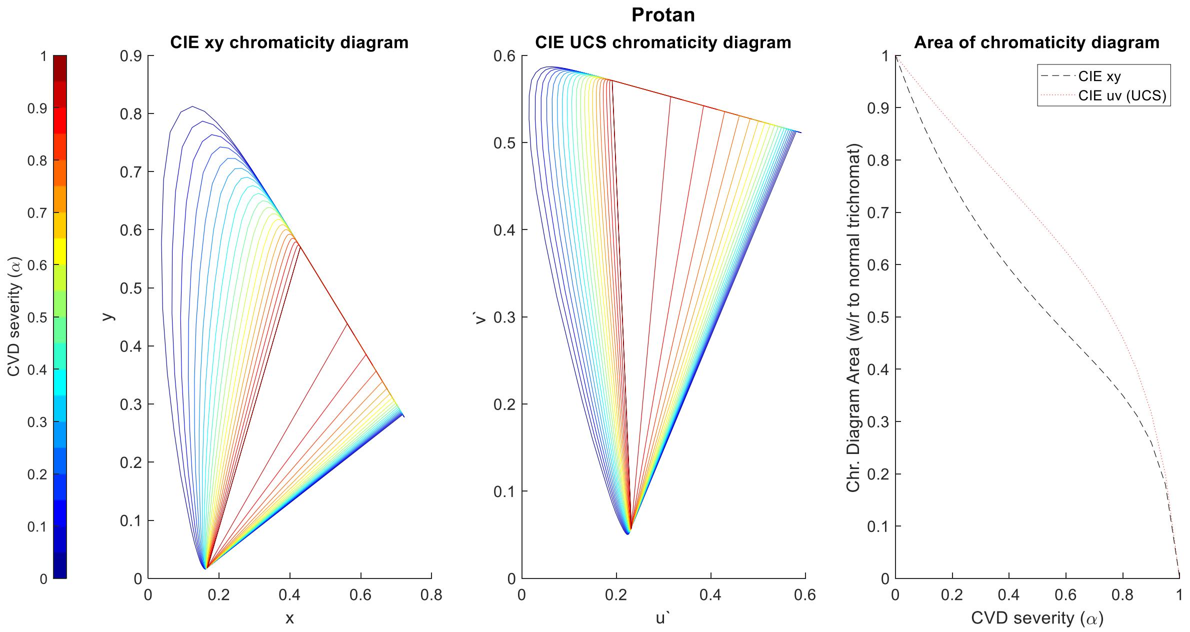

Figure 2-22: Chromaticity diagram reduction in protanomalous for various severity conditions (alpha = 0-1). CIE xy chromaticity diagram (left); CIE UCS chromaticity diagram (centre); reduction of chromaticity diagram inner area at various alpha values.

2.6.3 Anomaloscope colour matches

An anomaloscope is a relatively complex and expensive optical instrument used in the evaluation and diagnosis of red-green colour vision deficiency. It evaluates the ability of an individual to discriminate a monochromatic yellow light (~589 nm) with a mixture of monochromatic green (~645 nm) and red (~670 nm) stimuli, projected on to each of two semicircles forming a less-than 2-deg diameter bipartite field [77], [78]. By adjusting the luminance level of the yellow field, and the relative amounts of red and green in the mixed field, the individual is asked to match the brightness and colour of both fields. These primaries are chosen as they have negligible impact on the activation of the short-wave, or blue cone receptor (S-cone) [79]. Most commonly, the Nagel anomaloscope and its variations (such as the Neitz anomaloscope) are used clinically to test colour vision deficiency. Results of these tests are expressed in term of a red-to-green ratio scale, where 0 represents only green, and 73 is only red light, and yellow is expressed on a scale from 0 to 90.

According to standard trichromatic theory, a match is given when the quantum catches at the photoreceptor level is the same for both fields, in other words, when each cone is activated with the same intensity across both half-fields. In the case of a normal trichromat observer there is single or very narrow range of red-green mixture ratio that can match the hue and chroma of the yellow stimuli, and changes in brightness of the yellow stimuli are matched by adjusting the total intensity of the red-green mixed field, but not the mix-ratio. For the case of dichromats, any combination of red and green can be matched by simply adjusting the brightness or intensity of the yellow field, or alternatively, the match between both fields is only dependant on brightness or light intensity.

Figure 2-23 shows a simulation for the colour difference, ΔE_{uv}, between yellow (590 nm) and red-green mixture (670 and 545 nm respectively), as perceived by anomalous trichromats using the cone replacement model. A colour match is accepted when the colour difference, ΔE_{uv}, is less-than or close-to a value of 1. Note that the scale used in this figure for the red and green intensities are simply a scale-factor for the intensity of the monochromatic stimuli and is not related to the Rayleigh-match scale commonly used to represent the results from an anomaloscope test. The reason that the values for the red intensity are large in comparison to green is the small sensitivity, or value of the CMFs at 670 nm compared to 545 nm (see Figure 2-7).

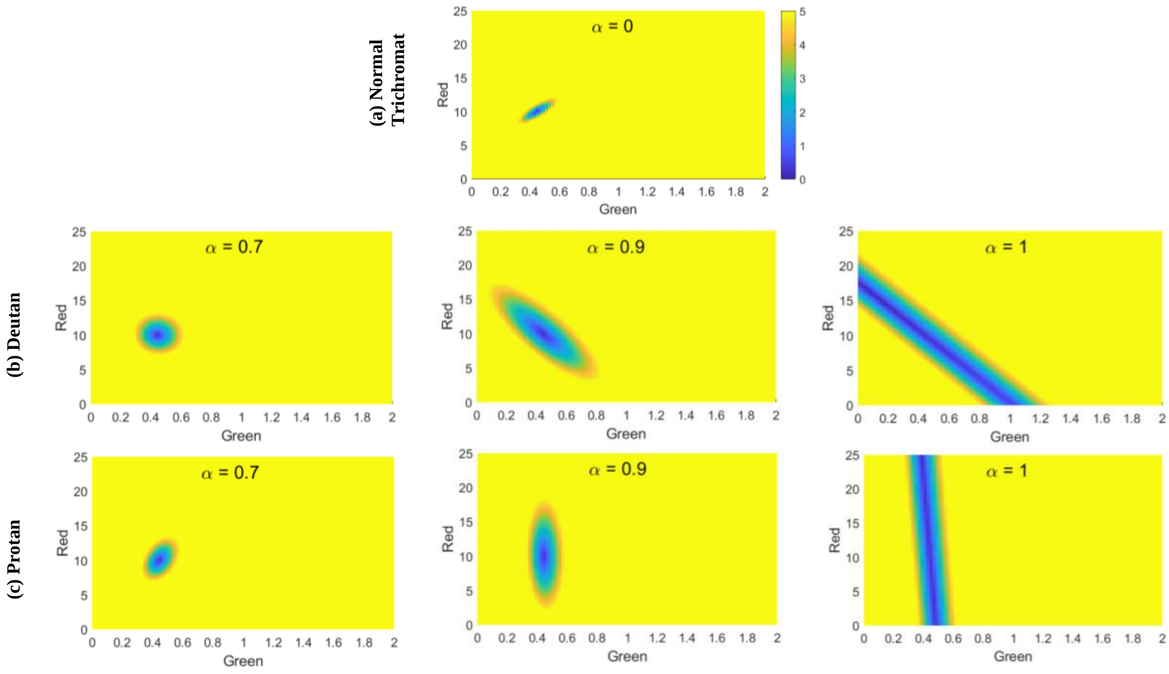

Figure 2-23: Colour difference, ΔE_{uv}, between a monochromatic yellow stimulus (590 nm), and various mix-ratios of green (590 nm) and red (670 nm) monochromatic stimuli. (a) Normal trichromat, (b) deuteranomalous, and (c) protanomalous, at various replacement factors, α. ΔE_{uv} is represented by the colourmap graph: dark-blue ($\Delta E_{uv} = 0$), to yellow ($\Delta E_{uv} \geq 5$), at various combinations and intensities of red (y-axis) and green (x-axis). Values expressed for the red and green intensities correspond to a scale-factor for the monochromatic stimuli, and do not correspond to the Rayleigh-match scale.

It can be observed that for a normal trichromat observer ($\alpha = 0$), there is a narrow combination of red-green mixture that matches the yellow stimuli, represented a small ellipse in the colourmap graph. The range of accepted matches is broadened as the condition of CVD is more severe (larger values for the replacement factor, α), and the ellipse is enlarged.

In the case of full-replacement ($\alpha = 1$), corresponding to dichromatic vision, the yellow stimuli can be matched by any combination of red and green, so long as they produce the same lightness value. This can be observed in the graph as a straight-line, representing the linear combination of red-and green that produce the same level of lightness, and is equivalent to the dichromat confusion lines presented in Section 2.6.1 . Note that for the protan case, the linear graph has a very steep slope, meaning that the match is almost independent from the red value, as protan observers are close to being “red-blind”, and the sensitivity towards the 670 nm stimuli is very close to zero.

While the vision model implemented in this work can predict dichromat confusion lines, as well as the broadening of the accepted matches in an anomaloscope test for anomalous trichromats, it does not predict shifts in the midpoint of the Rayleigh match. Future work should consider a closer examination of the vision model, and how the anomaloscope test was simulated, and how other factors such as optical density affect the results from this test.

2.6.4 Macbeth Colour Checker

The Macbeth colour checker, or Macbeth chart (Figure 2-24), is a commonly used colour calibration reference target, consisting of 24 squares of different coloured samples. First introduced by McCamy, Marcus, and Davidson in 1976 [80], it is manufactured today by X-Rite, formerly Gretag-Macbeth [81].

The spectral reflectances of the colour patches in this chart were designed with the intention of mimicking natural colours, such as vegetation and human skin, and to have consistent colour appearance under different light conditions.

It is widely employed in photography and video acquisition, mainly for fast assessment of colour rendering accuracy and calibration of imaging devices.

Figure 2-24: The Macbeth colour checker

Spectral reflectance data of the 24 coloured patches are presented in Figure 2-25. It consists of spectral reflectance data obtained from literature, consisting of the average spectral properties of each colour patch measured from a set of 30 different charts (Figure 2-25-a, dashed blue line), along with the standard deviation (Figure 2-25-b, dotted blue line) [82]; and the measured spectral reflectance of an 'X-Rite ColorChecker Classic Card' obtained using a

Perkin Elmer Lambda 750 spectrophotometer suited with an integrating sphere (Figure 2-25-c, continuous black line).

Differences from the manufacturing processes of the colour patches between different companies, and between versions of the same product released at different times, result in slight changes in the spectral properties of these. These differences can be observed in the form of the standard deviation.

Other differences can arise from the measurement itself, particularly if different techniques or instruments have been used. In the case of the measured data in this work, a Perkin Elmer Lambda 750 spectrophotometer was used; while in the reference data, 24 of the 30 data sets were measured with Eye-One Pro (*i.e*. i1Pro) spectrocolorimeters from X-Rite/GretagMacbeth, three with the X-Rite DTP20 (Pulse), two with the GretagMacbeth Spectrolino/Spectroscan, and one with the X-Rite DTP22 (Digital Swatchbook).

The colour values in the L^*a^*b colour system, for the different colour patches is presented in Table 2-2. In this table, we present the $L^*a^*b^*$ values derived from sRGB coordinates provided by GretagMacbeth [83], as well as the values calculated from reference and measured spectral reflectance (calculated using CIE2006 XYZ 2° CMFs).

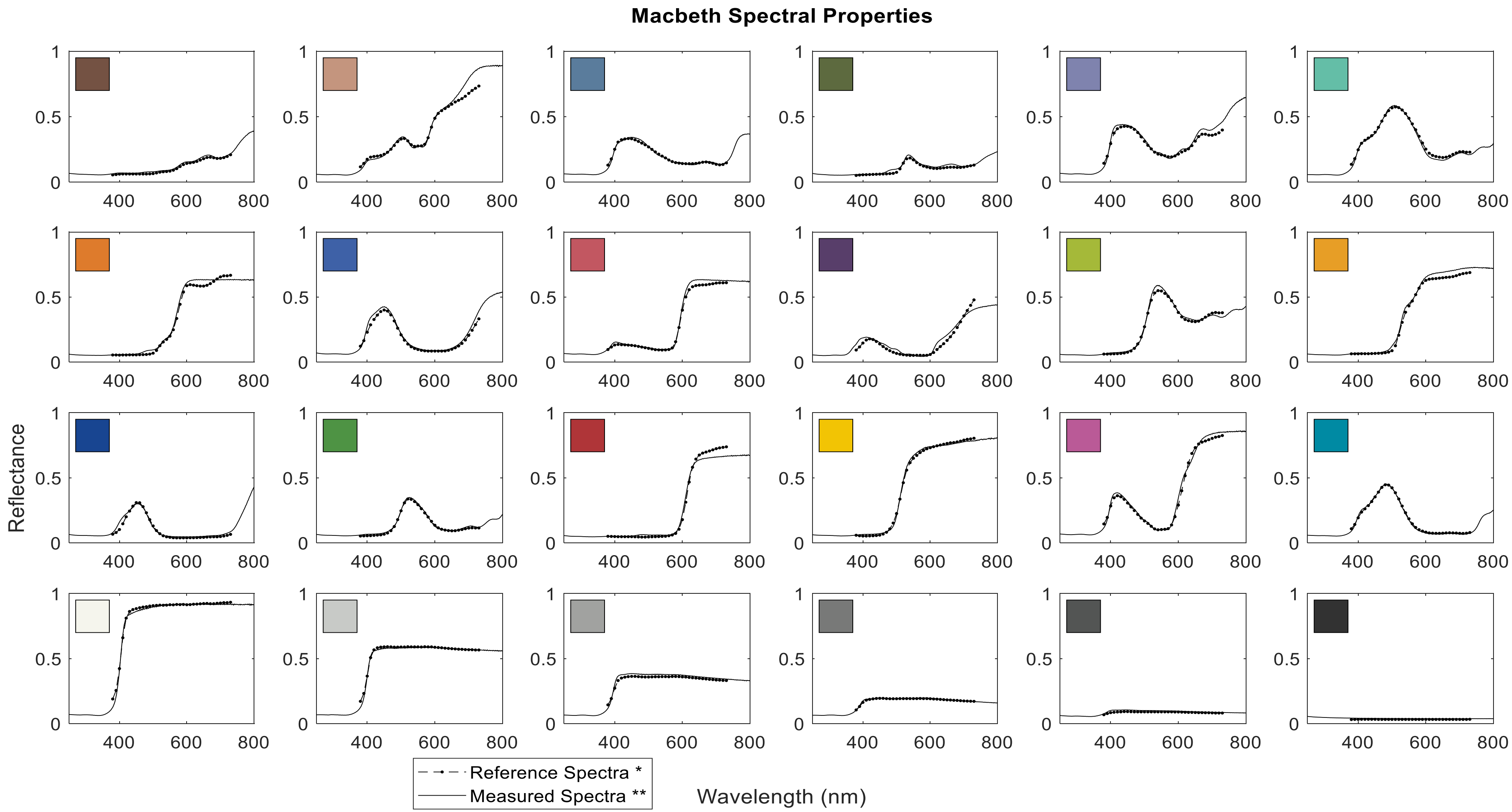

Figure 2-25: Measured and literature reference spectral reflectance of Macbeth colour patches. Reference data from literature, corresponding to the average spectra from 30 charts (from BabelColor [82]); and measured spectra, acquired using Perkin Elmer Lambda 750 spectrophotometer suited with an integrating sphere. Coloured squares correspond to the reference colour of each patch.

Table 2-2: L*a*b* values for the Macbeth colour checker patches under D65 illuminant. Comparison between values obtained from literature (sRGB (GMB)[83]), and calculated according to reference [82] and measured spectral data (diffuse UV/Vis spectrophotometry)

		sRGB (GMB) (ColorChecker 2005)[83]			From reference spectra (D. Pascalle)[82]				From measured spectra			
No	**Colour Name**	**L***	**a***	**b***	**L***	**a***	**b***	**ΔE^*_{ab}**	**L***	**a***	**b***	**ΔE^*_{ab}**
1	dark skin	38.02	11.8	13.66	37.99	12.26	14.12	**0.66**	39.87	11.48	13.63	**1.88**
2	light skin	65.67	13.67	16.9	65.51	14.66	18.98	**2.31**	65.43	15.28	20.05	**3.54**
3	blue sky	50.63	0.37	-21.6	50.73	-3.54	-20.94	**3.97**	50.69	-3.09	-22.13	**3.51**
4	foliage	43	-15.88	20.45	42.89	-13.16	22.43	**3.37**	44.81	-13.82	22.52	**3.44**
5	blue flower	55.68	12.76	-25.17	55.93	8.36	-23.40	**4.75**	56.48	9.45	-24.00	**3.60**
6	bluish green	70.99	-30.64	1.54	71.06	-32.56	3.13	**2.50**	70.40	-35.72	2.22	**5.16**
7	orange	61.14	28.1	56.13	61.40	33.07	56.75	**5.02**	63.25	33.08	55.39	**5.46**
8	purplish blue	41.12	17.41	-41.88	41.66	10.42	-41.80	**7.01**	42.94	11.16	-42.87	**6.59**
9	moderate red	51.33	42.1	14.88	50.83	44.11	15.53	**2.17**	51.95	45.92	16.28	**4.12**
10	purple	31.1	24.35	-22.1	30.72	20.87	-21.21	**3.61**	32.75	22.66	-21.51	**2.43**
11	yellow green	71.9	-28.1	56.96	71.70	-23.88	59.76	**5.07**	72.80	-24.83	59.85	**4.46**
12	orange yellow	71.04	12.6	64.91	70.63	17.86	67.57	**5.91**	72.06	17.01	68.09	**5.53**
13	blue	30.35	26.43	-49.67	30.69	14.60	-46.37	**12.29**	31.69	15.62	-44.39	**12.11**
14	green	55.03	-40.14	32.3	54.94	-37.78	34.76	**3.41**	55.40	-38.34	32.54	**1.86**
15	red	41.35	49.3	24.66	41.21	49.31	27.15	**2.49**	43.24	46.84	26.58	**3.65**
16	yellow	80.7	-3.66	77.55	81.01	2.07	82.02	**7.27**	81.62	1.40	80.53	**5.94**
17	magenta	51.14	48.15	-15.28	51.75	46.44	-15.54	**1.83**	52.55	47.74	-16.07	**1.67**
18	cyan	51.15	-19.73	-23.37	52.01	-27.66	-23.45	**7.98**	51.28	-27.34	-25.38	**7.87**
19	white 9.5 (.05D)	95.82	-0.18	0.48	96.48	-1.49	3.90	**3.72**	96.41	-1.56	4.91	**4.67**
20	neutral 8 (.23D)	80.6	0	0	81.20	-1.20	1.28	**1.85**	80.94	-1.06	1.80	**2.12**
21	neutral 6.5 (.44D)	65.87	0	0	66.48	-0.91	0.75	**1.33**	67.70	-1.02	0.03	**2.10**
22	neutral 5 (.70D)	51.19	-0.2	0.55	50.83	-0.90	0.45	**0.79**	51.18	-0.71	0.64	**0.52**
23	neutral 3.5 (1.05D)	36.15	0	0	35.88	-0.74	-0.01	**0.79**	37.49	-0.78	-1.40	**2.09**
24	black 2 (1.5D)	21.7	0	0	20.83	0.00	-0.11	**0.87**	23.21	-0.21	-0.54	**1.62**
							AVG	**3.79**			**AVG**	**4.00**

A simulation of the Macbeth colour checker appearance for red-green CVD is presented in Figure 2-26. The average and maximum colour difference between the Macbeth colour checker as seen by a normal trichromat and CVD observer is presented in Figure 2-27-a. The colour difference increases as a function of the replacement factor, both for protan and deutan observers, and is the largest for the dichromat case ($\alpha = 1$). The maximum colour difference between a normal and CVD is found at colour chips number 15 (red), 7 (orange), and 9 (moderate red) respectively (see Figure 2-27-b).

As an additional note, the values for colour differences shown in Figure 2-27 are large, and fall outside the range considered for the reliability of this metric. While other metrics can be considered to better address the issue of large colour differences [58], [84], this is still a topic of research, and there is no standardised formulation. Further discussion on this issue can be found in Chapter 5.

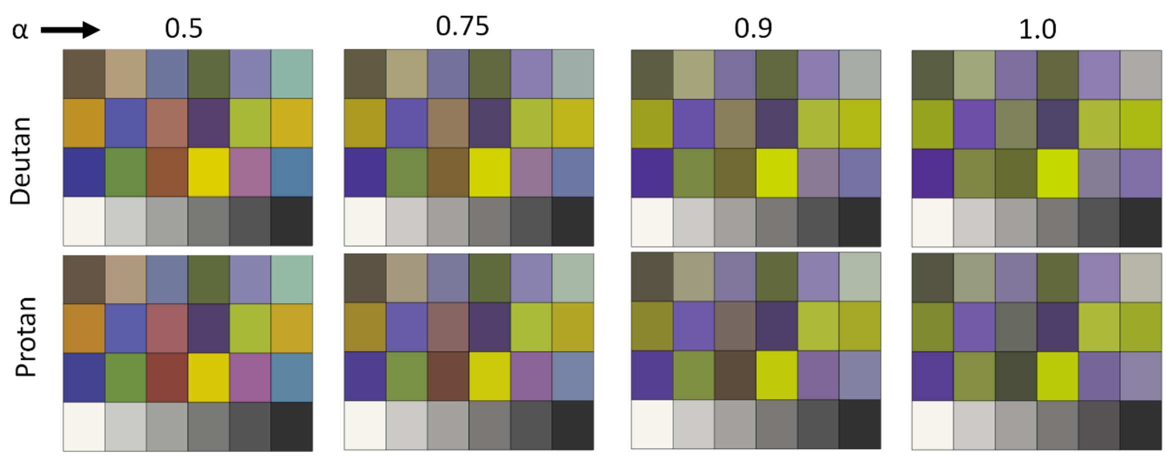

Figure 2-26: Simulation of red-green CVD colour appearance of the MacBeth colour chart.

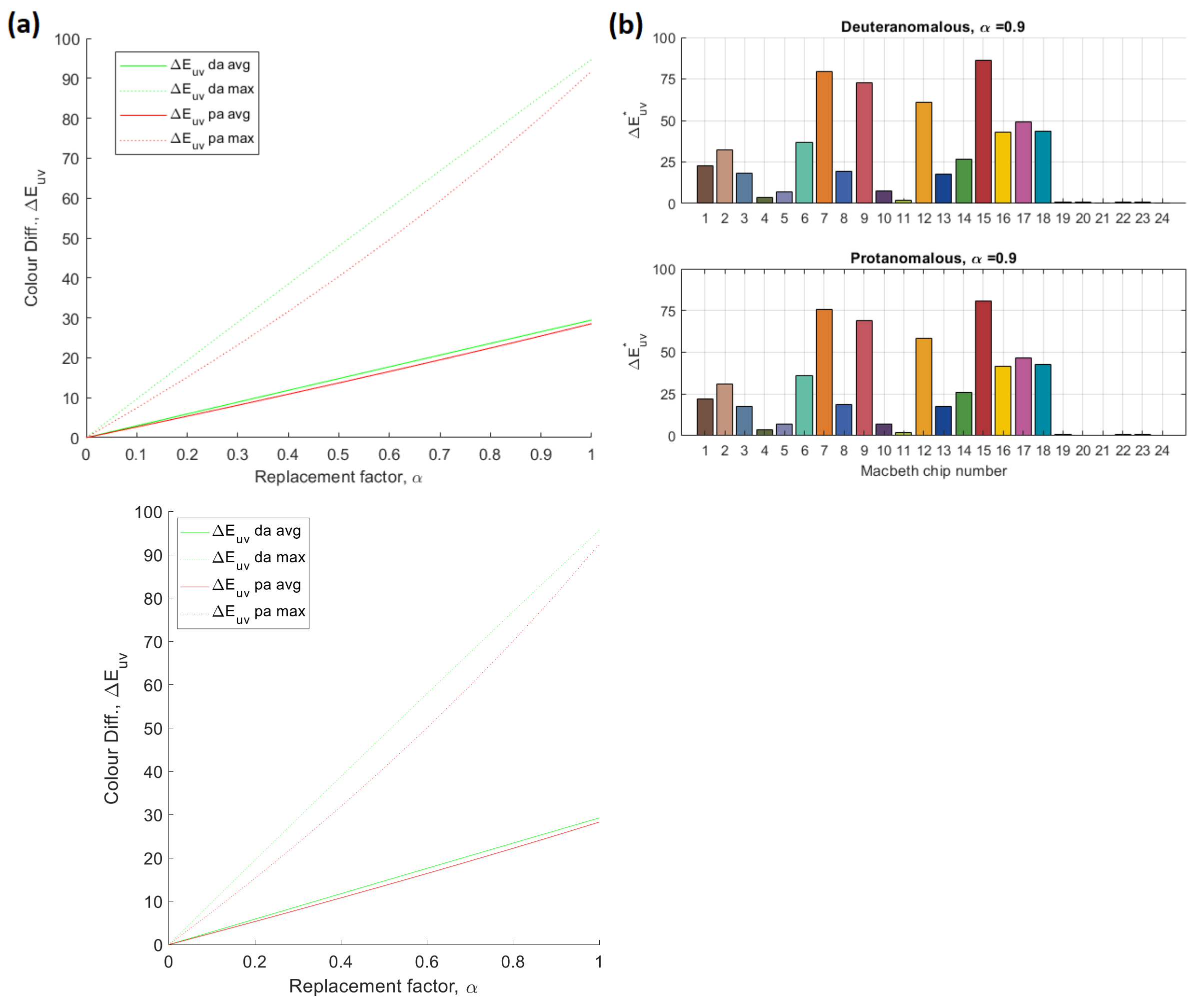

Figure 2-27: **(a)** Average and maximum colour difference ΔE_{uv}, between normal trichromat and anomalous trichromats, as a function of α. **(b)** Colour difference, ΔE_{uv}, between normal trichromat and anomalous trichromats ($\alpha = 0.9$), for every chip in the Macbeth colour checker.

2.6.5 Farnsworth-Munsell 100 hue test

The Farnsworth-Munsell 100-hue test is a vision test, often used for diagnosing colour vision deficiency conditions. Developed in the 1940s, it consists of the arrangement of a series of coloured caps, with constant lightness and chroma values. Small differences in colour perception between caps correspond to different hue values, covering all visual hues, as described by the Munsell colour system.

A database containing the reflectance spectra of 1269 matt Munsell colour chips, measured by spectrophotometry (Perkin-Elmer lambda 9 UV/VIS/NIR, available at [85]), was used in for the simulation of CVD, for protan and deutan observers, at various replacement factor values. Results are presented in the u'v' chromaticity diagram in Figure 2-28, and in the CIE-L*u*v* colour space in Figure 2-29, and Figure 2-30.

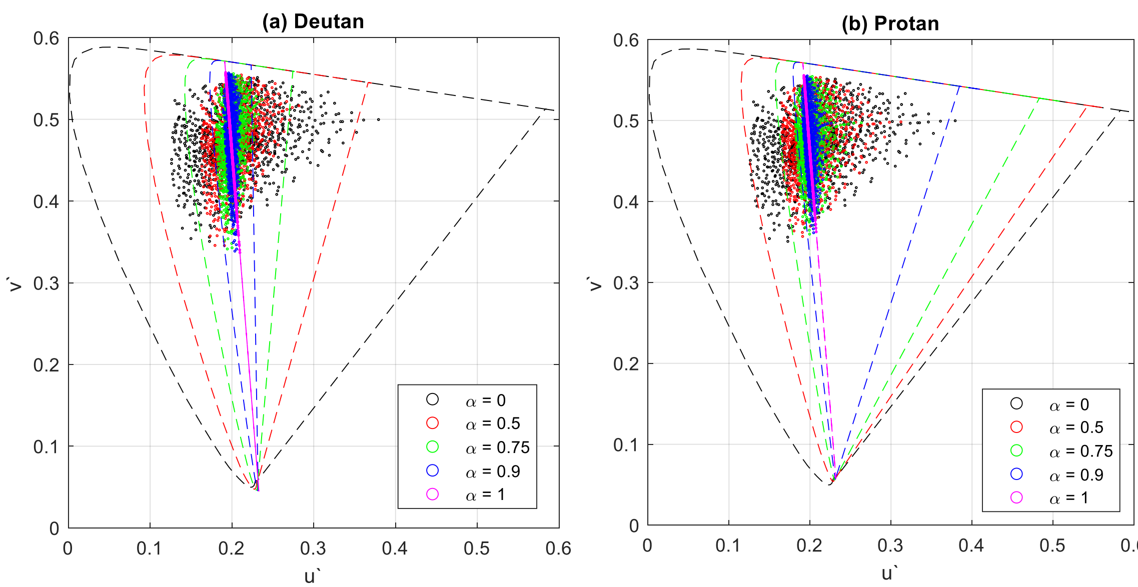

Figure 2-28: UCS chromaticity coordinates of the FM-100 test (1269 samples), for deutan **(a),** and protan observers **(b),** at various replacement factor values ($\alpha = [0, 0.5, 0.75, 0.9, 1]$). The limits for $\alpha = 0$, and $\alpha = 1$, correspond to the normal trichromat, and dichromat observers, respectively.

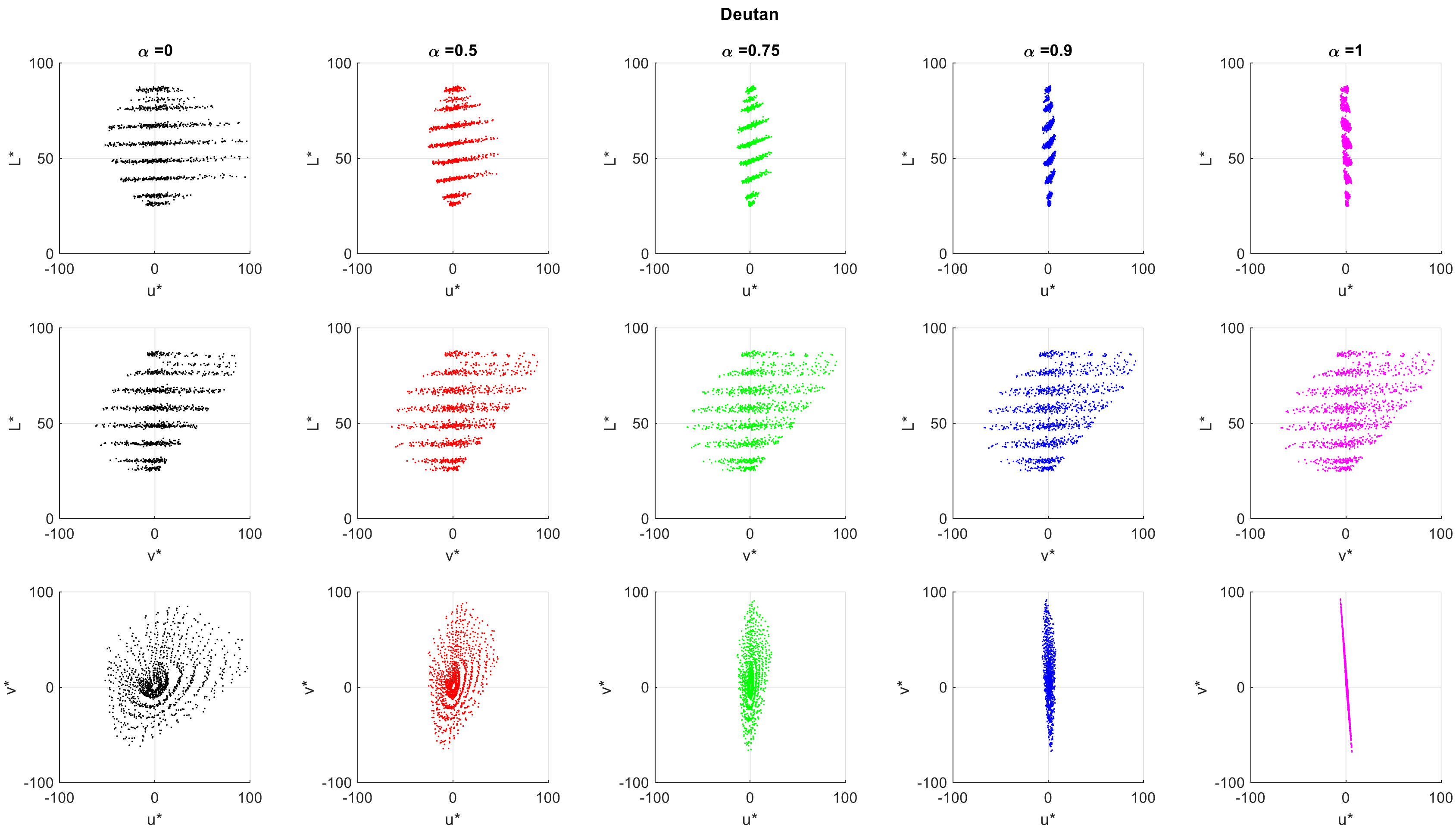

Figure 2-29: L*u*v* values of the FM-100 test, for a deutan observer at various replacement factors ($\alpha = [0, 0.5, 0.75, 0.9, 1]$).

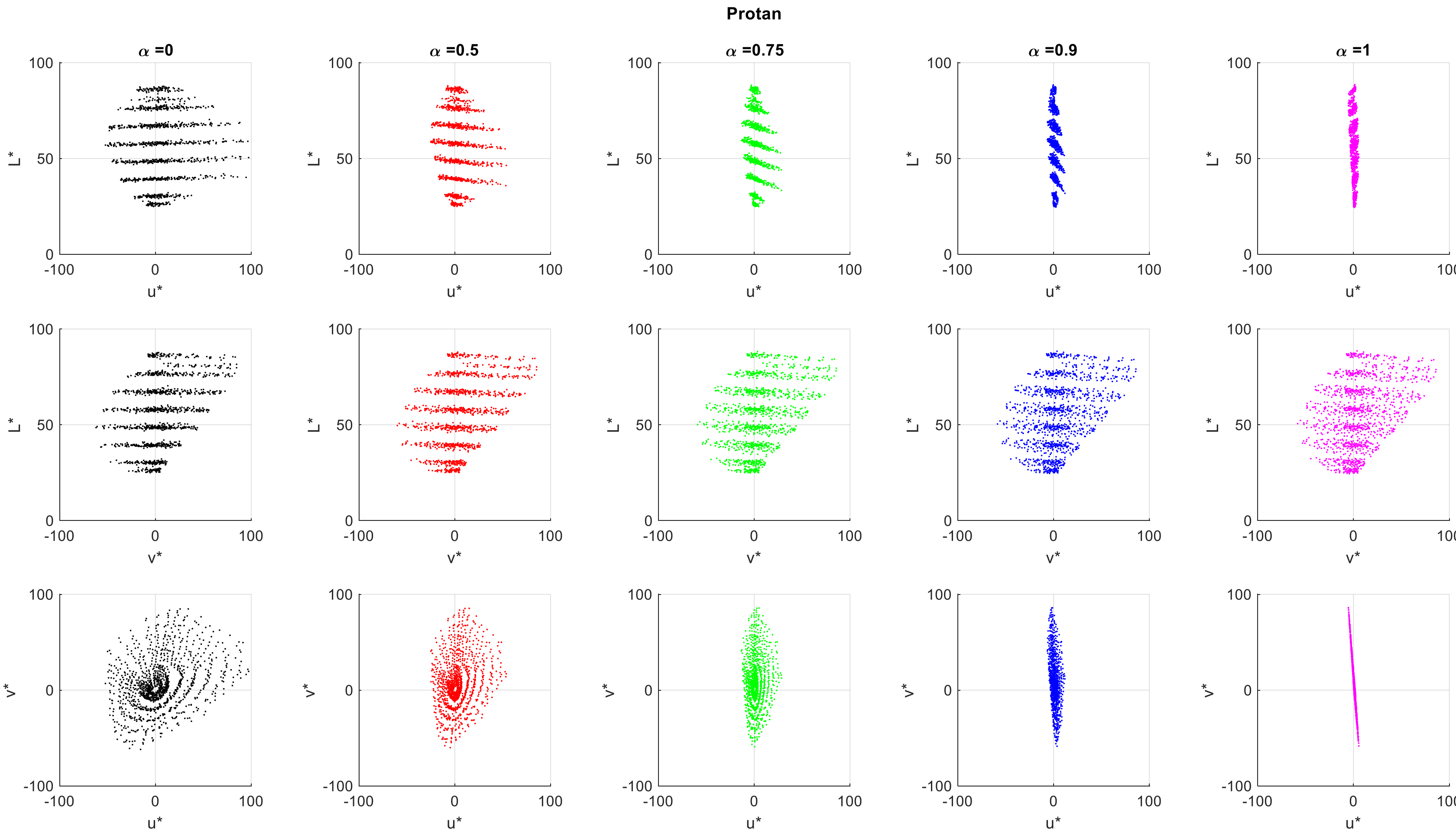

Figure 2-30: L*u*v* values of the FM-100 test, for a protan observer at various replacement factors ($\alpha = [0, 0.5, 0.75, 0.9, 1]$).

2.6.6 Spectral Images

From hyperspectral image data, examples for CVD perception of Ishihara test-plates, and natural scenes [85]–[87], were simulated and presented in Figure 2-31, and Figure 2-32. Note that the values for $\alpha = 0$, and $\alpha = 1$, represent the normal trichromat, and complete dichromat observer, respectively. These simulations are comprehensive examples of the colour vision deficiency condition, however, it is important to note that any colour representation is affected by the display media in which this work is presented, and the limitations of the primary colours and processing methods used in that particular display media (RGB video monitor, printed ink, *etc.*).

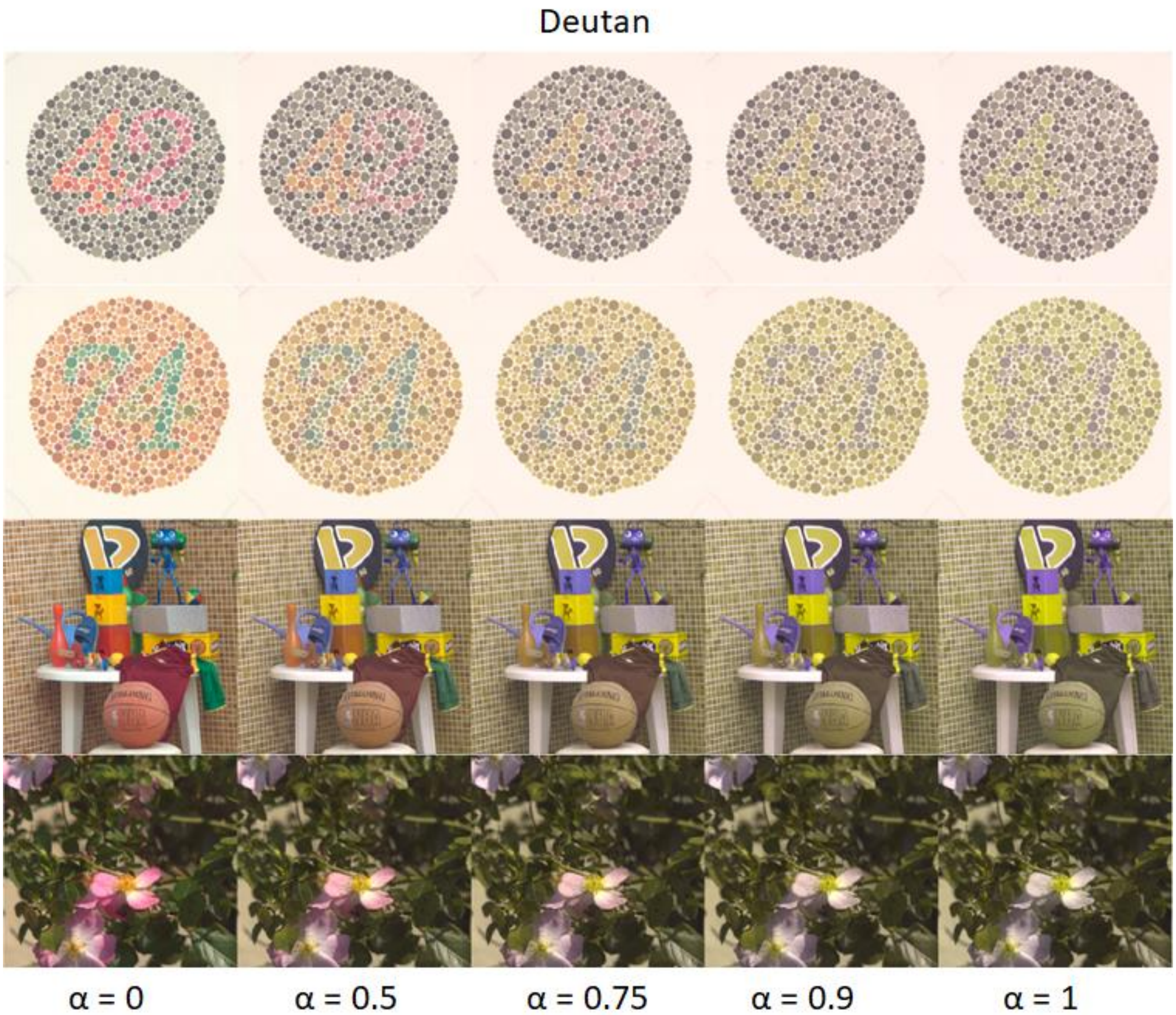

Figure 2-31: Hyperspectral image simulation for a deutan observer, at various replacement factor values (α).

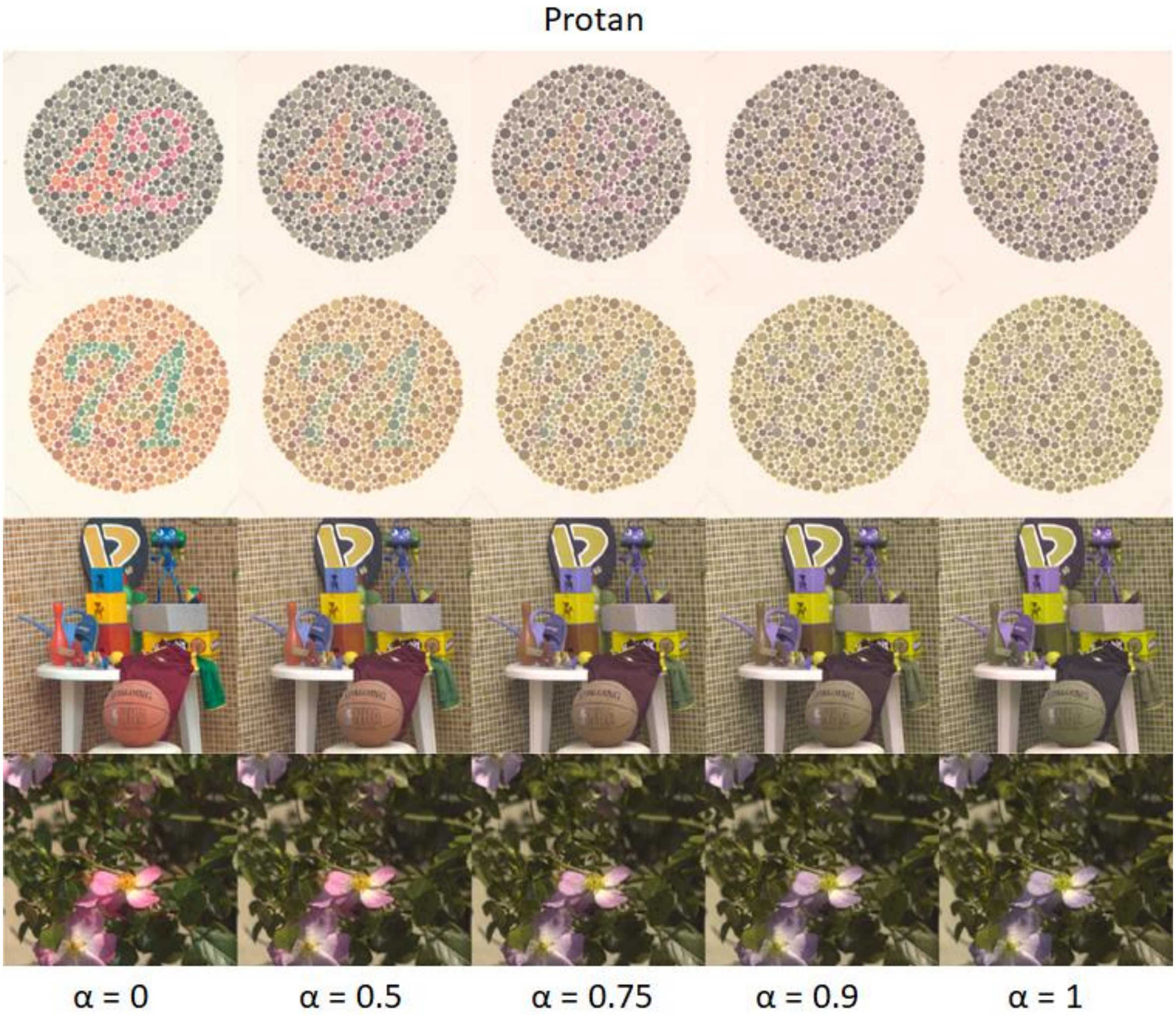

Figure 2-32: Hyperspectral image simulation for a protan observer, at various replacement factor values (α).

2.7 SUMMARY AND FINAL REMARKS

Colorimetry is the science that describes and quantifies human perception of colour. Colour is defined as the human neural interpretation to an external light stimulus with a particular spectral distribution. Light is absorbed by cone photoreceptors in the retina through the retinal cycle, generating an electrochemical response which is then processed and transmitted by the optic nerve and higher stages of visual processing, and finally it is interpreted in the brain. The interpretation of this information depends largely on the relative intensity of the signals generated by the different photoreceptors. Different cone photoreceptors are activated by light in different regions of the visible spectrum and can be classified accordingly in the long (L), intermediate (M), and small (S) wavelength sensitive photoreceptors.

Understanding the relation between the physical description of light and the subjective perception of colour is the main objective of the colour matching experiment and psychophysics. The experiment consists in matching the subjective response for a specific colour with a combination of two or more primary colours. By matching monochromatic colour stimuli across the visible spectrum, it is possible to describe the response of the human visual system in the form of colour matching functions (CMFs), and to estimate the sensitivity of the photoreceptors, described as the cone fundamental functions.

The *Commission Internationale de l'Éclairage* (CIE) issues information and standardized methods on the matters of light, illumination, and colour. Some of these include the standard luminous efficiency function $V(\lambda)$, the CIE XYZ standard colour matching functions (in 1931 and 1964, for 2° and 10° standard observers respectively), the CIELAB and CIELUV colour spaces, and the fundamental physiologically based LMS chromaticity diagram. These standards are widely used in all applications concerning colour measurement and colour perception, and the use of a particular standard or colour space will depend on the specific application for which it is used.

The main objective of colour appearance models is to allow for the prediction of subjective colour perception attributes under different conditions, such as changes in illumination. While the basic colorimetric functions and methods allow for a quantitative measurement of colour, they do not account for the effect of changes in the viewing conditions, and visual processing mechanisms such as chromatic adaptation. Colour appearance models are intended to explain and predict the human visual response according to these. Chromatic adaptation transforms (CAT) can be divided into three groups: those that occur as parts of uniform colour spaces (CIELAB, CIELUV); those that depend on normalization of cone responses (Von Kries); and those that form part of a colour appearance model (CAT97, CAT02).

While colour appearance models and colour spaces are well defined for the case of normal trichromacy, the application of these to colour vision deficiency (CVD) is not fully understood, and most models do not account for these cases. Some models have been used to simulate colour perception in red-green anomalous trichromats and dichromats, such as the cone replacement or hybrid photopigment model. The response of the anomalous cone sensitivity can be estimated using these models, by a linear combination of the original L and M-photopigment sensitivity curves. The severity of the condition is defined by the replacement factor, α ($0 \leq \alpha \leq 1$), and the resulting curve will have a maximum value at an intermediate wavelength between both the original curves (often referred to as a 'shift' in the maximum cone spectral response). While the replacement model allows for a simple computation, compatible with anomalous trichromatic and dichromatic vision, correction factors are need to partially account for discrepancies with well-established dichromatic models (Brettel method). The development of a consistent colour appearance model, and associated colorimetric methods applicable to all types of observers (normal trichromat, anomalous trichromats, and dichromats) represent the apex in the field of colour vision. However, the development of these methods is dependent on the set of colour matching functions for an individual, and the derivation of individual transformation matrices and colour formulae requires extensive psychophysical testing, and intensive computations. The proposed cone-replacement model, while capable of predicting the spectral shift of affected cones, dichromat confusion lines, and broadening of the Rayleigh match range in an anomaloscope test, was unable to predict the shift in Rayleigh match midpoints. The model, albeit its limitations, allows for a straightforward general calculation, compatible with current colour standards and methods in colorimetry, and general understanding of red-green colour vision deficiency.

In this work, a numerical implementation of the replacement model is used for the photometric simulation of red-green anomalous trichromacy. The Macbeth colour checker, a standard reference of coloured samples widely used in photography, was selected as the spectral database to evaluate the model. The implemented model can effectively estimate dichromatic confusion lines for the protan and deutan cases and can serve as a good estimation for anomalous trichromacy. However, the precision of the model for the anomalous trichromat case has not been evaluated in this work and requires validation through psychophysics and experimental data. Examples of CVD simulation for Farnsworth-Munsell 100-hue test (FM100, 1269 samples), and hyperspectral images are presented.

CHAPTER 3: DESIGN OF COLOUR CORRECTION FILTERS THROUGH NUMERICAL OPTIMIZATION

3.1 ABSTRACT

This chapter condenses the mathematical and physiological concepts of colour appearance and colour vision deficiency, and numerical optimization methods used to design and evaluate the potential use of optical filters to tailor and enhance certain aspects of colour vision. The designed filters are evaluated for their capability as colour correction devices for red-green anomalous trichromat observers, and for the statistical significance of these variations.

3.2 BACKGROUND AND MOTIVATION

While there is anecdotal evidence dating to the Renaissance about paint artists having issues identifying colours, the first serious descriptions of colour vision deficiency as a physiological condition are dated to the mid-17th century. It was not until the early 1800s when renowned scientists, such as John Dalton, put the subject of colour vision deficiency under the light of modern science, and formulated the first scientific theories attempting to explain this condition [49]. Later contributions on colour theory, such as Maxwell's experiments on colour mixtures, and the Young-Helmholtz trichromatic theory, further advanced the understanding and prediction capabilities of colour theory and colour vision deficiency [55], [88].

As colour theory progressed, awareness and interest on colour vision deficiency increased. The idea of providing solutions for CVD came with the first widespread accounts of the condition, ranging from charlatanic to serious research in medicine and science [89]. Among the latter, the most prevalent solution has been the use of tinted glasses. The initial idea of using tinted glasses is attributed to Seebeck [90], consisting of the individual looking through a red and green filter successively. A couple of decades later, Maxwell would resume Seebeck's work, and fashioned a pair of spectacles consisting of red and green filters covering each a different eye [91]. This type of spectacles makes use of the concept of differential interocular vision, allowing for discrimination between red and green colours by comparison of the relative brightening and darkening of a colour when observed through the different filters.

Some commercial examples of tinted filters, which are worn monocularly, are the X-Chrom lens and ChromaGen system. Clinical trials of the X-Chrom lenses have reported an increase in the performance of pseudo-isochromatic plate tests, such as the Ishihara test, but worsening the performance in colour arrangement tests, such as the Farnsworth-Munsell 100-Hue test (FM-100) [89]. While empirical evidence suggests that these filters can improve colour discrimination, even for dichromat observers [17], moderately dense filters can induce problems in visual acuity owing to the reduced luminance, and can induce visual distortions and impairment of depth perception. This impairment can be particularly detrimental in tasks requiring fine stereoscopic acuity, and under lower luminance levels, for example, driving at night.

To overcome the impairment of stereoscopic acuity, the use of the same filter in both eyes is desired. Advancements in optical filters design and manufacturing have allowed the introduction of band-pass and band-stop filters in the search for optical solutions for CVD. New commercial eyewear based on frequency selective filters, such as EnChroma and VINO glasses, have proliferated and gained attention from the general public owing to viral marketing campaigns and digital media. Even though clinical trials of band-pass filters in the past have generally yielded negative or inconclusive results, there is still no scientific consensus, and recent publications have yielded more optimistic results, in particular, for VINO glasses [87], [92], [93].

To this date, there is no definite solution for CVD, although gene therapy has been successfully tested in a few animal species [23], [25], and it is considered as the most promising definite solution. However, the ethical, safety, and legal framework considerations about the modification of human genes is highly contested [94], and it unlikely to be allowed for research and experimentation on human subjects in the short to mid-term.

3.2.1 Design of optical filters for colour vision deficiency

Many different variables play a role in the design and fabrication of optical filters, from the definition of the design objectives and performance metrics, to the technical and economic considerations associated with manufacturing and commercialization.

For applications in CVD wearable optics, design objectives are fairly open-ended, due to the subjective nature of colour perception, as well as the variety of conditions under which the device may be used (*e.g.,* luminance level, types of illumination, nature of the colour stimuli, *etc.*), and the variance between the perception of different observers.

In this work, the focus will be on the study of optical filters as a means on 'enhancing' colour perception in anomalous red-green trichromat observers, in particular, for deuteranomalous observers which represent the largest group within CVD.

Design objectives

As noted previously, in the literature, wearable optics for CVD have been tested and proven to improve performance of CVD individuals in some diagnostic tests (Ishihara test), in detriment of others (FM-100). The general consensus is that there is a trade-off between the enhanced discrimination between certain pairs of colours, at the expense of the decrease for others. Additionally, a higher optical density in the filter increases the effect, but will have a negative impact on other attributes of visual perception, such as decreased luminance which in turn can affect visual acuity.

In this work, we define the normal trichromat (NT) observer as the 'perfect' observer, meaning that the main objective of the filters is to allow the CVD observer to discriminate between similar colours as the normal trichromat is capable, within the physiological and optical limits. Consequently, the metrics used for the filter design are based on the relative difference (or distance) between colour perception attributes between the NT and CVD observers. The performance of the filters will be measured in terms of colour and chroma difference formulae between NT and CVD, the number of discernible colours (NDC), saturation, *etc.*

Considerations

Optical filters can alter colour perception, by means of selectively filtering light at specific frequencies, which, depending on the overall contribution of that frequency to cone activation, can make either a small or significant change in colour perception. This change will depend on both the cone spectral sensitivities at that specific wavelength, and on the spectral profile of the light stimuli itself. For example, Figure 3-1 shows cone spectral sensitivities, and a light stimuli from a mercury vapour lamp [95], [96]. It can be observed that the S-cone spectral sensitivity at 405 nm is small compared to 445 nm ($\bar{L}(405\,nm) = 0.122$, and $\bar{L}(445\,nm) = 0.992$), however, for a stimuli such as a mercury vapour lamp, the contribution of the first is significantly higher, due to the lack of 445 nm light ($I_{Hg-Lamp}(405\,nm) = 0.297$, and $I_{Hg-Lamp}(445\,nm) < 0.001$).

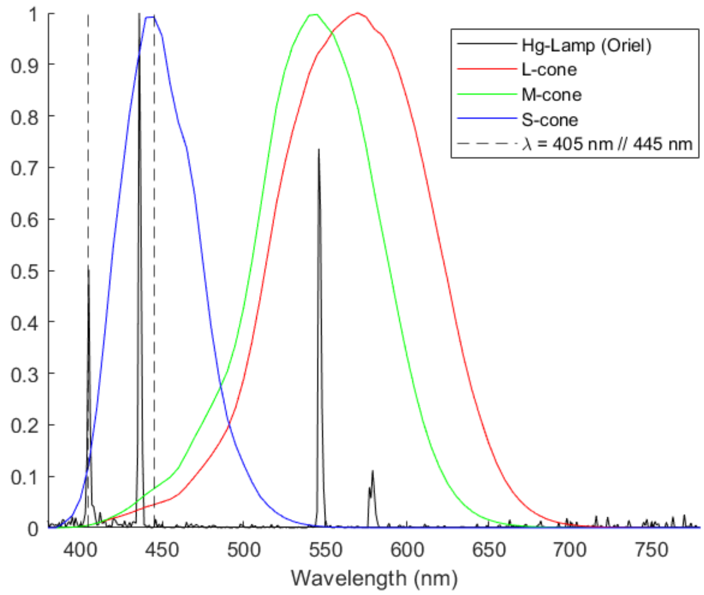

Figure 3-1: L, M and S-cone spectral sensitivities, and spectral power distribution for a mercury lamp (from [96]). Vertical lines are marked at 405 and 445 nm respectively. The contribution of each wavelength to the colour perception of the light stimuli will depend on both the cone spectral sensitivities and the relative spectral power of the colour stimulus at that wavelength.

The power-spectra distribution of the Hg-vapour lamp shown in this example is characterized by the atomic spectrum of mercury, consisting of a discrete set of monochromatic light at certain specific frequencies. For a human eye-wear device, targeted for general daily-activity, the data should have monochromatic stimuli such as the previous example. The reflectance spectral profile of most surfaces is generally given by the pigments present within it, which have a variety of absorbance spectra profiles, but are not monochromatic. Similarly, most illumination sources found on daily-life basis, such as daylight, incandescent lightbulbs, and other artificial lighting, have a smooth power spectra distribution. While some video display monitors, such as RGB-driven LEDs, can have much sharper profiles, this falls outside the scope of this work.

In the literature

Gómez-Robledo and collaborators published a study evaluating the effectiveness of colour vision deficiency correction glasses, manufactured by the EnChroma trademark [22]. They evaluated the effectiveness of these using two strategies: a clinical study based on classical tests of recognition (Ishihara plates), arrangement (Farnsworth-Munsell) and discrimination; and simulation of colour appearance using spectral transmittance data of the glasses in study. Their results show that while these glasses introduce a variation on the perception of colour, these do not improve results in diagnosis tests, nor allow for CVD individuals to have normal colour vision.

A group from Pacific University published a thesis work assessing EnChroma Cx-14 filters for colour vision deficiency correction, as well as red and green-tinted glass filters [97]. In a clinical test trial, they tested the subjective responses of various red-green CVD individuals (five severe deutans, two moderate deutans and two severe protans), for the pseudoisochromatic ColorDx software test and Farnsworth-Munsell 100-Hue tests. They concluded that the EnChroma filters had no significant effect on the performance of any of the CVD subjects, but it did improve the error score in two subjects (from severe to moderate protan and deutan, according to the ColorDx test). Additionally, they found that a red filter significantly improved colour discrimination from severe to mild deutan in all deutan cases.

In a recent publication, Martinez-Domingo *et al.* [92] used computational simulations to analyse the effect of spectral filters in the number of discernible colours (NODC) for normal trichromats, as well as red-green anomalous trichromats and dichromats. For this, they selected the best performing filters from a series of single and double band-pass and notch filters, simulated using Gaussian functions, with varying centre-wavelength and bandwidth. The number of discernible colours was determined by the number of 1-by-1-by-1 cubes in the

CIELAB colour space containing a colour stimulus from the sample spectra database, which approximates the general consideration that two colours are discernible when their colour difference is over 1 unit in the CIELAB space ($\Delta E_{ab} > 1$). No chromatic adaptation or change in the reference white due to the filter was considered. Their results show that while some filters can generate an improvement in the NODC, this improvement is small ($< 3\%$), and dependant on the reflectance sample database used for the computation.

As seen in a previous chapter, the limits of colour vision within a specific colour space are given by the primary light stimuli, as every possible light stimulus will be made-up of a weighted combination of these primaries. Full colour vision can be approximated by the combination of an indefinite number of primaries, given by the monochromatic light stimuli at every point within the visible spectrum. Optical filters cannot expand these limits, and thus should not increase NODC within the colour space. In fact, a filter should reduce the volume of the observable colour space, as some aspects of colour perception, such as lightness, can only be reduced by the filter. The small improvement observed by Martinez-Domingo is most likely a result from the discretization of the problem for numerical computation, and the selection of specific databases. The increase in the NODC for a filter is calculated with respect to the unfiltered NODC, which depends on the database used, so a filter could in fact increase the NODC with respect to the original unfiltered database, but should still lie within the same limits for the monochromatic light stimuli. In other words, the number of 1-by-1-by-1 cubes in the CIELAB space either remains unchanged or is reduced when using the optical filter. However, the number of cubes occupied by a colour stimulus from the reference database can in fact change, depending on how these references are distributed within the colour space.

Martinez-Domingo also reported that their selected filters did not show any improvement for simulated Ishihara plates and FM100 tests, however, simulations of the Ishihara test showed some improvement for simulations using commercial VINO glasses. This assessment is consistent to other publications by the same group, where they tested commercial filters EnChroma and VINO glasses, marketed towards CVD correction [22], [87]. They concluded that VINO glasses significantly changed colour perception, and in some cases, it can allow a CVD observer to pass a recognition test, such as the Ishihara test, but not an arrangement test, such as the FM100. This is most likely due to the nature of the tests: in the Ishihara test, samples consist in a set number of coloured circles, generally within the vicinity of two or three main stimuli (for example, different shades of red and green), and the test consists of differentiating between the main colours, which are generally arranged to form a number or a letter. To pass such test, the observer only needs to be able to generally differentiate between two or three main colour stimuli, and recognize the pattern formed by the arrangement within the plate. In the FM100 test, the observers must sort coloured caps with similar lightness and chroma, according to their hue between two fixed caps. In this test, the observer needs to differentiate between subtle changes in hue, requiring higher precision in colour perception as compared to the Ishihara test (Figure 3-2).

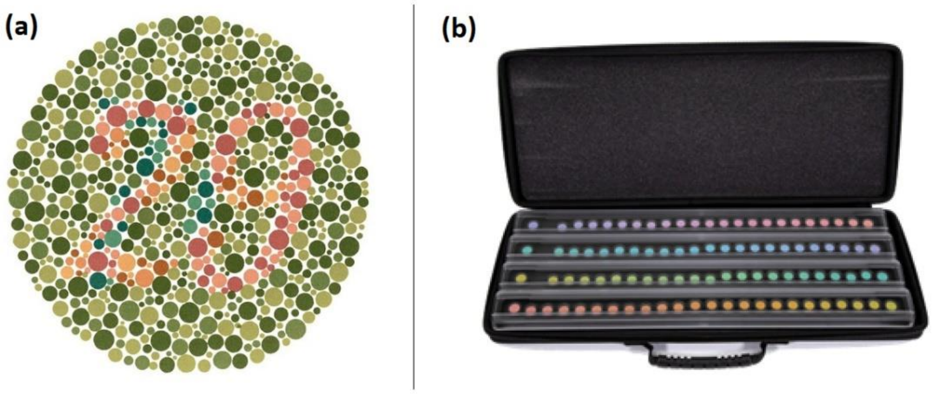

Figure 3-2: Examples of (a) Ishihara test plate, and (b) the Farnsworth-Munsell 100 test (FM100)

There are two important corollaries to this conclusion:

- The theoretical total number of discernible colours cannot be increased using optical filters, and all changes in colour perception are within the limits given by the monochromatic stimuli values. Thus, it is not possible for CVD individuals to achieve full trichromatic vision by the use of optical filters.
- However, the change in colour perception caused by these filters can in fact improve colour discrimination in some fringe scenarios, such as the Ishihara test. Whether an optical filter can cause a significant improvement on colour perception by CVD individuals, will depend on how this is measured. For example, if an improvement in the perception of a particular colour comes with a retrogression for a different colour, then the effectiveness of the device will depend on how these two stimuli are weighted within the performance function used to evaluate the device.

3.3 OBJECTIVES

The main aim of this work is to design and study the application of frequency selective filters as optical aids in colour perception of red-green colour vision deficiency. To achieve this, the following specific objectives are set:

- To implement numerical methods for colour appearance, and colour vision deficiency models.
- To implement numerical methods based on linear programming optimization to design the power spectra distribution of optical filters that optimize various aspects of colour perception, in collection of reflective samples databases.
- To compare results from different objective functions used in the optimization design.
- To compare the resulting filters to market available eyewear, commercialized as optical aids for colour vision deficiency.

3.4 METHODS

3.4.1 Standard colorimetry

Colour perception simulation will be performed using standard colorimetry for both normal and anomalous trichromats. The advantages and disadvantages of using standard colorimetry will be further discussed in following sections.

Tristimulus values for reflective stimulus are calculated according to:

$$\varphi_i = k \int_{\lambda} r(\lambda) s(\lambda) \bar{\varphi}_i(\lambda) d\lambda \qquad \text{Eq. 3-1}$$

Discretized:

$$\varphi_i = k \sum_{\lambda} r(\lambda) s(\lambda) \bar{\varphi}_i(\lambda) d\lambda \qquad \text{Eq. 3-2}$$

Vector form:

$$\varphi = \begin{bmatrix} \varphi_1 \\ \varphi_2 \\ \varphi_3 \end{bmatrix} = k\Phi^T S r \qquad \text{Eq. 3-3}$$

where φ is the tristimulus value, k is a normalizing factor, $r(\lambda)$ is the spectral reflectance of a reference sample contained within the vector $r = \begin{bmatrix} r(\lambda_1) \\ \vdots \\ r(\lambda_N) \end{bmatrix}$, $s(\lambda)$ is the spectral power distribution of the illuminant, contained in the diagonal matrix.

$$S = \begin{bmatrix} S(\lambda_1) & \cdots & 0 \\ \vdots & \ddots & \vdots \\ 0 & \cdots & S(\lambda_N) \end{bmatrix}$$

, and $\bar{\varphi}(\lambda)$ is the colour matching functions, contained in the matrix.

$$\Phi = [\varphi_1(\lambda) \quad \varphi_2(\lambda) \quad \varphi_3(\lambda)] = \begin{bmatrix} \overline{\varphi_1}(\lambda_1) & \overline{\varphi_2}(\lambda_1) & \overline{\varphi_3}(\lambda_1) \\ \vdots & \vdots & \vdots \\ \overline{\varphi_1}(\lambda_N) & \overline{\varphi_2}(\lambda_N) & \overline{\varphi_3}(\lambda_N) \end{bmatrix}.$$

For example, in CIE XYZ and LMS colour space:

$$\Phi_{xyz} = \begin{bmatrix} \bar{x}(\lambda_1) & \bar{y}(\lambda_1) & \bar{z}(\lambda_1) \\ \vdots & \vdots & \vdots \\ \bar{x}(\lambda_N) & \bar{y}(\lambda_N) & \bar{z}(\lambda_N) \end{bmatrix}, \text{ and, } \Phi_{LMS} = \begin{bmatrix} \bar{l}(\lambda_1) & \bar{m}(\lambda_1) & \bar{s}(\lambda_1) \\ \vdots & \vdots & \vdots \\ \bar{l}(\lambda_N) & \bar{m}(\lambda_N) & \bar{s}(\lambda_N) \end{bmatrix}.$$

The constant k is a normalizing factor, defined by the photopic luminous efficiency function, V_F:

$$k = \frac{100}{\int_\lambda S(\lambda)V_F(\lambda)d\lambda} \qquad \text{Eq. 3-4}$$

In matrix form:

$$k = \frac{100}{VS} \qquad \text{Eq. 3-5}$$

The colour appearance model was implemented based on the CIE LMS Physiological Axis, as explained in a previous chapter (see Chapter 2) [16], [59]–[61]. The model of colour appearance implemented in these methods needs to be consistent and applicable to different observers, with different colour matching functions that can result from a difference in age, or due to an inherited or acquired colour vision deficiency condition. Additionally, the model should account for different field sizes (*e.g.*, from 1°-10°) and for changes in the viewing conditions, such as changes in illumination or as a result of filtering light through an optical device.

An advantage for using this particular colour space is the fact that the LMS cone fundamentals represent the actual physical absorption of light in the three different cone photoreceptors in the human retina, which allows for a better understanding of the underlying physiological mechanisms of colour vision. This model also allows to estimate the cone fundamentals of different individuals according to their age, or other acquired or inherited conditions. Basing this model on physiological aspects of colour vision allows for a direct comparison between observers with different physiology, such as colour vision deficiency conditions that affect the cone photoreceptors sensitivity, or changes in absorption of the lens, macula, and other ocular media due to ageing or acquired conditions.

3.4.2 Colour vision deficiency simulation

The objective of this section is to estimate the cone fundamentals for observers with red-green colour vision deficiency, in order to be implemented into the colour appearance model.

As discussed in previous chapters, simulation of colour vision deficiency can be achieved by different methods from the normal LMS fundamentals [18], [59], [69]. This research seeks to establish a method that is consistent with the physiological aspects of the human visual process, and that is applicable to the full range of severity for anomalous trichromacy, from normal trichromat to fully dichromat observers.

The replacement model is useful for simulating red-green colour vision deficiency and is consistent with the expected “shift” in sensitivity of the affected cone in anomalous trichromats, as well as with the case of dichromat observers.

While the replacement model is applicable to the inherited red-green colour vision deficiency conditions, it does not accurately represent blue-yellow deficiency (tritanopia). The replacement model is generally discarded for the case of tritanopia due to the significant differences between the genes that define pigments of the S cone and the genes for the L and M-cones [74]. Because there is no genetic basis for the pigment substitution hypothesis in tritanopia, it is generally considered an acquired condition, as opposed to inherited condition [69].

Using the replacement model, for a replacement factor α ($\alpha = 0$: no replacement/trichromatic; $\alpha = 1$: complete replacement/dichromatic), the L and M-cone CMFs are calculated as:

$$L_{protan}(\lambda) = (1-\alpha) * L(\lambda) + \alpha * \kappa * \left(\frac{Area_L}{Area_M}\right) * M(\lambda) \qquad \text{Eq. 3-6}$$

$$M_{deutan}(\lambda) = (1-\alpha) * M(\lambda) + \alpha/\kappa\ * \left(\frac{Area_M}{Area_L}\right) * L(\lambda) \qquad \text{Eq. 3-7}$$

In matrix form, the anomalous colour matching functions can be calculated from their normalized form:

$$(L_n, M_n, S_n) = \left(\frac{L}{Area_L}, \frac{M}{Area_M}, \frac{S}{Area_S}\right) \qquad \text{Eq. 3-8}$$

$$(L'_n\ , M'_n\ , S'_n\ ) = \mathrm{A_i}\Phi^T \qquad \text{Eq. 3-9}$$

, where:

$$A_{protan} = \begin{bmatrix} (1-\alpha) & \alpha * \kappa & 0 \\ 0 & 1 & 0 \\ 0 & 0 & 1 \end{bmatrix} \qquad \text{Eq. 3-10}$$

$$A_{deutan} = \begin{bmatrix} 1 & 0 & 0 \\ \alpha/\kappa & (1-\alpha) & 0 \\ 0 & 0 & 1 \end{bmatrix} \qquad \text{Eq. 3-11}$$

The term κ corresponds to a scaling factor, which is used to adjust the model to better fit the Brettel model for dichromatic vision ($\alpha = 1$), and has a value of $\kappa = 0.96$ (see Section 2.5.3 Photopigment replacement).

While in normal trichromatic vision the luminous efficiency function can be approximated by the $\bar{y}$ function in CIE XYZ, for red-green cvd, the luminous efficiency depends on the replacement factor, as the luminous efficiency is a function of the L and M-cone sensitivities, under photopic vision conditions (see Section 2.3.5 , on Luminous Efficiency function) [61].

$$V_F = \Phi T_F \qquad \text{Eq. 3-12}$$

In LMS space (2° field):

$$V_F = 0.68990272\,\bar{l}(\lambda) + 0.34832189\,\bar{m}(\lambda)$$
$$T_F = \begin{bmatrix} 0.68990272 \\ 0.34832189 \\ 0 \end{bmatrix} \qquad \text{Eq. 3-13}$$

In LMS space (10° field):

$$V_{F,10} = 0.69283932\bar{l}_{10}(\lambda) + 0.34967567\,\overline{m_{10}}(\lambda)$$
$$T_{F,10} = \begin{bmatrix} 0.69283932 \\ 0.34967567 \\ 0 \end{bmatrix} \qquad \text{Eq. 3-14}$$

3.4.3 Opponent Colour Space

In order to compare and analyse difference in colour appearance between different observers, a uniform chromaticity space is needed.

In this work the CIELUV uniform chromaticity scale diagram (UCS) is used. This colour space corresponds to a projective transformation of the CIE x,y chromaticity diagram, resulting in a perceptually more uniform colour spacing. Other candidates for opponent colour spaces are the CIELAB and MacLeod-Boynton tristimulus space [50], [61], [98].

Note that the CIELUV colour space is defined in reference to the tristimulus values of the reference white in the viewing conditions. The reference white is calculated as the tristimulus values for the perfect reflecting diffuser ($\phi(\lambda) = 1, \forall\lambda$) under the specified light conditions. The value for the reference white tristimulus will change depending on the presence of a colour vision deficiency condition, and for the case of a stimulus observed through a frequency selective filter.

$$L^* = \begin{cases} \left(\frac{29}{3}\right)^3 \frac{Y}{Y_n}, & \frac{Y}{Y_n} \leq \left(\frac{6}{29}\right)^3 \\ 116\left(\frac{Y}{Y_n}\right)^{\frac{1}{3}} - 16, & \frac{Y}{Y_n} > \left(\frac{6}{29}\right)^3 \end{cases} \qquad \text{Eq. 3-15}$$

$$u^* = 13L^*(u' - u'_n) \qquad \text{Eq. 3-16}$$

$$v^* = 13L^*(v' - v'_n) \qquad \text{Eq. 3-17}$$

$$u' = \frac{4X}{X + 15Y + 3Z} \qquad \text{Eq. 3-18}$$

$$v' = \frac{9Y}{X + 15Y + 3Z} \qquad \text{Eq. 3-19}$$

The cylindrical representation of the CIELUV space is known as $CIELCh_{uv}$, represented by the axial height luminance, L^*, the radial distance in the $u^* - v^*$ plane corresponding to chroma, C^*, and the azimuth angle called hue, h_{uv}. Additionally, colour intensity can be represented by saturation, s_{uv}, which is proportional to the Euclidian distance between a colour and the reference white in the UCS chromaticity diagram. Highly saturated colours correspond to samples in the outer edges of the chromaticity diagram, which are made-up of, or close to, monochromatic stimuli. Highly saturated colours are regarded as 'vivid' or 'strong' colours.

Chroma
$$C^*_{uv} = \sqrt{(u^*)^2 + (v^*)^2} \qquad \text{Eq. 3-20}$$

Hue
$$h_{uv} = \arctan\left(\frac{v^*}{u^*}\right) \qquad \text{Eq. 3-21}$$

Saturation
$$s_{uv} = \frac{C^*}{L^*} = 13\sqrt{(u' - u'_n)^2 + (v' - v'_n)^2} \qquad \text{Eq. 3-22}$$

In this work, the transformation to opponent colour space, CIELUV, was considered as a fixed non-linear transformation from the calculated tristimulus values, independent from the observer's normal or anomalous condition. This condition assumes that neural postprocessing of visual information is the same for every observer, independent on whether they are normal trichromats or colour deficient individuals, and the only difference between observers is in the cone spectral sensitivities. While this assumption is debatable, the lack of information and precise computation methods for visual postprocessing by visual and neural systems makes this a common assumption in this type of research, and is commonly justified by comparison to previous publications on the subject.

3.4.4 Effect of frequency selective filter on colour appearance

A light stimulus with spectral properties $\phi(\lambda)$ that is transmitted through a frequency selective filter, with spectral transmittance $f(\lambda)$, will have a spectral property, $\phi'(\lambda)$:

$$\phi'(\lambda) = \phi(\lambda) \cdot f(\lambda) \qquad \text{Eq. 3-23}$$

On the other hand, the tristimulus values, $[L_w, M_w, S_w]$, for a reference white under illumination $S(\lambda)$, perceived through a filter $f(\lambda)$:

$$L_w{}' = k \int_\lambda f(\lambda) S(\lambda)\, \bar{l}(\lambda)\, d\lambda \qquad \text{Eq. 3-24}$$

$$M_w{}' = k \int_\lambda f(\lambda) S(\lambda)\, \bar{m}(\lambda)\, d\lambda \qquad \text{Eq. 3-25}$$

$$S_w{}' = k \int_\lambda f(\lambda) S(\lambda)\, \bar{s}(\lambda)\, d\lambda \qquad \text{Eq. 3-26}$$

The normalized reference white is calculated by normalizing by the maximum tristimulus value.

$$[L'_{wn}, M_{wn}{}', S_{wn}{}'] = \frac{[L'_w, M'_w, S'_w]}{\max\left([L'_w, M_w{}', S_w{}']\right)} \qquad \text{Eq. 3-27}$$

This normalized reference white is useful for the numerical design of the colour correction filters, particularly when considering chromatic adaptation. In the case of certain chromatic adaptation transformations, such as Von Kries adaptation, the value of the reference white is used to normalize the tristimulus values in the chromatic adaptation transform. However, this transformation will not only normalize for the chromaticity of the reference white, but also for its luminance value. By normalizing the reference white by its highest value, we allow to consider adaptation of the chromaticity values but not luminance, forcing the algorithm to find filters which transmit most light and avoiding results such as a perfectly dark filters, with very small transmission, which the algorithm will tend to output when considering chromatic adaptation without normalizing the reference white value.

3.4.5 Databases

To perform the numerical design and analysis, databases were selected containing the spectral information of illumination and reflective samples.

For illumination, the CIE standard illuminations where considered [98], [99], particularly the D65 illuminant, which is used as an approximation for daylight applications. For artificial sources, spectral information was obtained from online databases, such as [96], [100], [101].

In the case of reflective samples, different databases were selected for the numerical design of the filters, and for visualization. For ease in computation, the Macbeth colour cart (24 samples) was selected for computation and design of the optical filters.

The resulting filters from the optimization process in the Macbeth chart were further analysed using databases for the Farnsworth-Munsell 100 test (FM-100, 1269 samples), as well as an assortment of hyperspectral images for the Ishihara test plates, and natural scenes [85]–[87].

3.4.6 Illumination sources

The CIE standard illuminant series ‘D’, derived by Judd, MacAdam and Wyszecki, is a set of mathematically constructed illumination distributions, used to represent natural light. While the spectral profile of the ‘D’ series illuminant is hard to achieve artificially, they are easy to characterize mathematically, and replaced the previously used ‘B’ and ‘C’ illuminants. Each illuminant within the D series corresponds to a different correlated colour temperature, for example, D50, D55, and D65 represent a correlated colour temperature of approximately 5000, 5500, and 6500 K respectively. The D65 illuminant is a rough representation of midday light in Western/Northern Europe, from both direct sunlight, and diffused light in the sky.

In this work, the D65 illumination is considered in all cases for design of colour corrective filters, as the filters are designed for general outdoors eyewear applications. However, a brief analysis considering other light sources will be included, including incandescent, fluorescent, and light-emitting-diode (LED) illuminations, which are commonly used for artificial lightning.

The CIE standard illuminant ‘A’ represents a typical, domestic, tungsten-filament lightning. The spectral power distribution of this illuminant corresponds to that of perfect black body radiator (Planckian radiator), with a correlated colour temperature of 2856 K.

CIE standard ‘F’ series represent various types of fluorescent lighting. Illuminant F7 corresponds to a broadband fluorescent light, with multiple phosphors, used as an artificial simulator of daylight (6500 K). The F11 illuminant (4000 K) represents fluorescent light consisting of three narrowband emissions in the RGB regions of the visible spectrum.

Additionally, an LED illumination is included in the analysis, corresponding to the measured spectral power distribution of a streetlamp (LED LICA-Phillips, 3107 K, measured on-axis [95], [96]).

3.5 OPTIMIZATION ALGORITHM

The numerical methods employed in this work were programmed in the platform MATLAB R2018b. The objective is to find a solution in the form of a filter, $f(\lambda)$, to an optimization problem which minimizes the difference between normal and anomalous trichromatic vision, evaluated according to an appropriate fitness function which represents the difference in one or more aspects of colour vision.

Colour vision deficiency and colour appearance models were implemented according to the equations presented in chapter 2. The replacement model was used to simulate red-green anomalous trichromacy. The resulting optical devices designed using this method are presented in the form of spectral transmittance of a frequency selective filter, which corresponds to the idealized spectral properties for the optimum filter found according to the restrictions and fitness function used to evaluate the device.

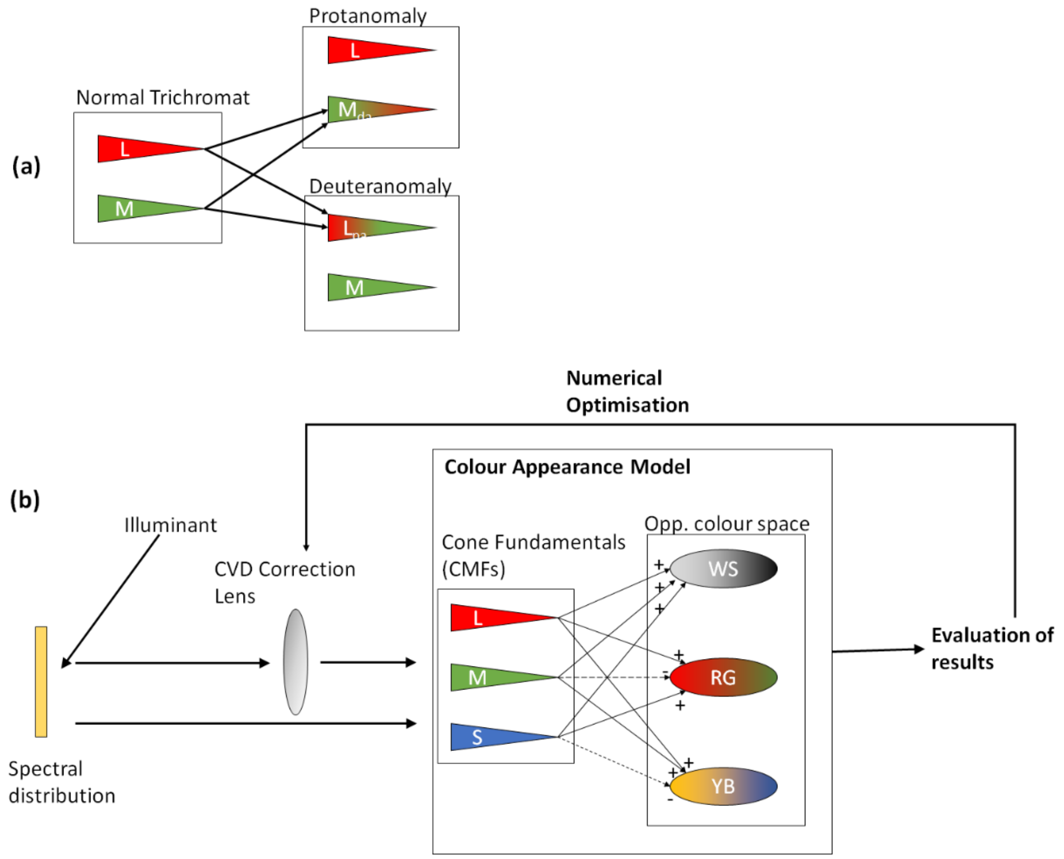

Figure 3-3: Conceptual diagram of numerical methods employed in this work. (a) Red-green colour vision deficiency (RG-CVD) replacement model estimates anomalous cone sensitivities. (b) Finding CVD correction lenses implementing colour appearance models based on cone spectral sensitivities by numerical optimisation.

In summary, the colour vision model implemented in this work follows the subsequent calculations:

1) Calculation of anomalous colour matching functions, from normal trichromat CMFs in LMS space, Φ_{LMS}, and replacement factor, α:

$$(\Phi_{LMS})^{\mathrm{T}}_{CVD} = A_{cvd}(\Phi_{\mathrm{LMS}})^{\mathrm{T}} \quad \text{Eq. 3-28}$$

$$A_{deutan} = \begin{bmatrix} 1 & 0 & 0 \\ \alpha/\kappa & (1-\alpha) & 0 \\ 0 & 0 & 1 \end{bmatrix} \quad \text{Eq. 3-29}$$

$$A_{protan} = \begin{bmatrix} (1-\alpha) & \alpha * \kappa & 0 \\ 0 & 1 & 0 \\ 0 & 0 & 1 \end{bmatrix} \quad \text{Eq. 3-30}$$

$$\kappa = 0.96 \quad \text{Eq. 3-31}$$

2) Calculation of the anomalous luminous efficiency function, $(V_F)_{cvd}$, and normalizing factor, k:

$$V_F = \Phi_{\mathrm{LMS}} T_F \quad \text{Eq. 3-32}$$

$$(V_F)_{cvd} = (\Phi_{\mathrm{LMS}})_{cvd} T_F \quad \text{Eq. 3-33}$$

In LMS space (2° field):

$$T_F = \begin{bmatrix} 0.68990272 \\ 0.34832189 \\ 0 \end{bmatrix} \quad \text{Eq. 3-34}$$

$$k = \frac{100}{V_F^T S} \quad \text{Eq. 3-35}$$

Where S_I is a diagonal matrix containing

$$S_I = \begin{bmatrix} S(\lambda_1) & \cdots & 0 \\ \vdots & \ddots & \vdots \\ 0 & \cdots & S(\lambda_N) \end{bmatrix} \quad \text{Eq. 3-36}$$

3) For each sample, $r(\lambda)$, within the objective database, calculation of tristimulus values for the normal trichromat:

$$t = \begin{bmatrix} X \\ Y \\ Z \end{bmatrix} = k\Phi^T_{\mathrm{XYZ}} S_I \vec{r} \quad \text{Eq. 3-37}$$

$$\Phi_{\mathrm{XYZ}} = \mathrm{T}_{(LMS\to XYZ)}\Phi_{\mathrm{LMS}} \quad \text{Eq. 3-38}$$

4) For the anomalous trichromat provided with a filter with spectral power distribution, given by $f(\lambda)$, calculate the tristimulus values:

$$\varphi_{CVD_f} = k_{CVD}\Phi_{\mathrm{CVD}}^{T} SF\vec{r} \quad \text{Eq. 3-39}$$

$$F = \begin{bmatrix} f(\lambda_1) & \cdots & 0 \\ \vdots & \ddots & \vdots \\ 0 & \cdots & f(\lambda_N) \end{bmatrix} \quad \text{Eq. 3-40}$$

5) Transformation from LMS tristimulus, to CIELUV:

$$L^* = \begin{Bmatrix} \left(\frac{29}{3}\right)^3 \frac{Y}{Y_n}, & \frac{Y}{Y_n} \le \left(\frac{6}{29}\right)^3 \\ 116\left(\frac{Y}{Y_n}\right)^{\frac{1}{3}} - 16, & \frac{Y}{Y_n} > \left(\frac{6}{29}\right)^3 \end{Bmatrix} \quad \text{Eq. 3-41}$$

$$u^* = 13L^*(u' - u'_n) \quad \text{Eq. 3-42}$$

$$v^* = 13L^*(v' - v'_n) \quad \text{Eq. 3-43}$$

$$u' = \frac{4X}{X + 15Y + 3Z} \quad \text{Eq. 3-44}$$

$$v' = \frac{9Y}{X + 15Y + 3Z} \quad \text{Eq. 3-45}$$

6) Evaluation of colour difference formulae, and fitness function.

3.5.1 Fitness function

The fitness function is the objective function that is being optimized by the numerical algorithm. Optimisation algorithms are programmed to find solutions to the problem:

$$x_s = \min[F(x)], \qquad x \in Dom_F \quad \text{Eq. 3-46}$$

where x_s is the solution to the optimisation problem, $F(x)$ is the fitness function, and Dom_F is the domain of definition for the fitness function.

In the case of this study, the author seeks to design a filter with spectral properties $f(\lambda)$, to minimize the difference in terms of colour appearance between a normal trichromat and a CVD individual looking through this filter. The selection of an appropriate fitness function is vital for the design and success of the optical device. The fitness function takes $f(\lambda)$ as an input, where $f(\lambda)$ is the transmittance (or reflectance) of a filter, defined numerically as a 1-by-N vector containing the transmittance of the filter for each wavelength. The output is a metric comparing some aspect of colour appearance, as perceived by both a normal trichromat and a red-green anomalous trichromat.

The selected metrics for this study were forms of Euclidian distance, such as total colour difference and chroma difference. These metrics were selected for being well established functions used as standard for many applications regarding colour measurement:

Total colour difference:

$$\Delta E_{uv}^{*}{}^{2} = (\Delta L^*)^2 + (\Delta u^*)^2 + (\Delta v^*)^2 = \begin{bmatrix} (L^* - L^*_{cvd,f}) \\ (u^* - u^*_{cvd,f}) \\ (v^* - v^*_{cvd,f}) \end{bmatrix}^T \begin{bmatrix} (L^* - L^*_{cvd,f}) \\ (u^* - u^*_{cvd,f}) \\ (v^* - v^*_{cvd,f}) \end{bmatrix} \qquad \text{Eq. 3-47}$$

Chroma difference:

$$\Delta C_{uv}^{*}{}^{2} = (\Delta u^*)^2 + (\Delta v^*)^2 = \begin{bmatrix} (u^* - u^*_{cvd,f}) \\ (v^* - v^*_{cvd,f}) \end{bmatrix}^T \begin{bmatrix} (u^* - u^*_{cvd,f}) \\ (v^* - v^*_{cvd,f}) \end{bmatrix} \qquad \text{Eq. 3-48}$$

In this study, the author seeks to find a solution which works not only for a single colour, but in general. A database containing spectral properties for samples of different colours within the chromatic mosaic is used, and the final metric of the function will be some form of averaging across all samples within the selected database. The following forms were considered for this study:

Mean square averaging:

$$\text{fitness} = \frac{1}{N}\sum F^2 \qquad \text{Eq. 3-49}$$

Higher power averaging:

$$\text{fitness} = \frac{1}{N}\sum F^n, \qquad n = 3,4\ \ldots \qquad \text{Eq. 3-50}$$

In the case of the mean-square averaging, the optimization problem at hand corresponds to a least-squares optimisation in the form:

$$\min_{\mathrm{f}}\left(E\left\{\left\|\mathcal{F}(\vec{t}) - \mathcal{F}(\vec{t}_{cvd,f})\right\|^n\right\}\right) \qquad \text{Eq. 3-51}$$

$$l_b = 0 \le f \le u_b = 1 \qquad \text{Eq. 3-52}$$

where $E\{\ldots\}$ is the expected value of the expression between brackets, calculated as the arithmetic mean over an ensemble of reflective samples, $\mathcal{F}(\varphi)$ is the 3-by-1 non-linear transformation from tristimulus to CIELUV space, $\vec{t}$ is the 3-by-1 vector containing the tristimulus values in XYZ space for one reflective sample. The subscript '*cvd,f*' is used to denote that the values correspond to a CVD individual using a pair of corrective filters, while no subscript corresponds to the normal trichromat. The domain for the filter transmittance, f, is restricted by its lower and upper bounds, corresponding to total reflection, $l_b = 0$, and total transmission by the filter, $u_b = 1$, respectively. While other restrictions can be applied, such as limits for minimum accepted transmitted luminance, only the upper and lower limits indicated above were considered in this work.

Because the transformation $\mathcal{F}$ is non-linear, the optimisation problem at hand is also non-linear. Consequently, numerical optimisation methods, such as those based on gradient descent, can yield non-optimal solutions particularly if the problem presents one or more local minima. Different approaches can be used to ensure that the global optimum is reached numerically:

- Approximating the fitness function to a linearised form, transforming the problem to least-squares optimisation, which has a global optimum, and subsequently refining the solution according to the original non-linear fitness function using gradient methods.
- Using random heuristic search methods to provide an initial solution and refining that solution by gradient descent methods.

3.5.2 Linearisation of the optimisation problem: First order approximation

Consider the following expression, consisting of the mean square difference between the values taken by function $\mathcal{F}$, evaluated at two points $\vec{t}_1$ and $\vec{t}_2$:

$$F = E\left\{\left\|\mathcal{F}(\vec{t}_1) - \mathcal{F}(\vec{t}_2)\right\|^2\right\} \qquad \text{Eq. 3-53}$$

The first order Taylor expansion terms, in the vicinity of $\vec{t}$, approximates this expression [102]:

$$F \approx E\left\{\left\|J_{\mathcal{F}}(\vec{t}_1) \cdot (\vec{t}_1 - \vec{t}_2)\right\|^2\right\} \qquad \text{Eq. 3-54}$$

where $\mathcal{F}$ represents the 3-by-3 non-linear transformation, from CIE XYZ to CIELUV, and $J_{\mathcal{F}}$ is the Jacobian Matrix for the transformation $\mathcal{F}(\vec{t})$, with respect to $\vec{t}$. The analytical expression for each component of $J_{\mathcal{F}}$ can be bound in Annex 4. This first order expansion is a good approximation for small differences between $\vec{t}_1$ and $\vec{t}_2$, and its validity for the differences between normal and anomalous trichromacy will be discussed later in the results section.

When optimising the function F in terms of the filter transmittance, f, one seeks the values of f for which the fitness function's gradient has a value of zero. This can be written as a system of equations of size N-by-N, where N is the number of points in the discretised wavelength spectrum for the filter transmittance, therefore, it corresponds to the number of variables in the optimisation problem. The proof that function F has a global optimum, with no local optimums, is equivalent to proving that the system of equations in Eq. 3-56 has a unique solution.

$$\nabla(F) = 0 \qquad \text{Eq. 3-55}$$

Represented by N-by-N system of equations

$$\begin{gathered} \frac{\partial}{\partial f_1}(F) = 0 \\ \vdots \\ \frac{\partial}{\partial f_N}(F) = 0 \end{gathered} \qquad \text{Eq. 3-56}$$

Consider the following notation, where subscript 'k' represents a reflective sample within the selected database, subscript 'l' represents the elements for the CIELUV coordinates, subscript 'j' represents the elements of the XYZ tristimulus values, and subscript 'i' represents the points in the discretised wavelength space:

Table 3-1: Index notation for fitness function representation

N° reflective samples	$\boldsymbol{k = 1, \dots, M}$
N° points in discretized wavelength space	$i = 1, \dots, N$ (for $\lambda = 380, \dots, 780$ nm)
Tristimulus coordinates	$j = 1, 2, 3$ (for X, Y, Z respectively)
Coordinates in CIELUV	$l = 1,2,3$ (for L^*, u^*, v^* respectively)

The fitness function is dependent on the following parameters:

Transmittance of corrective filter, f.

$$\vec{f} = [f_i] \qquad \text{Eq. 3-57}$$

Reflectance of sample 'k'.

$$\vec{r}_k = [r_{ik}] \qquad \text{Eq. 3-58}$$

CMFs in XYZ.

$$\tau_{(Nx3)} = [\tau_{ij}] \qquad \text{Eq. 3-59}$$

CMFs in LMS.

$$\Phi_{(Nx3)} = [\Phi_{ij}] \qquad \text{Eq. 3-60}$$

Illuminant spectral power distribution.

$$S = [S_i] \qquad \text{Eq. 3-61}$$

The tristimulus values for a particular sample, 'k' are calculated as follows:

For the normal trichromat:

$$t_{jk} = \sum_{i=1}^{N} \left(k * r_{ij} * S_i * \tau_{ij} * \Delta\lambda\right) \qquad \text{Eq. 3-62}$$

For the case of CVD, provided with a filter of transmittance given by vector f:

$$t_{jk}^{cvd,f} = \sum_{i=1}^{N} \left(k^{cvd} * r_{ij} * S_i * \tau_{ij}^{cvd} * f_i * \Delta\lambda\right) \qquad \text{Eq. 3-63}$$

where k is the luminance normalising factor, r is the reflectance of a sample, S is the illuminant spectral power distribution, τ is the XYZ CMFs, f is the filter transmittance, and $\Delta\lambda$ is the distance between discretised points in the wavelength spectrum:

Transformation of CMFs from LMS to XYZ

$$\tau^T = T_{(LMS\to XYZ)}\Phi^{\mathrm{T}} \qquad \text{Eq. 3-64}$$

Anomalous CMFs

$$\Phi_{\mathrm{cvd}}^{T} = A_{cvd}\Phi^{\mathrm{T}}$$
$$\tau_{cvd}^{T} = \left(T_{(LMS\to XYZ)}\right)\left[A_{cvd}\left(T_{(LMS\to XYZ)}\right)^{-1}\tau^{\mathrm{T}}\right] \qquad \text{Eq. 3-65}$$

Normalizing factor

$$k = \frac{100}{V^T\vec{S}} \qquad \text{Eq. 3-66}$$

$$k_{cvd} = \frac{100}{V_{cvd}^{T}\vec{S}} \qquad \text{Eq. 3-67}$$

Luminous efficiency

$$V = \Phi T_F \qquad \text{Eq. 3-68}$$

$$V_{cvd} = \Phi_{\mathrm{cvd}}T_F \qquad \text{Eq. 3-69}$$

In LMS space (2° field):

$$T_{(LMS\to XYZ)} = \qquad \text{Eq. 3-70}$$

$$T_{F,2} = \begin{bmatrix} 0.68990272 \\ 0.34832189 \\ 0 \end{bmatrix} \qquad \text{Eq. 3-71}$$

Anomalous CMF transformation, for deuteranomalous and protanomalous

$$A_{deutan} = \begin{bmatrix} 1 & 0 & 0 \\ \alpha/sr & (1-\alpha) & 0 \\ 0 & 0 & 1 \end{bmatrix} \qquad \text{Eq. 3-72}$$

$$A_{protan} = \begin{bmatrix} (1-\alpha) & \alpha * sr & 0 \\ 0 & 1 & 0 \\ 0 & 0 & 1 \end{bmatrix} \qquad \text{Eq. 3-73}$$

Scale ratio factor

$$sr = 0.96 \qquad \text{Eq. 3-74}$$

The expression in Eq. 3-53 can be rewritten in terms of this notation. Let one consider the mean square colour difference optimisation (Eq. 3-47):

Global fitness function is the mean value for M samples within the selected reflective database.

$$F = \frac{1}{M}\sum_{k=1}^{M}\left(\left\|\mathcal{F}(\vec{t}_k) - \mathcal{F}(\vec{t}_k^{cvd,f})\right\|^2\right) = \frac{1}{M}\sum_{k=1}^{M}\left|\left|\Delta\mathcal{F}_k\right|\right|^2 \qquad \text{Eq. 3-75}$$

$\Delta\mathcal{F}_k$ represents the fitness for a single sample, k.

$$\left|\left|\Delta\mathcal{F}_k\right|\right|^2 = \sum_{l=1}^{3}\left(\Delta\mathcal{F}_{l,k}\right)^2 = (\Delta L_k^*)^2 + (\Delta u_k^*)^2 + (\Delta v_k^*)^2 \qquad \text{Eq. 3-76}$$

Using the first order approximation, for a single CIELUV coordinate in sample k:

$$\Delta\mathcal{F}_{l,k} = \Delta\mathcal{F}_l(\vec{t}_k) = \sum_{j=1}^{3} J_{l,j,k}\left(t_{j,k} - t_{j,k}^{cvd,f}\right) \qquad \text{Eq. 3-77}$$

For the case of chroma difference (Eq. 3-48), the expression in Eq. 3-77 only changes in that index ‘l’ goes from 2 to 3 ($\Delta C_k = (\Delta u_k^*)^2 + (\Delta v_k^*)^2$).

The global fitness function is rewritten extensively as:

$$F = \frac{1}{M}\sum_{k=1}^{M}\left(\sum_{l=1}^{3}\left(\sum_{j=1}^{3} J_{l,j,k}\left(t_{j,k} - t_{j,k}^{cvd,f}\right)\right)^2\right) \qquad \text{Eq. 3-78}$$

$$F = \frac{\Delta\lambda^2}{M}\sum_{k=1}^{M}\left(\sum_{l=1}^{3} J_{l,j,k}\left(\sum_{l=1}^{3}\left(k\, r_{ij}\, S_i\, \tau_{ij} - k^{cvd}\, r_{ij}\, S_i\, \tau_{ij}^{cvd}\, f_i\right)\right)^2\right) \qquad \text{Eq. 3-79}$$

Note that in Eq. 3-78 the only term dependent on f is $t_{j,k}^{cvd,f}$, which is a first order polynomial with respect to f_i (Eq. 3-63). Therefore, the first order Taylor approximation of function F, expressed in Eq. 3-79, is a second order polynomial with respect to f_i, and the mean square optimization should yield a unique global solution. Furthermore, one can prove this by calculating the gradient, and showing that $\nabla F = 0$ has a unique solution.

For the optimisation problem, one seeks to calculate the gradient of the fitness function with respect to the filter transmittance. For the 'n^{th}' component of the filter transmittance spectrum, the derivative of the fitness function, F, is:

$$\nabla_{\mathrm{n}} F \coloneqq \frac{\partial}{\partial f_n} F \qquad \text{Eq. 3-80}$$

$$\nabla_{\mathrm{n}} F = \frac{1}{M}\sum_{k=1}^{M}\sum_{l=1}^{3}\frac{\partial}{\partial f_n}\left|\left|\Delta\mathcal{F}_{l,k}\right|\right|^2 \qquad \text{Eq. 3-81}$$

$$\nabla_{\mathrm{n}}\left[\left|\left|\Delta\mathcal{F}_{l,k}\right|\right|^2\right] = 2\Delta\mathcal{F}_{l,k}\frac{\partial}{\partial f_i}\left(\Delta\mathcal{F}_{l,k}\right) = 2\Delta\mathcal{F}_{l,k}\frac{\partial}{\partial f_i}\left(J_{l,k}\vec{t}_k - J_{l,k}\vec{t}_k^{cvd,f}\right) \qquad \text{Eq. 3-82}$$

$$\nabla_{\mathrm{n}}\left[\left(J_{l,k}\vec{t}_k - J_{l,k}\vec{t}_k^{cvd,f}\right)^2\right] = 2\left(J_{l,k}\vec{t}_k - J_{l,k}\vec{t}_k^{cvd,f}\right)\frac{\partial\left(-J_{l,k}\vec{t}_k^{cvd,f}\right)}{\partial f_n} \qquad \text{Eq. 3-83}$$

$$\frac{\partial\left(-J_{l,k}\vec{t}_k^{cvd,f}\right)}{\partial f_n} = -J_{l,k}\sum_{i=1}^{N}\left(k^{cvd}\, r_{i,j,k}\, S_i\, \tau_{i,j}^{cvd}\, \Delta\lambda\, \frac{\partial f_i}{\partial f_n}\right) \qquad \text{Eq. 3-84}$$

$$\frac{\partial f_i}{\partial f_n} = \begin{Bmatrix} 1, & for\ (i = n) \\ 0, & for\ (i \neq n) \end{Bmatrix} \qquad \text{Eq. 3-85}$$

Therefore,

$$\frac{\partial\left(-J_{l,k}\vec{t}_k^{cvd,f}\right)}{\partial f_n} = -J_{l,k}\left(k^{cvd}\, r_{n,j,k}\, S_n\, \tau_{n,j}^{cvd}\, f_n\, \Delta\lambda\right) \qquad \text{Eq. 3-86}$$

$$\nabla_{\mathrm{n}} F_{l,k} =$$

$$\Delta\lambda^2 * 2 \left[\sum_{j=1}^{3} J_{l,j,k} \left\{ \sum_{i=1}^{N} \left(k\, r_{i,j,k}\, S_i\, \tau_{i,j} - k^{cvd}\, r_{i,j,k}\, S_i\, \tau_{i,j}^{cvd}\, f_i \right) \right\} * J_{l,j,k} \left[-k^{cvd}\, r_{n,j,k}\, S_n\, \tau_{n,j}^{cvd} \right] \right] \quad \text{Eq. 3-87}$$

$$\nabla_{\mathrm{n}} F = \frac{1}{M} \sum_{k=1}^{M} \sum_{l=1}^{3} \nabla_{\mathrm{n}} F_{l,k} \quad \text{Eq. 3-88}$$

$$\nabla_{\mathrm{n}} F = \frac{2 * \Delta\lambda^2}{M} \sum_{k=1}^{M} \sum_{l=1}^{3} \left[\sum_{j=1}^{3} J_{l,j,k} \left(k\, r_{i,j,k}\, S_i\, \tau_{i,j} - k^{cvd}\, r_{i,j,k}\, S_i\, \tau_{i,j}^{cvd}\, f_i \right) \right] * J_{l,j,k} \left[-k^{cvd}\, r_{n,j,k}\, S_n\, \tau_{n,j}^{cvd} \right] \quad \text{Eq. 3-89}$$

$$\nabla_{\mathrm{n}} F = \frac{2 * \Delta\lambda^2}{M} \sum_{k=1}^{M} \sum_{l=1}^{3} \left[\sum_{j=1}^{3} J_{l,j,k} \left\{ \sum_{i=1}^{N} \left(t_{i,j,k} - \boldsymbol{t}_{\boldsymbol{i,j,k}}^{\boldsymbol{cvd,f}} \right) \right\} \right] * J_{l,j,k} \left[-t_{n,j,k}^{cvd} \right] \quad \text{Eq. 3-90}$$

Note that the only term in Eq. 3-90 that depends on the value of f_i is the term $t_{i,j,k}^{cvd,f}$, which is linear with respect to f_i. The last term, $t_{\boldsymbol{n},j,k}^{cvd}$, is independent of *f* as a variable, but depends on the index of the gradient subproblem, '*n'*.

In terms of the variables f_i, combining Eq. 3-90 and Eq. 3-91 one can rewrite the expression as a weighted summation (linear combination) of the N-variables ($f_{i=1,..N}$). This results in an N-by-N linear system of equations:

$$\nabla F = 0 \quad \text{Eq. 3-91}$$

Is equivalent to:

$$b_n + \sum (a_n)_i f_i = 0 \quad \text{Eq. 3-92}$$

The full N-by-N system of equations:

$$\begin{matrix} b_1 + \sum (a_1)_i f_i = 0 \\ \vdots \quad \vdots \quad \vdots \\ b_N + \sum (a_N)_i f_i = 0 \end{matrix} \quad \text{Eq. 3-93}$$

Expressed in matrix notation:

$$A\vec{f} = -\vec{b} \qquad \text{Eq. 3-94}$$

Where $(a_n)_i$ is represents the numerical value for the weight of f_i, in the 'n^{th}' equation in the system, and b_n is the offset for the weighted summation. Matrix A contains the values for $(a_n)_i$, and vector $\vec{b}$ is the offset. The linear system will have a unique solution, so long matrix A is non-singular (determinant is different to zero), meaning that the equations within the system are independent from each other (an equation cannot be written as a linear combination of others), and consistent (no conflicting or contradicting equations).

3.5.3 Numerical optimisation methods

Gradient-based optimisation

Gradient-based methods are algorithms for numerical optimisation of the form:

$$\min_{x}\{F(x), x \in Dom(F)\} \qquad \text{Eq. 3-95}$$

where $F(x)$ is the objective function being optimised, and $Dom(F)$ is the domain of function F. The idea of gradient-based methods is to iterate from a starting solution, x, by taking steps in a direction given by the gradient of F at the current point of iteration.

The function *fmincon*, implemented in Matlab's Optimisation Toolbox, is a gradient-based constrained optimisation method, designed to work on problems with a continuous objective and constrain functions.

The method is based on Trust Region Reflective Algorithm, whose basic idea is to approximate the objective function, $F(x)$, to a simpler function, q, which reasonably represents the behaviour of F in a neighbourhood around x (trust-region). A trial-step, s, is computed by an approximate minimisation of q in the trust-region, N.

$$\min_{s}\{q(s), s \in N\} \qquad \text{Eq. 3-96}$$

From an initial solution, each iteration updates the current position to $(x + s)$, if $F(x + s) < F(x)$; otherwise, the position remains unchanged and the trust-region, N, is shrunk and the iteration is repeated. The algorithm continues until one of multiple stopping-criteria is met, for example, when the change in the function's value for one iteration is less than the accepted tolerance, or when reaching the maximum number of iterations.

In the standard trust-region method, function q is approximated by the second order (quadratic) Taylor expansion:

$$\min_{s}\left\{\frac{1}{2}s^T Hs + s^T g, such\ that\ \left\|Ds\right\| \leq \Delta\right\} \quad \text{Eq. 3-97}$$

where g is the gradient vector of function F, at the current point of iteration, x, and H is the Hessian matrix of F. The term D corresponds to a diagonal scaling matrix, Δ is a positive scalar, and $\left\|.\right\|$ is the quadratic norm. The gradient and Hessian can be defined using an analytical expression provided by the user or approximated numerically by Matlab.

Typically, algorithms for solving Eq. 3-97 involve the computation of all eigenvalues of the Hessian matrix, and the use of Newton's root-finding method applied to the secular equation:

$$\frac{1}{\Delta} - \frac{1}{\left\|s\right\|} = 0 \quad \text{Eq. 3-98}$$

The method, while accurate, can be time intensive for large-scale problems as it requires several factorizations of matrix H. Solvers in Matlab's Optimisation Toolbox, such as fmincon, address this using an approximation, by restricting the trust-region subproblem to a two-dimensional subspace, S. This subspace is determined as the linear space spanned by s_1 and s_2, where s_1 is in the direction of the gradient, g, and s_2 is either an approximate Newton direction (solution to Eq. 3-99) or a direction of negative curvature (Eq. 3-100).

$$Hs_2 = -g \quad \text{Eq. 3-99}$$

$$s_2^T Hs_2 < 0 \quad \text{Eq. 3-100}$$

The choice of subspace S is based on the idea of forcing global convergence, *via* steepest descent or negative curve direction, and achieving fast convergence *via* Newton's method when possible.

In summary, the solver fmincon follows these steps:

1. Formulate the two-dimensional trust-region subproblem.
2. Solve Eq. 3-97 to determine the trial step s.
3. If $f(x + s) < f(x)$, then $x = x + s$.
4. Adjust Δ.

The advantage of gradient methods is their fast convergence, small number of computations required, and precision. The main disadvantage of gradient-based optimisation methods is their inability to handle local optimums, which generally causes the algorithm to return a solution which corresponds to a local optimum rather than the global optimum. Additional information on fmincon can be found in [103], [104].

Random Heuristic Search

Random search is a family of numerical optimisation methods, that do not require the computation of the gradient, and therefore can be used on functions that are discontinuous or non-differentiable [105]. The ‘random’ term comes from the fact that there is at least one way in which the method is using a random number generator, for example, in the generation of a staring solution or in computation of an iterative step.

Owing to the random nature of these methods, there can be a decrease in performance of across two iterations, which can slow down the convergence, and result in lesser optimal solutions. However, it has the advantage of allowing the algorithm to “escape” local optimums, by stepping in a direction against the gradient.

The heuristic varies across different methods, and generally give the name to the optimisation method and defines how the algorithm works in general.

Genetic algorithm is a random search method, based on the general ideas of heritage, natural selection, and gene mutation. In this method, an initial set of solutions is generated at random, and ranked according to the value of the objective function evaluated at each of these points. The heuristic involves selecting the “fittest” individuals (best performing solutions), to create a new generation of solutions. New generations are created by “cross-over” of genes (numeric bits) between selected individuals, and a probability of random mutation of these genes. By iterating over various generations, the average performance of the population is generally increased, as well as improving the performing individual which will become the final solution.

3.5.4 Statistical analysis

Wilcoxon signed rank test is a nonparametric statistical hypothesis test used to compare a pair of dependent samples, assessing whether the population mean ranks differ. This paired difference test is used as an alternative on the paired Student t-test, when the data cannot be assumed to have a normal distribution. It is used in similar situations as the Mann-Whitney U-test, and the main difference is that Wilcoxon signed rank tests is used for related variables, while Mann-Whitney U-test is used for independent variables.

Assumptions:

1) The dependant variable is measured at ordinal (*e.g.*, a 7-point scale from “strongly agree” to “strongly disagree” on a questionnaire) or continuous level (*e.g.*, reaction time of an individual).
2) Independent variable consists of two categorical, “related groups” or “matched pairs”.
3) Distribution of the differences between the two related groups must be symmetrical.

Null hypothesis: H_0: median difference between pairs of observations is zero (follows a symmetrical distribution around zero).

The Wilcoxon signed rank test is used in this work to evaluate the whether the designed frequency selective filters generate a statistically significant reduction on the average colour difference between normal trichromacy, and a colour vision deficient individual provided with the colour corrective filter. Alternatively, the effect of the filter on other aspects of colour appearance can be evaluated, such as the reduction in the chroma difference between normal and anomalous trichromacy, as well as changes in hue and saturation.

3.6 RESULTS

The numerical optimisation approach to the optical filter design problem requires the selection of an objective function, which appropriately describes the aspects or characteristics of the optical system which are going to be optimized by the algorithm. The construction and selection of this function is crucial to both the efficiency of the algorithm, as well as the performance of the final optical system.

This section summarises the results obtained from the filter optimisation for correction of red-green anomalous trichromacy. Various fitness functions were used as an optimisation target. The Macbeth colour chart was selected as a small, but representative dataset for reflective samples considered by the optimisation algorithm, and all results shown in this section result from an optimisation over this dataset. Other datasets were considered exclusively for results analysis and discussion. Chromatic adaptation transforms are not considered in this section.

It is important to note that the colour difference metric was formulated for small colour differences, and the predicted differences between the normal and anomalous observers are very large in comparison. However, the issue of an adequate metric for large colour differences is still a topic of research and falls outside the scope of this investigation. Further discussion with regards to this issue can be found in Chapter 5.

3.6.1 Linearised optimisation

To ensure that a global optimum is reached by the selected numerical solver, three approaches were considered, and the solutions were compared:

(1) Solving the original optimisation problem using fmincon, using a randomised initial solution within the function's domain ($0 \leq f \leq 1$).
(2) Solving a linearised form of the optimisation problem, with a 1st order approximation to the merit function (see Eq. 3-54), using fmincon as numerical solver. Subsequently, using the solution to the linearised problem as an initial solution in (1).
(3) Solving the original optimisation problem using various random heuristic search methods (genetic algorithm, particle swarm optimisation, and simulated annealing), and refining the solution using fmincon.

Results are shown in Figure 3-4, for optimisation of the mean-square colour differences (${\Delta E^*_{uv}}^2$), considering a deuteranomalous observer with a severe condition ($\alpha = 0.9$). In the case of the linearised optimisation, the solution presents a wide stopband centred around 500 nm, while the solution to the non-linearised original function shows two narrow bands centred at 480 and 580 nm. The solution to the non-linearised optimisation seems unaffected by the starting point.

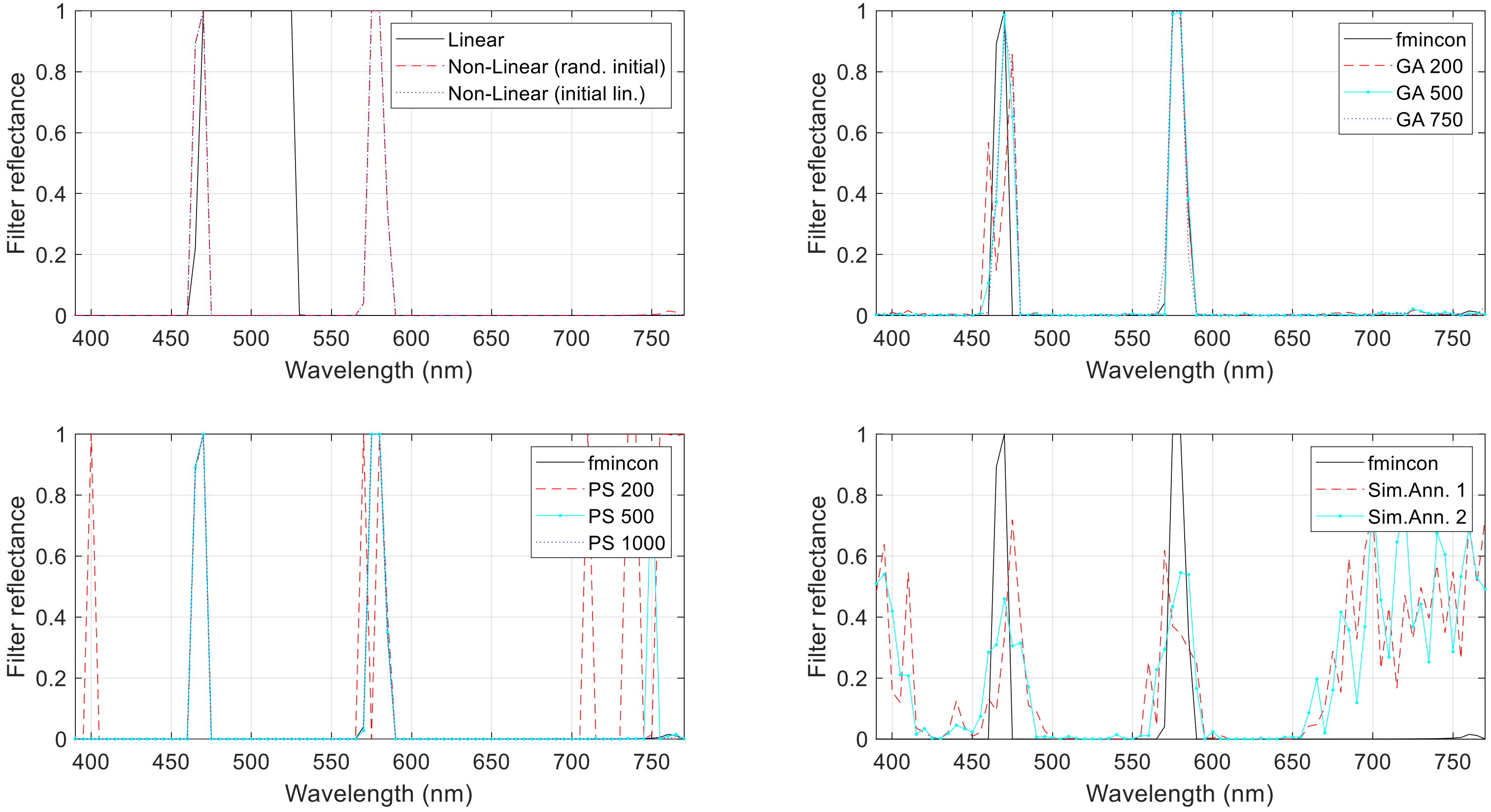

Figure 3-4: Filter design from numerical optimisation, for fitness ΔE^2, deuteranomalous ($\alpha = 0.9$): (a) Solution to the 1st order approximation (linearised), non-linearised, and to the non-linearised function using the solution from (a) as the initial point (using fmincon solver in all cases); (b) solution to non-linearised using genetic algorithm search (population = 200, 500, and 750); (c) solution to non-linearised using particle swarm optimisation (population = 200, 500, and 1000); (d) solution to non-linearised using simulated annealing optimisation (two cases shown).

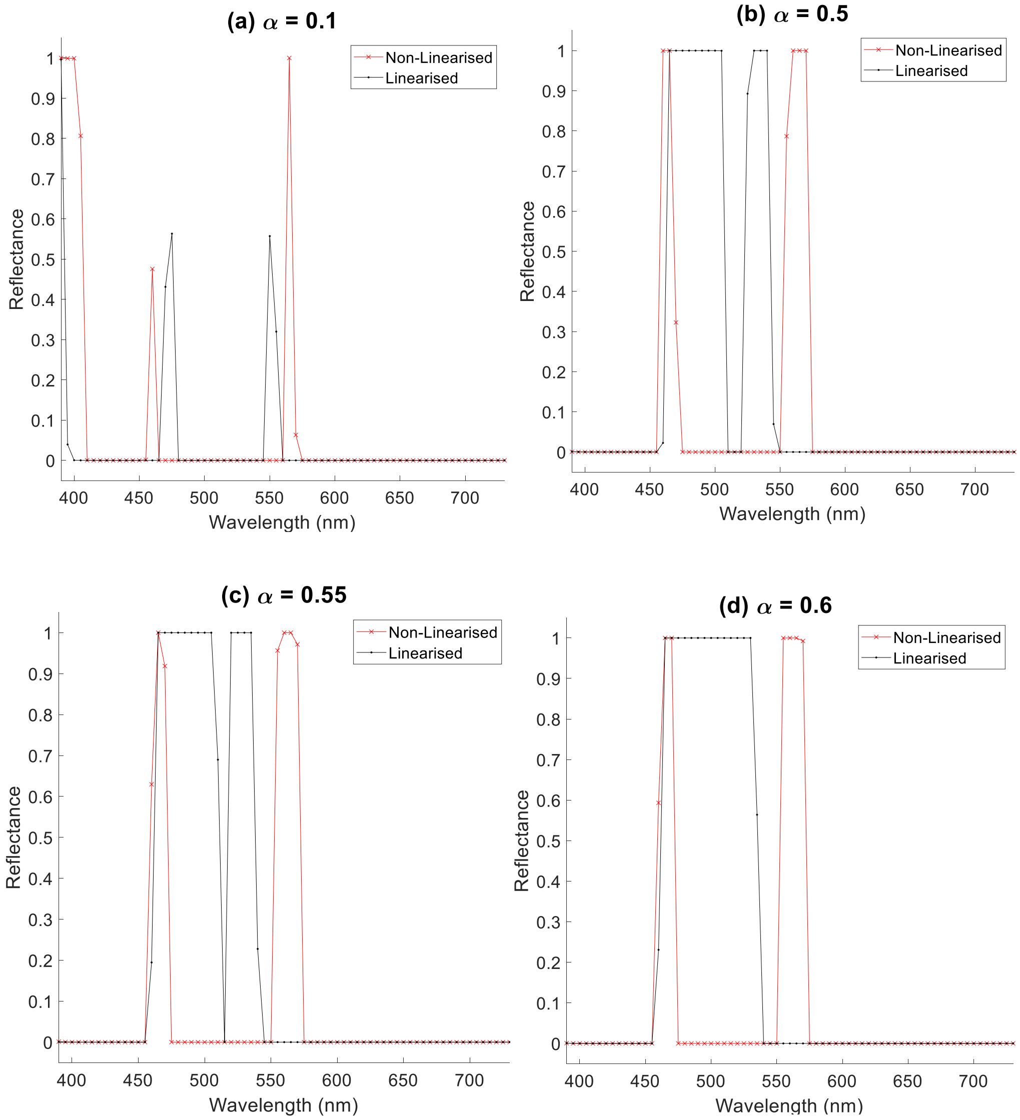

Figure 3-5: Results from filter design optimisation, for fitness ΔE^2. Comparative results for linearised optimisation (Eq. 3-54) and original non-linear problem (Eq. 3-53) using fmincon for numerical optimization. Each graph corresponds to a different replacement factor: **(a)** $\alpha = 0.1$, **(b)** $\alpha = 0.5$, **(c)** $\alpha = 0.55$, and **(d)** $\alpha = 0.6$.

3.6.2 Average total colour difference $(\overline{\Delta E^*_{uv}})$

Minimizing the average colour difference between an anomalous trichromat observer, aided by a colour correction filter, and a normal trichromat observer, the optimisation algorithm yields a filter with optical properties as shown in Figure 3-6. For the deuteranomalous case, two non-full stop bands are present at 460 and 600 nm, while in the protanomalous case only one band appears at 575 nm. In both cases, wider bands are present in the limits of the visible spectrum, however, the cone spectral sensitivity is small in those ranges, and their contribution to colour correction is limited.

The colour difference between the anomalous and normal trichromat observers is presented in Figure 3-7, as well as the colour difference considering the use of the colour correction filter. It can be observed that the colour correction provided by the filter is very small in comparison, in fact, the colour difference correction would be imperceptible for any observers ($\Delta E < 1$, as shown in Figure 3-8).

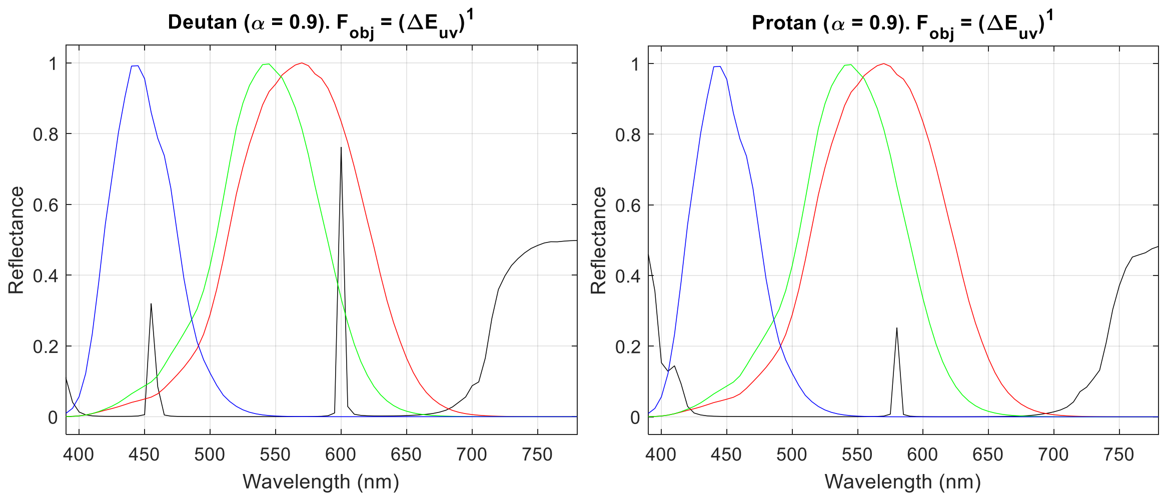

Figure 3-6: Spectral reflectance of colour correction filter designed by numeric optimisation, and cone fundamentals. Case deuteranomalous (left) and protanomalous (right); $\alpha = 0.9$; fitness $= (\overline{\Delta E_{uv}^{*}})$.

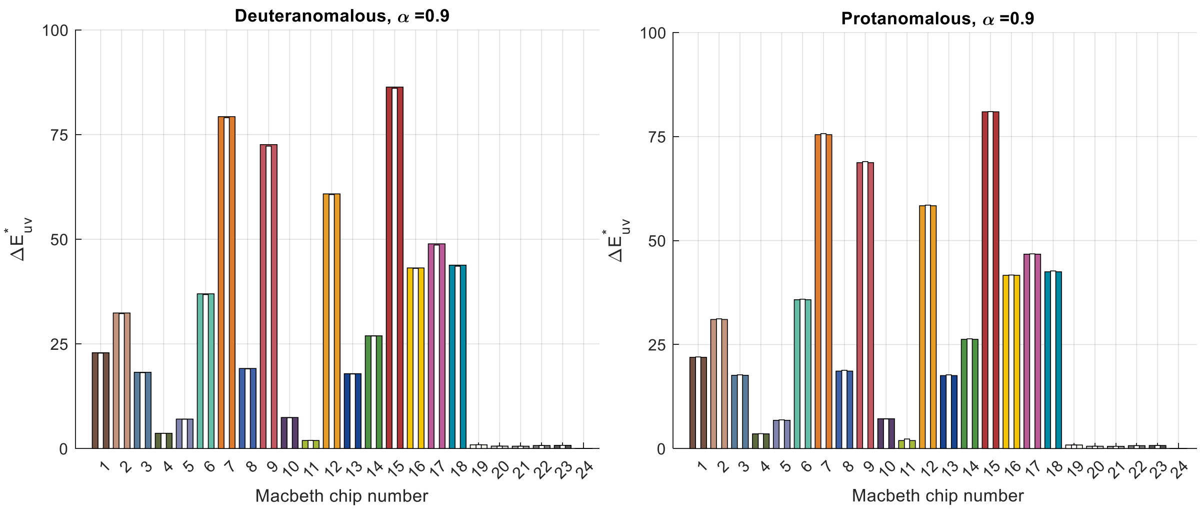

Figure 3-7: Colour difference, ΔE_{uv}^{*}, of the Macbeth colour checker between normal and anomalous trichromats (coloured bars), and between normal an anomalous trichromat wearing corrective filter (overlaid white bars). Case deuteranomalous (left) and protanomalous (right); $\alpha = 0.9$; fitness $= (\overline{\Delta E_{uv}^{*}})$.

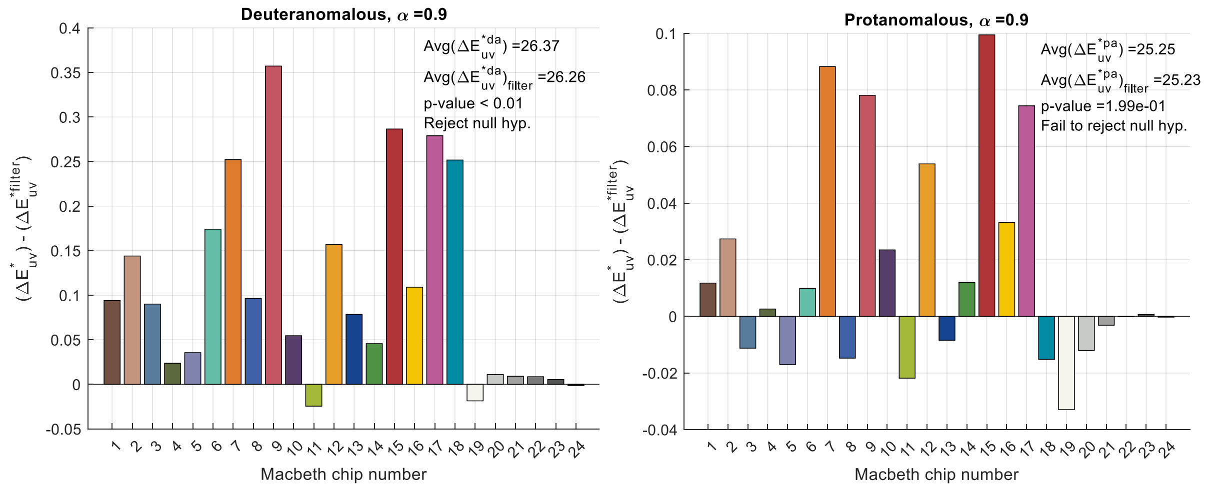

Figure 3-8: Colour difference between anomalous trichromat observer with and without the use of a colour correction filter, with respect to a normal trichromat observer. Positive values indicate that the colour difference between the normal and anomalous observer is reduced by the colour correction device. Results of the Wilcoxon signed rank test are presented in the legend text box; $\alpha = 0.9$; fitness $= (\overline{\Delta E^{*}_{uv}})$.

With respect to the statistical significance of the colour difference correction, tested using the Wilcoxon signed rank test, it was found that the colour difference provided by the colour correction filter is statistically significant for the case of deuteranomalous (p-value = $1.15 * 10^{-4}$), and is not significant for the case pf protanomalous (p-value = $1.99 * 10^{-1}$).

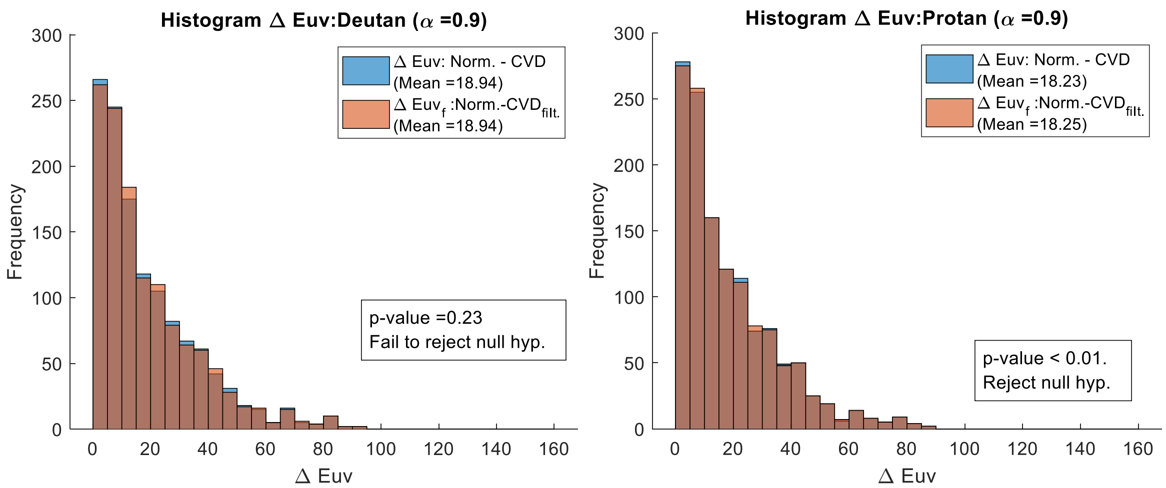

Figure 3-9: Frequency histogram for total colour difference in FM-100 test, between a normal trichromat, and an anomalous trichromat, with and without the use of colour corrective optical filters (blue and orange bars respectively). Results of the Wilcoxon signed rank test are presented in the legend text box; $\alpha = 0.9$; fitness $= (\overline{\Delta E^{*}_{uv}})$.

3.6.3 Average square total colour difference $\left(\overline{\Delta \mathbf{E}_{\mathbf{uv}}^{*}{}^{2}}\right)$

From the previous section, it was found that by optimizing the average colour difference between normal vision and anomalous trichromacy provided with a colour correction filter, the optimum filter can only achieve very small improvements, which are imperceptible to the average observer. While some improvements can be made for certain colours, particularly for colours such as red, pink, and orange (*e.g.*, chips n° 7, 9, 15, 17), which produce the largest difference between normal and anomalous colour vision, the improvement in this colours trade-off in the detriment of others.

For a more impactful result, the design strategy can be set to prioritize those colours which have a larger difference with respect to normal colour vision, sacrificing the discrimination in other colours which are less affected by the CVD condition. A strategy is to set a fitness function which is not uniform across all colours, for example, the average square summation of all colours will prioritize those colours which have a larger difference between the CVD and normal observers.

From Figure 3-10 it can be observed that optimizing for $\overline{\Delta E_{uv}^{*}{}^{2}}$, two stop-bands appear at 475 and 570 nm for the deuteranomalous case, and at 400, 480, and 550 nm for protanomalous. These are complete stop-bands (in the normal direction), blocking all the light within that band, in contrast with the partial bands when optimizing for $\overline{\Delta E_{uv}^{*}}$ in Figure 3-6.

Comparing the effect of colour corrective filters designed for a fitness function with normal averaging ($\overline{\Delta E_{uv}^{*}}$, Figure 3-8) and square averaging ($\overline{\Delta E_{uv}^{*}{}^{2}}$, Figure 3-11) of the total colour difference change, it can be observed that in the latter the effect of the filter on individual colours is more pronounced, in some cases having differences of ΔE_{uv}^{*} large enough to be perceived by experienced observers ($\Delta E > 1$), while in the case of normal averaging, the differences produced by the filter are all imperceptible to all observers ($\Delta E < 1$).

Note that while the effect produced by the filter shown below can be large enough in certain individual colours to be perceived by some observers, the average effect is very small, as the detriment in the discrimination of other colours is also larger. The Wilcoxon signed-rank statistical analysis showed that the colour corrective effect is statistically significant in the case of protanomaly but fails to reject the null hypothesis for the case of deuteranomaly.

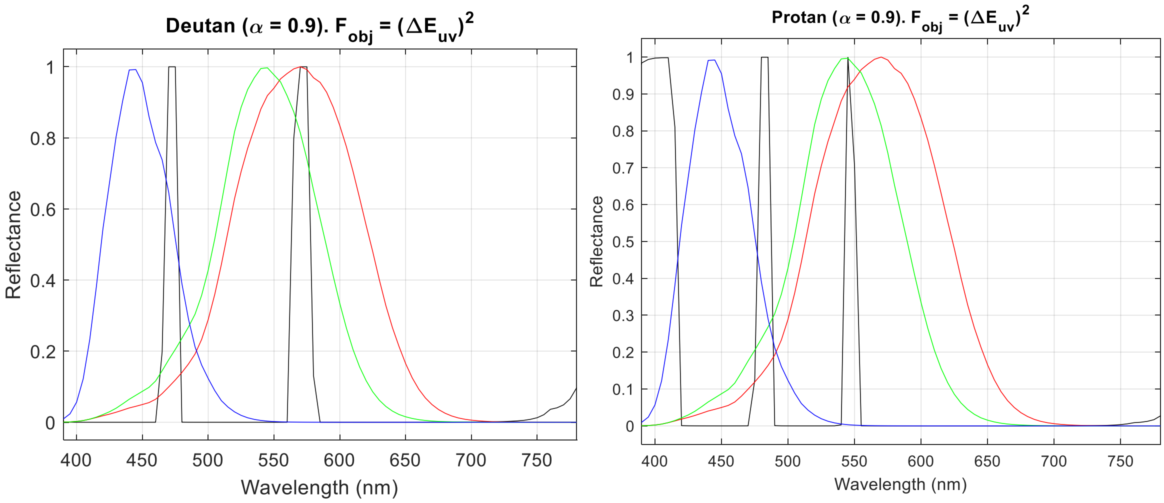

Figure 3-10: Spectral reflectance of colour correction filter designed by numeric optimisation, and cone fundamentals. Case deuteranomalous (left) and protanomalous (right); $\alpha = 0.9$; fitness = $(\overline{\Delta \mathrm{E}_{\mathrm{uv}}^{*}{}^{2}})$.

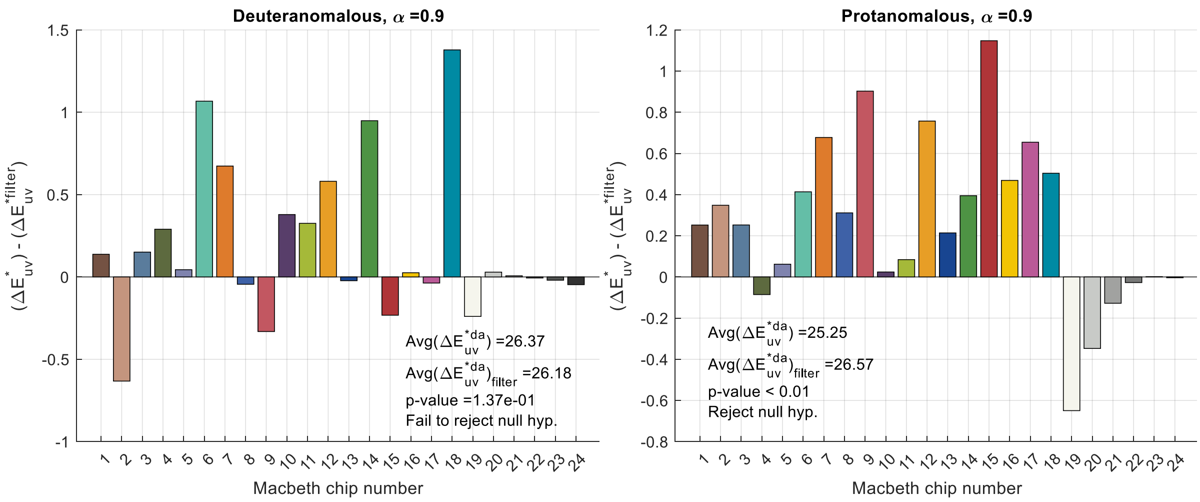

Figure 3-11: Colour difference between anomalous trichromat observer with and without the use of a colour correction filter, with respect to a normal trichromat observer. Positive values indicate that the colour difference between the normal and anomalous observer is reduced by the colour correction device. Results of the Wilcoxon signed rank test are presented in the legend text box; $\alpha = 0.9$; fitness = $(\overline{\Delta E_{uv}^{*}{}^{2}})$.

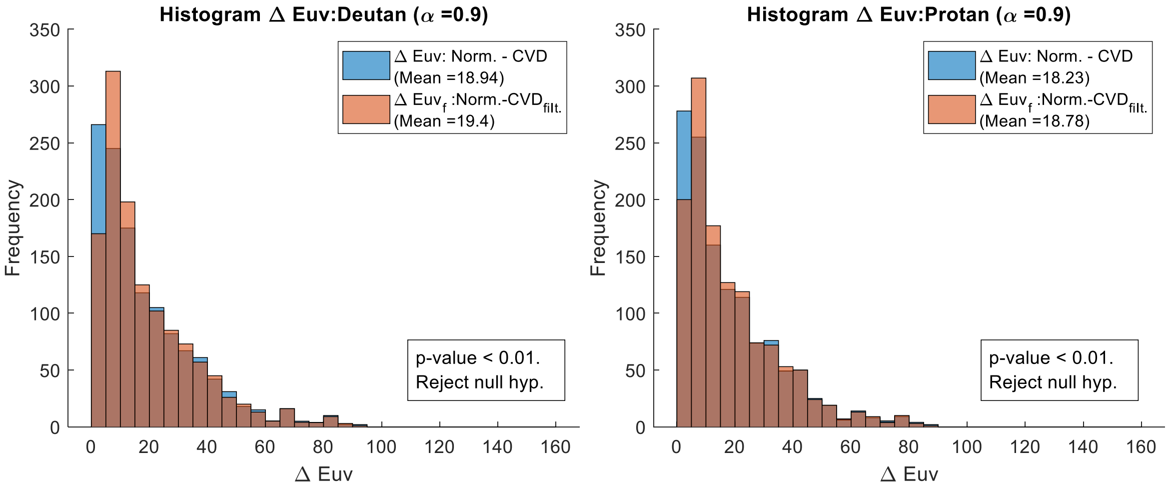

Figure 3-12: Frequency histogram for total colour difference in FM-100 test, between a normal trichromat, and an anomalous trichromat, with and without the use of colour corrective optical filters (blue and orange bars respectively). Results of the Wilcoxon signed rank test are presented in the legend text box; $\alpha = 0.9$; fitness $= (\overline{\Delta E_{uv}^{*}}^{2})$.

3.6.4 Average chroma difference $(\overline{\Delta C_{uv}^{*}})$

Alternatively to the total colour difference used as a design objective in the previous section, in this section presents the results for the filter design and optimisation when considering chroma difference. In contrast with the total colour difference, the chroma difference does not consider the lightness (L^*) of the sample, and considers only the chromatic coordinates, u^* and v^*. Results are presented below in Figure 3-13.

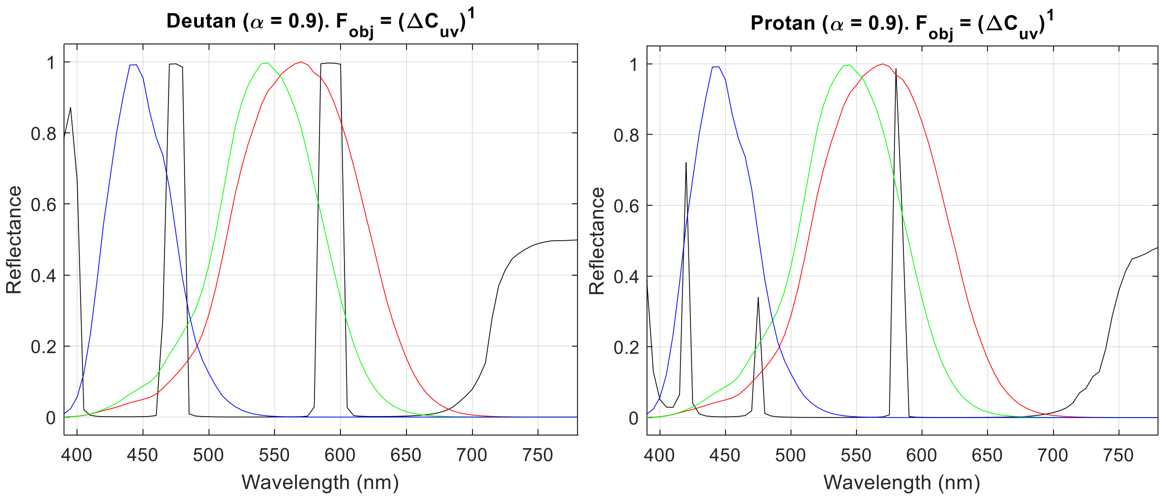

Figure 3-13: Spectral reflectance of colour correction filter designed by numeric optimisation, and cone fundamentals. Case deuteranomalous (left) and protanomalous (right); $\alpha = 0.9$; fitness $= (\overline{\Delta C_{uv}^{*}})$.

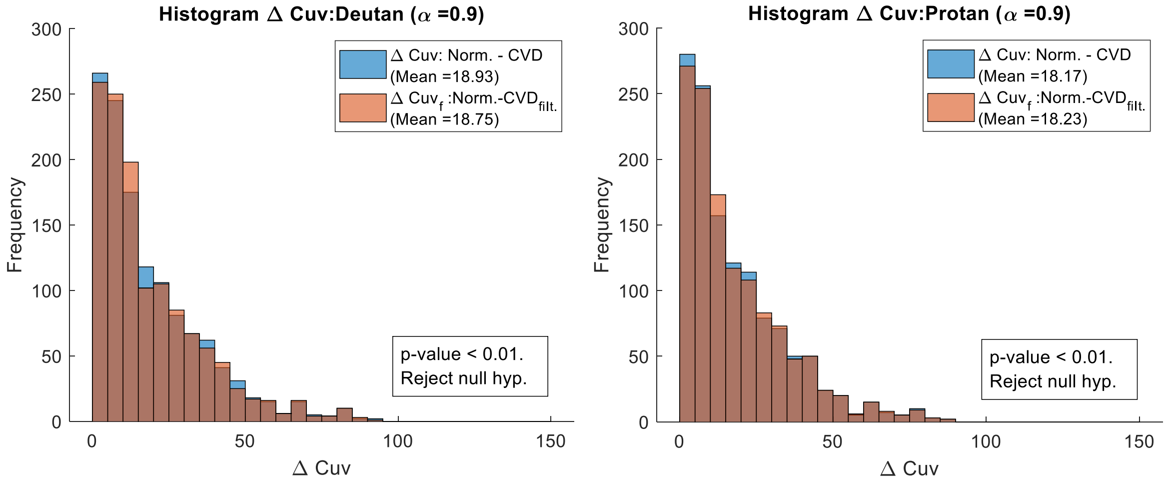

Figure 3-14: Frequency histogram for chroma difference in FM-100 test, between a normal trichromat, and an anomalous trichromat, with and without the use of colour corrective optical filters (blue and orange bars respectively). Results of the Wilcoxon signed rank test are presented in the legend text box; $\alpha = 0.9$; fitness = $(\overline{\Delta C^*_{uv}})$.

3.6.5 Average square chroma difference $\left(\overline{\Delta C^*_{uv}}^{2}\right)$

The results for the numerical design of CVD colour corrective considering the average square sum of chroma differences between normal and CVD observers are presented below in Figure 3-15.

The resulting differences between normal and square averaging of the chroma differences are similar to those showed for ΔE^*_{uv} in the previous section. The squared fitness function results in wider and more pronounced stopbands as compared to the linear averaging design. Additionally, the effect on the individual colour's chroma difference is more pronounced for those samples with a larger difference between CVD and normal colour vision.

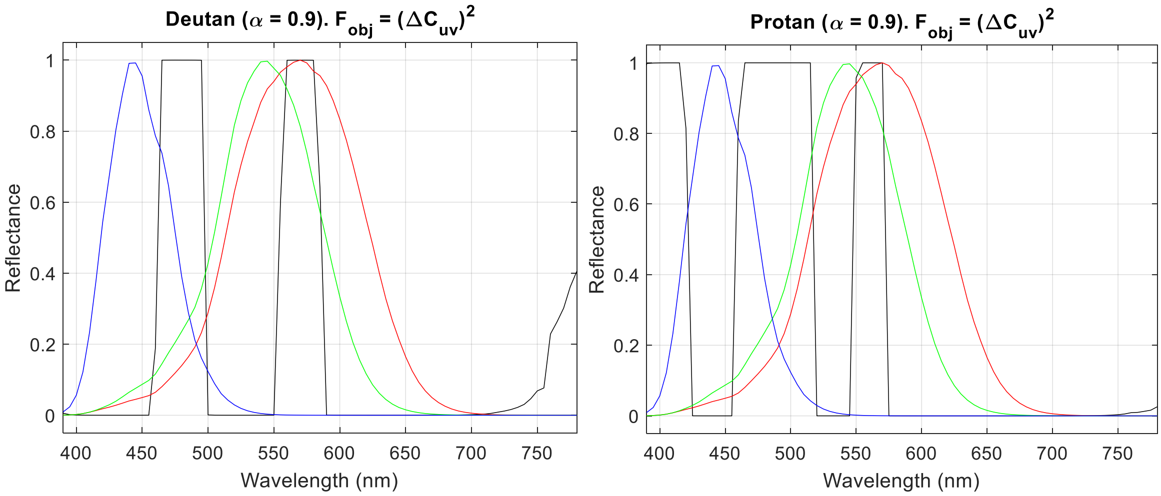

Figure 3-15: Spectral reflectance of colour correction filter designed by numeric optimisation, and cone fundamentals. Case deuteranomalous (left) and protanomalous (right); $\alpha = 0.9$; fitness $= (\overline{\Delta C_{uv}^{*}}^{2})$.

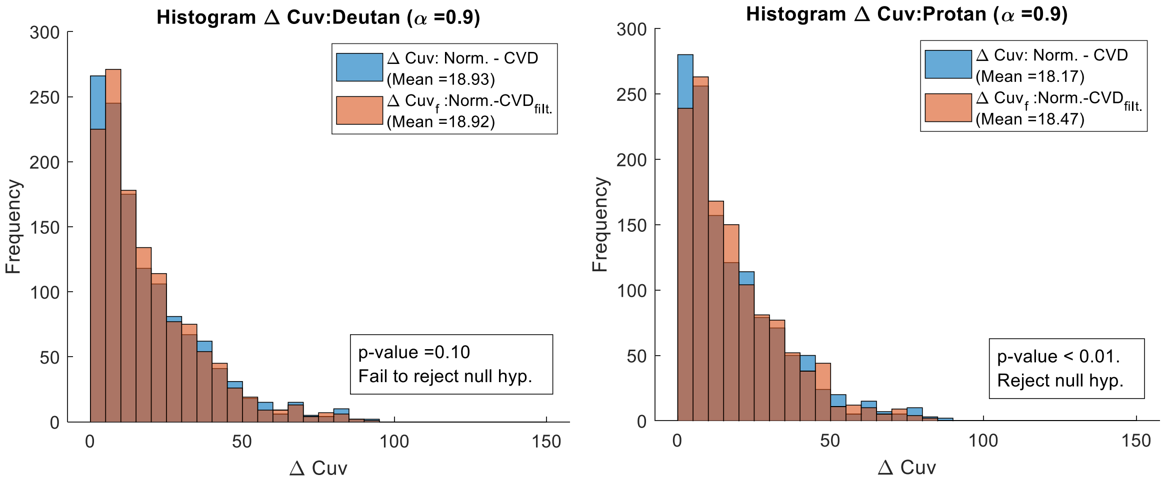

Figure 3-16: Frequency histogram for chroma difference in FM-100 test, between a normal trichromat, and an anomalous trichromat, with and without the use of colour corrective optical filters (blue and orange bars respectively). Results of the Wilcoxon signed rank test are presented in the legend text box; $\alpha = 0.9$; fitness $= (\overline{\Delta C_{uv}^{*}}^{2})$.

3.6.6 Higher power fitness functions

From the previous section it can be observed that when optimizing for total colour and chroma difference between the normal and anomalous observers ($\overline{\Delta E_{uv}^{*}}$, and $\overline{\Delta C_{uv}^{*}}$), the resulting filters produce very small, statistically non-significant changes to colour perception, within the range of non-perceptible to most observers ($\Delta E^{*} < 1$). This results from the fact that any change in colour perception is evenly weighted in the function averaging, for every sample within the objective database. The improvement in the colour perception of some of the samples is a trade-off, and there will be detriment in the perception of other samples. So, in order to produce a considerable effect in colour perception, there needs to be a priority, or weighting factors, for those samples where we want to produce the greatest effect.

To address this issue, a few different approaches can be considered. As stated before, weighting factors can be applied for the contribution of each sample within the objective spectral database. However, these factors would have to be tuned and tailored when different databases are used. A general function can be programmed according to the colour perception indicator of interest, for example, giving higher weighting factors to those samples which are further away from the normal trichromat perception. Consider the following function, where W_i is the weighting factor, and F_i is the fitness (ΔE^*_{uv} or ΔC^*_{uv}) for sample 'i':

$$\text{fitness} = \sum W_i \, (F_i) \qquad \text{Eq. 3-101}$$

If we consider:

$$W_i = F_i \qquad \text{Eq. 3-102}$$

Then,

$$\text{fitness} = \sum (F)_i \, (F)_i = \sum (F)_i^2 \qquad \text{Eq. 3-103}$$

When raising the fitness function to an even-power (*e.g.* $\overline{(\Delta E^*_{uv})}^2, \overline{(\Delta E^*_{uv})}^4, \overline{(\Delta E^*_{uv})}^8$, *etc.*), the function prioritizes those samples or colours which have a larger difference with respect to the normal trichromat perception ($\Delta E^*_{uv} \gg 1$), while diminishing the weight of those close to normal trichromat perception ($\Delta E^*_{uv} < 1$). This is represented in Figure 3-17, showing the single term *n*-th degree polynomial ($f(x) = x^n$, for $n = 2, 4, 8,\ etc.$) around $x = 1$.

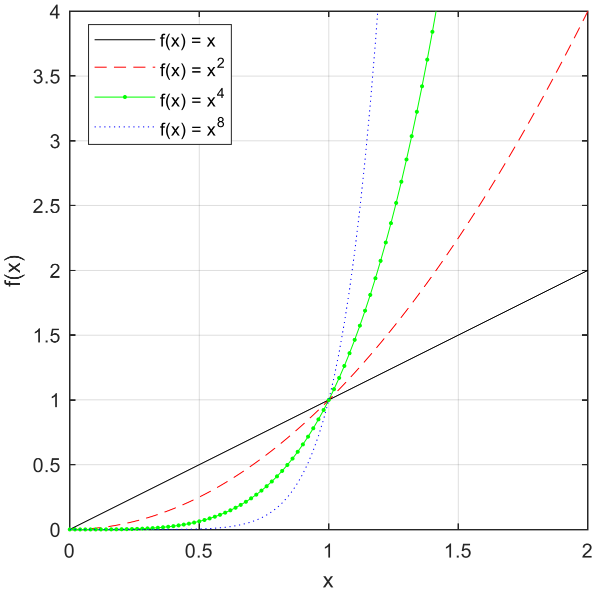

Figure 3-17: Graphical representation of the function $f(x) = x^n$, for $n = 1, 2, 4, 8$. Note that $x^1 > x^2 > x^4 > x^8$, when $x < 1$, while the opposite is true for $x > 1$. The rate at which the slope changes within these functions is higher for the higher powers ($df/dx = nx^{(n-1)}$).

The following results show the effect of higher power fitness functions resulting from filter optimisation for a deuteranomalous observer, $\alpha = 0.9$, using the MacBeth colour chart for spectral reflectance database. Figure 3-18 shows the resulting filters for a fitness function $\overline{(\Delta E^*_{uv})}^n$, where $n = 1, 2, 4, 8$.

It can be observed that when increasing the power of the fitness function, the stopbands around 450-500 and 550-600 nm, which coincide with the S-M and M-L cones sensitivity overlap regions, become more pronounced and band-width increases.

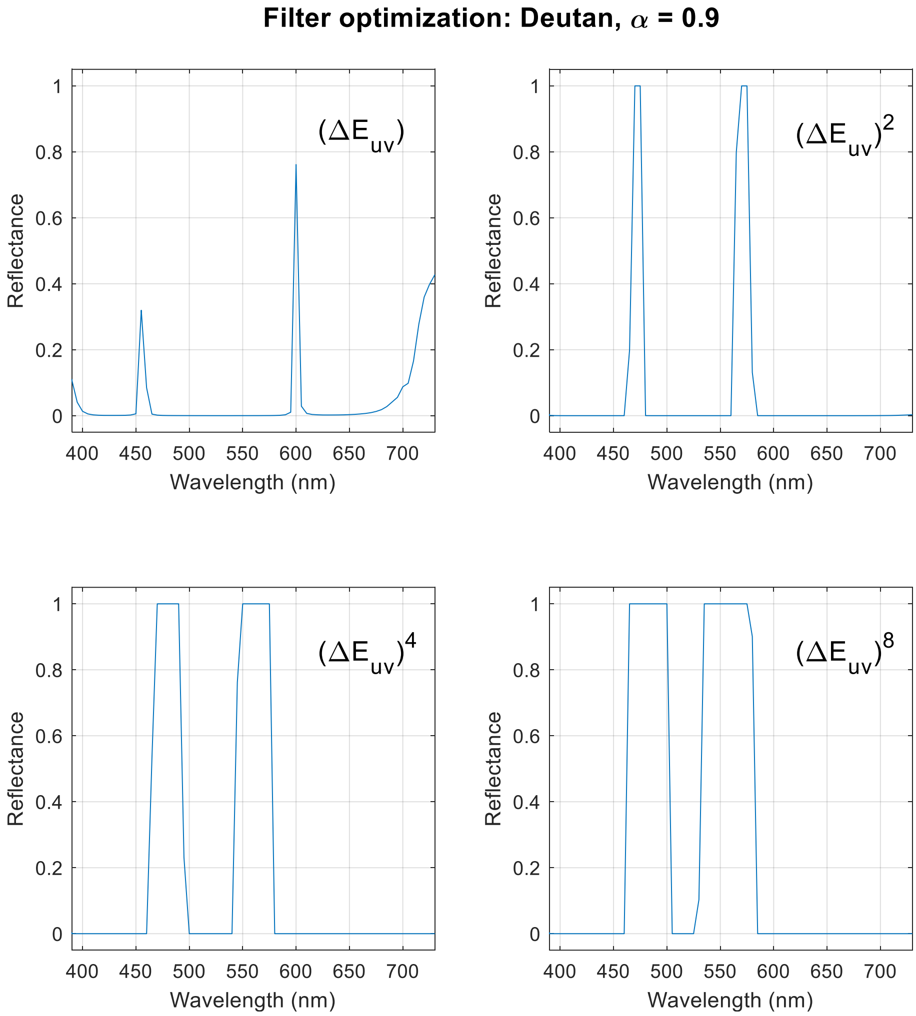

Figure 3-18: Fitness function comparison from MacBeth optimisation, for deuteranomalous ($\alpha = 0.9$). Comparison of filter reflectance obtained *via* optimization for different fitness functions (top to bottom: $(\Delta E_{uv}), (\Delta E_{uv})^2, (\Delta E_{uv})^4, (\Delta E_{uv})^8$).

3.6.7 Number of discernible colours (NDC) and chromatic diversity

To study the effect in colour perception, the number of discernible colours, chromaticity, and saturation, were considered. The number of discernible colours (NDC) can be estimated from the $L^*u^*v^*$ space, as colours are considered to be discernible for a Euclidean distance, $\Delta E_{uv}^* > 1$.

Numerical estimations of the NDC can be performed, for example, by dividing the space in a series of sub-spaces representing the limits of colour discrimination $\Delta E = 1$ (*e.g.* cubic spaces of unitary side), and counting the number of occupied subspaces for the spectral database of interest [92], [106]. While many sources agree that the theoretical maximum for a normal trichromat observer is close to 2 million colours, these estimations can change considerably depending on the assumptions. Additionally, these theoretical values come from the perfectly monochromatic theoretical stimulus, which are hardly found in natural, or even artificial lighting scenes. Linhares *et al.* reported an estimation based on hyper-spectral data from 50 natural scenes, and found the NDC to be as low as 30% of the theoretical maximum [107].

In this study, the focus will be on the relative change in this number, rather than the actual value for this number. The NDC is reported a ratio or percentage relative to the normal trichromat observer. The NDC for any observer is considered proportional to the volume of the convex hull encompassing every point in the spectral database.

Results in this section correspond to Farnsworth-Munsell FM-100 test, using the filters in shown Figure 3-19. Here it can be observed that for a deuteranomalous observer ($\alpha = 0.9$), the NDC within the FM-100 database is about 90% less than the normal trichromat observer. This number is not affected by the filter ($\overline{\Delta E_{uv}^{*}}$) and this filter, as shown in the previous section, will not produce any significant difference in colour perception. The NDC starts decreasing as the filter becomes more opaque, resulting from the higher power fitness functions used in the design. This decrease is mainly caused by the decrease in the luminance value, which is expected as the result of light being blocked by the filter.

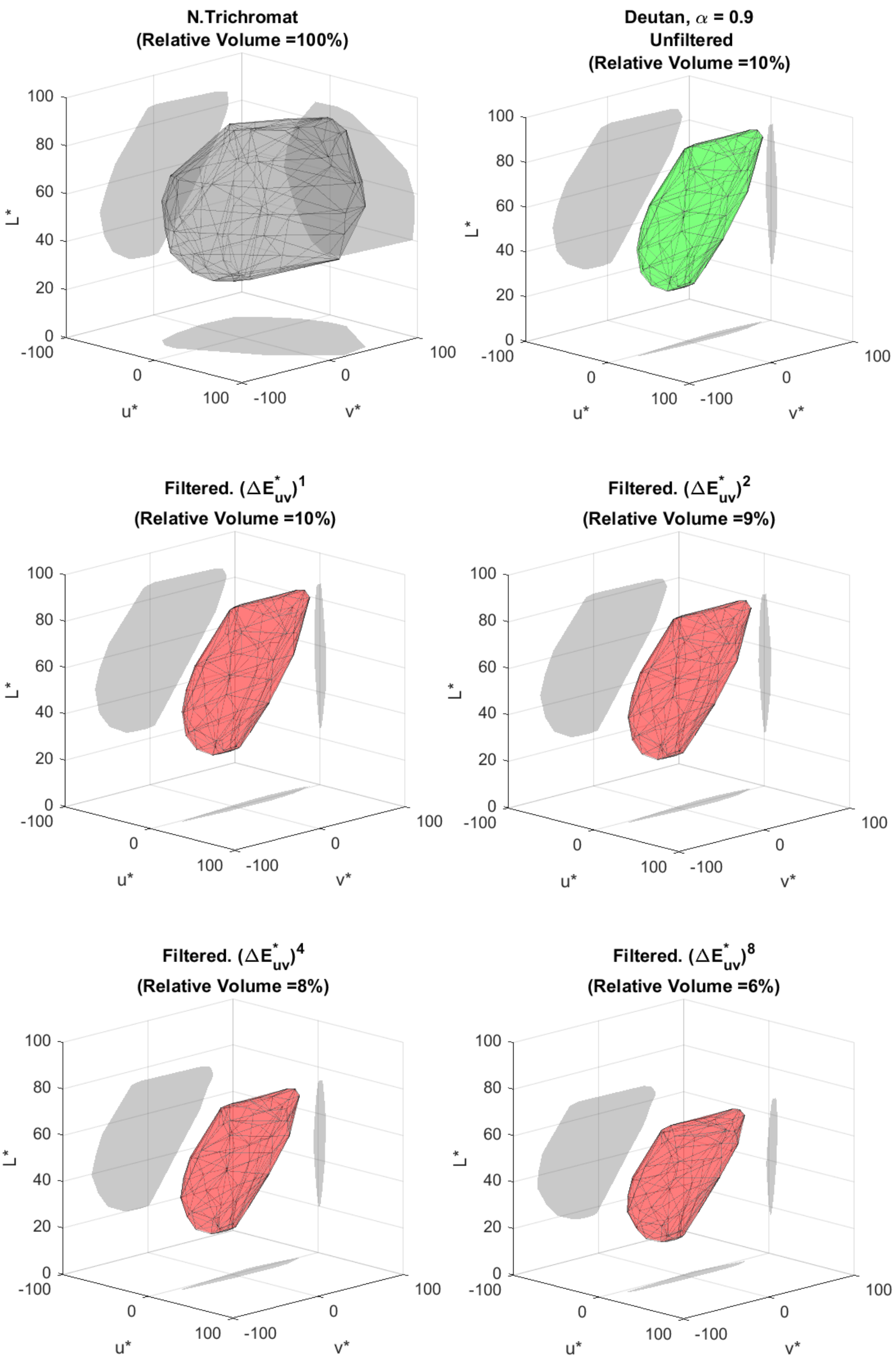

Figure 3-19: Convex hull encompassing the FM-100 database in the CIE L*u*v* colour space for a normal trichromat observer (relative volume =100%), deuteranomalous $\alpha = 0.9$ (r.v.=10%), and the same deuteranomalous observer using various filters designed from the fitness functions: $\left(\overline{\Delta E^*_{uv}}\right)$ (r.v.=10%), $\left(\overline{\Delta E^*_{uv}}\right)^2$ (r.v.=9%), $\left(\overline{\Delta E^*_{uv}}\right)^4$ (r.v.=8%), $\left(\overline{\Delta E^*_{uv}}\right)^8$ (r.v.=6%). Chromatic adaptation and change in the reference white are not considered.

To understand the effect of the filters in chromatic perception, regardless of luminance, the chromaticity values u'v' are considered. Figure 3-20 shows results from the same experiment as Figure 3-19, for a deuteranomalous observer ($\alpha = 0.9$) but expressed in the UCS u'v' chromaticity diagram. The area of the convex hull surrounding the chromaticity coordinates is an indicator of the number of discernible chromaticity values, independent of luminance values. This is reported as a percentage, relative to the area corresponding to the unfiltered anomalous trichromat observer. It is observed that filters with wider stop-bands, corresponding to the designs resulting from higher power fitness functions, increase the relative area in the chromaticity diagram (109%, 125%, and 135% for the fitness functions $\overline{\Delta E^*_{uv}}^2$, $\overline{\Delta E^*_{uv}}^4$, and $\overline{\Delta E^*_{uv}}^8$ respectively). The change in the reference white due to the filter is observed as a general shift in the chromaticity values, which can be accounted by chromatic adaptation. Figure 3-20 additionally shows results for Von-Kries chromatic adaptation, considering the adapting field reference white as the trichromatic values for the dot product between the illuminant spectral power distribution (D65) and the filter spectral transmission. By performing this chromatic adaptation, the chromaticity values are shifted according to the unfiltered illuminant, and reduces the relative area with respect to the non-adapted values (108%, 117%, and 119% for $\overline{\Delta E^*_{uv}}^2$, $\overline{\Delta E^*_{uv}}^4$, and $\overline{\Delta E^*_{uv}}^8$ respectively), however, still representing a significant increase with respect to the unfiltered values.

This effect can be further observed in the saturation values. Saturation corresponds to a measurement of colour intensity and is proportional to the Euclidian distance between a sample and the reference white in the UCS chromaticity diagram. An increase in saturation is a common objective for tinted eyewear, particularly for outdoors activities such as hunting, where an increase in saturation can help the observer to identify and differentiate between foliage and live animals, for example.

While the limits for saturation are given by the monochromatic spectrum, and cannot be expanded by selective light filtering, natural scenes are mostly comprised by combinations of non-saturated colours, as most colours in reflective natural scenes are given by light absorptive molecules, called dyes, which have spectral power distributions with smooth transitions, and very rarely display monochromatic or sharp spectra. An exception for this is the occurrence of structural colour in nature, found for example in some species of butterfly scales, beetle shells, fish scales, and feathers, *etc*. Results regarding the increase in saturation for the filters presented in Figure 3-18 is shown in Figure 3-21. From the unfiltered deutan observer, with an average saturation of $\overline{s_{uv}} = 0.388$, a statistically significant increase in saturation is observed for the higher power fitness functions, both with and without consideration of chromatic adaptation (Von-Kries). Note that the increase in saturation, and relative hull area in the UCS $u'v'$ diagram, is possible due to the nature of the FM-100 test samples, corresponding to an assortment of reflective surfaces, owing their colour to a combination of light absorptive dyes, far from pure monochromatic stimuli.

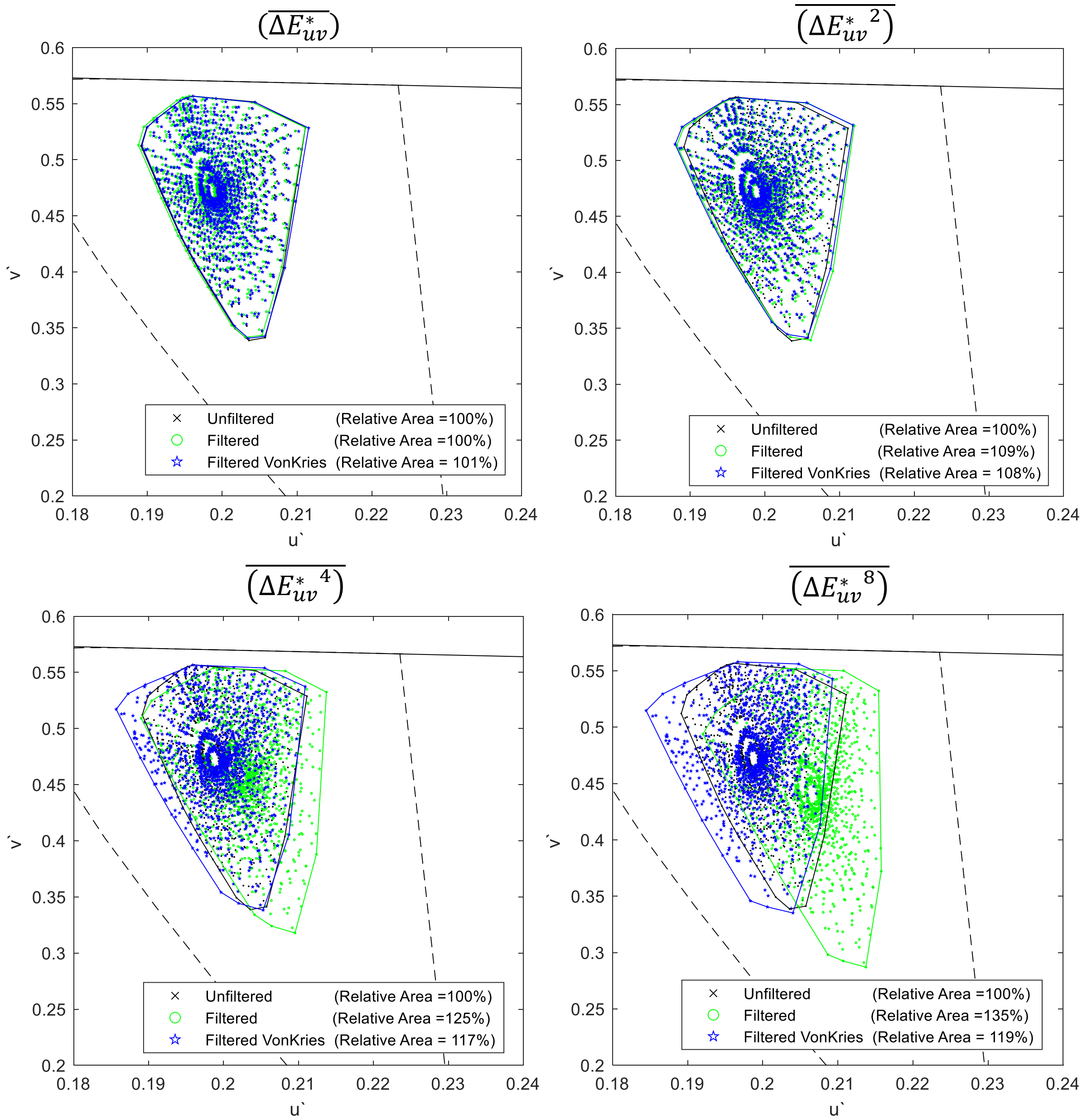

Figure 3-20: CIE u'v' Chromaticity diagram (UCS) coordinates of the FM-100 database for a deuteranomalous observer, $\alpha = 0.9$: unfiltered (black), filtered with no chromatic adaptation (green), and filtered considering VonKries adaptation (blue). Each figure corresponds to a different filter designed from the fitness functions: $\overline{(\Delta E^*_{uv})}$, $\overline{(\Delta E^*_{uv}{}^2)}$, $\overline{(\Delta E^*_{uv}{}^4)}$, and $\overline{(\Delta E^*_{uv}{}^8)}$.

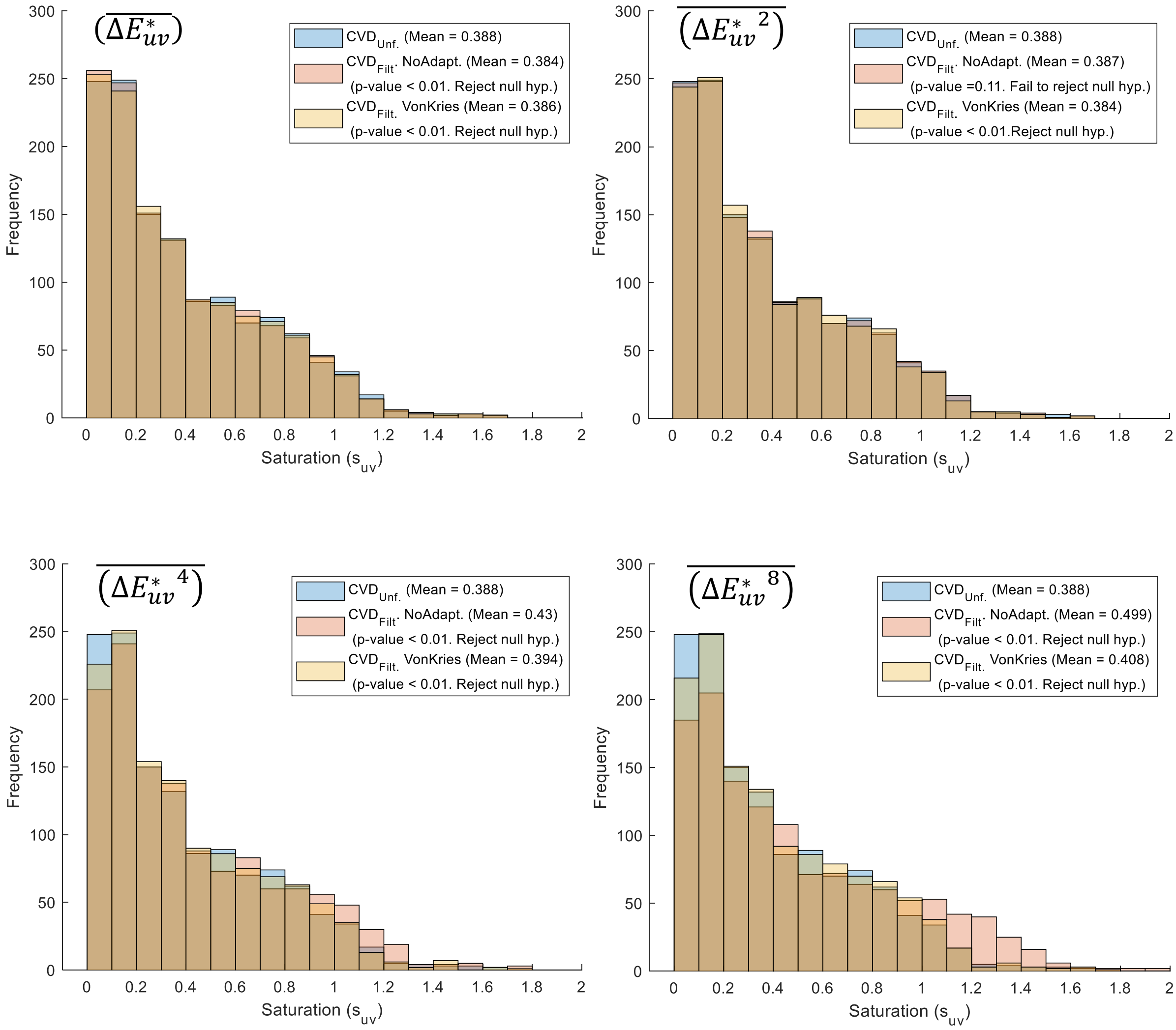

Figure 3-21: Frequency histogram for saturation, s_{uv}, of the FM-100 database, for a deuteranomalous observer ($\alpha = 0.9$). Unfiltered (blue bars), and filtered with no chromatic adaptation (red bars), and adapted using Von-Kries (yellow bars). Each graph corresponds to a different filter, given by the fitness function $\left(\overline{\Delta E^*_{uv}}\right)^n$ (n=1, 2, 4, and 8. See Figure 3-18).

3.6.8 Replacement Factor (α):

An interesting factor to study is the effect of the severity of the anomalous trichromacy condition, indicated by α ($\alpha = 0$: no replacement, normal trichromacy; $\alpha = 1$: full replacement, dichromacy).

As observed in Figure 3-22, the band-stop frequency is shifted toward the red for higher values of α in the case of deuteranomaly, and towards the blue for the case of protanomaly. This is an expected result, as a higher replacement of the anomalous cones results in the anomalous M-cone being shifted towards the red, and the L-cone is shifted towards the blue, for deuteranomaly and protanomaly respectively.

Another aspect to consider is that a higher replacement factor generally results in a wider stopband. A more severe condition, *i.e.*, with a higher α value, is characterized by a greater overlap between the L and M cones, and a wider stopband can compensate for this.

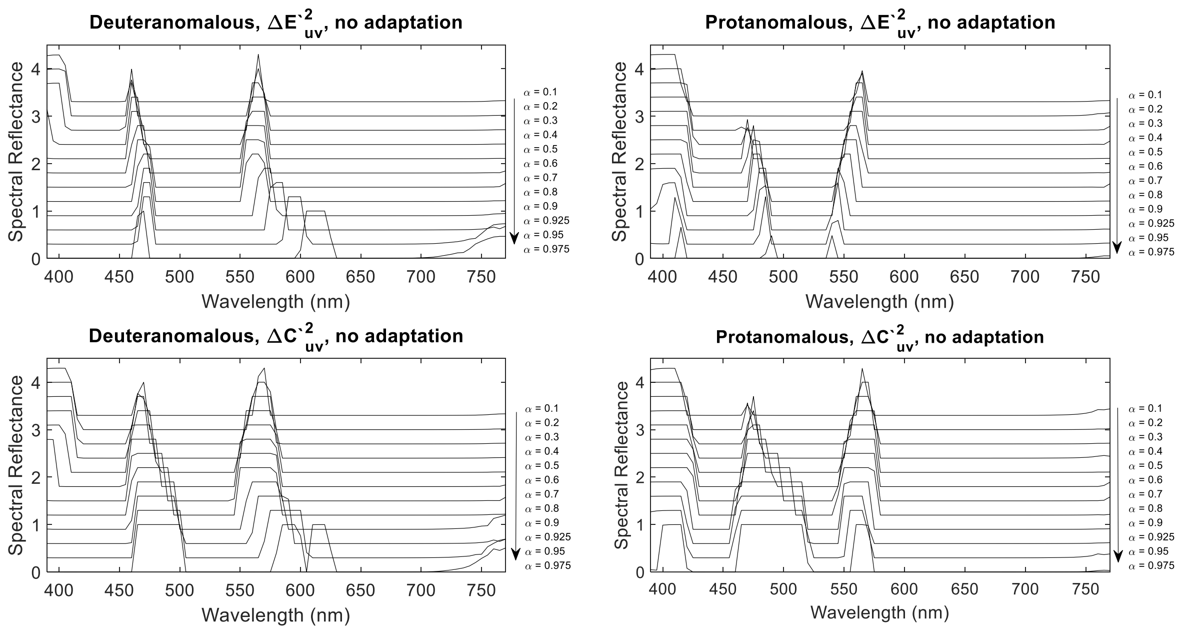

Figure 3-22: Colour correction filters designed by numerical optimisation, for deuteranomalous (left) and protanomalous (right) conditions at various replacement factor values (α). Optimizing for average square total colour difference, ΔE^*_{uv} (top); and for average square chroma difference, ΔC^*_{uv} (bottom). Plot lines displaced vertically for presentation.

3.6.9 Chromatic adaptation

Von Kries

The process of chromatic adaptation plays a key role in the perception of colour. So far, results have been presented for CVD-correction filter design without chromatic adaptation. Considering adaptation in the optimisation problem for filter design requires some assumptions and considerations, including:

- Type of adaptation (Von Kries, CAT02, white point adaptation, *etc*.)
- Calculation of reference white for filtered stimuli.
- Changes in adaptation mechanism for CVD observers.

With respect to the type of adaptation, four different cases for chromatic adaptation were evaluated: no adaptation, white point adaptation, Von Kries, and CAT02. A summary of these results is presented in Figure 3-23 and Figure 3-24, for the effect of different chromatic adaptation considered on the design of colour correction filters, for a fitness function of average square differences of the total colour difference and chroma difference respectively.

For the filtered stimuli, the white point is calculated as the tristimulus values for the spectral distribution of the filter, normalized by its maximum value. That is:

$$[L'_w, M'_w, S'_w] = k_{CVD}\Phi^T_{\mathrm{CVD}} S\vec{f} \qquad \text{Eq. 3-104}$$

$$[L'_{wn}, M_{wn}', S_{wn}'] = \frac{[L'_w, M'_w, S'_w]}{\max\left([L'_w, M_w', S_w']\right)} \qquad \text{Eq. 3-105}$$

The white point adaptation (1/UCS white) corresponds to the transformation to CIELUV, considering the white point of the filtered stimulus as calculated by the above equations.

The Von Kries transform is a linear transformation, normalising the cone response values, $[\rho;\gamma;\beta]$, by the ratio between the reference white under the first illuminant (D65), $[\rho_{wA}, \gamma_{wA}, \beta_{wA}]$, and the white point in the adapted field (filtered white point), $[\rho_{wB};\gamma_{wB};\beta_{wB}]$.

$$\begin{bmatrix} X_B \\ Y_B \\ Z_B \end{bmatrix} = (M_{VK})^{-1} \begin{bmatrix} \rho_{wB}/\rho_{wA} & 0 & 0 \\ 0 & \gamma_{wB}/\gamma_{wA} & 0 \\ 0 & 0 & \beta_{wB}/\beta_{wA} \end{bmatrix} (M_{VK}) \begin{bmatrix} X_A \\ Y_A \\ Z_A \end{bmatrix} \qquad \text{Eq. 3-106}$$

$$\begin{bmatrix} \rho_{w_i} \\ \gamma_{w_i} \\ \beta_{w_i} \end{bmatrix} = M_{VK} \begin{bmatrix} X_{w_i} \\ Y_{w_i} \\ Z_{w_i} \end{bmatrix} \qquad \text{Eq. 3-107}$$

For D65:

$$M_{VK}^{D65} = \begin{bmatrix} 0.40024 & 0.70760 & -0.08081 \\ -0.22630 & 1.16532 & 0.04570 \\ 0 & 0 & 0.911822 \end{bmatrix} \qquad \text{Eq. 3-108}$$

CAT02

The CAT02 adaptation corresponds to a non-linear transformation, and it is the adaptation mechanism considered for the CIECAM02 model. The full equations can be found in Annex-2, however, a summary of the calculations is presented below:

1) Calculate RGB values for the sample under the first illuminant (R_A, G_A, B_A), and reference white under reference and adapting illuminants (R_{wA}, G_{wA}, B_{wA}) and (R_{wB}, G_{wB}, B_{wB})

$$[R_i\ G_i\ B_i\ ] = M_{CAT02}[X_i\ Y_i\ Z_i\ ] \qquad \text{Eq. 3-109}$$

$$M_{CAT02} = \begin{bmatrix} 0.7328 & 0.4296 & -0.1624 \\ -0.7036 & 1.6975 & 0.0061 \\ 0.0030 & 0.0136 & 0.9834 \end{bmatrix} \qquad \text{Eq. 3-110}$$

2) Calculate the factors, D_r, D_g, D_b. The parameter D corresponds to the degree of adaptation, which is a function of the luminance of the adapting field (L_A). A value of $D = 0.95$ was set in this work, corresponding to typical viewing conditions for reflecting colours.

$$D_r = (Y_{WA}/Y_{WB})D(R_{WB}/R_{WA}) + 1 - D \qquad \text{Eq. 3-111}$$

$$D_g = (Y_{WA}/Y_{WB})D(G_{WB}/G_{WA}) + 1 - D \qquad \text{Eq. 3-112}$$

$$D_b = (Y_{WA}/Y_{WB})D(B_{WB}/B_{WA}) + 1 - D \qquad \text{Eq. 3-113}$$

3) Calculate the corresponding RGB values for the sample in the second illuminant:

$$R_B = D_r * R_A \qquad \text{Eq. 3-114}$$

$$G_B = D_g * G_A \qquad \text{Eq. 3-115}$$

$$B_B = D_b * B_A \qquad \text{Eq. 3-116}$$

4) Transformation to XYZ tristimulus values

$$[X_i\ Y_i\ Z_i\ ] = (M_{CAT02})^{-1}[R_i\ G_i\ B_i\ ] \qquad \text{Eq. 3-117}$$

$$(M_{CAT02})^{-1} = \begin{bmatrix} 1.0961 & -0.2789 & 0.1827 \\ 0.4544 & 0.4735 & 0.0721 \\ -0.0096 & -0.0096 & 1.0153 \end{bmatrix} \qquad \text{Eq. 3-118}$$

It can be observed that the consideration of chromatic adaptation transformations does not change the general shape of the colour corrective filter, particularly for the deuteranomalous case.

A summary of the Macbeth colour checker as perceived by protanomalous and deuteranomalous observer ($\alpha = 0.8$) through a set of different CVD corrective filters is presented in Table 3-2. It can be observed that when optimizing for a higher power of either total colour difference or colour and chroma difference ($\overline{\Delta E_{uv}^{*}{}^{n}}$, $\overline{\Delta C_{uv}^{*}{}^{n}}$), the stop-bands at ~475 and 575 nm become wider with the higher power of 'n'. By visual inspection, it is possible to observe that for higher powers of 'n', the perception of colour is increasingly altered, particularly for colours close to red, green, and oranges (*e.g.*, chips n° 6, 7, 12, 14, 15, 17), which are the samples that have the largest distance between the normal and anomalous trichromat observers. The wider stopbands account for the larger overlap between the anomalous L and M cones.

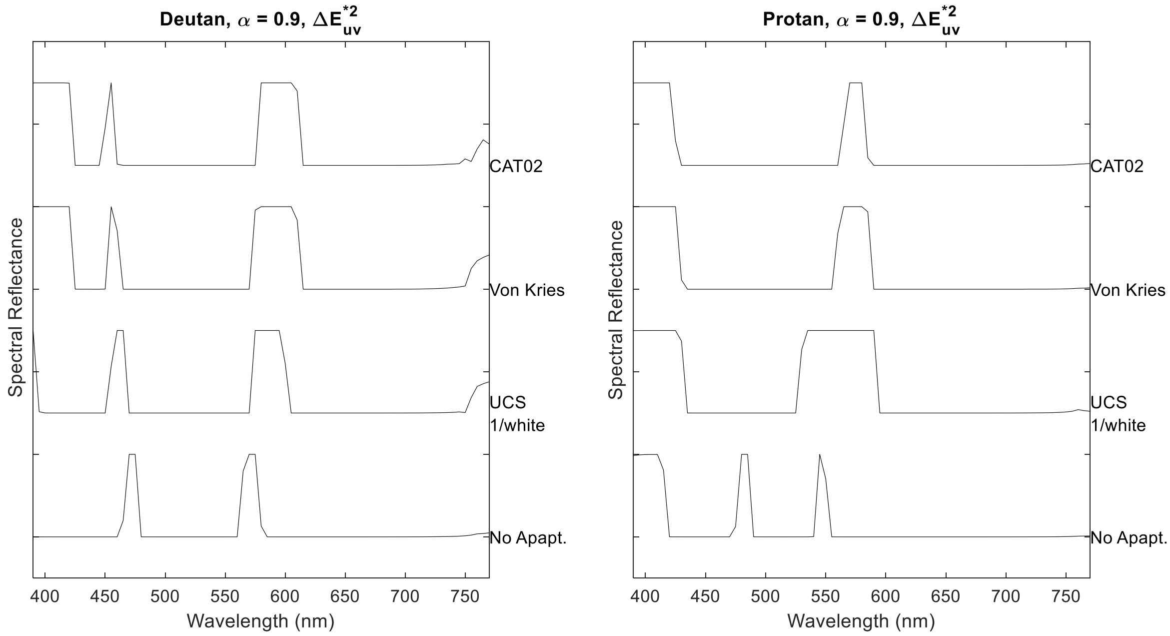

Figure 3-23: Effect on type of chromatic adaptation considered for numerical design of CVD colour correction filter. Optimized for average square of total colour difference $(\Delta\overline{E_{uv}^{*}{}^{2}})$. Plot lines displaced vertically for presentation.

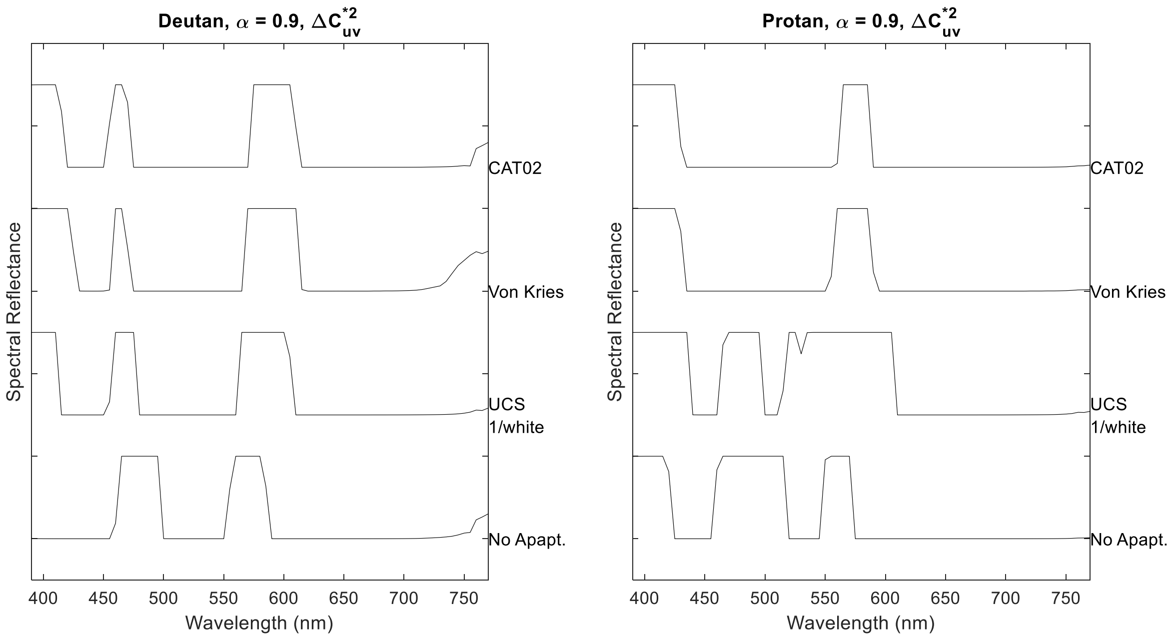

Figure 3-24: Effect on type of chromatic adaptation considered for numerical design of CVD colour correction filter. Optimized for average square of chroma difference $(\Delta\overline{C_{uv}^{*}{}^{2}})$. Plot lines displaced vertically for presentation.

3.6.10 Hyperspectral images

The following section serves as an illustrative representation of the effect of optical filters in colour perception in anomalous trichromats. In this section, a series of hyperspectral images are presented as examples for the simulation of anomalous red-green trichromacy, and the effect caused by some of the designed optical filters in colour perception. Images presented correspond to the MacBeth colour chart (Table 3-2), Ishihara test-plates (Figure 3-25, and Figure 3-26), and natural scenes (Figure 3-27, and Figure 3-28). For the MacBeth colour chart, results for both protanomalous and deuteranomalous observers ($\alpha = 0.9$) are presented, while only deuteranomalous observers are presented for the Ishihara test-plates and natural scenes. Adapted results according to chromatic adaptation transforms CAT02 and Von Kries are presented for comparison.

In RGB images, each pixel contains colour information represented by 3 values, corresponding to the tristimulus values for that pixel in RGB space. In hyperspectral images, each pixel is represented by 'N' values, corresponding to 'N' number of chromatic channels. For a high number of chromatic channels, the information of the hyperspectral image can be interpreted as the spectral power distribution for each pixel within the image.

To produce the range of Figure 3-25 to Figure 3-28, and Table 3-2, the colour model expressed in Eq. 3-62 trough Eq. 3-74 is applied for the spectral distribution given by the hyperspectral information on each pixel. In the cases where applies, chromatic adaptation was performed according to expressions in Eq. 3-104 through Eq. 3-118, considering a reference white for the adapted field as the tristimulus value for a perfect reflecting diffuser under D65 illumination, as perceived by the anomalous observer through the filter. In the case of CAT02 adaptation, a value of $D = 0.95$ was set for the degree of adaptation, to represent typical viewing conditions for reflective colours.

From visual inspection of Figure 3-25, a slight improvement in discrimination can be observed. This plate, among others, serves to identify mild and strong red-green colour vision deficiency in the Ishihara test. A normal trichromat is expected to clearly identify the number 42, while only the number 4 should be visible for a strong deutan observer (in the case of a strong protan, the number 2 should be identified). A mild deutan, on the other hand, should easily identify the number 4, and the number 2 with some difficulty (the opposite result is expected for protans). This discrimination improves for more opaque filters, due to the widening of the transmission stopbands around 475 and 570 nm, and the contrast between both numbers (4 and 2) increases.

Figure 3-26 shows a different test-plate used for identification of red-green colour vision deficiency. In the Ishihara test, a normal trichromat observer should identify the number 8, while a person with red-green deficiency should identify the number 3, regardless of the type of red-green deficiency. However, a visual inspection reveals that from this simulation, most of the contrast is lost against the background, and it is not possible to discriminate any number or shape, for a strong deuteranomalous observer. While the use of optical filters could improve discrimination, it seems insufficient in this case. The discrepancy between the expected results as marked by the guide to the Ishihara test, and the observed results from this simulation, can be owed to several factors. A low resolution in the spectral image is a possibility, particularly with respect to the number of chromatic channels.

Furthermore, from Figure 3-27 and Figure 3-28 it can be observed that when dealing with natural scenes, the large amount of different colours present, and their distribution across the entire image, makes colour discrimination more difficult. It is regarded that for natural scenes, the colour difference between samples should be larger.

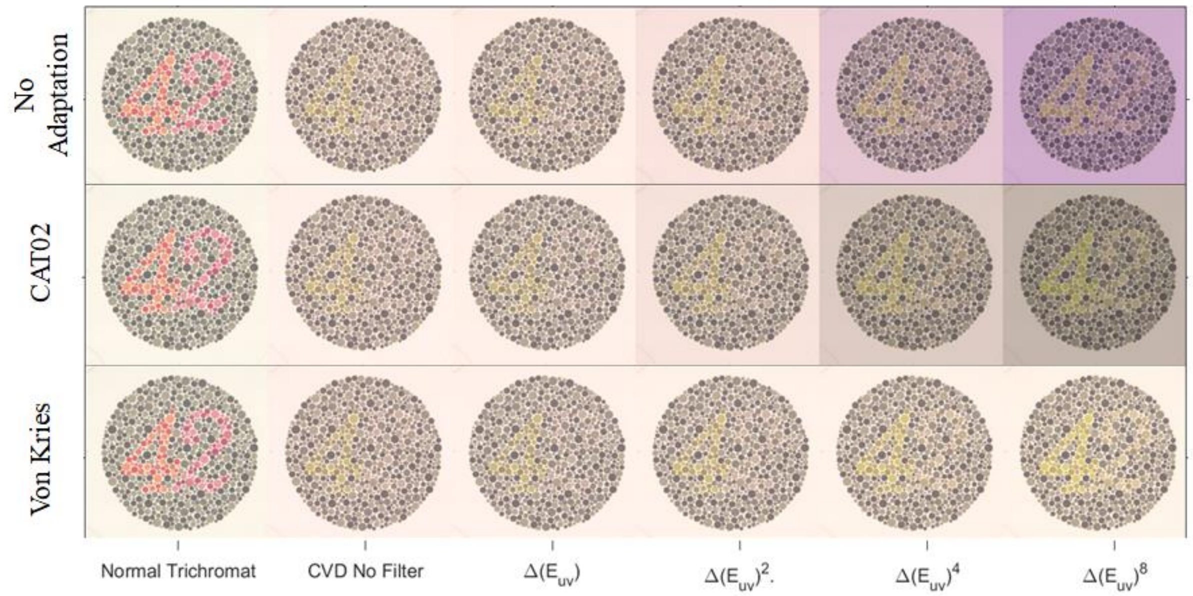

Figure 3-25: Simulation of the Ishihara test-plate n°17, for a normal trichromat, and deuteranomalous observer ($\alpha = 0.9$), with and without the use of optical filters. Each filter comes from the optimisation of a different fitness function ($(\Delta\overline{E_{uv}^*})^n$, as presented in Figure 3-18). Results are presented with no chromatic adaptation, as well as considering the CAT02 and Von Kries transforms.

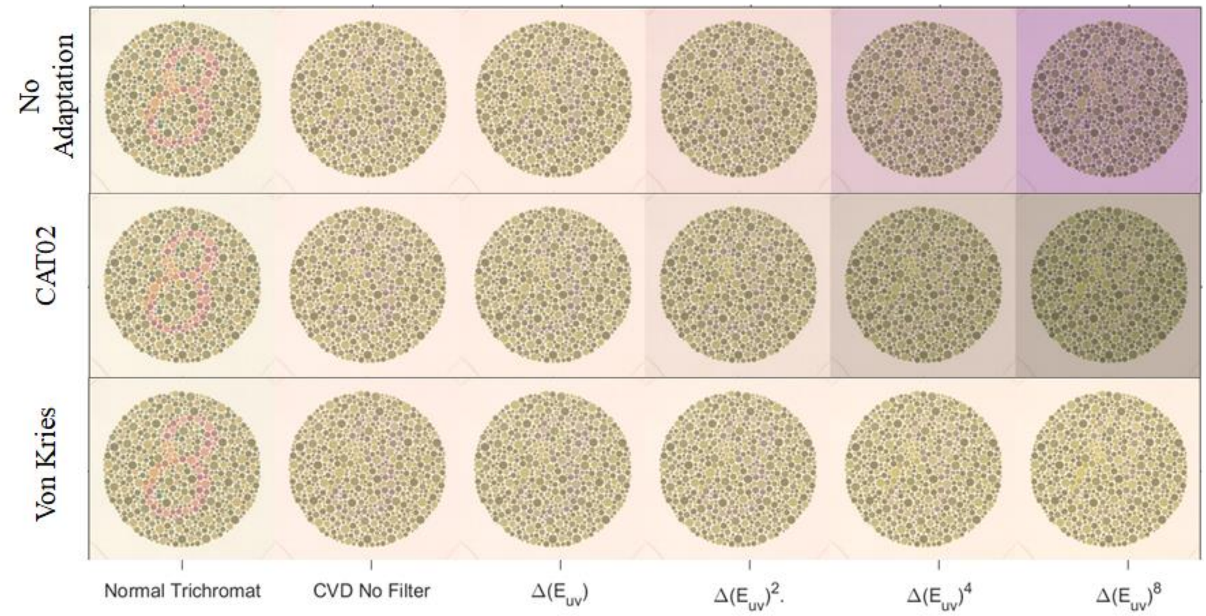

Figure 3-26: Simulation of the Ishihara test-plate n°2, for a normal trichromat, and deuteranomalous observer ($\alpha = 0.9$), with and without the use of optical filters. Each filter comes from the optimisation of a different fitness function ($(\Delta\overline{E^*_{uv}})^n$, as presented in Figure 3-18). Results are presented with no chromatic adaptation, as well as considering the CAT02 and Von Kries transforms.

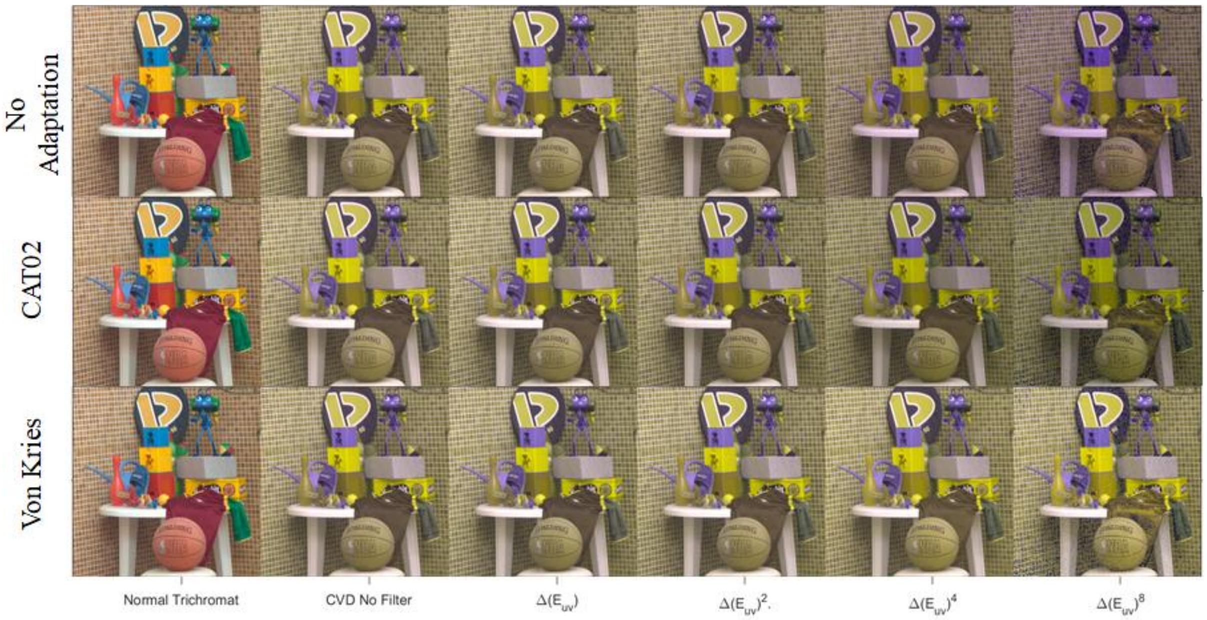

Figure 3-27: Simulation of a natural scene, for a normal trichromat, and deuteranomalous observer ($\alpha = 0.9$), with and without the use of optical filters. Each filter comes from the optimisation of a different fitness function ($(\Delta\overline{E^*_{uv}})^n$, as presented in Figure 3-18). Results are presented with no chromatic adaptation, as well as considering the CAT02 and Von Kries transforms.

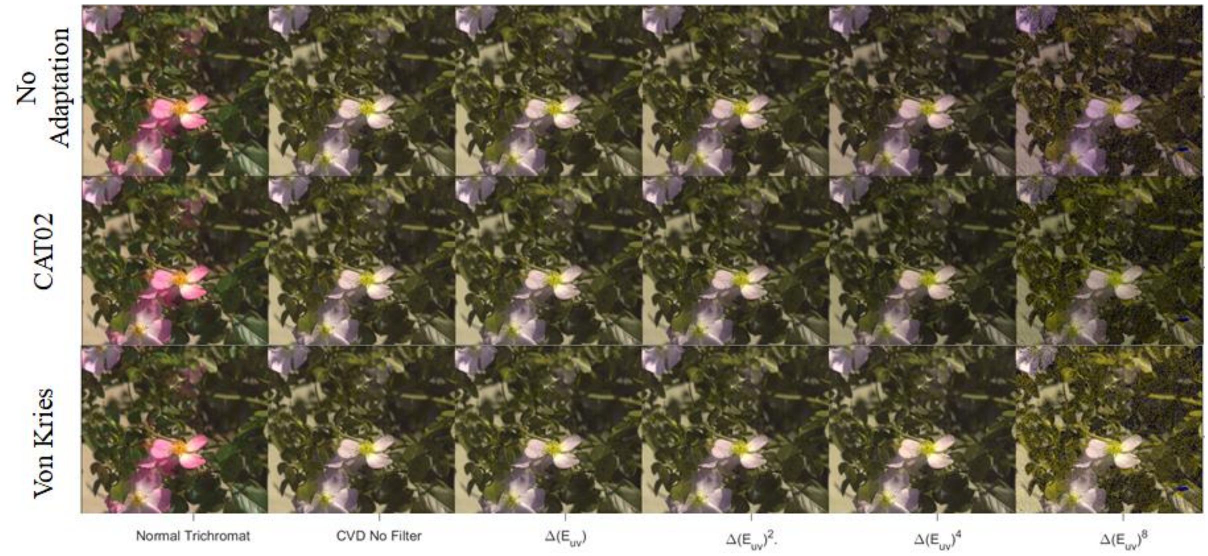

Figure 3-28: Simulation of a natural scene, for a normal trichromat, and deuteranomalous observer ($\alpha = 0.9$), with and without the use of optical filters. Each filter comes from the optimisation of a different fitness function ($(\Delta\overline{E^*_{uv}})^n$, as presented in Figure 3-18). Results are presented with no chromatic adaptation, as well as considering the CAT02 and Von Kries transforms.

Table 3-2: Colour appearance of the Macbeth colour checker, as perceived by deutan and protan anomalous trichromats ($\alpha = 0.8$) through colour corrective filters, considering different chromatic adaptation transformations. All filters designed for deute ranomalous, $\alpha = 0.9$.

Fitness	Filter	No Adaptation	Von Kries	CAT02	
$\overline{\left(\Delta E_{uv}^{*}{}^{2}\right)}$	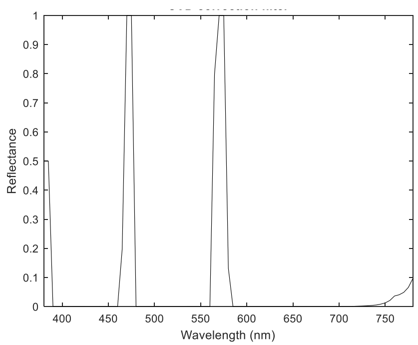	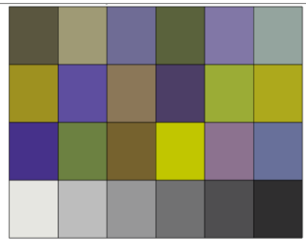	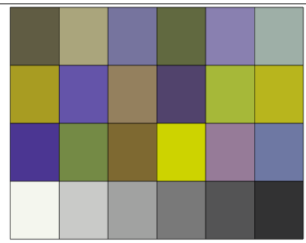	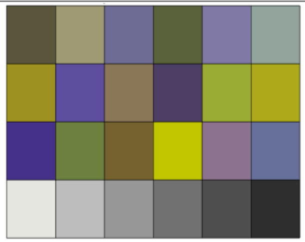	Deutan
		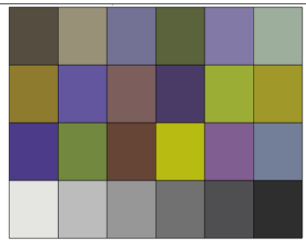	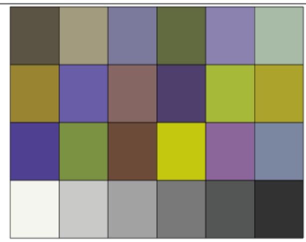	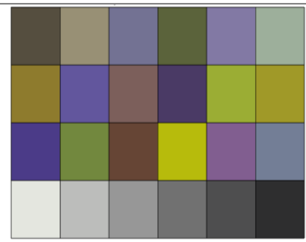	Protan
$\overline{\left(\Delta E_{uv}^{*}{}^{4}\right)}$	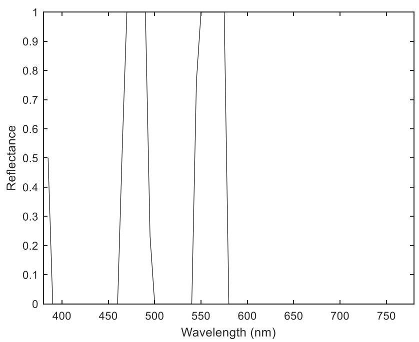	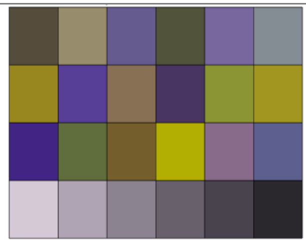	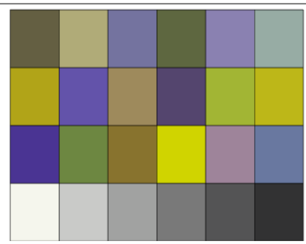	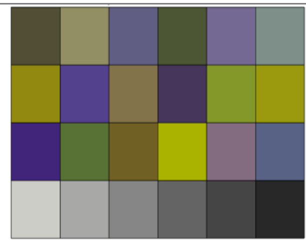	Deutan
		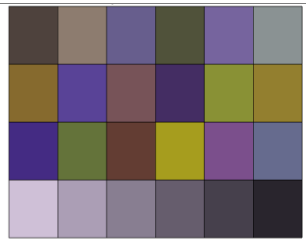	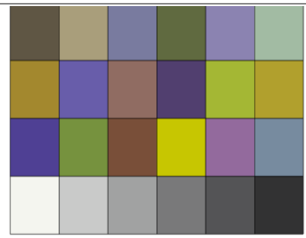	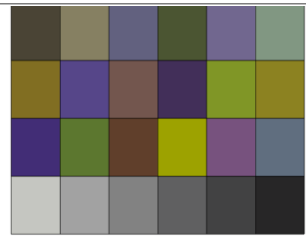	Protan

Table 3-2: Colour appearance of the Macbeth colour checker, as perceived by deutan and protan anomalous trichromats ($\alpha = 0.8$) through colour corrective filters, considering different chromatic adaptation transformations. All filters designed for deute ranomalous, $\alpha = 0.9$.

Fitness	**Filter**	**No Adaptation**	**Von Kries**	**CAT02**	
$\overline{\left(\Delta {C^*_{uv}}^{2}\right)}$	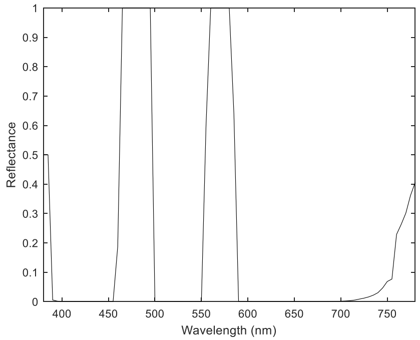	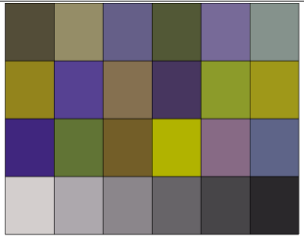	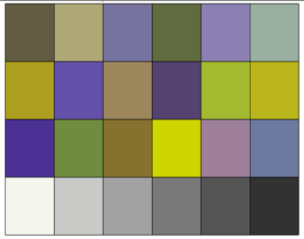	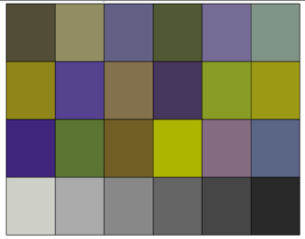	Deutan
		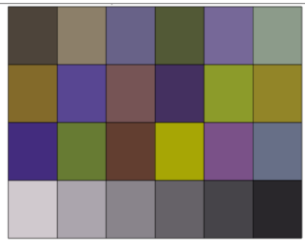	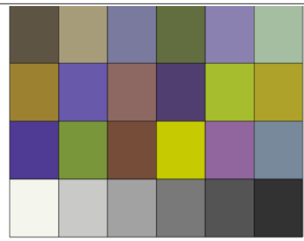	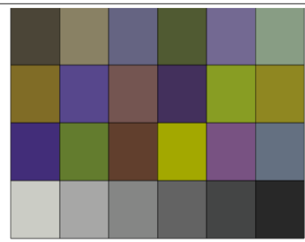	Protan
$\overline{\left(\Delta {C^*_{uv}}^{4}\right)}$	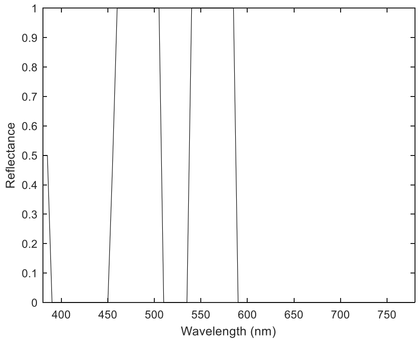	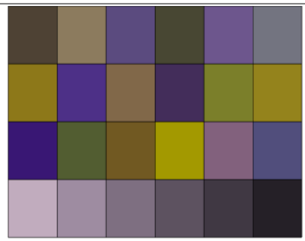	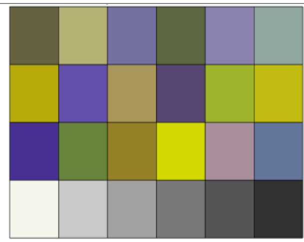	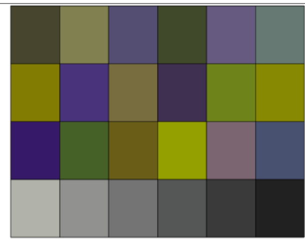	Deutan
		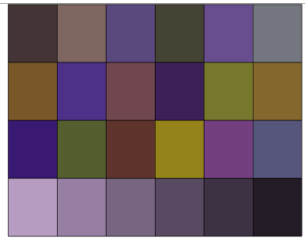	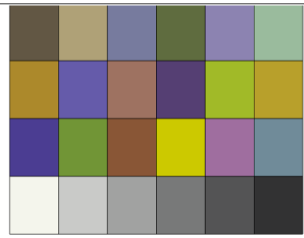	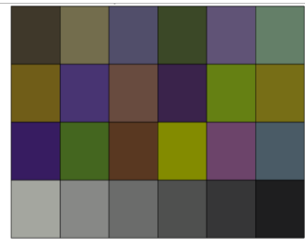	Protan

3.6.11 Other illumination sources

As stated previously, colour appearance can be significantly influenced by the illumination source, particularly, by the spectral power distribution of the incident light in a reflective surface, and the state of adaptation given by the illuminant tristimulus values. The filters designed in this work are targeted for outdoors daylight applications, therefore, the ‘D’ series of the CIE standard illuminants should be considered. However, for the purpose of analysis, and in the interest of potentially expanding the application to a broad range of lightning conditions, other light sources are considered.

In this section, a comparison between different illumination sources is presented with respect to a single corrective filter. The spectral power distribution of the illuminants, and the corrective filter used for this analysis are presented in Figure 3-29. An interesting factor when considering sources such as fluorescent or LED lightning, is the potential overlap between the filter stop-bands and the sharp emission-bands from the source. This can result in considerable darkening, or a significant change in the perception of colour if the emission-bands from the source are being blocked unevenly.

A simulation for the Ishihara test-plate $n°$17 is presented in Figure 3-30. Images were produced from a hyperspectral image, using the methodology presented in Section 3.6.10 , for various illuminations. The simulation includes the results for a normal trichromat, deuteranomalous, and protanomalous observers ($\alpha = 0.9$). Results for the CVD observers are presented both without and with the use of a colour corrective filter. This filter corresponds to the resulting design from the optimization algorithm, for a deuteranomalous observer ($\alpha = 0.9$, no chromatic adaptation, fitness = $\overline{\left(\Delta C^{*}_{uv}{}^{4}\right)}$, from now on referred to as C4 filter). Additionally, results are shown with no chromatic adaptation, and adapted to D65 light according to the Von Kries transform.

For this case, it can be observed that warm-lights (‘A’, ‘F11’, and ‘LED’) can make discrimination of the red numbers easier, as the source contains more long-wave light, resulting in brighter red colours. Besides this, no significant difference can be observed at simple sight between light sources of similar characteristics, *e.g.*, no difference is easily observed among cool-lights (‘D65’ and ‘F7’).

However, an exception to the previous statement can be observed in this example. A difference is observed for the 'F11' source, when compared to 'A' and 'LED', as the reference white is noticeable different when observed through the filter (see Figure 3-30

Figure 3-30, F11 source, no adaptation). The warm 'F11' source becomes 'cooler' when observed through the filter, and the reference white is closer to that of the filtered 'D65' and 'F7'. This is caused by the complete overlap between the filter stop-band centred on 575 nm, and the emission-band of the 'F11' close to 550 nm, which corresponds to the green channel of the RGB light.

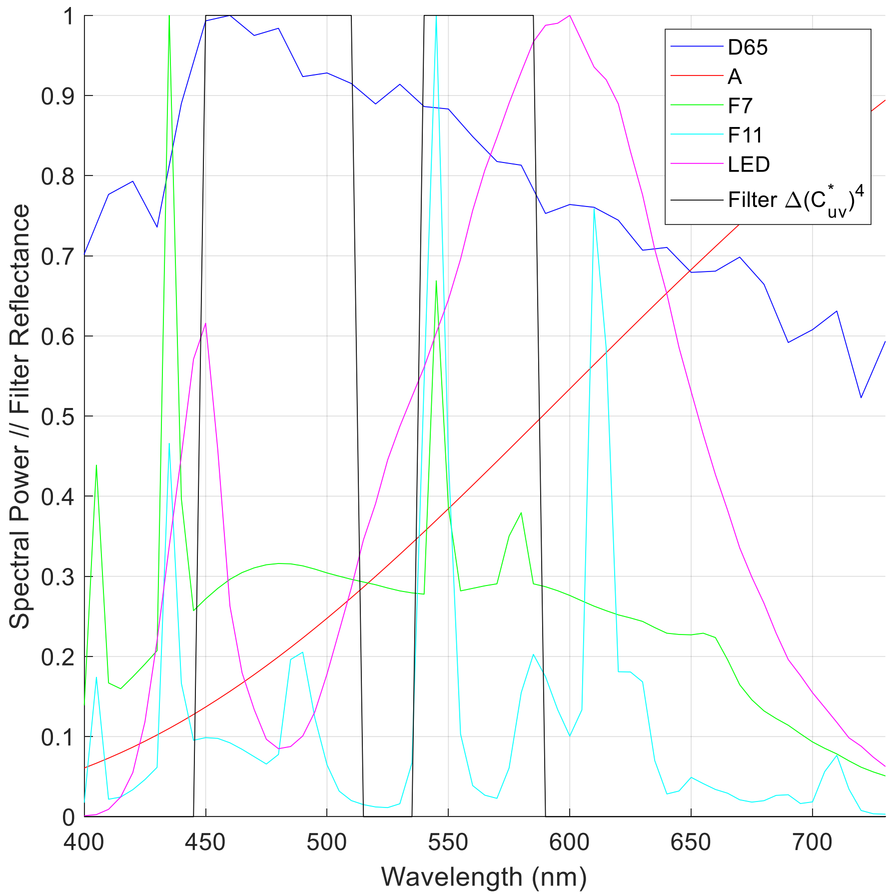

Figure 3-29: Spectral power distribution (normalized to unity peak)) for different CIE illuminants 'D65' (6500K), 'A' (2856K), 'F7' (6500K), and 'F11' (4000K). The 'LED' illumination corresponds to a LED LICA-Philips streetlamp (3107K) [56], [95]. The spectral reflectance of the filter corresponds to the C4 filter.

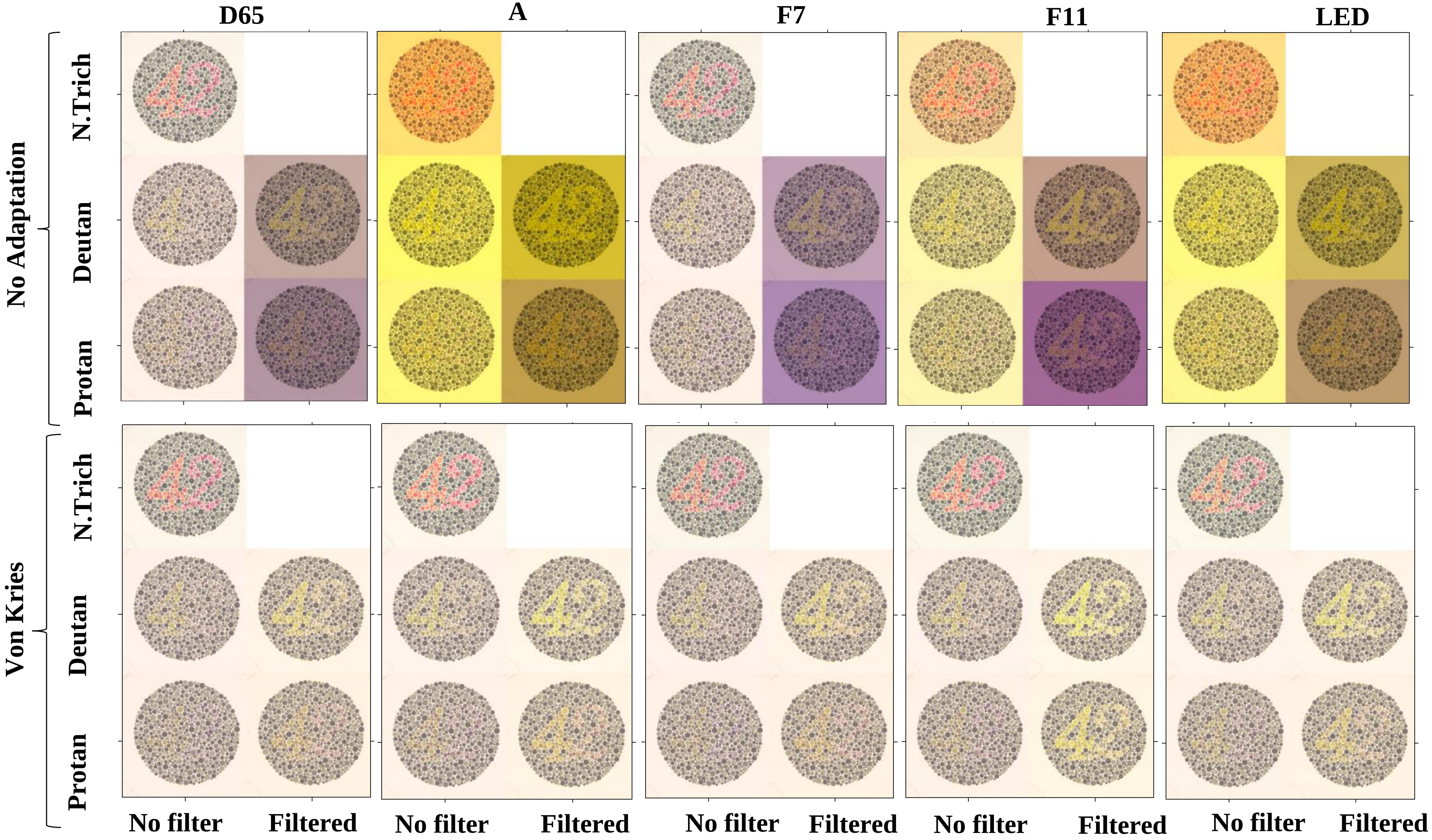

Figure 3-30: Simulation of Ishihara test plate n°17 under different illumination sources, for a normal trichromat, deuteranomalous, and protanomalous observers ($\alpha = 0.9$). Filtered results for CVD correspond to a filter obtained by the optimization algorithm (for deutan, $\alpha = 0.9$, fitness = $\overline{\left(\Delta {C_{uv}^{*}}^{4}\right)}$). Chromatic adaptation corresponds to Von Kries transform, adapted to D65.

3.6.12 Comparison to commercial CVD eyewear aids

The following section provides a visual comparison between commercial eyewear marketed as CVD aids, EnChroma and VINO, and the filter C4, introduced in a previous section. The spectral transmittance distribution of these filters is presented in Figure 3-31. Examples for multispectral images simulated for protanomalous and deuteranomalous observers.

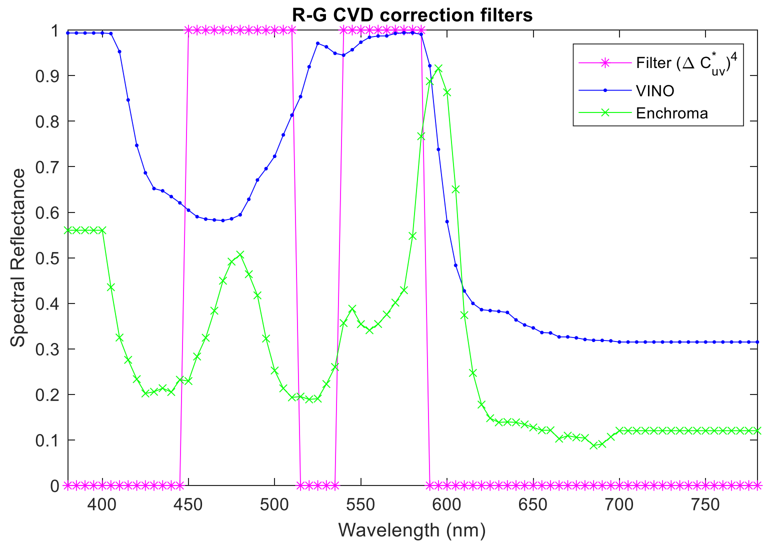

Figure 3-31: Spectral transmittance of commercial VINO, EnChroma glasses, and the C4 filter presented in this work.

Simulations of Ishihara tests-plates from hyperspectral images are presented in Figure 3-32, and Figure 3-33 (for methods, see Section 3.6.10). Results in the Ishihara simulation obtained for the commercial glasses are consistent with recent publications, and an enhancement in red-green discrimination can be observed for the VINO glasses, while the EnChroma glasses appear to have little effect [87], [92], [108]. With respect to the C4 filter, presented in this work, it appears to have a similar effect to the VINO filter, which has been reported to have some good results in the literature, especially for the Ishihara test [87], [92], [93]. This can be observed in Figure 3-32, particularly for the deuteranomalous case, where an enhancement in discrimination results from the brightening of the red numbers, compared to the background. A comparative advantage of the C4 filter, compared to the VINO glasses, is its lower optical density, *i.e.*, VINO glasses are more opaque.

Comparative results for the FM-100 database are presented in Figure 3-34. It can be observed that all three glasses result in an increase of the convex-hull area in the UCS chromaticity diagram, which is an indicative of an increase in the chromatic diversity that can be achieved for this particular database. However, when considering Von Kries chromatic adaptation, the VINO glasses actually generate a reduction in the convex-hull area.

The C4 filter results in an increase representing 136% of the area for the unfiltered observer (126% when adapted using Von Kries), VINO increases to 111% (reduced to 93% when adapted), and EnChroma increases to 118% (111% adapted). An increase in the average saturation can be observed for all filters in the non-adapted condition, which decreases in the Von Kries-adapted condition. In the case of the C4 and VINO filters, there is an increase in the average saturation with respect to the unfiltered case even after adaptation (from s_{uv} = 0.388, to 0.409 and 0.411 respectively), while EnChroma shows a reduction (0.374). In all three cases, the change in saturation is statistically significant according to the Wilcoxon signed rank test.

An interesting difference is observed in the chromaticity diagram for the VINO glasses when applying chromatic adaptation, which appears to rotate the chromaticity values. This glasses, while advertised as an aid for CVD, were designed to enhance the contrast of oxygenated red-blood cells seen through the skin, by orthogonalizing red and blue responses [109].

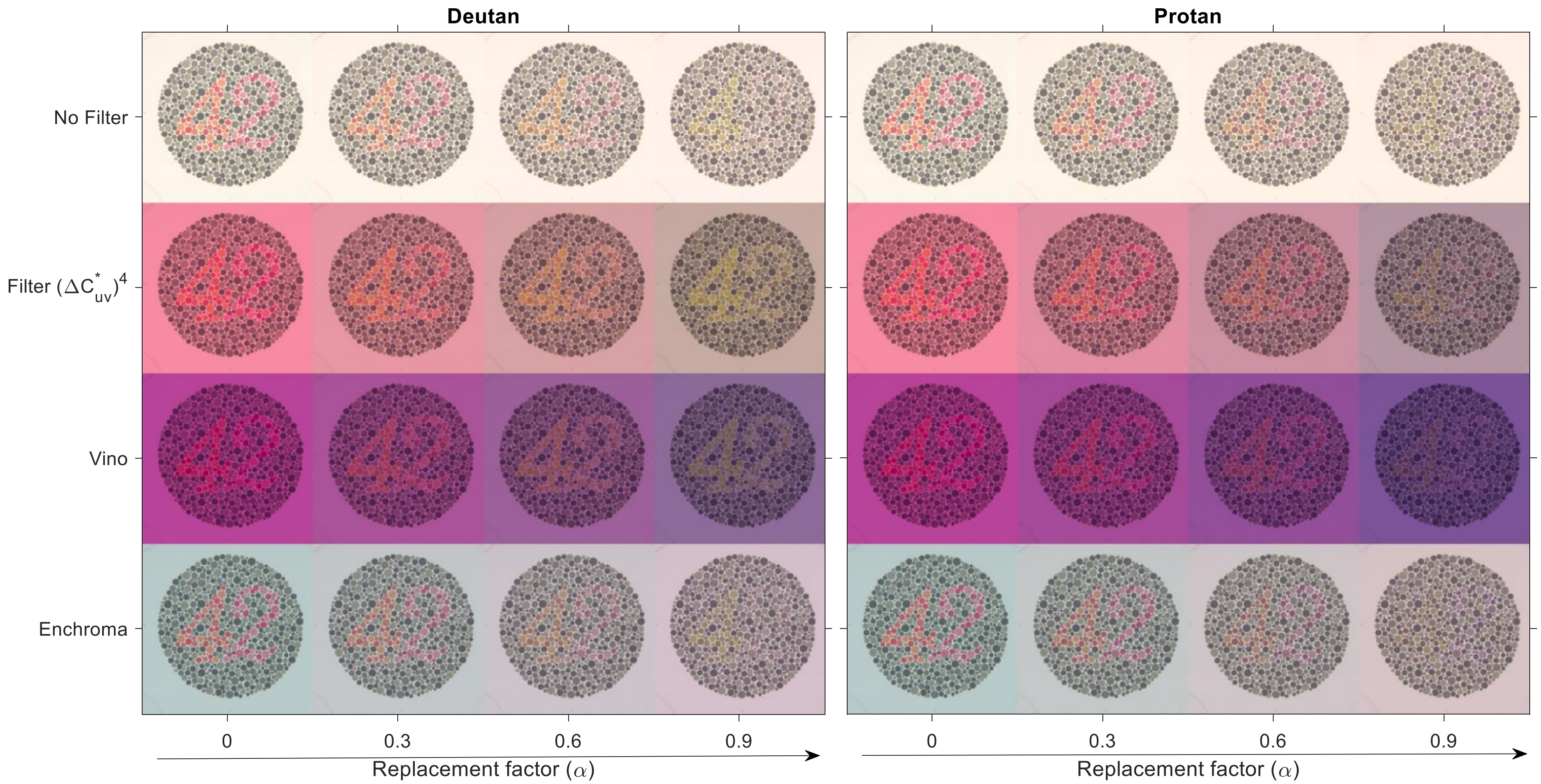

Figure 3-32-a: Spectral simulation of Ishihara test plate n° 17 as perceived by normal (N.T.) and anomalous trichromat observers (replacement factor, $\alpha = \{0, 0.3, 0.6, 0.9\}$). Comparison between unfiltered and filtered images, for filters shown in Figure 3-31.

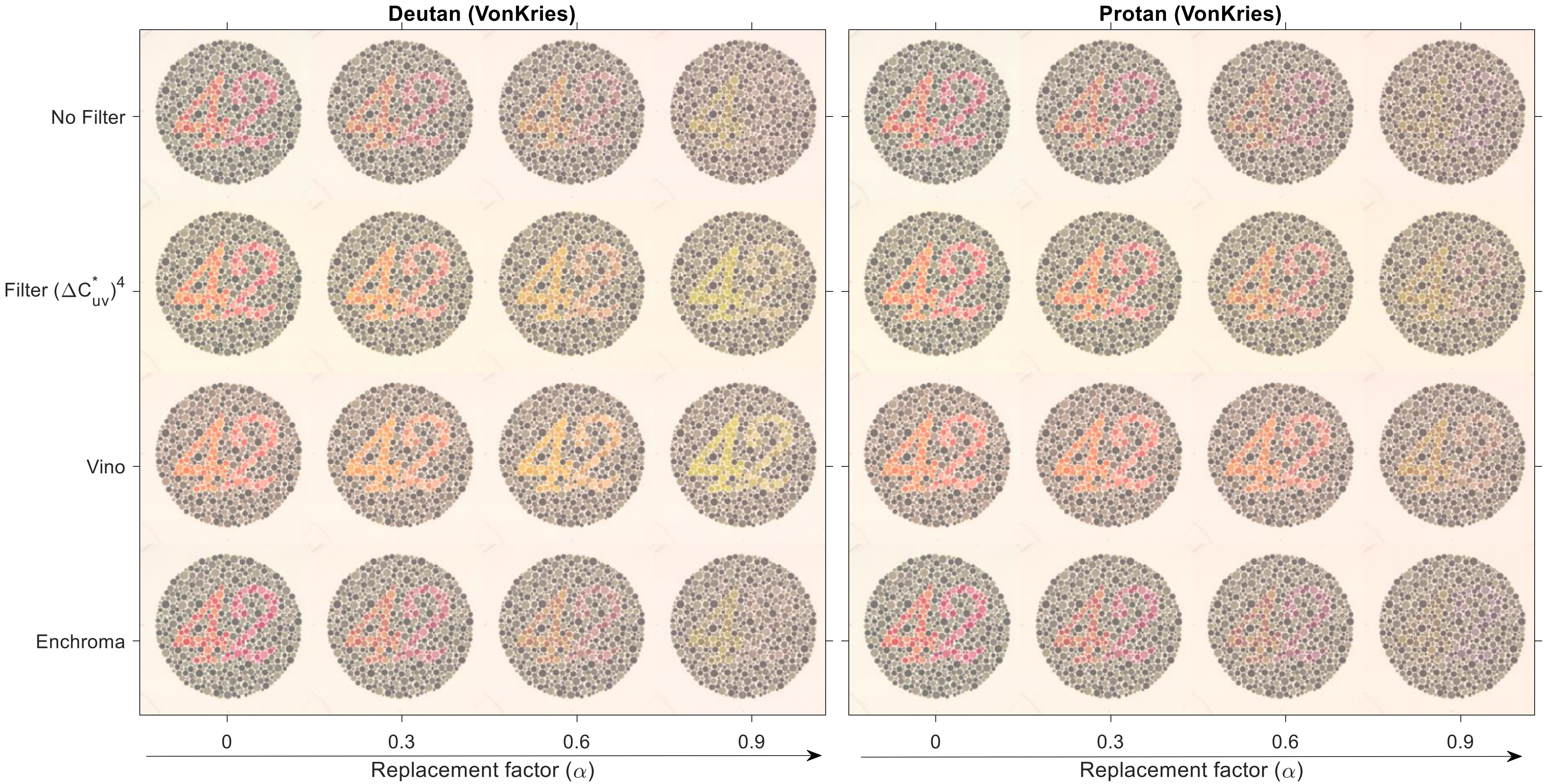

Figure 3-32-b: Spectral simulation of Ishihara test plate n°. 17 as perceived by normal (N.T.) and anomalous trichromat observers (replacement factor, $\alpha = \{0, 0.3, 0.6, 0.9\}$). Comparison between unfiltered and filtered images, for filters shown in Figure 3-31, considering Von Kries chromatic adaptation.

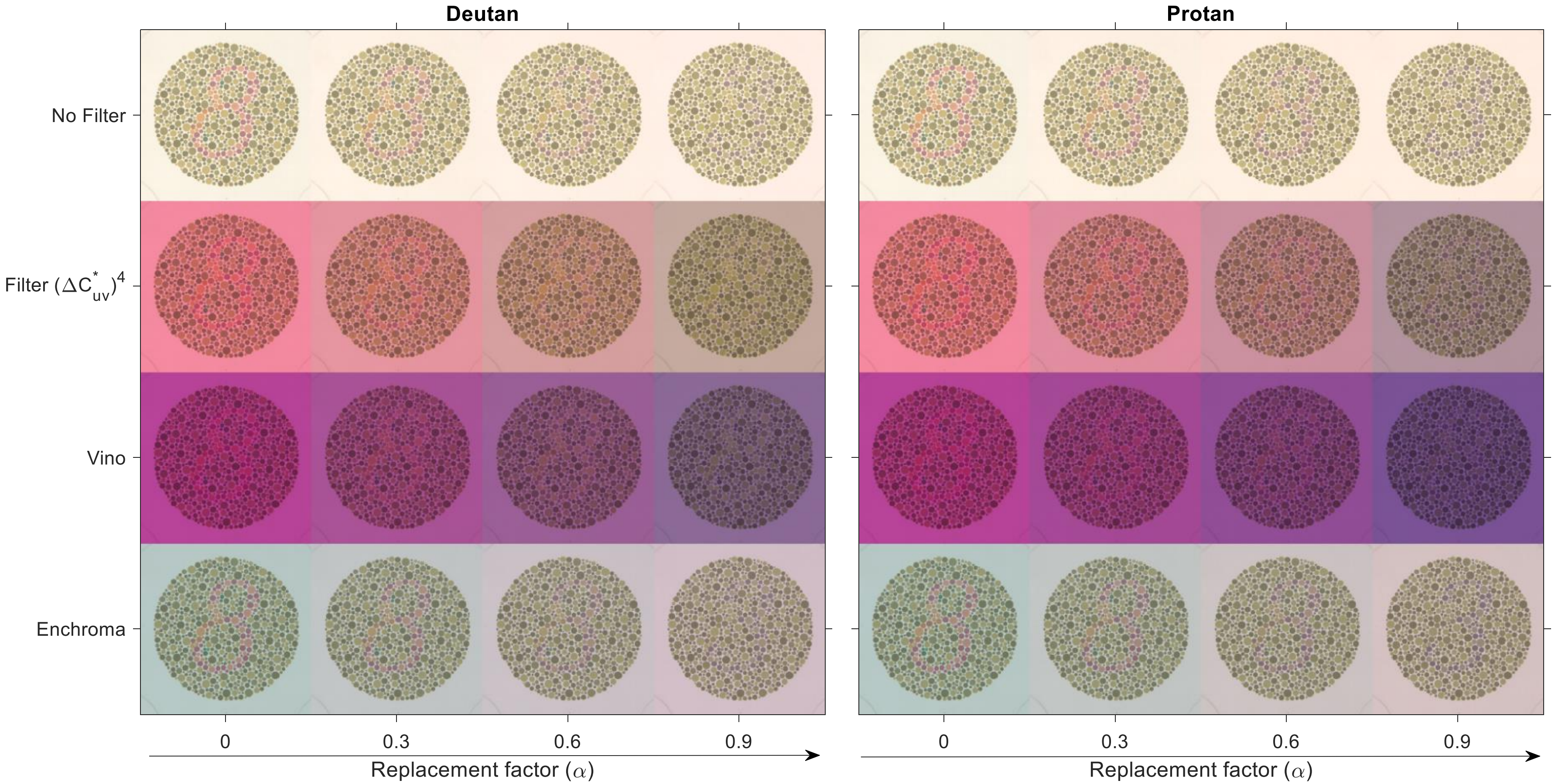

Figure 3-33-a: Spectral simulation of Ishihara test plate $n°$ 2 as perceived by normal (N.T.) and anomalous trichromat observers (replacement factor, $\alpha = \{0, 0.3, 0.6, 0.9\}$). Comparison between unfiltered and filtered images, for filters shown in Figure 3-31.

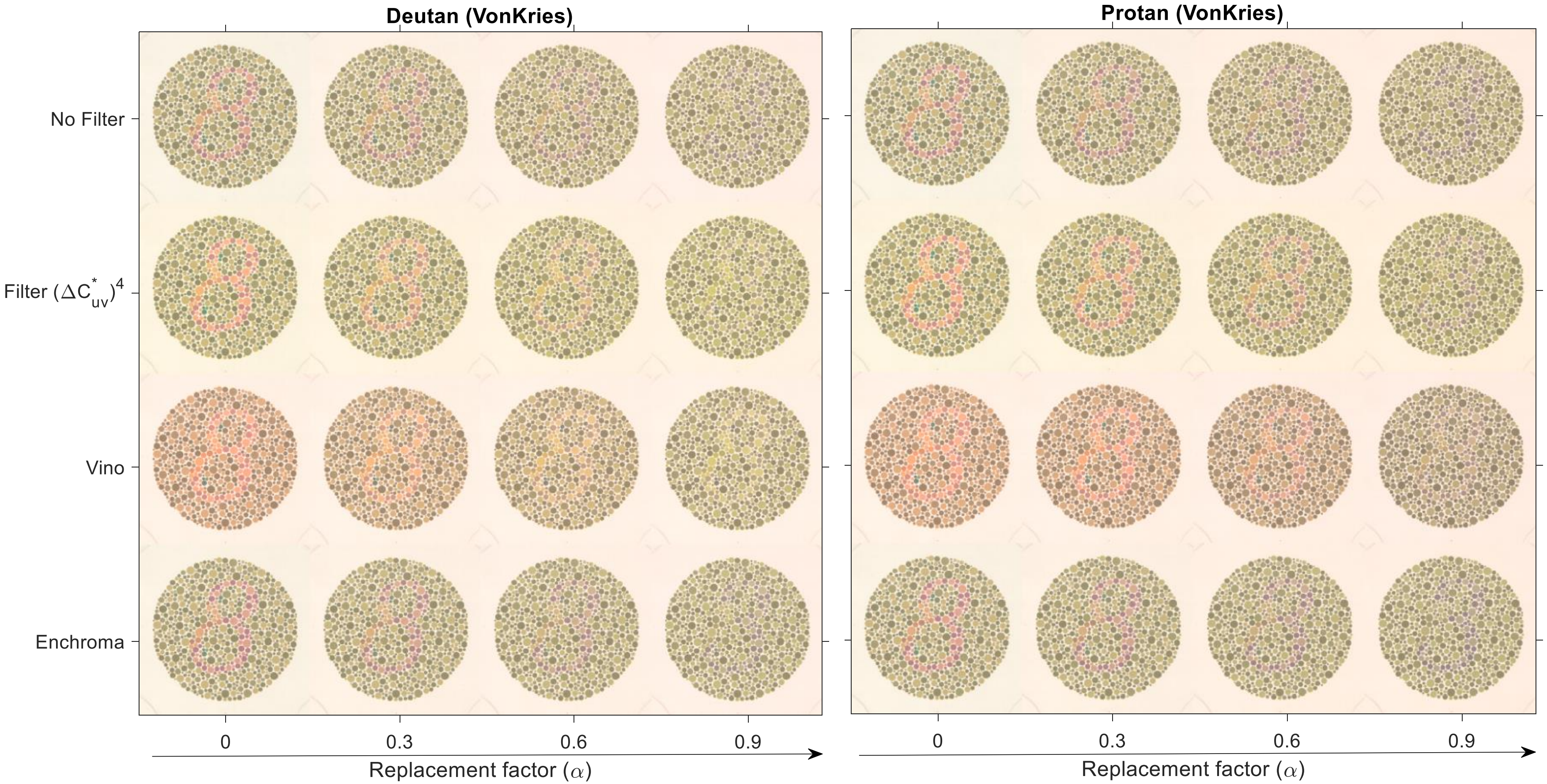

Figure 3-33-b: Spectral simulation of Ishihara test plate n°. 2 as perceived by normal (N.T.) and anomalous trichromat observers (replacement factor, $\alpha = \{0, 0.3, 0.6, 0.9\}$). Comparison between unfiltered and filtered images, for filters shown in Figure 3-31, considering Von Kries chromatic adaptation.

3.7 DISCUSSION

The findings of this study are consistent with other studies available in the literature. Frequency selective filters are appealing candidates for correction of anomalous trichromatic vision. However, the improvement in the colour and chroma differences is small and falls within the range of imperceptible for most or all observers. In order to achieve significant differences, there must be a trade-off, and an improvement for a particular set of colours can be achieved in detriment of others. A stop-band filter can decrease the overlap between the L and M cone spectral responses but does not necessarily improve colour discrimination for CVD observers. In the case of dichromat observers, decreasing overlap between cone responses is not a solution, as the missing information from the lack of one type of cones cannot be complemented by selective filtering of the observed light stimuli. In anomalous trichromats, however, the decreased overlap between cone responses can improve colour discrimination between certain stimuli due to increased contrast but will be detrimental for discrimination between other stimuli with different spectral properties. This trade-off between the enhancement and detriment of colour discrimination means that while some colours can be slightly improved, particularly those that are more affected by the CVD condition, other colours will be negatively affected, and the average effect is close to none.

While the theoretical maximum number of discernible colours cannot be increased by the use of optical filters, as the limits are given by the monochromatic light stimuli, there can be an increase of the limits given by a smaller colour sub-space defined by non-monochromatic stimuli. Natural scenes and reflective surfaces, under most types of illuminations, are comprised of non-monochromatic stimuli, and have generally smooth transitions across the visible spectrum. A colour space defined by a set of samples with these characteristics represent only a small subspace of the entire visible spectrum, and the limits of this space can be expanded. In particular, it was found that the limits defined by the convex hull enclosing all samples, in the UCS chromaticity diagram, can be expanded significantly. Even so, the increase in the chromaticity diversity will be accompanied by a decrease in luminance, thus the total number of discernible colours in the full spectrum is reduced.

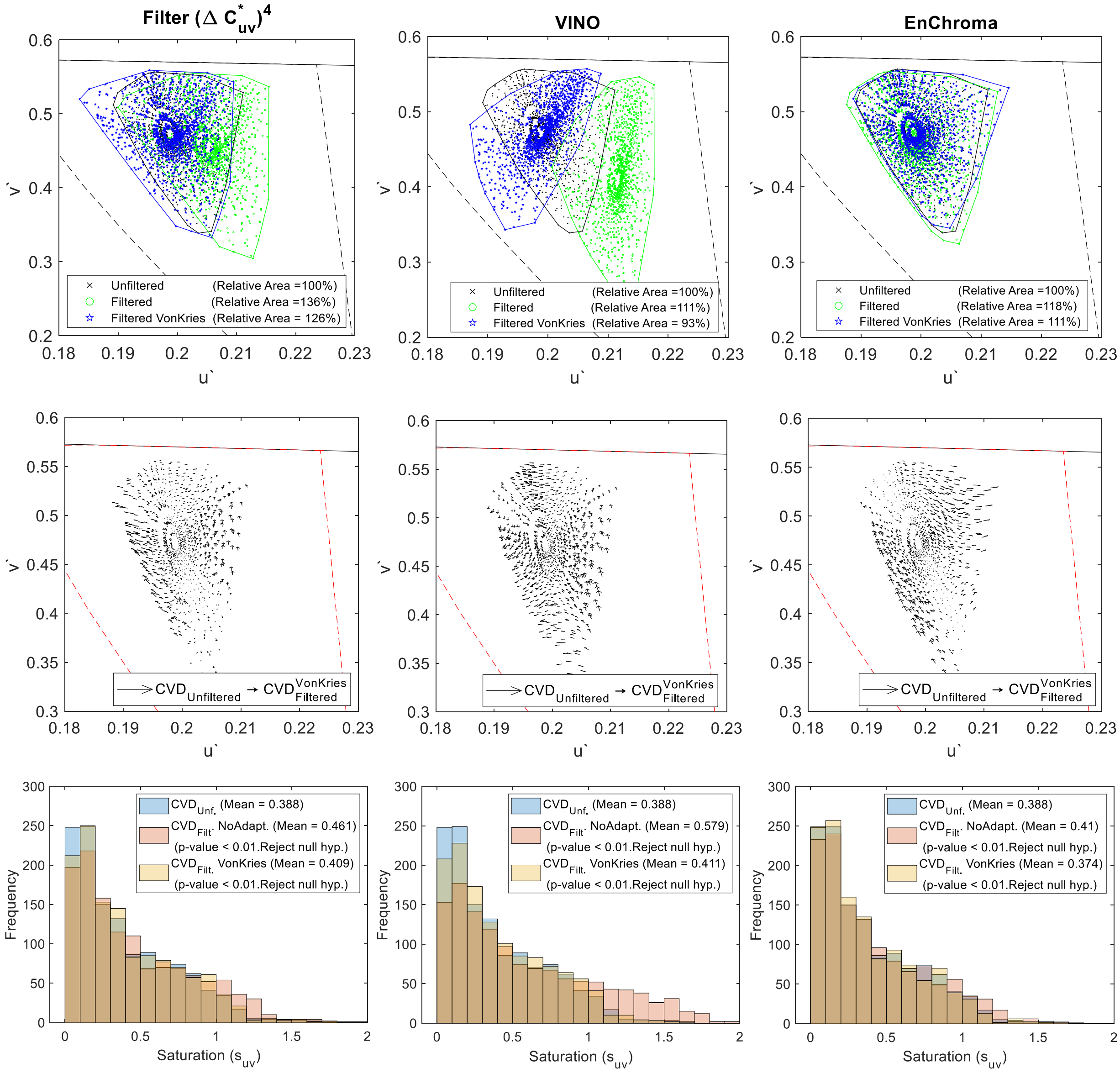

Figure 3-34: Comparison of results from FM-100 database, for deuteranomalous observer ($\alpha = 0.9$), for commercial VINO, and EnChroma glasses, and the C4 filter. Spectral transmittance of the filters presented in Figure 3-31. Top: UCS chromaticity values. Centre: vector field (scaled) representing the change in chromaticity from unfiltered, to filtered-adapted (Von Kries). Bottom: Histogram of frequencies for saturation values.

It is interesting, however, that discrimination of some colours can indeed be significantly improved, and depending on the specific details of the practical application for which these filters are being designed, these could potentially still be very effective. For example, this study has proved that the discrimination for red (or green) can be improved beyond the threshold of what is distinguishable for experienced observers ($\Delta E > 1$, when optimizing for $\overline{\Delta E_{uv}^{*}{}^{2}}$). Based on this idea, a custom filter can be designed for individuals with red-green CVD to be used in practical jobs which require good discrimination between red and green, for example, in fruit selection labours where the ripeness of the selected fruit is evaluated visually. A particular example, which has been discussed in literature, is the improvement in results for the Ishihara test. However, it can negatively affect other tests, such as the FM-100 test.

Other potential ways of improving the effectiveness of these corrective filters are by making use of differential binocular vision, *i.e.*, making different sets of filters for each of the two eyes, so that the user can discriminate some colours by contrast of the lightness value perceived by each eye. This strategy has been used in the past, and empirical evidence based on laboratory studies suggest that monocular tinted spectacles can improve colour discrimination in dichromats [17], [108]. A disadvantage of this approach is that it can negatively affect depth perception and other attributes related to stereoscopic acuity.

It is important to note that the representability of the results from this study depend largely on the different assumptions and selections made throughout the implementation of these methods. As mentioned in previous sections some critical factors include the selection of an adequate colour appearance model, an opponent colour space which allows for a good metric evaluating the colour perception of individuals with different retinal cone sensitivities, a representative database for the coloured samples spectral information, a representative model or database for the cone spectral sensitivities in anomalous trichromats, *etc*.

Some important notes on the selection of a fitness function need to be considered when analysing the results from this work. First, colour difference formulae, such as Eq. 3-47 and Eq. 3-48, have been developed with data sets having a limited range of colour-difference magnitudes, and their performance are uncertain when applied to wider ranges of colour differences. While researchers have proposed several variations on standard formulae to address large colour differences [84], [110], there is still no definite agreement on a one particular formulation, and most published literature on the topic of colour perception uses the standard CIELab and CIELuv formulae. In a recent publication by Fairchild and collaborators [84], variations on the Euclidean and "city-block" distances were examined, and concluded that the lightness difference should be addressed differently to chromatic values. In this work, the issue is addressed by considering both Euclidean colour and chroma differences, which differ in the inclusion of lightness as a part of the metric.

Another important consideration for the application of colour difference formulae in this work is that while the metrics for colour differences can be examined, tested, and fitted to psychophysical experimental data for a particular individual, the comparison of perception across different observers is inherently challenging, particularly, for observers with significant differences in their colour matching functions. In the derivation of the Stockman and Sharpe cone fundamentals, unilateral dichromats were tested in order to find the colour match between trichromatic and dichromatic perceptions [16], [60]. While this kind of test can avoid the problem of matching the perception for two different individuals, it is limited by the very small percentage of CVD observers with this condition. From an examination of current literature, there are currently no unchallenged or agreed formulations for metrics applicable to the direct comparison across observers with different conditions regarding to colour vision deficiency.

In particular, the use of standard colorimetry for CVD observers is limited, and a more rigorous methodology would include a personalised set of transformations and functions for each observer (transformations, colour space, colour difference formulae, *etc*.), however, this is a considerably more complex, and impractical approach, which remains as an open problem in the field [69], [92].

Some aspects that were not considered within this study, however partially or fully implemented within the same methods, are the effect of considering different field of vision sizes, and the effect of chromatic changes within a filter in different areas within the field of vision. Effects such as this occur in some optical coatings used in ophthalmic and sunglasses which have iridescent behaviour and their spectral properties depend on the angle of incidence of light, or in non-uniform coatings such as sunglasses which are darker on the top in order to account for the sun's position above the observer.

While there are clinical trials evaluating the effectiveness of colour correction glasses [97], as well as numerical evaluation of the colour appearance aspects of these filters [22], these studies are based on filters which have been designed and fabricated by a commercial trademark and are available in the market. However, these studies can only make conclusions on the specific filters being tested, and their conclusions cannot be generalized to other filters with different spectral properties. Some trademarks have patented design methods based on similar numerical optimization methods, such as linear programming optimization [111], however scientific research articles based on this methods are scarce, and the general question on whether frequency selective filters can improve colour discrimination in anomalous trichromatic vision is not fully answered.

3.8 CONCLUSIONS

The design and application of optical filters for as a passive aid for red-green colour vision deficiency was studied. Using the methods and available information from standard colorimetry, colour vision deficiency simulation, and linear optimization, a methodology was established to design and evaluate a series of frequency selective filters as candidates for colour correction or enhancing devices. The design of each filter is determined by the observer's characteristics, lightning conditions, a spectral database for a set of reflective samples, and an objective function.

The observer's characteristics are represented by their colour matching functions, which are calculated from the physiologically based LMS colour matching functions using the replacement model, dependant on the type and severity of the CVD condition. The objective function is used to evaluate the performance, or fitness, of a filter with respect to one or more specific aspects of colour appearance. The design of a filter is achieved by numerical optimization of this function, with respect to the filter's spectral properties. The shape and characteristics of this function will depend on the intended use for the device, what characteristics are desired, and how these characteristics are evaluated within the function. In this work, the metrics for colour and chroma difference in CIELUV colour space are used, comparing the anomalous filtered perception to that of a normal trichromat. While it is not possible to achieve full trichromatic vision by means of an optical filter, the main idea is to set a reference frame for comparison, on what is desirable in colour vision. It was found that when optimising for both colour and chroma difference, the designed filters do not make any significant change in colour perception. However, when raising the function to a higher power the function will prioritize correcting colours which are further away from trichromatic vision in detriment of others, *i.e.*, prioritize colours which are more problematic to the CVD observer at the cost of those which are less problematic. The designed filters present stopbands roughly around 475 and 570 nm, which correspond to the overlap section between the three cone fundamentals. Higher powers for the fitness function result in the widening of these bandgaps, increasing the change in colour perception while making the filter opaquer. Depending on the severity of the condition, represented by the replacement factor, the position of these stopbands will change, in accordance with the shift in position of the anomalous cone fundamental. More severe conditions will also result in wider stopbands.

While the total number of discernible colours was not increased, but rather reduced by the filters, it was found that the use of these filters can significantly increase the average saturation and widen the chromaticity diversity given by the convex-hull surrounding the test samples in the UCS chromaticity diagram. For the FM-100 test database, an increase in the chromaticity hull-area was observed. Depending on whether chromatic adaptation is considered, up to 35% or 19% increase was observed, for no adaptation and Von Kries respectively.

Commercial eyewear marketed as colour discrimination enhancers for CVD observers was compared to some the filters designed in this work. Similar results to the commercial VINO glasses were observed for the Ishihara test-plate simulation, with a noticeable discrimination enhancement for some plates, while EnChroma glasses were ineffective according to our simulation. These results are consistent with recent publications regarding these commercial filters, and the performance of the filters designed in this work is satisfactory with this regard.

The results obtained in this work are a promising starting ground in the design and fabrication of CVD correction filters, and further investigation is recommended for a future work. To our knowledge, this is the first scientific publication to specifically show the numerical design and evaluation methods of frequency selective filters for the correction of red-green colour vision deficiencies.

CHAPTER 4: DESIGN AND MANUFACTURING OF MULTILAYER OPTICAL FILTERS

4.1 ABSTRACT

This chapter focusses on the design and fabrication methods for optical components, with spectral properties given by a predefined design objective. Multilayer optical filters were designed using three different numerical approaches: refinement from an initial candidate solution, needle synthesis, and synthesis *via* genetic algorithm. Multilayer devices were fabricated using plasma-enhanced chemical vapour deposition (PECVD), and their optical characteristics were studied for both normal and oblique incidence. Additionally, an exploratory study is presented on the fabrication of colloidal crystals and inverse-opal optical systems.

4.2 INTRODUCTION

Optical filters are devices designed to selectively transmit light, depending on one or more properties, such frequency, magnitude, phase, or polarization. The selective transmission or blocking of light can be partial or complete, and the characteristics of the filter are determined by its transmission profile. Practical applications of optical filters are numerous, including spectroscopy [112], [113], microscopy [114], astronomy [115], photography [116], [117], wearable optics [118], *etc*. In particular, the industry of wearable optics benefits from a variety of optical filters such as light absorbent sunglasses, anti-reflective optical coatings, and polarizers. The focus of this work is on the design and use of frequency selective optical filters for wearable optics applications. Frequency selective optical filters can be categorized either by their optical behaviour, *e.g.*, band-pass, short/long-pass, neutral density, *etc*. – or by the principle used to filter light, such as light absorbing, or interference filters.

Light absorbing filters are usually produced by introducing dyes, which are light absorbing molecules. The type of absorbing filter is commonly found in protective eyewear (sunglasses, welding and laser goggles, *etc*.), or to protect components from light-induced degradation (for example, UV-sensitive polymer components in automobiles) [119].

Interference filters, on the other hand, work on the basis of light refraction and wave superposition. Controlling the internal geometry and optical density of an optical device allows to selectively transmit light by means of constructive or destructive light interference. Light being transmitted through the device can interact with the components of itself which are being reflected and diffracted by a change in refractive index within the device. The most prominent type of interference optical filters are thin-film layered devices. Optical thin films are used to control the transmission or reflection of light, by tailoring its thickness and refractive index, to produce light interference within the film. Multi-layered devices are used to 'stack' the effect of thin-film interference, to produce highly efficient interference filters.

The design of optical filters for practical and commercial applications, such as wearable optics, is fundamentally constrained by availability and properties of the constituent materials, as well as the capabilities and precision of the fabrication process. The cost and quality of raw materials, as well as the technical and economic limitations intrinsic to each fabrication process, play a significant role in the design of optical filters intended for commerce. In addition, optical-film designers must consider several other technical factors, such as the scalability and productivity of the selected fabrication process, variance in the device's operating conditions (luminance level, temperature, *etc.*), durability, impact resistance, *etc.*

4.2.1 Thin film optics

In optics, thin films are defined as layers of material with thicknesses in the order of magnitude of the visible light. These films can have very interesting optical behaviours, owing to constructive and destructive light wave interference. Optical coatings consist of single or multiple thin layers of material deposited on an optical component, such as a lens or a mirror, designed to alter the way light is being transmitted, reflected, or polarized by the optical device. Typically, these are made up of oxides, metals, rare earth materials, and dielectric materials. Examples of optical coatings include anti-reflection coatings, dielectric mirrors, band-pass and band-stop filters, *etc.* [120], [121]. Some examples of thin film optic devices are presented below in Figure 4-1.

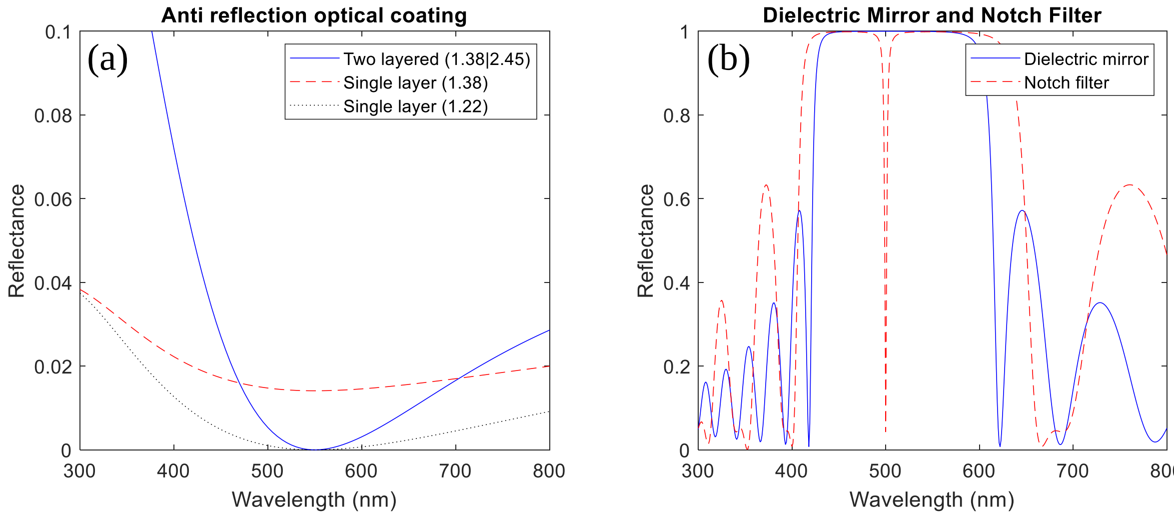

Figure 4-1: Spectral reflectance of thin film optical coatings: **(a)** anti reflection optical coatings, consisting of a single reflectionless quarter-wave slab ($n = \sqrt{n_{air} n_{glass}} = 1.22$; $nl = \lambda_0/4$); a single layer quarter wave slab ($n = 1.38$, $nl = \lambda_0/4$); and two quarter-wave slabs ($n_1 = 1.38$, $n_2 = 2.45$, $n_i l_i = \lambda_0/4$). (b) Dielectric mirror, consisting of 17 total alternating quarter-wave layers ($n_H = 2.32$, $n_L = 1.38$, $n_i l_i = \lambda_0/4$), and Notch filter, with the same multilayer structure as the dielectric mirror with a half wave cavity in the centre layer [121].

What makes thin film optical devices useful in numerous applications is their design flexibility and accuracy for producing devices with highly tuned spectral performance. Their optical performance depends on the refractive index and geometric thickness of each constituent layer, which are variables that can be controlled in terms of materials choice and layer thickness. Although a variety of materials have been used in optical coatings [122]–[124], there are highly restrictive limitations to the availability and compatibility in the selection of the constituent materials. Different materials can require different technologies and equipment to produce the optical coatings, and the use of multiple fabrication processed is generally impractical, expensive, or technically unviable. In general, multilayer optical devices are made-up of only a few different materials, and the most prevalent type are binary systems.

The flexibility of thin-film optical devices, however, comes from the ability to tailor their spectral properties by controlling the geometric thickness and number of layers in the device. Deposition technologies, such as physical and chemical vapour deposition (PVD and CVD respectively) allow for a very fine control of layer thickness, with precision in the nanometre range, which allows for the production of highly tuned optical devices.

4.2.2 Spectral properties of multilayer systems: Rouard's recursion

The spectral properties of multilayer optical structures are given by light interference resulting from the partial reflection and transmission in the multiple optical boundaries within the structure. These effects are determined by the phases and amplitudes of the interacting waves which, in thin film optics, is determined by the layer thicknesses and refractive indexes of the constituting layers. Variations with respect to the layer thickness alter the phase relationship between reflected waves, while variations in the refractive index also affects the amplitude of these waves [125].

A simple recursive method can be used to calculate the spectral properties of an optical multilayer system, according to the elementary reflection coefficients for each layer. The method, referred to as Airy-like summation, or Rouard's recursion, is equivalent to first order numerical integration of the coupled-mode equations [126]. The extensive mathematical derivation of this method is readily available in the relevant literature [121], [126]–[128], but a brief description is presented in this section.

A representation of an optical multilayer system is presented in Figure 4-2, consisting of 'M' alternating layers of optic materials with different refractive indices (n_1, n_2,…,n_M). Consider a linearly polarized electric field (E_1), incident at an angle θ_a to a multilayer device.

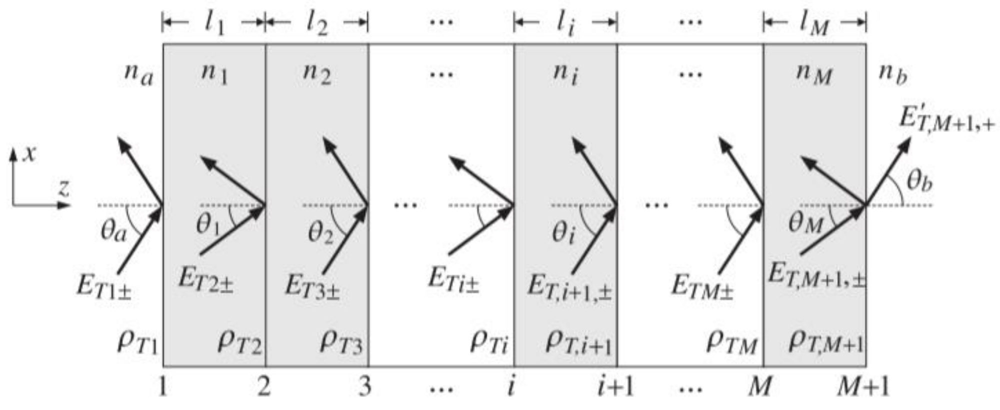

Figure 4-2: Oblique incidence on a multilayer dielectric structure [121].

The electric (E) and magnetic (H) fields travelling towards the '*i-th*' interface, at position z_i, can be rewritten in terms of the forward (+) and backward (-) moving fields:

$$E_i = E_{i(+)} + E_{i(-)} = E_{1(+)}e^{-jkz_i} + E_{1(-)}e^{jkz_i} \qquad \text{Eq. 4-1}$$

$$H_i = \frac{1}{\eta}\left[E_{i(+)} - E_{i(-)}\right] = \frac{1}{\eta}\left[E_{1(+)}e^{-jkz_i} - E_{1(-)}e^{jkz_i}\right] \qquad \text{Eq. 4-2}$$

$$\eta = \sqrt{\mu/\varepsilon} \qquad \text{Eq. 4-3}$$

where η is the intrinsic impedance of the medium, and μ and ε are the material's permeability and permittivity respectively, and θ is the angle of incidence. Combining these equations, an expression for the forward and backwards electric fields can be derived in terms of the total electric and magnetic field:

$$E_{i(+)} = \frac{1}{2}(E_i + \eta H_i) \qquad \text{Eq. 4-4}$$

$$E_{i(-)} = \frac{1}{2}(E_i - \eta H_i) \qquad \text{Eq. 4-5}$$

Two important quantities for light transmission through interfaces are the wave impedance (Z), and reflection coefficient (Γ):

$$Z_i = \frac{E_i}{H_i} \qquad \text{Eq. 4-6}$$

$$\Gamma_i = \frac{E_{i(-)}}{E_{i(+)}} \qquad \text{Eq. 4-7}$$

Using Eq. 4-4 through Eq. 4-7, a relation can be derived between these two quantities:

$$Z_i = \frac{\eta(1+\Gamma_i)}{1-\Gamma_i} \qquad \text{Eq. 4-8}$$

$$\Gamma_i = \frac{Z_i - \eta}{Z_i + \eta} \qquad \text{Eq. 4-9}$$

Ultimately, the purpose of the method is used to calculate the reflectance, $R(\lambda)$, and transmittance, $T(\lambda)$, of an optical device. These correspond to the ratio between the intensity of the incident field, to the reflected and transmitted components, respectively. The reflectance of a multilayer device can be calculated from the reflection coefficient in the first interface, Γ_1, while transmittance can be calculated from the reflectance, assuming the media is lossless and non-absorbent:

$$R(\lambda) = \left|\frac{E_{1(-)}}{E_{1(+)}}\right|^2 = |\Gamma_1(\lambda)|^2 \qquad \text{Eq. 4-10}$$

$$T(\lambda) = 1 - R(\lambda) = 1 - |\Gamma_1(\lambda)|^2 \qquad \text{Eq. 4-11}$$

The relation between the reflection coefficients at the different interfaces is given by the propagation of the light wave. Consider a layer of material with thickness $\Delta z = (z_2 - z_1)$, the forward electric fields are given by:

$$E_{2(+)} = E_{0(+)} e^{-jkz_2} \qquad \text{Eq. 4-12}$$

$$E_{1(+)} = E_{0(+)} e^{-jkz_1} = E_{0(+)} e^{-jk(z_2-\Delta z)} \qquad \text{Eq. 4-13}$$

Then, $$E_{1(+)} = E_{2(+)} e^{+jk\Delta z} \qquad \text{Eq. 4-14}$$

and similarly, $$E_{1(-)} = E_{2(-)} e^{-jk\Delta z} \qquad \text{Eq. 4-15}$$

Combining these equations, the reflection coefficient of the first interface can then calculated from the second:

$$\Gamma_1 = \frac{E_{1(-)}}{E_{1(+)}} = \frac{E_{2(+)}e^{+jk\Delta z}}{E_{2(-)}e^{-jk\Delta z}} = \Gamma_2 e^{-2jk\Delta z} \qquad \text{Eq. 4-16}$$

In oblique incidence, the reflection/refraction angles at each interface are related to each other by Snell's law (Eq. 4-17). The transverse impedance (Eq. 4-18) and refractive indexes (Eq. 4-19) in each medium are defined by the type of polarization and angle of incidence:

$$n_a \sin\theta_a = n_i \sin\theta_i = n_b \sin\theta_b \qquad \text{Eq. 4-17}$$

$$\eta_{T_i} = \begin{cases} \eta_i \cos\theta_i\,, & TM, parallel, p-polarization \\ \dfrac{\eta_i}{\cos\theta_i}, & TE, perpendicular, s-polarization \end{cases} \qquad \text{Eq. 4-18}$$

$$n_T = \begin{cases} \dfrac{n_i}{\cos\theta_i}, & TM, parallel, p-polarization \\ n_i \cos\theta_i\,, & TE, perpendicular, s-polarization \end{cases} \qquad \text{Eq. 4-19}$$

Rouard's method consists of calculating the reflection coefficient of an interface, from the coefficients in subsequent layers. Assuming no backwards waves in the right-most medium, the reflection response, Γ_i, and impedance, Z_i, will satisfy the following recursive relation:

$$\Gamma_i = \frac{\rho_i + \Gamma_{i+1}e^{-2jk_il_i}}{1 + \rho_i\Gamma_{i+1}e^{-2jk_il_i}} \qquad \text{Eq. 4-20}$$

$$Z_i = \eta_i \frac{Z_{i+1} + j\eta_i \tan(k_il_i)}{\eta_i + jZ_{i+1}\tan(k_il_i)} \qquad \text{Eq. 4-21}$$

The term, ρ_i, corresponds to the elementary reflection coefficient from the left of the *'i-th'* interface:

$$\rho_i = \frac{\eta_i - \eta_{i-1}}{\eta_i + \eta_{i-1}} = \frac{n_{i-1} - n_i}{n_{i-1} + n_i} \qquad \text{Eq. 4-22}$$

To calculate the reflectance of a multilayer, the recursive relation in Eq. 4-20 is used to calculate Γ_1, initialized at the (M+1) interface, using the values:

$$\Gamma_{M+1} = \rho_{M+1} \qquad \text{Eq. 4-23}$$

, and

$$Z_{M+1} = \eta_b \qquad \text{Eq. 4-24}$$

For unpolarised light, reflectance can be calculated as the weighted summation from both types of polarization. Assuming there are equal amounts of s-, and p-polarized light, then:

$$R_{eff} = \frac{1}{2}\left(R_s + R_p\right) \qquad \text{Eq. 4-25}$$

To obtain the full reflectance/transmittance spectrum of an optical device within a specific range of frequencies/wavelengths, the recursion is repeated changing the corresponding values for permittivity, $\varepsilon(\lambda)$, and permeability, $\mu(\lambda)$, of the constituting materials at that wavelength.

4.2.3 Design of multilayer systems

The prediction of the spectral properties of a given multilayer system can be calculated using various exact or approximate methods, such as the previously mentioned Rouard's method. These mathematical methods, however, are generally non-reversible, and the so-called inverse problem, or design problem, cannot be solved directly. Finding a multilayer system with a given spectral behaviour, in the process known as *synthesis*, is a much more complex problem.

The objective of thin-film design and synthesis is to determine the physical parameters defining an optical multilayer system, such as layer thickness and refractive index profile, to produce an optical system with a spectral performance equal, or similar, to what was predetermined in the design objectives. Many literature resources can be found covering the design aspect of optical thin films and multilayer systems [129]–[133], but generally, some grade of simplification or approximation is required. The two main strategies consist of finding an exact solution to a simplified model, or finding an approximate numerical solution to a more realistic or general model [130].

While exact solutions allow for a straightforward calculation and are generally easier to produce once a general solution has been found, they are limited to very simple devices or scenarios, where various assumptions can be made to simplify and solve the analytical mathematical model, without detracting too much from the original problem. On the other hand, approximate solutions allow for the design of more complex devices in realistic situations, but they are also limited by the errors and precision intrinsic to the numerical and computational methods. In general, approximate solutions are more prevalent in industry, since they can be applied more generally to produce various designs, and are readily available in commercial software programs for optical design.

The process of thin film design can be grouped into two main categories: refinement and synthesis. In the former, a starting design is optimized using a suitable numerical algorithm as a function of one or more parameters, such as layer thickness or refractive index. The resulting design is sensitive to the starting point, which is usually determined by known exact solutions, semi-analytical methods, and previous experience. In synthesis, the starting point is not predetermined, and solutions to the problem are generated by analytical, semi-analytical, or purely numerical methods. Refinement is generally part of the synthesis process but is not essential. Synthesis is more flexible and requires less prior knowledge of the solution.

To measure the correspondence between the desired and the actual spectral performance for an optical device, the merit function, MF, is used to determine how 'good' or 'bad' is a candidate solution. While this function can be defined in various ways, a form of mean square differences is widely employed in literature, as presented below [102], [122], [134]:

$$MF(R') = \frac{1}{N}\left(\sum_{i=1}^{N}\left[\frac{R_{obj}(\lambda_i) - R'(\lambda_i)}{\Delta R_i}\right]^2\right)^{\frac{1}{2}} \qquad \text{Eq. 4-26}$$

where R_{obj} is the objective spectral reflectance, and R' is the reflectance for a candidate solution. The term ΔR_i is the tolerance of the merit function at wavelength λ_i. Note that when tolerances are set constant to 1%, the equivalent merit function corresponds to the mean root square deviation (in the 0-100% range).

4.2.4 Needle optimization

First introduced by Tikhonravov in the early 1980s [135], the needle method is probably the most popular and most successful thin film synthesis technique. The basic algorithm for the needle optimization synthesis method is presented in Figure 4-3. An initial design, consisting of single or multiple layers, is refined by optimizing the merit function in terms of layer thickness or refractive index, generally following a gradient based optimization method.

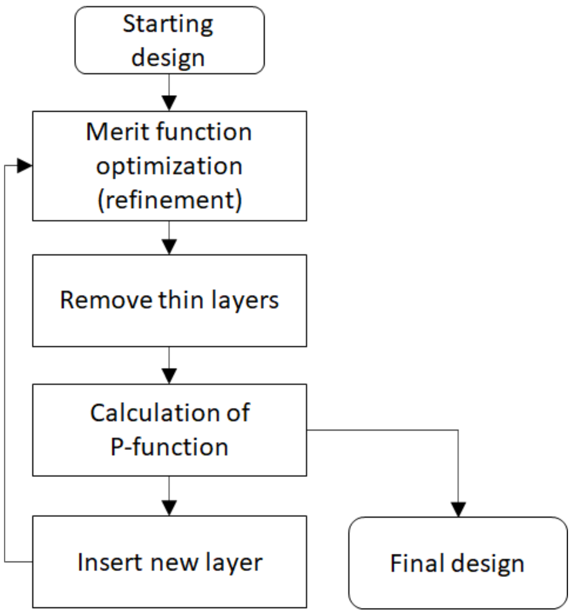

Figure 4-3: Schematic of numerical synthesis by needle optimization algorithm.

The iterative optimization stops when the merit function cannot be further improved within the specified tolerance, and new physical effects must be introduced to proceed. This can be done by inserting new layers of material to the structure to change the refractive index profile of the structure (Figure 4-4). The process is called needle variation, owing its name to the infinitesimally thin layer insertions, and is the essence of needle optimization.

The power of this method is that the algorithm can identify the existence, optimal position, and material for the insertion of a new layer, such that the merit function is improved, without the actual insertion of the new layer [125]. The determination for the position of needle variations is determined by a perturbation function, the P-function, and needles are inserted where P(z) has its most negative value (Figure 4-4). An analytical expression for $P(z)$ is derived from an expansion series of the merit function differential with respect to the thickness of the new layer [125], [136]. The rigorous mathematical considerations used to determine P(z) can be found in [136].

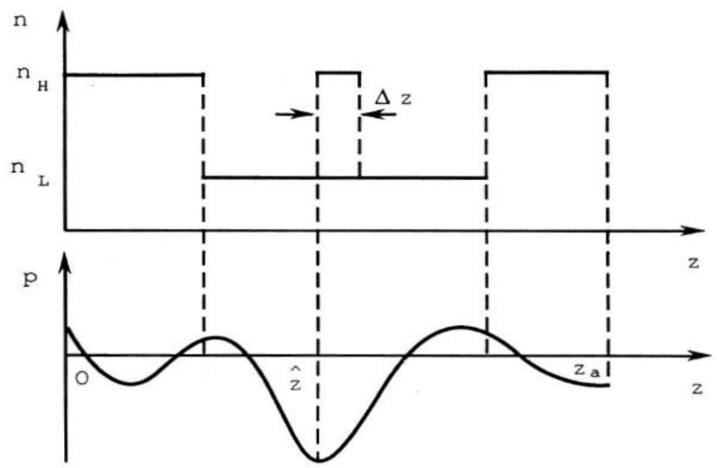

Figure 4-4: Insertion of new layers in needle optimization. Top: Function $n(z)$ represents the refractive index profile of the multilayer system, alternating between materials with a high (n_H) and low (n_L). Bottom: insertion of a needle at a position is determined by the function $P(z)$ [125], [136]

One disadvantage of the needle synthesis approach is the proliferation of very thin layers, resulting from the needle insertions. Manufacturing these very thin nanometric layers can be expensive, impractical, or downright impossible with the available technology. Thin layers are prone to aggregation and other difficulties during deposition, increasing the complexity and costs of manufacturing. Generally, a minimum layer thickness must be considered during the design stage, according to the available methods and manufacturing restrictions. Methods for thin layer removal have been implemented in commercial software for the needle method, generally consisting of a regular needle procedure, followed by an iterative step for removing thin layers, and subsequently refining the solution until all layers are within the desired thickness range. A trade-off is made between spectral performance and minimum layer thickness [129], [137].

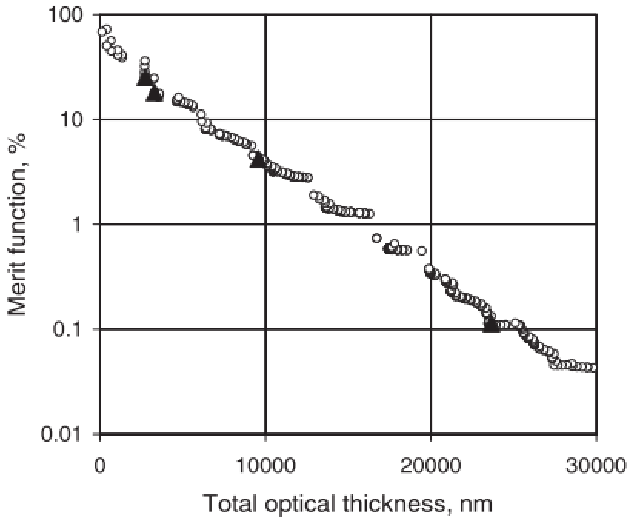

Figure 4-5: Example of achieved merit function *vs.* optical thickness using the needle method [138].

4.2.5 Evolutionary optimization

The genetic algorithm (GA) is a metaheuristic method of optimization inspired by the process of natural selection. It is a type of evolutionary algorithm, which is based on biologically inspired operators such as selection, mutation, and crossover [139], [140].

It belongs to the family of random heuristic search methods (RHS) [105]. These are a family of numerical optimization methods which seek to solve optimization methods not by searching solutions in the direction of the gradient, but by different heuristics applied and iterated for a random selection of initial solutions. The heuristic methods can be well defined or include a random or semi-random component in the iterative step. Some examples of random heuristic search include genetic algorithm, simulated annealing, Monte Carlo methods, *etc*. An advantage of these methods is that, unlike gradient based methods, they do not require for the function being optimized to be continuous or differentiable, while the random component of the heuristic makes these methods robust for finding global solutions in problems with a high number of local minima (or maxima).

The genetic algorithm method can be described in a few simple steps, as shown in Figure 4-6:

1. The genetic algorithm starts with a randomly generated set of potential solutions within the domain of definition of the fitness function. This collection of solutions, or 'individuals', corresponds to the population of the first generation of solutions.
2. Following this, each solution within that generation is evaluated according to the fitness function, which is the objective function being optimized.
3. The fittest individual, or 'champion', will be transmitted to the next generation.
4. Individuals above the average fitness are selected to create the next generation *via* crossover. Crossover is a stochastic operator, which combines the genetic information of two individuals to create an offspring. Most individuals in the new generations are created by crossover.
5. A fraction of the new generation is created by random mutations of randomly selected individuals.
6. The algorithm iterates steps 2 through 5 until a stopping criterion is met, and the best individual of the current generation is selected as the final solution. Stopping criteria include: maximum generations, maximum function evaluations, change in function fitness less than tolerance, *etc*.

Some adjustable parameters within the genetic algorithm are the population size, crossover fraction and mutation rate, the tolerance of the function to determine that an optimum has been found, and the maximum allowable number of generations. Note that, owing to the random factors in the genetic algorithm, multiple solutions can arise from different runs of the algorithm.

Increasing the population size decreases the probability of converging to a local rather than the global optimum, as well as increasing the precision of the final solution. On the other hand, increasing the population size can drastically increase computation times, as every individual within each generation is evaluated according to the objective function.

The crossover fraction refers to the fraction of individuals in every generation that is created by crossover, while the remaining will be generated by mutation and cloning of the best fit individuals. Decreasing the crossover fraction, and by consequence increasing the mutation rate, results in a more robust method to find global rather than local optima, as it increases the chances of an individual to 'escape' a local optimum where the population may be concentrated. Increased mutation rate, however, increases the computation times due to the slower convergence to a solution, and decreases the final solution precision. Balancing the values of these parameters is crucial when implementing this method.

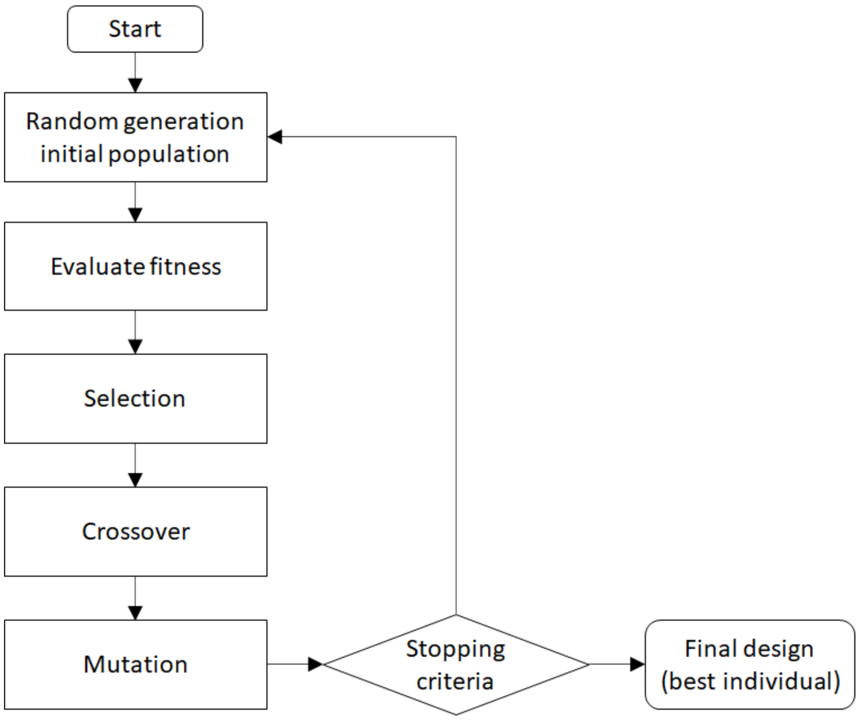

Figure 4-6: Schematic of genetic algorithm optimization

In the field of optical filters, the use of GA has been explored as a robust design tool. Investigators have proposed the use of GA to design optical filters which are less sensitive to layer thickness variations [141], [142]. This approach can allow to relax the precision or clearance in the manufacturing process, thus reducing costs and variance in the performance of multiple devices. Another example is the use of GA in the robust design of optical filters with respect to the angle of incidence of incoming light [143]. Small misalignments of optical equipment will affect the angle of incidence, which will affect the optical filter performance. Reducing the sensitivity of an optical device with respect to the angle of incidence allows the minimisation of errors caused by misalignment, reducing costs associated to equipment precision and calibration required for high precision equipment, or to potentially expand the application of optical filters to areas where there is a high variance in the operation conditions, such as wearable optics.

In a recent publication, the use of an evolutionary inspired algorithm was implemented by Barry *et al.* to design photonic structures, which numerically converged towards structures similar to biological photonic structures, such as 1-D periodic multilayer structures, often found in the shells of some species of beetles, and 2-D Xmas-tree-like structures, similar to those found in the wings of the Blue Morpho butterfly [144].

Benefits of using the GA approach include the capability of handling highly non-linear, discontinuous, or non-differentiable problems. It avoids local minima (or maxima) thanks to the stochastic nature of the operators used (crossover, mutation). The method, however, can be disadvantageous when handling objective functions that are computationally intensive, as each individual in every generation is evaluated according to this function. The method is sensitive to the mathematical complexity of the design problem, and an increase in the number of variables (or freedom degrees) can exponentially magnify the computational costs and reduce precision, increasing the probability of the algorithm converging to a local optimum, rather than the global solution. N

4.2.6 Fabrication of multilayer systems *via* PECVD

Plasma enhanced chemical vapour deposition (PECVD) is a widely utilized and well-established fabrication technique in which thin films of various materials are deposited from a gaseous state (vapour) to a solid state on a substrate through chemical reactions that occur after the formation of a plasma state from the reactant gases.

The reactant gases are introduced between two parallel electrodes: a grounded electrode and an RF (radio frequency)-energized electrode. These induce the formation of a plasma state in the reactant gas, ionizing a significant portion of the gas molecules. This plasma state induces a chemical reaction resulting in the deposition of a solid product on to the substrate, placed on the grounded electrode. The frequency of the RF electrode can be set to high (HF) or low (LF). Temperatures of the substrate typically vary between 250 and 350°C depending on the specific conditions required for a particular film. These are much lower temperatures compared to standard chemical vapour deposition (CVD), which typically require temperatures between 600 and 800°C. The lower temperature requirement can be critical in certain applications, where thermal induced stresses can result in damage of the films being deposited.

Films deposited through PECVD are typically made of silicon nitride (Si_xN_y), silicon dioxide (SiO_2), silicon oxy-nitride (SiO_xN_y), silicon carbide (SiC), and amorphous silicon ($\alpha - Si$). These are produced from reactant gases such as silane (SiH_4) and dichlorosilane (SiH_2Cl_2), combined with oxygen or nitrogen containing gases (N_2O, NH_3, $etc.$) to form silicon dioxide and silicon nitride respectively. Both silicon dioxide and silicon nitride are dielectric materials commonly used for the fabrication of electronic devices. An example of the chemical reactions taking place in a PECVD process are presented below:

$$3SiH_{4(g)} + 4NH_{3(g)} \rightarrow Si_3N_{4(s)} + 12H_{2(g)} \qquad \text{Eq. 4-27}$$

$$SiH_{4(g)} + 2N_2O_{(g)} \rightarrow SiO_{2(s)} + 2N_{2(g)} + 2H_{2(g)} \qquad \text{Eq. 4-28}$$

PECVD yields some of the fastest deposition rates and high film quality in terms of roughness and defects, as compared to other deposition techniques such as sputter deposition and thermal/electron-beam evaporation.

4.3 **OBJECTIVES**

The main objective of this section is to design frequency selective optical devices through numerical simulation and optimization and demonstrate the fabrication of these based on deposition techniques. To achieve this, the following specific objectives are proposed:

- Utilize commercially available software in optic design and implement the required computational design tools for designing multilayer systems with predefined spectral properties, including refinement, needle optimization, and evolutionary algorithms.
- According to manufacturing considerations, and other restrictions, to design a multilayer system and fabricate a device using well established deposition techniques, such as PECVD.

- To measure and characterize the optical properties of the fabricated devices, and evaluate them according to their performance in correction of colour vision deficiency.

4.4 METHODS: DESIGN OF OPTIC MULTILAYERS *VIA* NUMERICAL OPTIMIZATION

4.4.1 Spectra Calculation

Multilayer spectral properties were calculated using Rouard's recursive method, as described in previous sections. In particular, the MATLAB implemented method published by Orfanidis, "multidiel.m", was utilized [121], [145]. The input to this program is an N-by-1 vector, L, containing the optical thickness for N-layers in the multilayer system; an (N+2)-by-1 vector, n, containing the refractive index of the substrate, transmission medium (air), and each of the corresponding N-layers of dielectric isotropic material (in case of uniaxial and biaxial materials, this is a (N+2)-by-2 and (N+2)-by-3 respectively); a vector containing all wavelengths at which the function is evaluated, λ; angle of incidence, θ; and the polarization of the incident light, pol (TE or TM). The output to this program is the reflection coefficient, Γ, from which reflectance is calculated and transverse wave impedance, Z:

$$[\Gamma, Z] = multidiel(n, L, \lambda, \theta, pol) \qquad \text{Eq. 4-29}$$

$$R(\lambda) = |\Gamma(\lambda)|^2 \qquad \text{Eq. 4-30}$$

4.4.2 Design objective

In order to study the methods for numerical design of optical filters, the spectral distribution shown in Figure 4-7 was selected as the objective distribution used to determine the merit of the device. It consists of two stopbands, centred at ~480 and 560 nm, with a band width of ~45 nm. This spectral distribution was selected from previous results in optical filter design for improved colour discrimination in red-green colour vision deficiency (Chapter 3).

In particular, this design results from the optimization of a filter which minimizes the function $\overline{\left(\Delta C_{uv}^{*}{}^{4}\right)}\Big|_{deutan(\alpha=0.9)}^{normal}$.

Note that only the normal incidence direction is considered for the calculation and evaluation of the device spectral properties, however, due to the iridescent nature of the multilayer systems, these properties change depending on the angle of incidence. The case of oblique incidence is not considered in the design of multilayer optical devices within this work, however, it will be measured and compared to the expected behaviour predicted by Eq. 4-29 and Eq. 4-30. Three different design methodologies are considered in this work: refinement from an initial candidate solution, needle synthesis, and genetic algorithm.

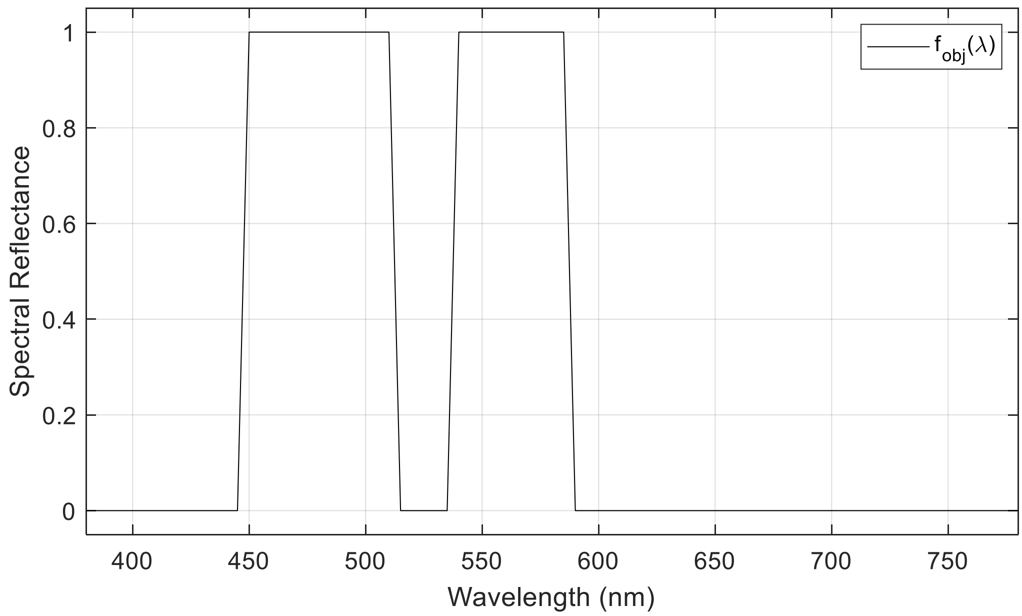

Figure 4-7: Spectral design objective for multilayer system.

4.4.3 Refinement of candidate solutions

The design strategy of the refinement approach consists of selecting an initial candidate solution, and subsequently refining the solution *via* numerical optimization methods. Three initial candidate solutions were selected, made-up of 20 alternating layers:

- Bragg reflector, or quarter-wave stack, centred at 530 nm.
- Notch filter, consisting of a quarter-wave stack, with a half-wave cavity centred at 530 nm.

- Double-quarter-wave, consisting of two quarter-wave stacks centred at 480 and 560 nm, with a half-wave cavity centred at 520 nm.

Numerical refinement was carried out using the Levenberg–Marquardt algorithm, implemented in the open-source OpenFilters [146].

4.4.4 Needle synthesis

Needle synthesis optimization was executed using OpenFilters [146]. This open-source software, published by Larouche and Martinu, provides numerical tools for thin film optics analysis and design. This software is available at the web portal of the Functional Coating and Surface Engineering Laboratory of the École Polytechnique Montreal [147].

4.4.5 Genetic algorithm

Numerical tools for thin film design *via* genetic algorithm were implemented in MATLAB. The function "GA.m", implemented in MATLAB's Global Optimization Toolbox [148].

$$x = ga(@Fun(x), N, A, b, A_{eq}, b_{eq}, l_b, u_b, @nonlcon, opt) \qquad \text{Eq. 4-31}$$

Where $@Fun(x)$ is the function handle being optimized with respect to x; N is the number of independent variables (size of x); A and b correspond to a N-by-N matrix and N-by-1 vector respectively indicating a linear restriction $A * x \leq b$; A_{eq} and b_{eq} indicate the equivalency restriction $A_{eq} * x = b_{eq}$; l_b and u_b are the lower and upper bounds for x ($l_b \leq x \leq u_b$); @nonlcon is a function handle indicating non-linear restrictions; and $opts$ is a structure containing the optimization parameters for the genetic algorithm (function tolerance, population size, max generations, crossover function, mutation rate, *etc*.).

In the case of this study, the function being optimized corresponds to the merit function of an optical filter (Eq. 4-26), which is being optimized in terms of the optical thickness vector, L, of a given multilayer. The method firstly calculates the spectral reflectance of the filter in the visible spectrum ($\lambda = [380, \ldots, 780]\ nm$) using Eq. 4-29 and Eq. 4-30, for normal incidence ($\theta = 0$). Following this, the merit function is evaluated according to Eq. 4-26, for a constant tolerance, $\Delta R_i(\lambda) = 10^{-2}$. The number of variables, N, corresponds to the number of layers in the multilayer device. The restrictions given A, b, A_{eq}, b_{eq}, and $@nonlcon$ were unused, and set to null ([]), while the boundaries l_b and u_b were set in terms of geometrical thickness restrictions, e, and the refractive index of the corresponding i-th layer, n_i:

$$l_{b_i} = e_{l_i} * n_i \qquad \text{Eq. 4-32}$$
$$u_{b_i} = e_{u_i} * n_i$$

The values for the lower and upper bounds of the geometrical thickness, e_l and e_u, are set according to manufacturing considerations (Table 4-1), and further discussed in subsequent sections. Within the options of the GA algorithm, the function tolerance was set to 10^{-4}, maximum number of iterations to 10^5, and maximum number of function evaluations to 10^6. Other options, unless specified otherwise, were set to their default values.

4.4.6 Materials, and manufacturing considerations

In order to design multilayer systems which can be manufactured by deposition techniques such as PECVD, some considerations must be included within the numeric design, such as available materials, sizing restrictions, time required for deposition, equipment availability, *etc*. These considerations can be coded as linear or non-linear restrictions within the numerical methods, such that the domain of possible solutions for the optimization problem is restricted by these.

For example, as an alternative to assuming the value of refractive indexes to be a continuous domain between specific boundaries, a discrete number of 'material candidates' are considered, according to material availability and deposition capabilities of the technique used for fabrication. The case of a bi-material device is the simplest form, consisting of alternating layers of two different materials. In this case, the number of independent variables is reduced to (N+1), consisting of N-independent optical thickness values, and one independent variable indicating the material for the first layer.

In terms of available materials, a dual system of silica ($n = 1.47$) and silicon nitride ($n = 1.87$) was selected. These materials were chosen due to the available knowledge and expertise, as these are standard materials widely employed by industry and researchers to produce electronic and optic devices *via* PECVD. Additionally, the system was restricted such that the sequence of layers are alternating materials, in the form $[SiO_2/Si_3N_4]_x$, where x is the number of periods ($N_{Layers} = x * 2$).

In terms of sizing restrictions, it was considered that the minimum thickness for a single layer is 30 nm, and the maximum total thickness of the device is 2 µm. The minimum layer thickness was established in order to avoid typical defects formed in ultrathin layers, such as aggregation and island/drop formation, and to ensure that a homogeneous layer is deposited in all the area of the substrate [149], [150]. These considerations were discussed and defined with the help of the expert PECVD technician in INL, summarized in Table 4-1.

Table 4-1: Summary of sizing and other manufacturing considerations.

Parameter		*Value*	*Considerations*
Materials (n = refractive index)	SiO_2	n = 1.47	Standard optical materials for PECVD. Material availability. Good refractive index contrast, minimizing number of layers required.
	Si_3N_4	n = 1.87	
Layer thickness	Minimum	≥ 30 nm	Avoid aggregation, island/drop formation and other defects in ultrathin film deposition.
	Maximum	≤ 200 nm	Consider only 1st order reflection. Minimize amount of material utilized and deposition time.
Total thickness	Minimum	-	Given by: $\min(Layer\ thickness) * N_{Layers}$.
	Maximum	≤ 2000 nm	Minimize amount of material utilized. Given by maximum deposition time and equipment availability.
Number of layers	Predefined	10-30 layers	Depending on other considerations.

4.5 RESULTS FOR NUMERICAL FILTER DESIGN

4.5.1 Refinement

The first design strategy considered in this work is the numeric refinement of an initial candidate solution. The initial candidates selected are based on quarter-waves, which are widely used optical devices due to their simplicity, both in terms of design and manufacturing, and high optical performance.

The centre wavelength of the initial candidates was selected to closely match the centre of the objective filter band-pass at 530 nm. The number of layers was set equal to 20 across all candidate solutions. The choice in the number of layers, while arbitrary, was based on an informed decision over the limitations and practicality in the manufacturing process.

The initial candidate filters, and the resulting final design from the refining process are presented in Figure 4-8. It can be observed that the initial double-quarter-wave (DQW) yielded the best result out of the three candidates. While the notch filter yielded a similar result in terms of merit, there is a significant difference in the optical thickness of the final designs, and the DQW yields a ‘thinner’ filter which translates to a smaller amount of material required, and deposition time. The resulting design from the Bragg filter, while having a smaller optical thickness, presents the lowest performance in terms of the merit function.

It is expected that initial solutions which have similar behaviour to the objective filter will yield better solutions in the final design. The notch and DQW filters were selected specifically for the presence of a passband at approximately 530 nm, similar to the objective filter. In addition to this passband, the DQW was manually designed and selected so that each of the constituent quarter-wave stacks were centred at 480 and 560 nm, matching the centre of the two stopbands in the objective filter.

While satisfactory results were achieved *via* the refinement approach, some of the method’s disadvantages can be observed. The method requires having an initial candidate solution, and the final design is highly dependent on the selection of this candidate. In the case of this work, the similar characteristics of the objective filter’s spectra, to the well-known notch filter, makes the finding of a good candidate solution rather simple. However, for more complex spectrum profiles, finding a good candidate solution can be much more difficult, and may require profound knowledge and/or extensive experience in the field.

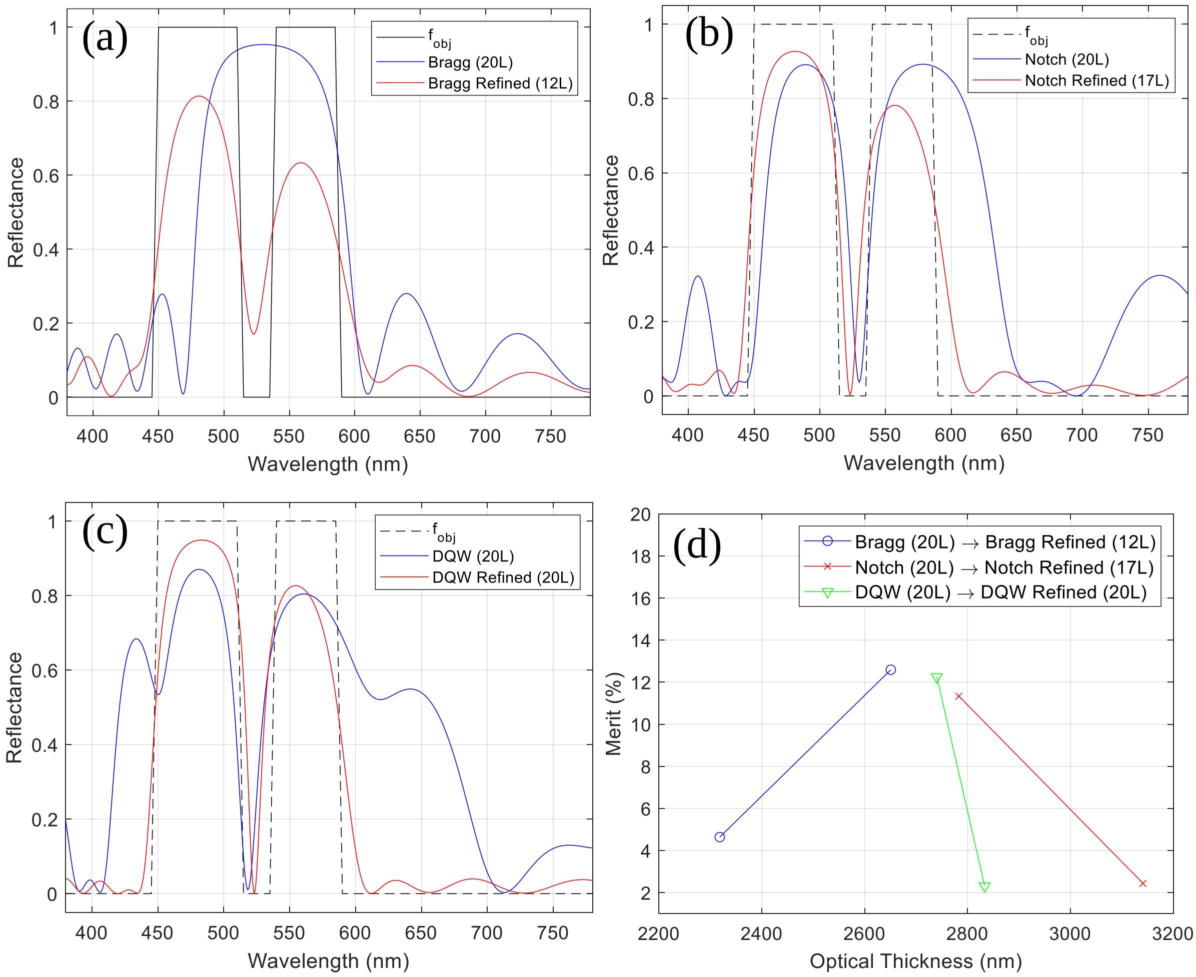

Figure 4-8: Spectra for filter designs obtained by refinement of candidate initial solutions (20 layers): from a quarter-wave stack (Bragg mirror) centred at 530 nm **(a)**, from a notch filter centred at 530 nm **(b)**, and from double quarter-wave stack centred at 480 and 560 nm (cavity centred at 520 nm). The number of layers for the initial and refined designs is shown in parenthesis on each graph legend. The merit of the initial and refined designs is presented in **(d)** as a function of the final design optical thicknesses.

4.5.2 Needle optimization

Results from needle optimization are presented in Figure 4-9. All designs result from needle optimization from a starting design of a single layer of silicon nitride of various thicknesses (250 to 5,000 nm). Merit of the final designs is presented as a function of the total number of layers and the optical thicknesses of the final designs.

The optical thickness and number of layers of final design are directly related to the thickness of the initial layer. The optical thickness of the final design is similar to the initial layer, and the choice of the initial layer thickness is a critical step in the design. The merit function value is also related to the initial layer thickness, and designs with higher optical power, given by their increased optical thickness, result in the best optical performance, as indicated by the reduced value of the merit function.

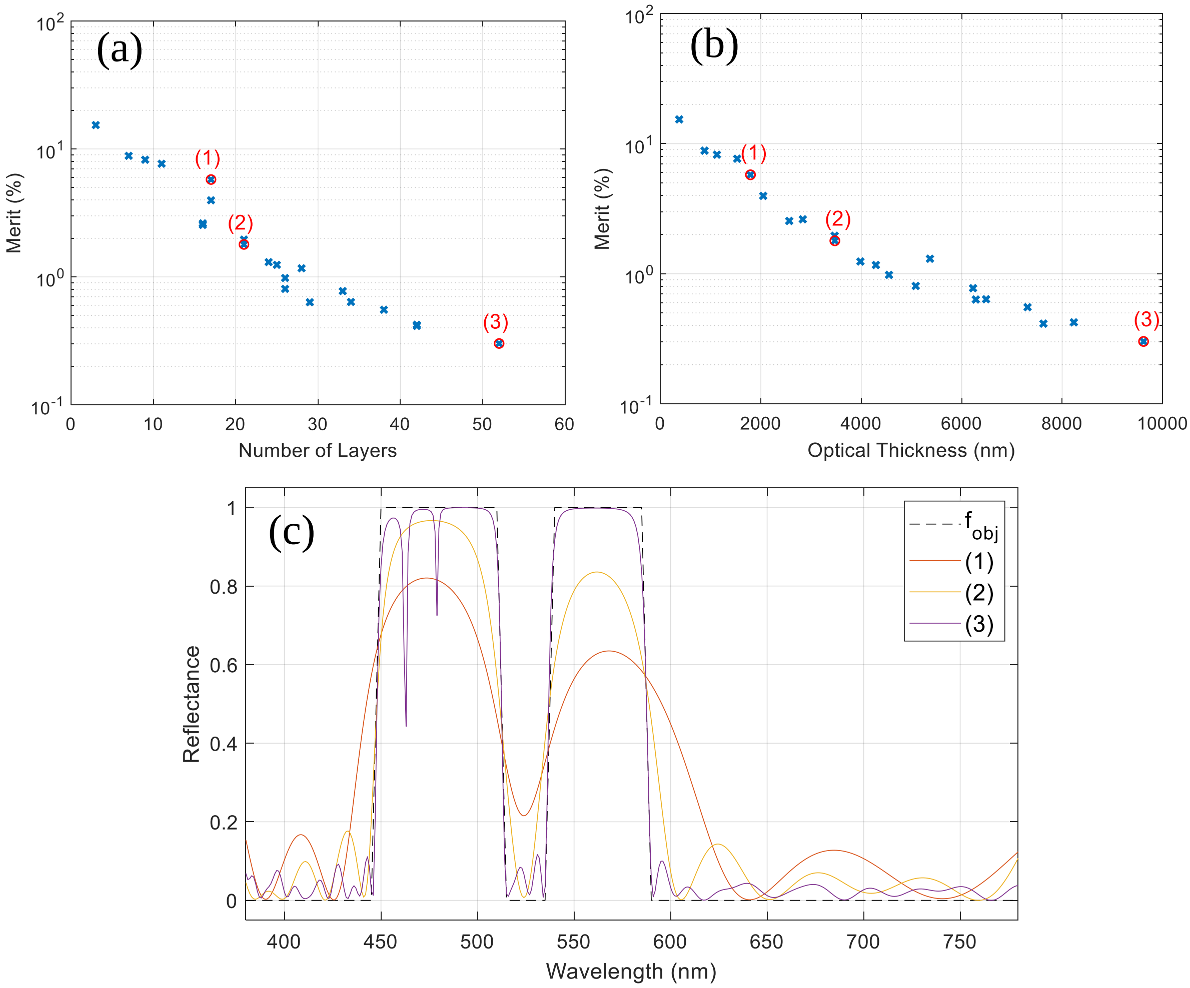

Figure 4-9: Summary of results for needle optimization synthesis, from an initial design consisting of a single Si_3N_4 layer (geometrical thickness range from 200-5000 nm). Merit is presented as a function of the number of layers **(a)**, and optical thickness of the final designs **(b)**. Spectral properties for 3 different designs marked in (a) and (b) are presented in **(c)**, along with the desired objective spectra.

A power law relation can be observed between merit and optical thickness, presented as a negative slope linear relation in a semi-log graph (see Figure 4-5 and Figure 4-9-b). This relation establishes a trade-off between the performance of the final design, and the materials and manufacturing costs associated to manufacturing such device. The most relevant conclusion from this power-law relation is that in order to further improve the performance of a device, the required optical thickness increases exponentially. In other words, any further improvement for high performance devices will significantly increase the amount of material required and deposition times, exponentially increasing the manufacturing costs for very small gains in performance.

4.5.3 Evolutionary algorithms

The genetic algorithm was studied as an alternative method for the design of multilayer optical devices. The merit of the resulting designs was studied as a function of the population size, and boundary conditions set for the genetic algorithm.

Population Size

One important parameter in genetic algorithm optimization is the population size. A large population generally leads to higher accuracy in the resulting solution; however, it increases the computational complexity and can largely increase computation times. The selection of an adequate population size is a crucial step when using genetic algorithm.

In general, a minimum threshold is required to ensure diversity in the initial population, increasing the reliability of the optimization. This threshold depends on the number of independent variables in the optimization problem, and a larger population is required for problems with increased number of variables. In the case of MATLAB's GA, the default population size is 50, for a problem with 5 or less independent variables, and 200 otherwise. Alternatively, the population size can be set as a factor of the number of variables, for example, to 20 times the number of variables ($PopSize = 20 * N_{Var}$). While traditional GA uses a fixed population size, researchers have found that an adaptive population size through generations can increase the accuracy of the final solution, while reducing the time for convergence [151].

This section will compare results obtained using genetic algorithm for optical multilayer design, using a fixed population size of various sizes (200, 1,000, and 10,000). A summary of results is presented in Figure 4-10.

Computation time increases significantly with population size (Figure 4-10-b), while the effect in the merit of the final designs is less pronounced (Figure 4-10-a). To assess the small differences in the merit value of the solutions, a log-log regression of merit as a function of both the number of layers and final optical thickness is presented in Figure 4-11.

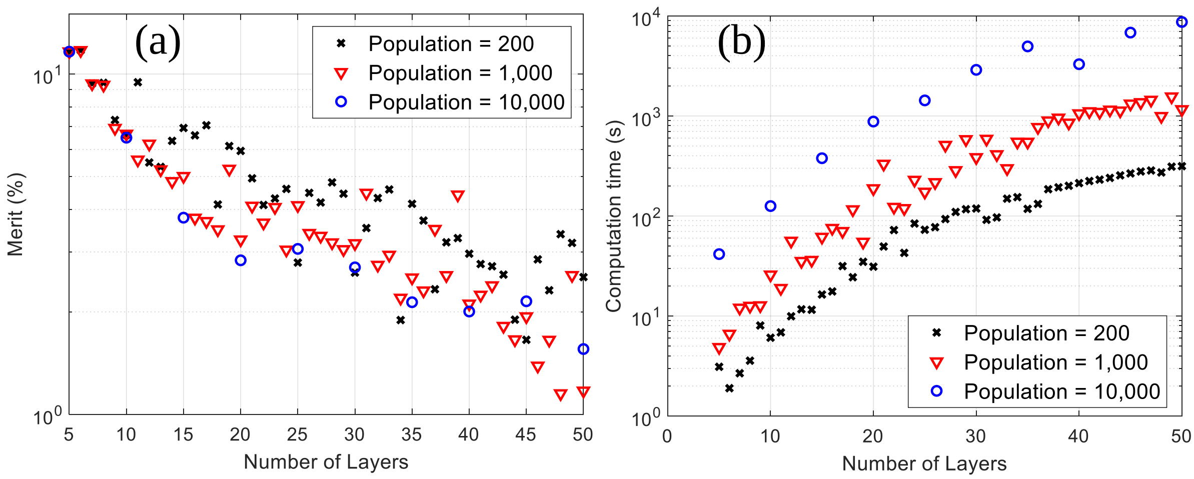

Figure 4-10: Effect of population size in multilayer design *via* genetic algorithm. Merit (a), and computation time (b) as a function of the number of layers, for a population of 200 (black cross); 1,000 (red triangle); and 10,000 (blue circle).

A summary of the linear regression parameters is presented in Table 4-2. These regressions show a moderate-to-high linear relationship ($0.70 < R^2 < 0.97$) and show that while there is a decrease in the negative slope between populations of 200 and 1,000, the difference between populations of 1,000 and 10,000 is very small, even presenting a slight increase in slope. Dispersion of the data is considerable due to the stochastic nature of the genetic algorithm, and becomes more significant when dealing with an increased number of independent variables (number of layers). This effect is observed as a widening in the data dispersion towards the right-side of the graph, resulting from the fact that the search space becomes larger with every added layer, which in mathematical terms equals to adding an extra dimension, and the variability and diversity of the population increases.

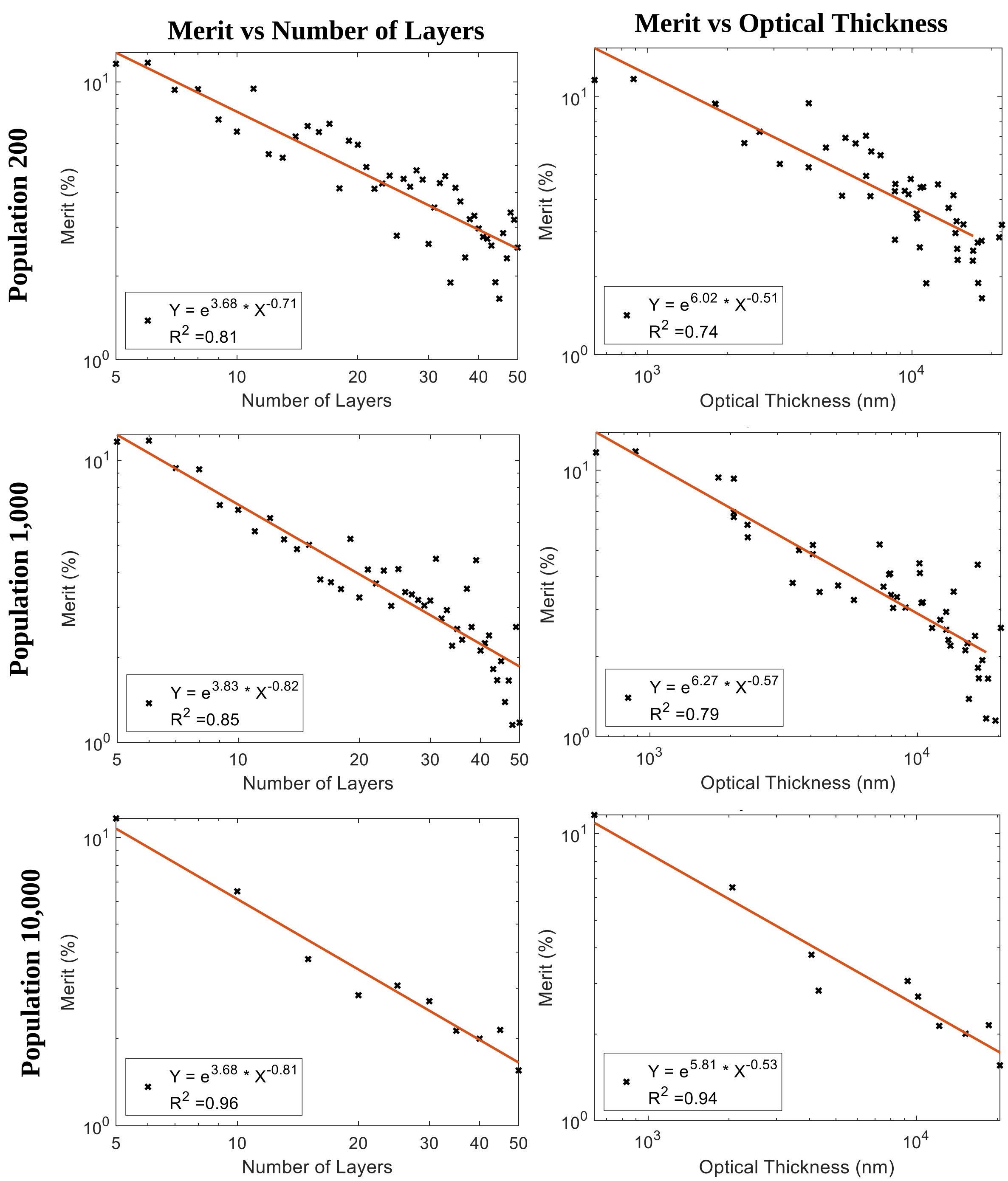

Figure 4-11: Log-log regression: merit as a function of the number of layers (left column), and optical thickness (right column) in multilayer design *via* genetic algorithm. Results for three different population sizes (top to bottom: 200; 1,000; 10,000).

Table 4-2: Regression coefficients for merit as a function of the number of layers and optical thickness. Regression in the form: '$log(Y) = m * log(X) + n$', or '$Y = e^n * X^m$'.

	Merit (%) vs Number of Layers			Merit (%) vs Optical Thickness (nm)		
Population Size	**Intercept (n)**	**Slope (m)**	R^2	**Intercept (n)**	**Slope (m)**	R^2
200	3.6843	- 0.707	0.807	6.023	- 0.509	0.740
1,000	3.8353	- 0.822	0.846	6.274	- 0.566	0.790
10,000	3.6776	- 0.811	0.964	5.811	-0.531	0.939

Boundary conditions:

The boundary conditions of the multilayer design problem determine the maximum and minimum optical or geometric thickness for each layer in the device. In general, these boundaries are subject to manufacturing considerations such as layer thickness control, deposition time, and material use. These considerations give the absolute boundaries for the manufacturing process, namely, they give the absolute maximum and minimum values for layer thickness which can be produced *via* the chosen manufacturing method. Beyond these considerations, the choice of boundary conditions in the design problem can considerably increase or decrease the performance of the algorithm used for the numerical design of the device. The influence of the boundary conditions on the merit of the final solution can be observed in Figure 4-12.

In the genetic algorithm, a small search space allows for increased accuracy of the final solution, as the solution will converge faster, however, the global optimum (as well as other local optima) can be excluded from the search space if the space is reduced excessively. A larger search space could increase the probability that the global optimum is contained within this domain, however, increases the number of generations (iterations) and computation time required for convergence, and the final solution will not be as refined.

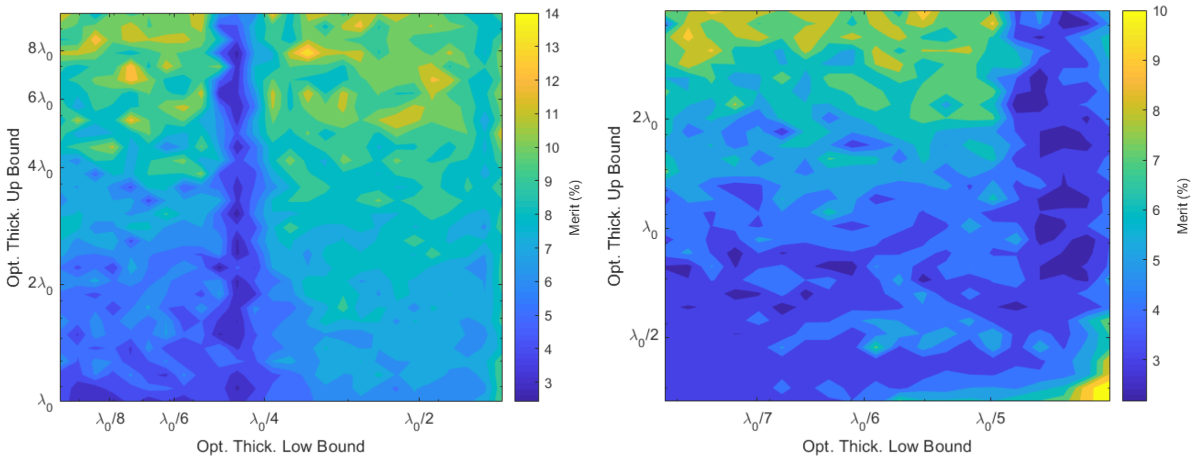

Figure 4-12: Merit as a function of the layer optical thickness upper and lower boundaries, for multilayer filters designed *via* genetic algorithm (20 layers, population size 200, function tolerance 10^{-6}). Boundaries are shown as a factor of λ_0 (550 nm).

The best results in this design experiment were achieved setting the optical thickness lower limits in the range from $\lambda_0/5$ to $\lambda_0/4$; and upper boundaries between $\lambda_0/2$ and λ_0. The value, $\lambda_0 = 550\,nm$, represents a rough mid-point of the visible spectrum, close to the objective filter band-pass at $\lambda = 530\,nm$. A transformation of the optical thickness boundaries to the equivalent geometric thickness is presented in Table 4-3, for the corresponding materials used in for design and manufacture during this study ($n_{SiO_2} = 1.47$; $n_{Si_3N_4} = 1.87$). Note that the overall limits for geometric thicknesses will be given by the high refractive index material in the lower limit, and by the low refractive index material in the upper limit (marked in bold).

Table 4-3: Transformation of optical thickness upper and lower boundaries to geometric thickness, for materials used for manufacturing in this work.

		Optical thickness ($\lambda_0 = 550\ nm$)			
	Material	$\lambda_0/5$	$\lambda_0/4$	$\lambda_0/2$	λ_0
Geometric thickness (nm)	Silica (n=1.47)	74.8	93.5	187.1	**374.1**
	Silicon nitride (n=1.87)	**58.8**	73.5	147.1	294.1

The selection of boundary conditions appears to be very relevant to the performance of the final design. A simple strategy to ensure an adequate set of boundary conditions is to make an initial exploratory design, with a wide search-space, and gradually reducing the boundaries towards the values obtained in the exploratory runs. However, from the above results it can be inferred that a good starting point is in the range of $[\lambda_0/6 - 2\lambda_0]$, where λ_0 can be the centre wavelength for a feature of interest in the design objective, or the mid-point in the range of wavelengths in study.

While the boundary conditions shown in Table 4-3 improve the performance of the final solution found by the genetic algorithm, limitations given by the manufacturing process cannot be overlooked. As discussed in previous sections (4.3 Methods), manufacturing considerations set a strict limit to the geometric thickness of the deposited layers, from a technical, economic, and practical perspective. In accordance with these considerations, all the designs outside of this section considered lower and upper boundaries for the layer geometric thickness of 30 and 200 nm, respectively (see Table 4-1).

4.5.4 Effect in Colour Vision

During the numerical design of optical filters, the least square difference formulae are used to evaluate the mean difference of a solution to the desired objective filter. However, it does not necessarily reflect the performance of that particular solution in the final application. In this section, comparative results in colour vision applications are presented. These filters are the result of from three different design strategies under study:

1) Numerical refinement from a double quarter-wave stack.
2) Genetic algorithm synthesis, refined final solution.
3) Needle synthesis.

The spectral reflectance of these filters, along the original objective spectra, are presented in Figure 4-13. In the same figure, results from colour appearance simulation are presented for the FM-100 database. The area of the convex-hull enclosing all samples in the UCS chromaticity diagram is used to represent the diversity in chromaticity values that can be achieved for this set of samples using each different filter as a passive correction device for CVD. A summary of these results is presented in Table 4-4.

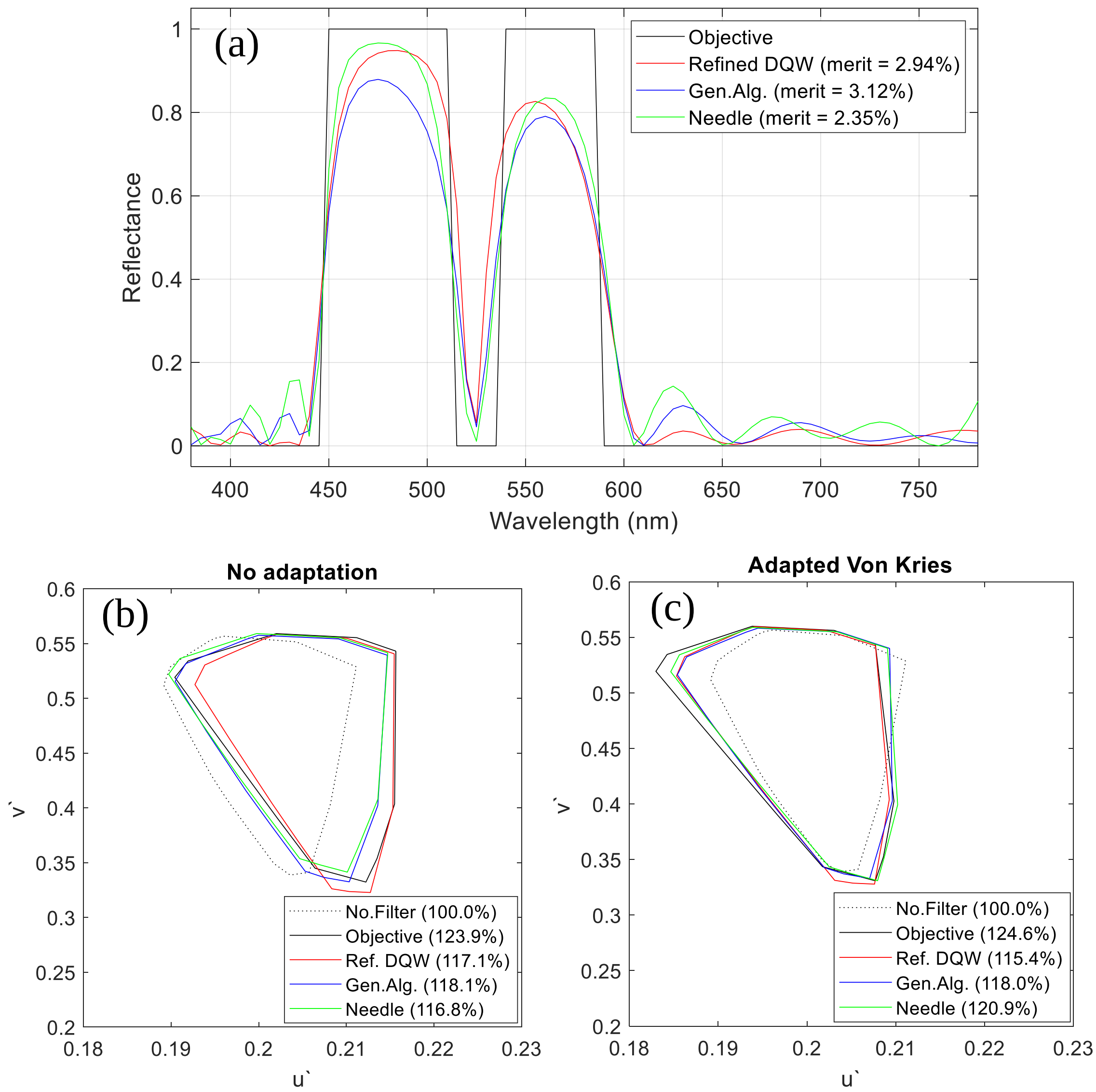

Figure 4-13: Reflectance spectra of the objective filter, and the resulting designs from refinement, genetic algorithm, and needle synthesis **(a)**. Convex-hull of FM-100 database in the UCS chromaticity diagram, resulting from simulation for a deuteranomalous observer ($\alpha = 0.9$), without chromatic adaptation **(b)**, and adapted using Von Kries transform **(c)**.

The selection of a particular design for manufacturing will depend on various factors. While the merit value for a particular filter is a good rough indicator on the performance of a filter, it does not necessarily represent its performance in the final application in colour vision applications. From the results presented in Table 4-4, it can be observed that while the genetic algorithm design presents the poorest merit value (3.12%), it represents the highest increase in the relative convex-hull area in the chromaticity diagram (118%). when no chromatic adaptation is considered. On the other hand, when considering chromatic adaptation, the genetic algorithm design presents a higher increase in the chromaticity convex-hull relative area (118%), compared to the refined DQW design (115%), but smaller that the needle design (120%). In addition, other important factors to consider in the choice of a design for manufacturing include those related to material usage and deposition times. The total optical (or geometric) thickness of a filter is an indicator of these factors, and designs with lesser total thickness are more desirable to reduce manufacturing costs. Results for the colour appearance simulation of hyperspectral images, for the same deuteranomalous observer ($\alpha = 0.9$) are presented in Figure 4-14, and Figure 4-15 (for methods, see Section 3.6.10).

Table 4-4: Summary of design characteristics, and colour appearance results for three different filter design strategies.

				UCS chromaticity convex-hull relative area (FM-100)	
	Number of layers	**Optical thickness (nm)**	**Merit (%)**	**No chromatic adaptation**	**Adapted (Von Kries)**
Objective filter	-	-	0 %	123.9 %	124.6 %
Refined from DQW	20	2833	2.94 %	117.1 %	115.4 %
Genetic Algorithm	21	3183	3.12 %	118.1 %	118.0 %
Needle Synthesis	21	3473	2.35 %	116.8 %	120.9 %

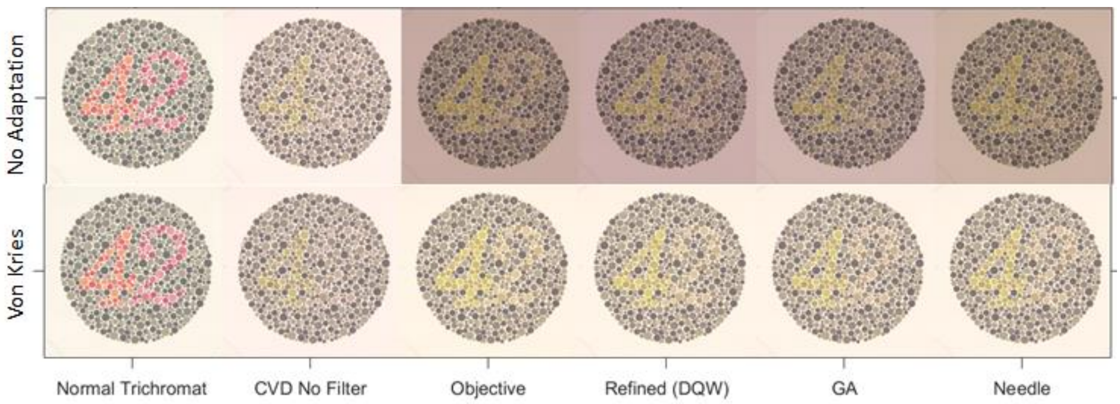

Figure 4-14: Simulation of the Ishihara test-plate n°17, for normal trichromat, and deuteranomalous observer ($\alpha = 0.9$), provided with different optical filters. **Top**: no chromatic adaptation. **Bottom**: Adapted to D65 illumination using the Von Kries transform.

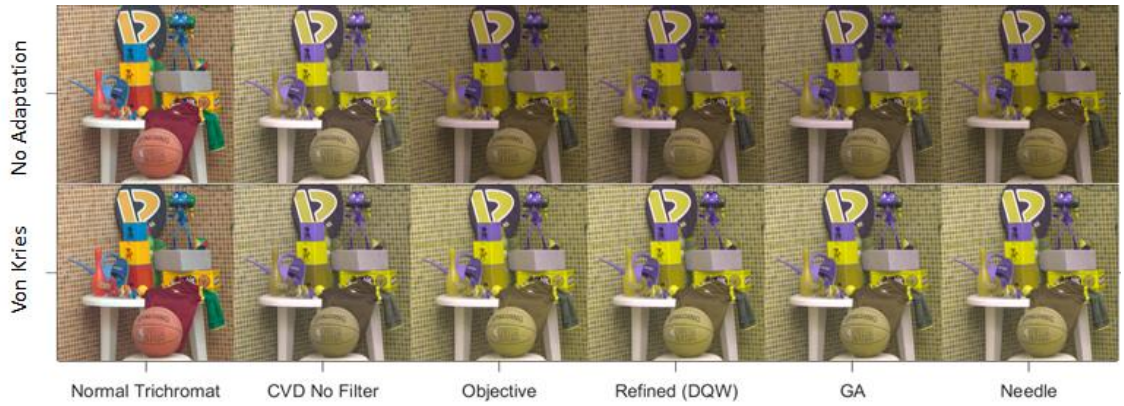

Figure 4-15: Simulation of a natural scene, for normal trichromat, and deuteranomalous observer ($\alpha = 0.9$), provided with different optical filters. **Top**: no chromatic adaptation. **Bottom**: Adapted to D65 illumination using the Von Kries transform.

4.6 DISCUSSION ON FILTER DESIGN

Three different numerical design strategies were considered in this work: refinement of an initial solutions, needle synthesis, and genetic algorithm syntesis. While all strategies were succesful at producing optical filters, the performance of the final designs varied across all three methods. Every method has its own advantages and disadvantages, and the choice of a design strategy will depend on the particular characteristics, limitations, and priorities of the design.

Refinement of an initial candidate solution is a straightforward process, widely used in the industry due to its efficiency and simplicity. However, the need of an initial candidate solution, as well as the sensitive dependance on the quality of the initial candidate, can highly constrain the applicability of the method.

The needle synthesis approach is a well-tested, highly efficient method, which can produce very high performance and precision. Indeed, the best results with respect to merit were found using the needle synthesis method. Additionally, the method is very efficient in terms of computation, its widepread use has resulted in the proliferation of highly optimized optical design software based on this method.

The genetic algorithm synthesis approach, while interesting, was not able to produce designs with ultra-high performance (merit $< 1\%$), as opposed to the needle synthesis. However, for a small number of layers (≤ 20 layers), the performance of the genetic algorithm was similar to the needle synthesis approach. Other disadvantages of the genetic algorithm are the intensive computation time and resources associated, due to the large number of function evaluations and iterations required. The stochaistic nature of the method can be both an advantage or disadvantage, as it reduces the probability of converging to a local minimum, rather than the global, but it can yield low precision and noisy results.

The comparative performance of the needle and genetic approaches, as a function of the number of layers and optical thickness, is presented in Figure 4-16.

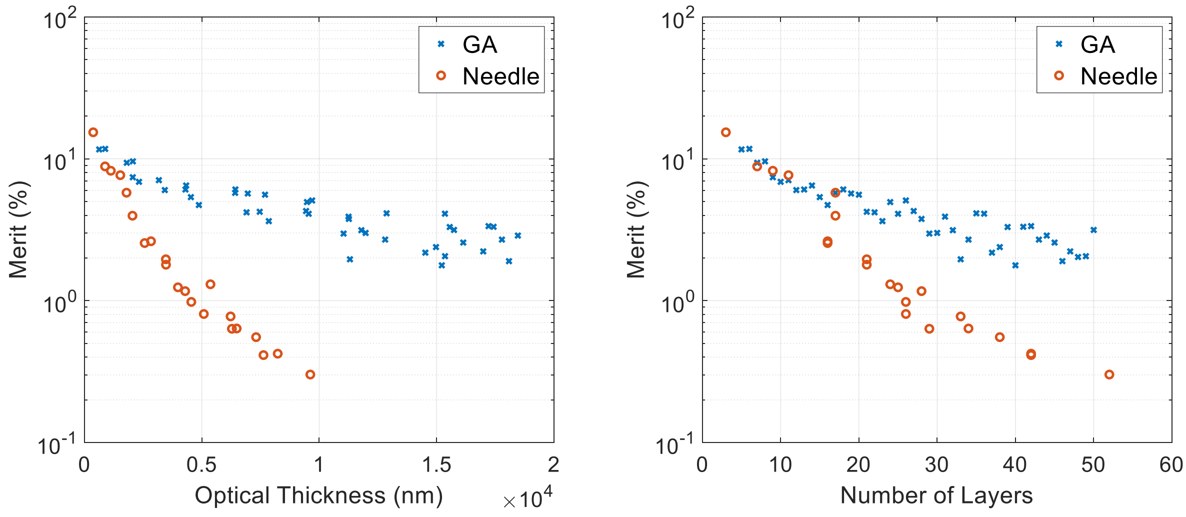

Figure 4-16: Comparison between genetic algorithm (GA) and needle optimization for multilayer synthesis and design. Merit as a function of total optical thicknesses **(a)**, and as a function of the number of layers of the resulting designs **(b)**.

There are many differences between the needle and genetic synthesis methods. Needle synthesis is based on a single device, which is modified in each iteration by means of inserting new layers, and adjusting the optical thicknesses. The GA synthesis, on the other hand, requires the creation of numerous potential solutions, and each iterative step corresponds to a new set of solutions. Another important difference is that while the needle method is mainly deterministic (new layers inserted according to P(z), and refinement is gradient-based), GA uses a number of non-deterministic operators (random generation of initial population, cross-over, and mutation).

The main advantage of the genetic algorithm approach, over needle synthesis, is its flexibility. The needle synthesis method is specifically designed for a fitness function based on the mean-square difference (Eq. 4-26), which derives in the creation of the P(z) function. While the use of the P(z) function for the insertion of new layers is what makes this method so efficient, it also limits its applicability to other different merit functions. The use of a different merit function would require to re-define or derive a new P(z) function, which may not have the same behaviour and efficiency. The derivation of a new P(z) requires a deep and extensive knowledge of the mathematics and physics involved. On the other hand, the genetic algorithm can be applied to virtually any function, and requires very little information about the merit function.

For the case of this study, since the merit function for the design problem was defined as the least square-difference, the needle synthesis overperforms the other methods. What is interesting about the genetic algorithm is that the design problem can de re-defined, for example, to directly design an optical filter with respect to the performance in the final application, or to penalise the merit function regarding costs associated to materials, and production times. For the case of this work, it could allow for a single-step design of a multilayer system, according to its performance in colour apearance applications. While reducing the design problem to a single-step could allow for better solutions to be found, in the particular case of this study it was impractical, as computing the colour appearance performance of a single filter requires evaluation of the merit function for every sample within the spectral reflectance database, and the exponential increase in the number of evaluations makes computation times impractical for the scope and resources of this investigation.

Alternatively, a combination of genetic algorithm synthesis with the process of refinement can considerably improve the precision of the final design. In complex designs, the use of refinement methods is limited to the existence of adequate initial candidate solutions, however, the genetic algorithm can be used to generate candidate solutions, which can be further improved by numeric refinement. A modified version of the genetic algorithm, called memetic optimization, uses local optimization as an intermediate refinement step in order to improve the individual solutions on each generation. The quick partial refinement of individual solutions before the creation of each new generation by the evolutionary operators (cross-over, mutation) can substantially increase precision and computation speed [129], [152], [153].

4.7 FABRICATION OF MULTILAYERS *VIA* PECVD

The main objective of this section is to demonstrate the fabrication of optical filters *via* PECVD, and to evaluate their actual spectral performance in normal and oblique incidence, with respect to the spectra of the original designs. For this, three different multilayer devices were selected for fabrication, based on the binary system [SiO_2|Si_3N_4]:

- Notch filter: 27 layers, centred at 530 nm.

- Double quarter-wave with cavity: 27 layers, quarter waves centred at 480 and 560 nm, and cavity at 520 nm.

- Genetic algorithm design: 21 layers, described in a previous section (Figure 4-7, Section 4.4.2).

4.7.1 Methods

Film deposition and multilayer fabrication was undertaken in collaboration with the International Iberian Nanotechnology Laboratory (INL) [154]. Figure 4-17 shows an image of the PECVD equipment used in this work, where numbers indicate different components of the equipment:

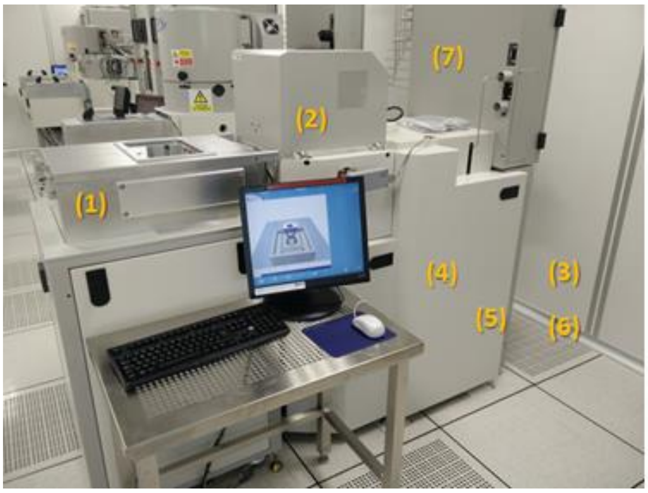

1. Double carousel loadlock (MPX).
2. Process chamber.
3. Mechanical pumps.
4. DC and RF distribution cabinet.
5. RF generators and matching units.
6. De-ionized heat exchanger.
7. Gas cabinet.

Figure 4-17: Image of STS MPX PECVD equipment, located at International Iberian Nanotechnology Laboratory (INL), Braga, Portugal.

4.7.2 Designs for manufacturing

Reflectance spectra of filters selected for manufacturing *via* PECVD are displayed in Figure 4-18, Figure 4-20 and Figure 4-22, corresponding to a notch filter (27 layers), a double quarter-wave with cavity (27 layers), and a multilayer designed by genetic algorithm (21 layers) respectively. A diagram showing the thickness and the optical path length (OPL) of each layer within the multilayers systems is shown in Figure 4-19, Figure 4-21 and Figure 4-23.

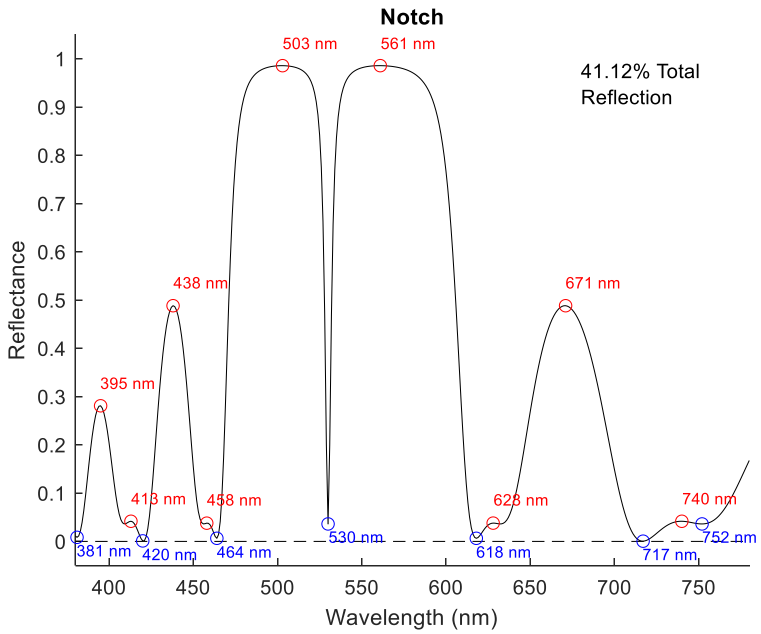

Figure 4-18: Reflectance of notch filter calculated using numerical simulation. Local maxima and minima are shown in red and blue markers respectively.

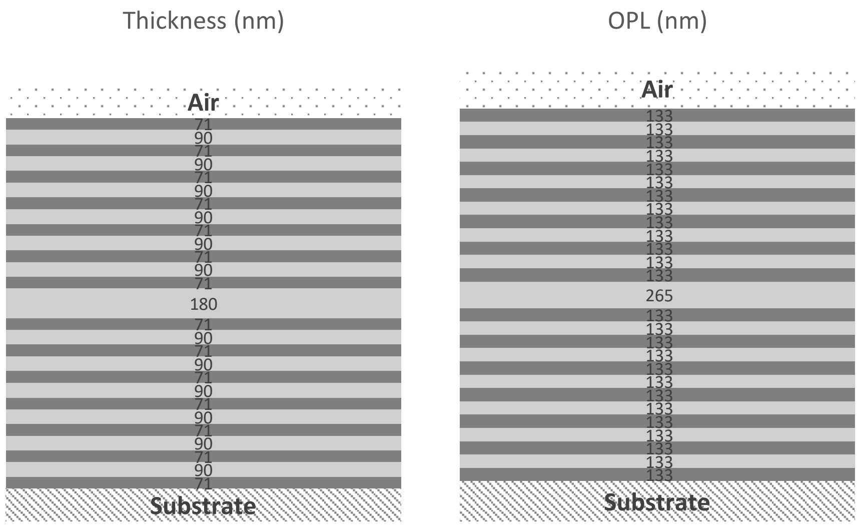

Figure 4-19: Thickness (left) and optical path length (OPL) (right) for each layer in multilayer system for Notch filter. Values displayed in nanometres.

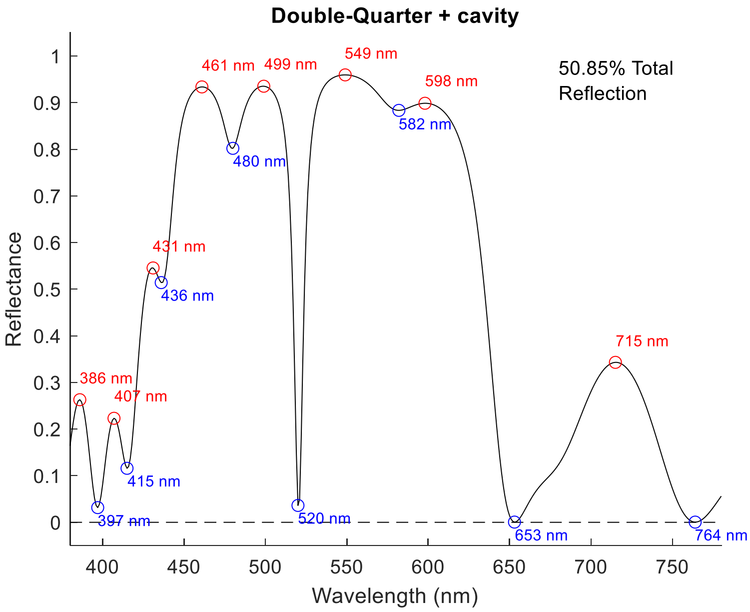

Figure 4-20: Reflectance of double-quarter-wave w/cavity (DQW) filter calculated using numerical simulation. Local maxima and minima are shown in red and blue markers respectively.

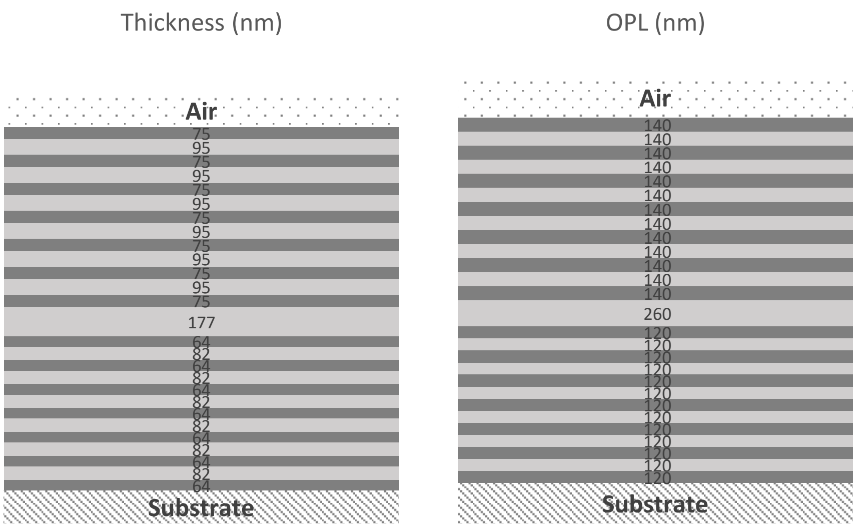

Figure 4-21: Thickness (left) and optical path length (OPL) (right) for each layer in multilayer system for DQW filter. Values displayed in nanometres.

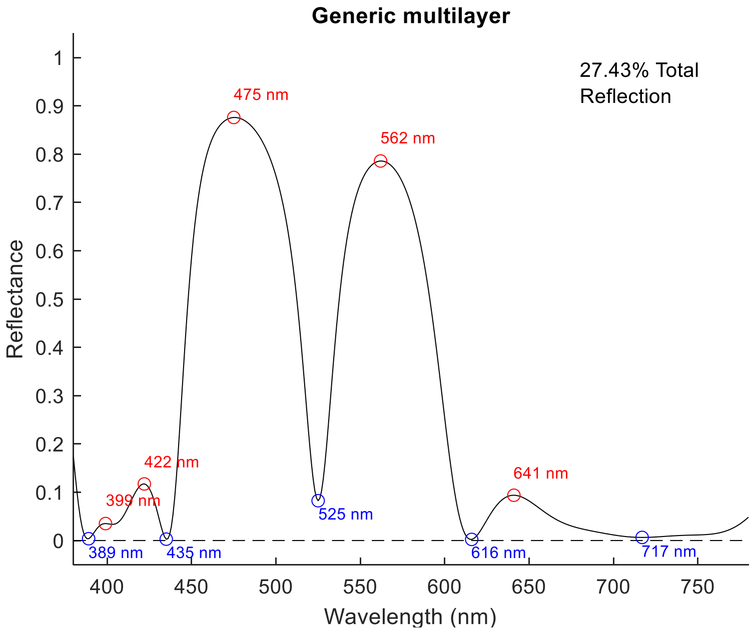

Figure 4-22: Reflectance of generic multilayer filter calculated using numerical simulation. Local maxima and minima are shown in red and blue markers respectively.

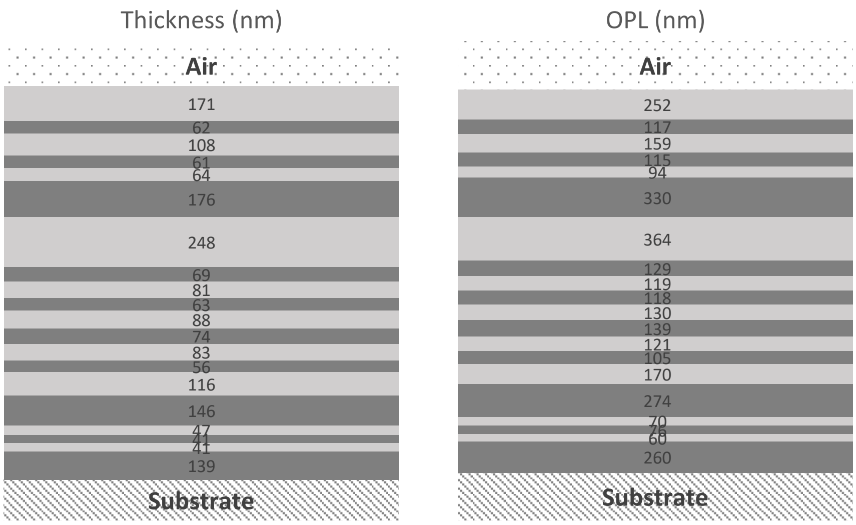

Figure 4-23: Thickness (left) and optical path length (OPL) (right) for each layer in multilayer system for generic multilayer filter. Values displayed in nanometres.

4.8 RESULTS FROM OPTICAL CHARACTERIZATION

Normal incidence reflectance was measured using a custom-made white-light epi-illumination reflectance microscope. White-light illumination, provided by tungsten lamp (Thorlabs OSL-1) is collimated and focused on the sample with an objective lens (Nikon 40x/0.75), and collected light is focussed on to an optical fibre (Thorlabs) in a confocal configuration [155]. Fourier transform image spectroscopy (FTIS) was performed using a modified configuration of the previous setup, allowing for measurement of reflectance over the whole numerical aperture, providing information on the optical properties as a function of collection angle.

4.8.1 Normal incidence

The measured and calculated spectral properties at normal incidence of the fabricated multilayer systems is presented in Figure 4-24. It can be observed in this figure that the predictive model, used in the numeric design of the multilayers, is a good match of the measured optical properties of these devices.

Some differences are observed, however, in terms of position and height of the bands. These spectral shifts are small (< 5 nm), within the expected margin of error arising from the manufacturing and measuring techniques. The difference between the measured and calculated spectral reflectance is presented in Figure 4-25.

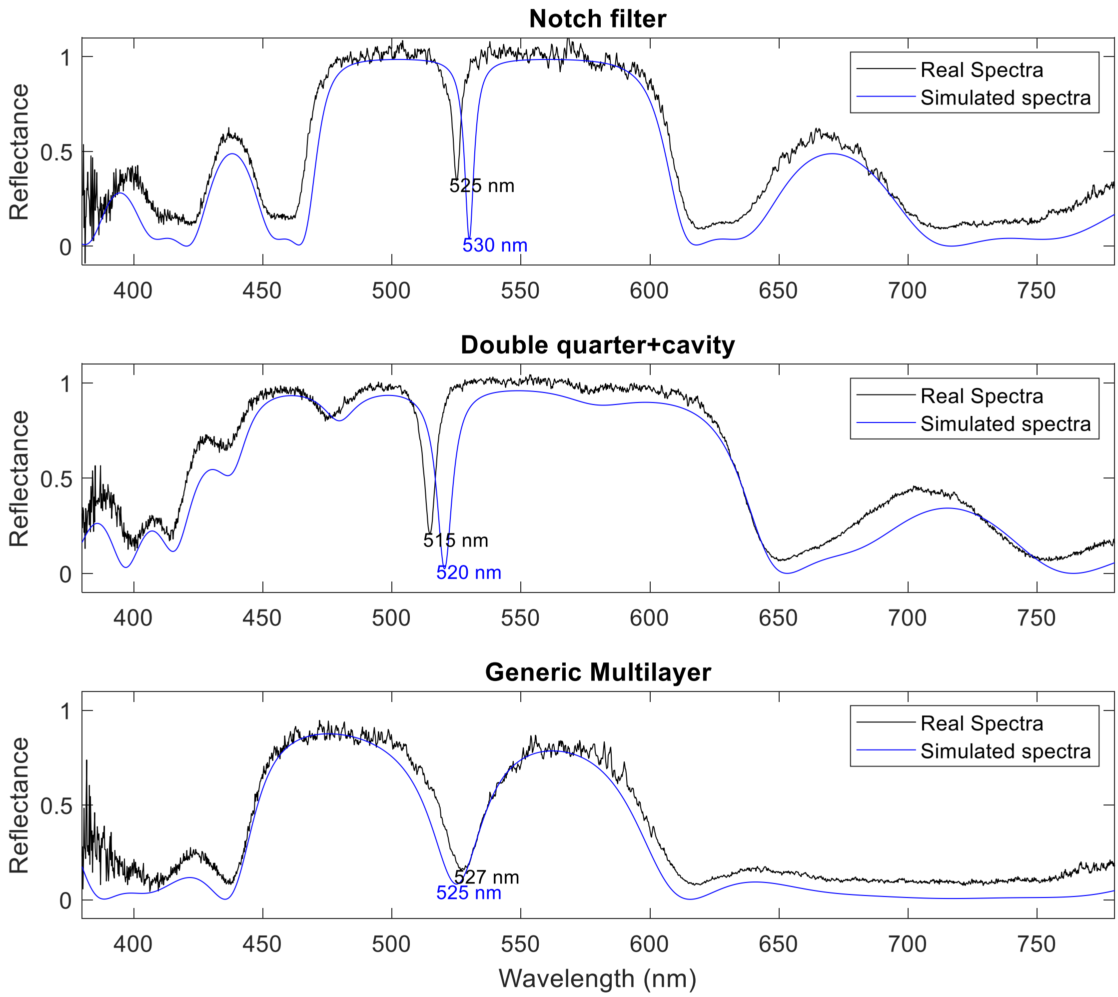

Figure 4-24: Multilayer devices spectra at normal incidence, notch filter (top), double quarter wave with cavity (centre), and generic multilayer designed by genetic algorithm (bottom). Spectra correspond to the measured reflectance (real spectra), and simulated spectra using TMM (simulated spectra).

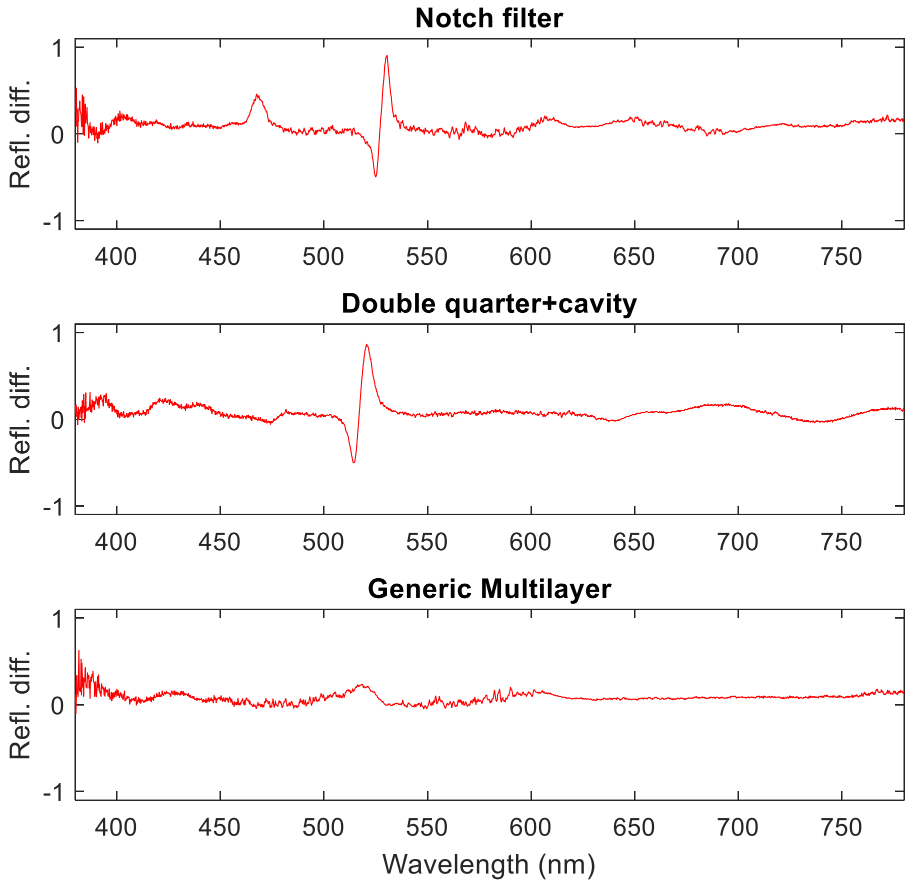

Figure 4-25: Differential spectra between the measured and simulated spectra, for notch filter (top), double quarter wave with cavity (centre), and generic multilayer designed by genetic algorithm (bottom)

4.8.2 Angle dependence

The spectral properties angle dependence of the multilayer system designed *via* the GA method is presented in Figure 4-26. The spectral properties of the multilayer measured *via* FTIS is compared to the estimated properties calculated using TMM method. The results from this comparison show a good agreement between the measured and calculated spectral properties.

When the angle of incidence increases, so does the travel time for incoming light. The geometry of the system forces oblique incident light to travel a further distance in order to go through each of the layers within the system (see Figure 4-2), and longer travel times result in the shift of the spectral properties towards the red end of the spectrum. This effect can be observed in Figure 4-26 for both the measured and calculated spectra.

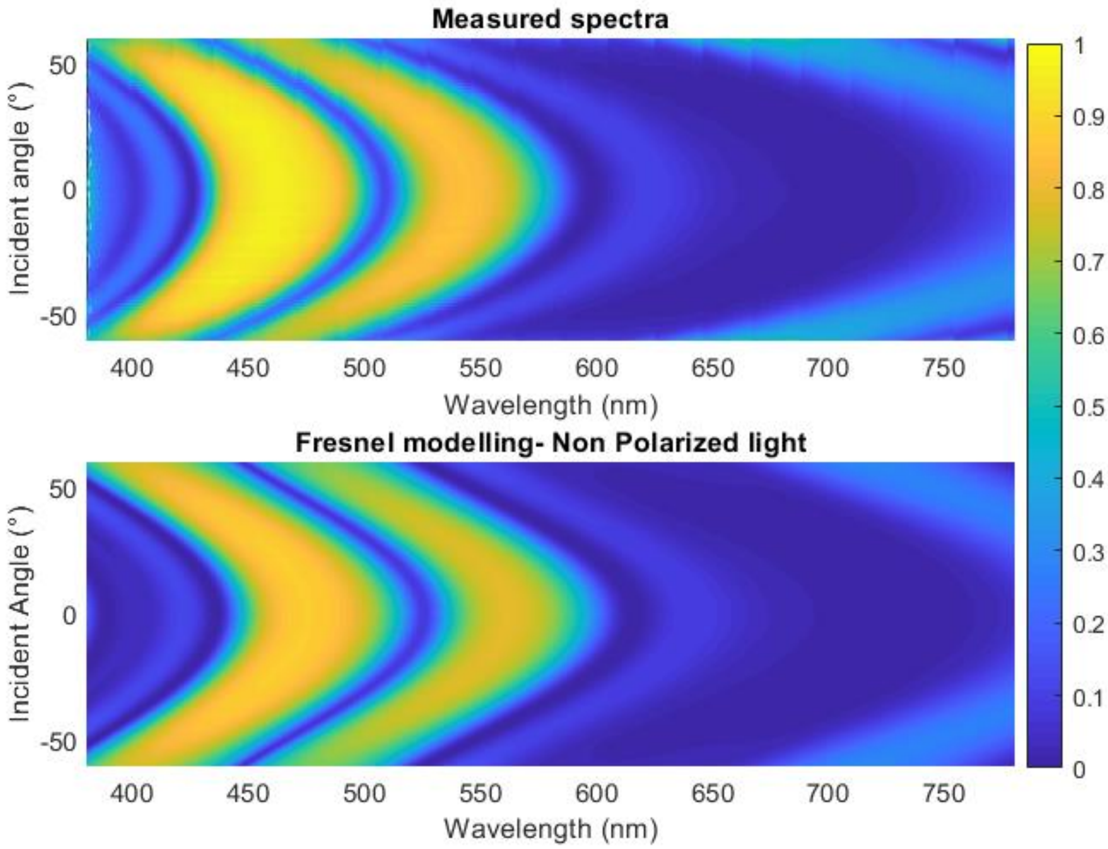

Figure 4-26: Spectral reflectance of the generic multilayer designed by genetic algorithm and fabricated *via* PECVD. Measured spectra using FITS (top), and expected spectra as calculated using TMM (bottom).

Some aberrations however can be observed in the measured spectra, specifically, spectra appear to be non-continuous with wavelength, especially for the wider angles of incidence. Figure 4-27 shows a zoomed in section of the measured spectra, displaying this continuity issues in the measured spectra. Measurement of the spectral reflectance is done in sections within the visible spectrum, every 20 nm, and the full spectrum is obtained by combining the different spectra measured in all ranges within the visible spectrum. The continuity issues are observed every 20 nm, which corresponds to a full measurement of a section of the spectrum. This is caused by an optical effect within the measuring device similar to chromatic aberration, where the wavelength dependence of the refractive index of the optical components within the device causes light at both ends of the measured spectrum to be refracted un-equally, causing misalignment between the upper and lower limits of consecutive sections of the spectrum. While this effect can be artificially corrected using image processing tools, the effect of this aberration is small, and is within the accepted precision limits for the purposes of this investigation.

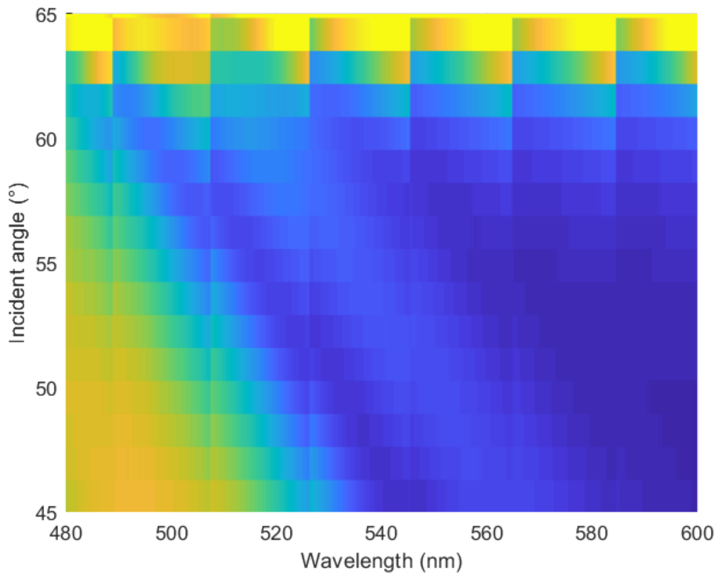

Figure 4-27: Detail of the measured spectra for generic multilayer designed by genetic algorithm showing continuity issues.

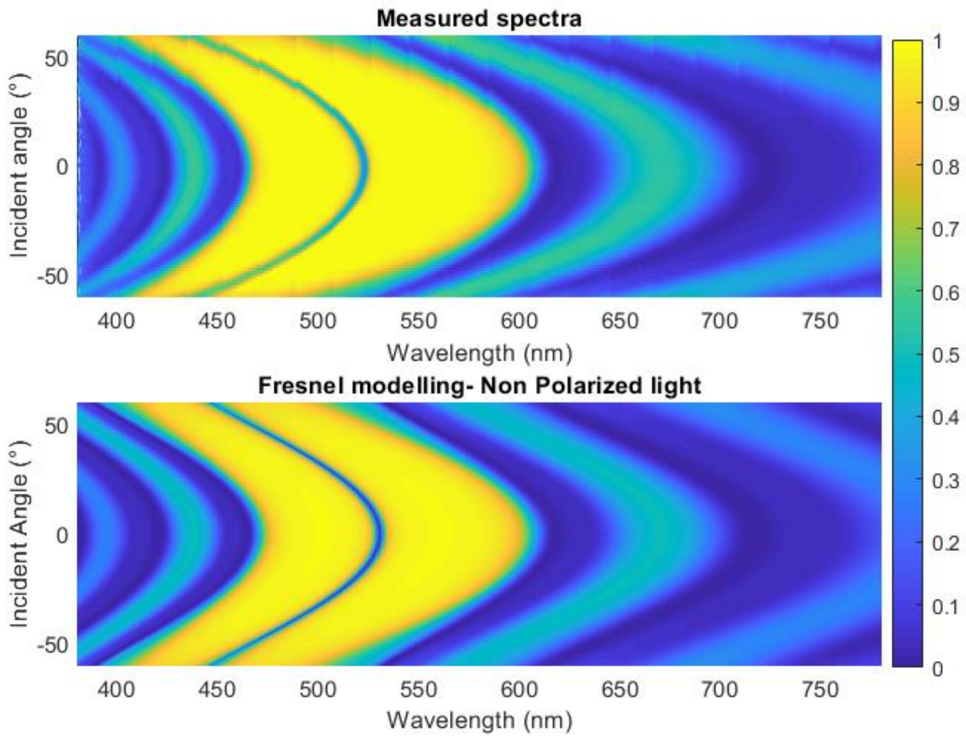

Figure 4-28: Spectral reflectance of Notch filter fabricated *via* PECVD. Measured spectra using FITS (top), and expected spectra as calculated using TMM (bottom).

The angular dependence of the notch filter is presented in Figure 4-28, for the measured and calculated spectral properties. Results from this comparison are similar to the case of the generic multilayer, there is good agreement between the predicted and measured spectral reflectance.

4.8.3 Evaluation of results and sources of error

Frequency-dependant refractive index

The refractive index of a medium is wavelength dependant. In general, the refractive index of a material increases with frequency, in other words, smaller wavelengths are deflected (or refracted) in greater extent than long wavelengths. This effect can be observed in Figure 4-29, for the materials utilized in this work in the fabrication of multilayer devices.

For the selected materials and frequency ranges (visible light) relevant to this work, it can be observed that the frequency-dependant refractive index can be relevant for wavelengths closer to the UV-range of light ($\lambda < 400\ nm$), particularly in the case of silicon nitride, and becomes less significant at longer wavelengths. For this reason, it is expected that predictions made by the model, which considers refractive index to be a wavelength/frequency independent constant, will be subject to a higher error in predictions at smaller wavelengths.

This assumption can be removed by using a vector of refractive index values corresponding to the values at different wavelengths instead of a single constant value, reducing the error associated to that assumption. A disadvantage of this, however, is that it increases the required data to run the model, increasing processing times and required memory to run the model. This increase can be very small, however, it can still be relevant for some numerical methods, such as genetic algorithm, which require evaluating the model for a large number of individuals within a population, and iterating over a sufficient number of generations.

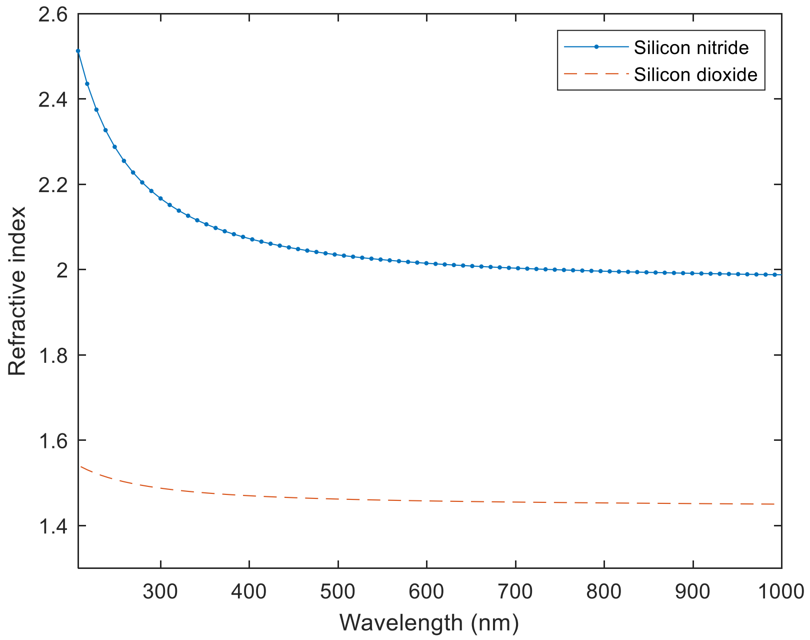

Figure 4-29: Refractive index as a function of wavelength. Fused silica (fused quartz) Malitson, 1965. Si_3N_4 (silicon nitride) Philipp, 1973. Data obtained from [156].

Real vs. reference values for refractive index

Real refractive index of the deposited material may vary with respect to the reference values obtained from literature. These differences can arise from the specific composition of the material, polymorphisms and other structural differences arising from the processing and deposition, as well as defects within the structure of the material created during deposition, such as trapped air bubbles and aggregation.

Thickness control

The real thickness of each layer within the device may vary from reference values depending on differences or estimation errors in the rate of deposition of material. While PECVD allows for high precision in the thickness control of the deposited material, small errors in various layers can be augmented to greater differences in the optical behaviour of the multilayer component, with respect to the initially estimation or design objectives.

Errors from characterization

Misalignment in angle of incidence during optical characterization. In the case of normal incidence, a deviation from the normal angle should result in a shift of the spectra towards the red end of the spectrum. This effect can be observed in Figure 4-26, where the angle dependence of the multilayer spectral properties can be observed.

4.9 FABRICATION OF COLLOIDAL CRYSTALS AND INVERSE OPAL STRUCTURES

Photonic crystals are periodic, ordered microstructures, built from an arrangement of dielectric materials, with a periodicity in the scale of visible light wavelength (~200-700 nm). Diffraction effects caused by the spatially periodic variation of the refractive index and dielectric function of these materials creates a photonic bandgap (PBG) in the visible spectrum, inhibiting or forbidding the propagation of light at certain wavelengths; analogue to the electronic bandgap in conventional semiconductors [30]–[32].

The concept of photonic bandgap structures (PBG) was first proposed by Yablonovich and John in 1987 [33], [34], and has been the subject of extensive research up to this date due to the wide field of possible applications, such as photonics [35], [36], catalysis [37], [38], chemical [39], [40] and biochemical sensing [41], [42], sensors [43], and solar energy harvesting [44], [45].

Photonic bandgap structures can be classified according to the structure's periodicity as one-dimensional (1-D), two-dimensional (2-D), or three-dimensional (3-D). The simplest form of PBG materials are 1-D thin film stacks, or Bragg reflectors, consisting of alternating thin layers of high and low refractive index materials, that display structural colour owing to thin film and multilayer interference. 2-D PBG usually consist of a regular array of dielectric rods, or periodically perforated dielectric slabs. 3-D photonic crystals on the other hand, are more complex structures. Some simple forms of 3D PBG structures are those formed by an ordered array of closed packed of colloidal particles (colloidal crystals). The case of a face centred cubic packing of colloidal spheres is known as an opal, which can be found in nature (natural opals) or artificially formed by the process of colloidal self-assembly. The case where colloidal particles are replaced by air, in a dielectric matrix is known as an inverse opal.

Colloidal self-assembly is a process of interest, due to the comparatively low cost and ease in processing for the fabrication of photonic structures. It is based on the phenomenon where colloidal particles in suspension will assemble spontaneously into ordered structures under the appropriate conditions. For example, this can be achieved by means of gravitational and centrifuged sedimentation [43] or horizontal and vertical deposition [157]–[159]. These materials are often referred to as synthetic opals, due to similarities with natural opal gems. The main challenge in the fabrication of these opal structures is to obtain large areas (in the scale of mm^2) and reduce the number of internal defects in the sample, such as vacancies, dislocations, and grain boundaries.

A similar analysis to the multilayer interaction with light can be applied to more complex, higher order 3D photonic crystals. The reflectance maximum value can be estimated according to the refractive index of the constituent materials, and to the interplanar distance between planes of reflection of the 3D structure [27]–[29]:

$$m\lambda = 2d_{hkl}\sqrt{n_{avg}^2 - \sin^2\alpha} \qquad \text{Eq. 4-33}$$

where α is the angle of incidence, d_{hkl} is the spacing between the close-packed planes (h,k,l), and n_{avg} is the average refractive index, which can be calculated from the materials volume fraction, ϕ, and lattice parameter, D:

$$n_{avg} = \phi_1 n_1 + (1-\phi_1)n_2 \qquad \text{Eq. 4-34}$$

$$d_{hkl} = \frac{D\sqrt{2}}{\sqrt{h^2+k^2+l^2}} \qquad \text{Eq. 4-35}$$

These equations illustrate how the optical properties, particularly the reflected wavelength, is related to the structure's physical parameters such as interplanar spacing (or lattice parameter) and refractive index.

4.9.1 Methods

Vertical deposition by colloidal self-assembly was selected as a manufacturing technique due its simple and straightforward methodology, as well as the relative low cost of materials and laboratory equipment required, as compared to other manufacturing techniques (*e.g.*, photolithography, chemical vapour deposition, coating techniques, *etc*.). Another great advantage of colloidal self-assembly lies in the scaling capability of the technique.

Methodology was adopted from the work by Hatton and collaborators [157], summarized in Figure 4-30. A solution was prepared containing tetraethyl orthosilicate (TEOS 98%, Aldrich) (1.07 ml), 0.1 M HCl solution (Fisher Scientific) (1 ml), and ethanol (≥99.8%, Sigma Aldrich) (1.9 ml), and left to react for 1 h at room temperature under constant stirring (1:1:1.5 weight ratio). Then, this solution is added to a PS colloidal suspension (Thermo scientific, 0.24-1.0 µm; Sigma Aldrich, 0.5 µm) (20 ml) in deionized water (0.125 wt%), and stirred for 30 min at room temperature. For polymer direct opals, methodology was the same, except that no silica precursor solution was added.

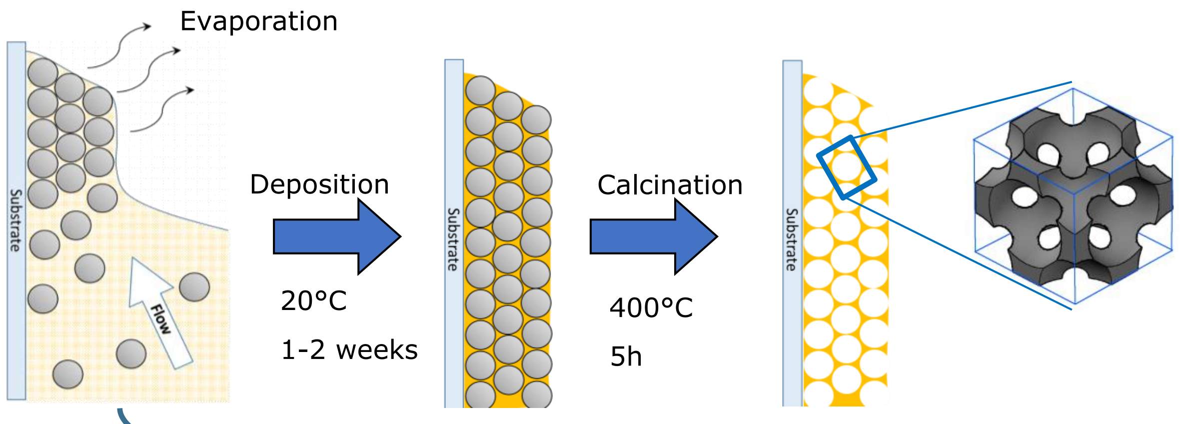

$$n\,Si(OR)_4 + 2n\,H_2O \xrightarrow{H^+} n\,Sio_2 + 2n\,R(OH)$$

Figure 4-30: Co-assembly of PS colloidal structures in a soluble silica matrix precursor, and inverse opal structure formed after colloidal template removal [157].

The optical properties of the prepared samples were studied using Diffuse reflectance UV-vis spectroscopy (Lambda 900 uv/vis/nir spectrometer) with an integrating sphere. This technique allows to determine the wavelength at which reflection/transmission is at its maximum/minimum value, which directly relates to the stopband positions of the photonic structure. Scanning electron microscopy (SEM) was used to study the microstructure, and to evaluate the level of order and periodicity of the samples.

4.9.2 Structure and optical characterization of opal and inverse opal structures

An *in-situ* optical micrograph of the colloidal self-assembly process in presented in Figure 4-31. In this horizontal deposition for a direct opal, colloidal particles are dragged to the exterior part of the liquid drop, as evaporation occurs primarily in the meniscus formed at the glass-liquid-air interface; this promotes the photonic array to grow inwards as solvent evaporates. This particular phenomena can be observed in the formation of a single ring of micrometric particles in coffee stains, and it is widely known as the “coffee ring” effect [160].

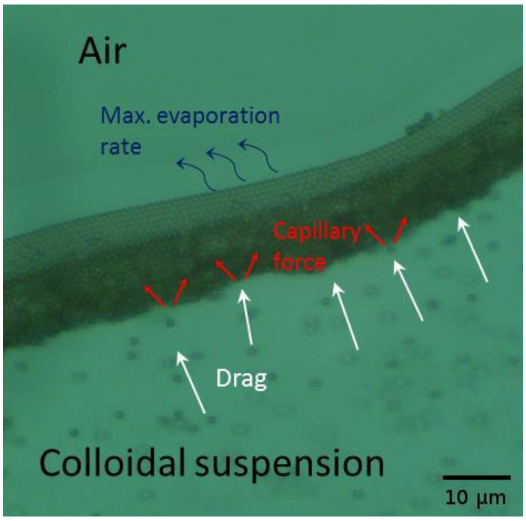

Figure 4-31: *In-situ* optical microscopy of polymer colloidal suspension (Φ=1 μm) self-assembly by horizontal deposition

Photographs of the prepared silica inverse-opals are shown in Figure 4-32. Samples exhibit iridescent behaviour, displaying different colours (or transparency) depending on the observer and the light source relative position and angle. The PS-240 nm template shows a bright green colour when observed at a slight angle, whilst the 500 nm displays an orange-red colour (Figure 4-32-a, and -b). On the other hand, 1000 nm samples show no evident colour upon reflection (Figure 4-32-c), but a wide range in colours (red-green) on transmission. Interestingly, the samples present a wrinkled pattern along the growth direction (multiple contact lines). It is well established that self-assembly in colloidal suspensions occurs by water evaporation, primarily by the “coffee ring” effect. Evaporation rate from a pinned drop is greatest at the edge or contact line, causing the solvent to flow in the direction of the contact line, dragging the colloidal particles towards the edge. When particles are close together, capillary forces act as the driving force and particles are driven towards the niches formed in the interstices of other already pinned particles, leading to the formation of an ordered array.

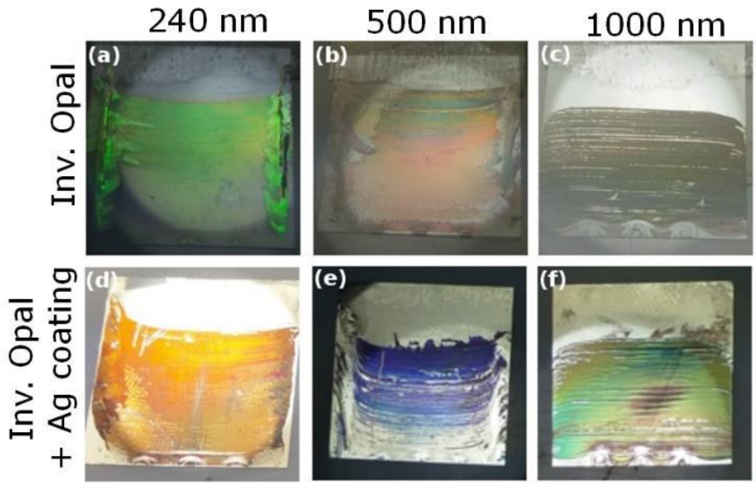

Figure 4-32: Photographs of prepared silica inverse opals (a, b, c) and silver coated silica inverse opals (d, e, f), showing angle-dependant coloration. Colloidal particle size has a direct effect on the observed colours: 240 (a, d), 500 (b, e), and 1000 nm (c, f).

An interesting effect was observed when samples were coated with a 15 nm silver layer, enhancing reflection and contrast of the samples, and shifting the reflected colour (Figure 4-32 d-f). The coated 240 nm inverse opal shows a bright orange colour, while 500 nm and 1000 nm samples show a strong blue and green colour. The addition of a metal layer, such as the Ag coating, has an evident impact on the optic behaviour of photonic crystals. Similar findings were reported by Ozin and collaborators, who found that impregnation of TiO_2/clay Bragg reflectors with silver nanoparticles, by $AgNO_3$ impregnation and $NaBH_4$ reduction, generated a red shift of ~100 nm; attributed to the increased refractive index and lattice spacing caused by the silver particles filling [161]. Additionally, it was observed that the iridescent behaviour of the device disappears, and observed colour seems to be independent of the incidence angle, which suggest that other phenomena take effect, such as plasmon resonance on the 2D periodic metal layer. However, this is yet to be verified by studying the optical spectra at different angles, and by an in-depth study of the resonant modes and plasmonic effects; all are theoretical estimations.

Figure 4-33, and Figure 4-34 present SEM images of $PS\text{-}SiO_2$ opals and inverse opals before and after calcination. It can be observed that colloidal particles assemble in a regular array with hexagonal ordering in the surface plane. As noted in the available literature, this corresponds to a FCC packing, with the (111) plane matching the material's surface [43], [157], [160].

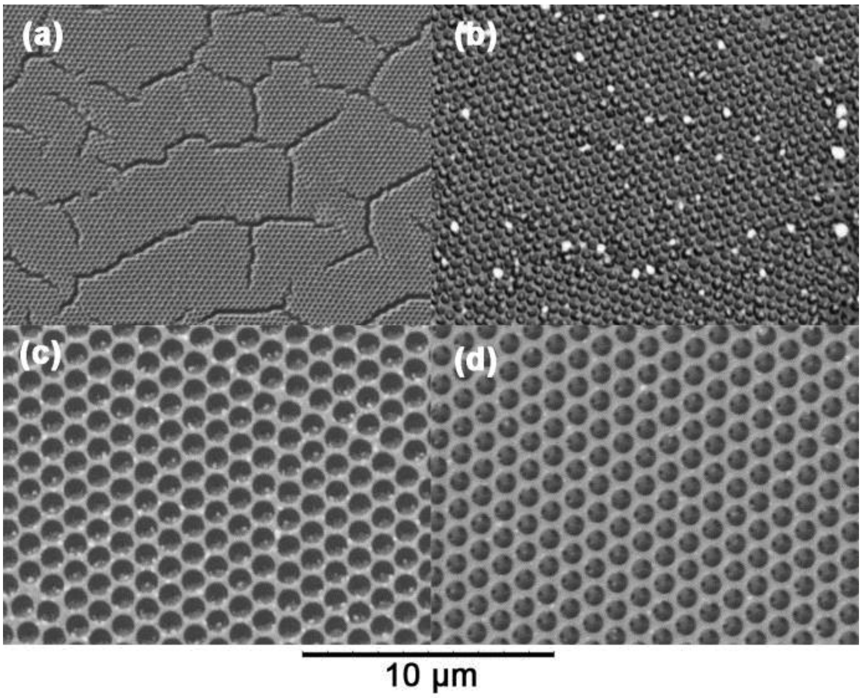

Figure 4-33: SEM images from silica inverse structures using 240nm (a), 500 nm (b), and 1000 nm (c-d) PS colloids as template.

For the smaller 240 nm colloids, micro-cracks can be observed, which could be formed due to shrinkage of the silica matrix during consolidation and drying of the gel. From optical micrography (Figure 4-34) it can be observed that these cracks run along large areas, and are aligned in parallel, and at a 60° angle with respect to each other. These correspond to the (110) planes of the FCC structure and according to the work in which this methodology was based, are expected in thick films (>20 layers) and develop during the co-assembly of silica gel and colloidal particles [157].

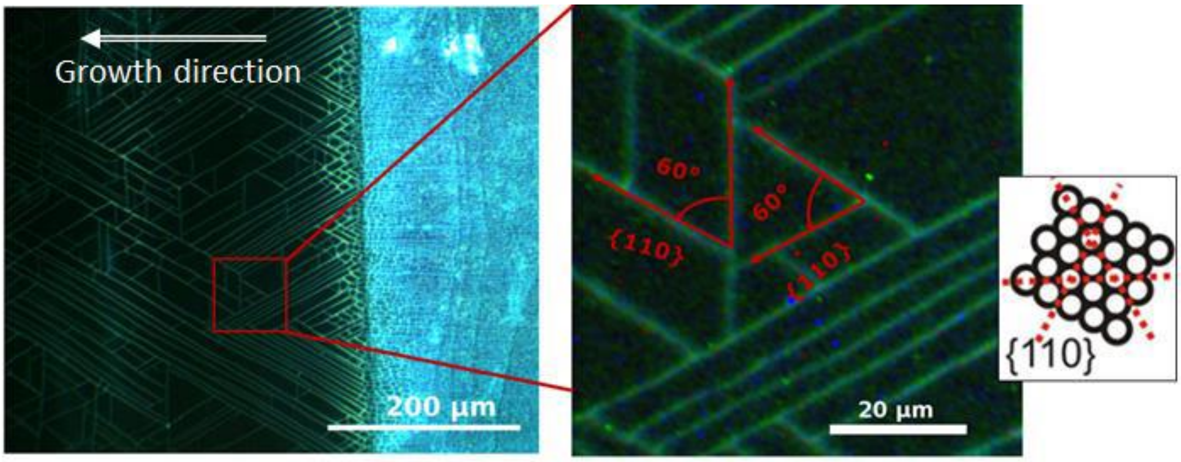

Figure 4-34: Optic microscopy of 240 nm template inverse opal showing cracks along the (110) plane.

For larger particles (≥ 500 µm) it was possible to observe smaller holes interconnecting the order mesopores of the inverse opal, as displayed in Figure 4-35. This suggests that the deposited material could form a bi-continuous composite structure if cracking of the silica phase can be eliminated. Even if cracking occurs, the air phase of the composite structure is still continuous, which is a relevant condition if the structure is going to be infiltrated on a following process, avoiding the formation of enclosed air-filled regions.

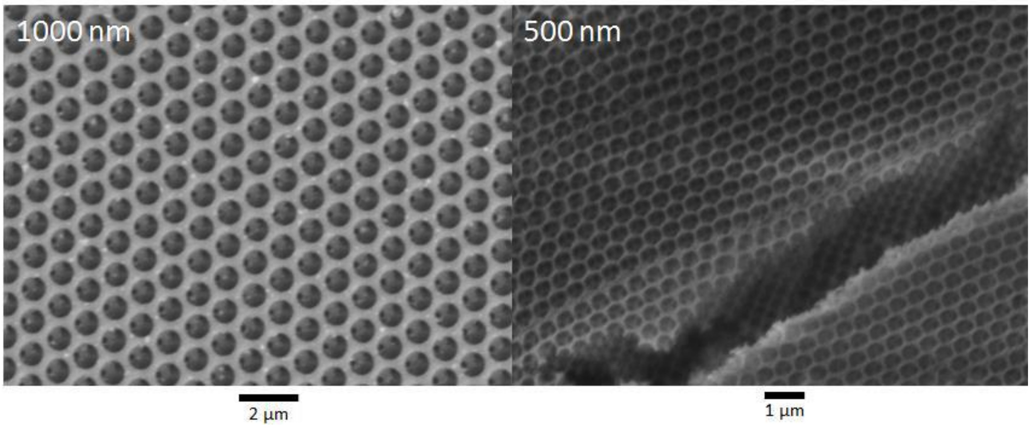

Figure 4-35: Close-up of silica inverse opals, showing fully interconnected network of micropores.

4.9.3 Optical characterization of colloidal crystal structures

The diffuse reflectance spectra of polymer opals and silica inverse opals of various colloidal template sizes is presented in Figure 4-36 and Figure 4-37. It can be observed that all samples absorb light in the ultraviolet region of the spectrum ($\lambda < 400\ nm$), which is caused by absorption on the glass substrate. On the other hand, selective absorption and reflection can be observed in different sections of the visible spectrum depending on the size of the polymer colloid template. The expected maximum reflection positions of the first three orders of Bragg reflection peaks are presented in Table 4-5, calculated using Eq. 4-33, and Eq. 4-35.

Table 4-5: Estimation of Bragg reflection maximum of polymer opals and silica inverse opals

	Plane ($h\ k\ l$)	Colloid diameter (nm)	$\lambda ref{-}max$ (nm) First Order (m=1)	Second order (m=2)	Third order (m=3)
Polystyrene opals	(1 1 1)	240	551	276	184
		310	712	356	237
		500	1149	574	383
		1000	2298	1149	766
	(1 1 0)	240	616	308	205
		310	796	398	265
		500	1283	642	428
		1000	2566	1283	855
	(1 0 0)	240	778	389	259
		310	1005	502	335
		500	1620	810	540
		1000	3241	1620	1080
Silica Inverse Opals	(1 1 1)	240	542	271	181
		310	700	350	233
		500	1130	565	377
		1000	2259	1130	753
	(1 1 0)	240	603	302	201
		310	779	390	260
		500	1257	629	419
		1000	2514	1257	838
	(1 0 0)	240	758	379	253
		310	979	490	326
		500	1579	790	526
		1000	3159	1579	1053

For the 240 nm polymer opal there is a peak in the optical spectrum around 550 nm, which corresponds to the first order Bragg reflection of the (111) planes. This value is in agreement with the observed colour of the opal (bright green). The splitting of this peak may be caused by grain border defects, with multiple grain orientations, however a more detailed analysis should be carried on in order to confirm this. For the 310 nm opal, the first order reflection of this plane is expected around 710 nm, which can be observed as a slight increment in the spectra, however it is not fully conclusive as the infrared absorption of the substrate hides the peak. The 500 nm opal present peaks around 580 and 630 nm, which are near the predicted wavelengths of the second order diffraction of the (111) and (110) planes respectively. Finally, for the larger 1000 nm opals it is not possible to distinguish any relevant peaks in the visible spectrum, as they are expected to appear at lower frequencies in the infrared region.

For the silica inverse opals, it is not possible to find the same concordance with the expected values of Bragg's reflections, and only a peak at 710 nm can be observed for the 500 nm colloid template. This can be caused by the lower refractive index contrast of silica and air, or the higher disorder caused by cracks on the silica phase.

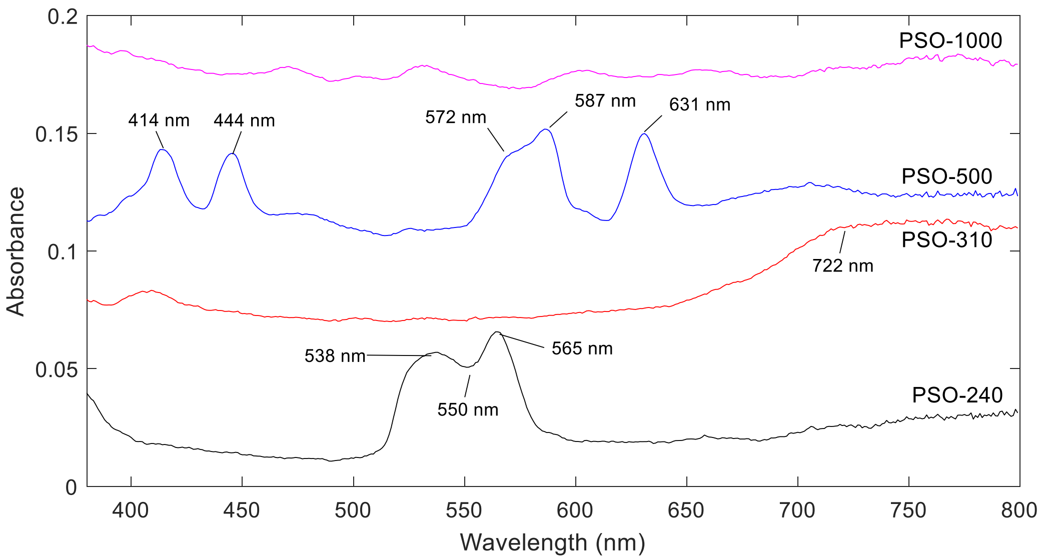

Figure 4-36: Diffuse UV/vis spectra for PS opals.

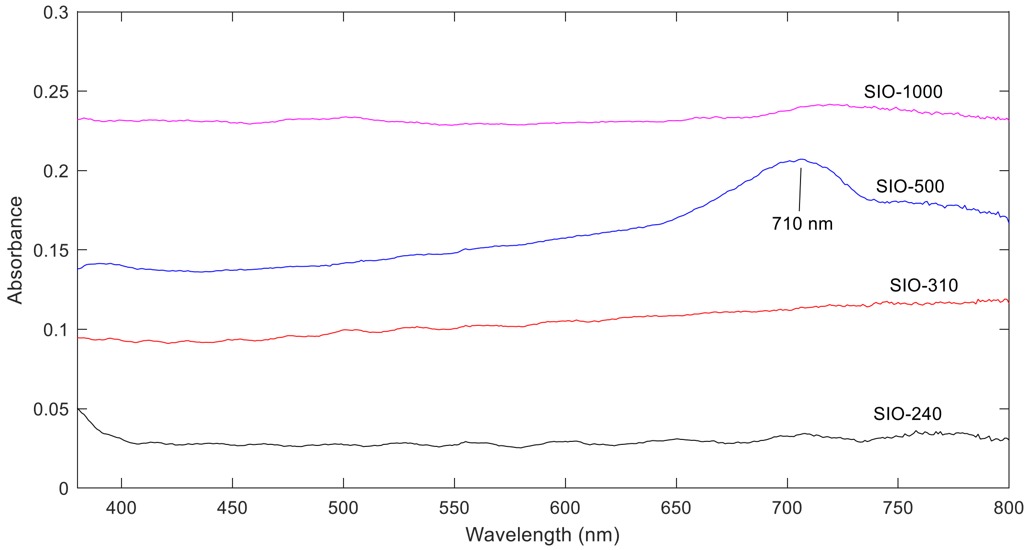

Figure 4-37: Diffuse UV/vis spectra silica inverse opals.

4.10 CONCLUSIONS AND FUTURE WORK

Optical devices based on thin film optics can be used in a variety of applications, and today most optical components include some form of thin film optic components. These components can be designed using analytical solutions to the equations describing the physics and behaviour of light when interacting with the optic component. However, when there is no known analytical solution, numerical methods based on the same equations can be implemented in order to find a numerical approximation to the solution of the design problem.

The use of numerical methods can be advantageous in cases where there is no known analytical solution, or in cases where the known analytical solutions do not completely satisfy the design requirements for the optical component. Numerical design of optical filters can be broadly classified into two categories: refinement and synthesis.

In the first, an initial candidate solution is then subjected to numerical optimization methods to improve its performance, and/or satisfy the design requirements. This straightforward process is widely employed in industry and academics, and depending on the optimization methods and initial solution, it can yield high precision and performance at low computational costs. The approach, however, is sensitive to the initial candidate solution, and finding an adequate initial solution can be problematic in complex devices.

The synthesis process, on the other hand, generates its own solutions, which can be further improved by refinement of the final design, or during intermediate steps in the synthesis process. The most prevalent synthesis process in optical filter design is the needle synthesis algorithm, which broadly consists of adding thin layers (needles) of optic material at specific locations into a system and adjusting the layer thicknesses using refinement methods. The final design is obtained by iteration of these steps. The high performance of the final designs, and fast computation, makes this a very attractive and efficient method.

While needle synthesis has become somewhat of a standard in multilayer optical filter design, other alternatives have been proposed by numerous researchers. The main disadvantage of the needle synthesis process is that it was specifically designed for optimising a specific merit function: the least square differences of the filter's spectral reflectance/transmittance, with respect to an objective. The insertion of new layers at specific optimal positions depends on a function P(z), which is specifically derived from the least squares merit function. Changing the way in which the algorithm evaluates the merit of a solution would require a new function P(z), which depending on the new merit function, may be difficult to derive and may not present the same characteristics that make the needle process so efficient.

Flexible alternatives for global search and optimization can be an attractive alternative in optical filer design. Numerical methods, such as those based on random heuristic search, are useful in problems where the defining functions are non-continuous or non-differentiable, or with local minimums, where traditional gradient-based methods can fail. These methods, however, can be computationally intensive as they require a high number of operations and evaluations of the objective function, and the balance between precision of the solution and computation time can be critical. The genetic algorithm is a type of random heuristic search based on evolutionary concepts of selection, mutation, and crossover, and was selected in this work for the numerical design of multilayer systems due to the highly non-linear nature of the optic behaviour of multilayer systems, allowing for a generic design of multilayers not subject to particular restrictions on geometric or other relations between the constituent layers within the system, and because it is a robust method to find global optimums avoiding local optima. The selection of the optimization algorithm parameters (population size, crossover fraction, function tolerance, *etc.*) is a balance between the precision of the final solution and the computational time and resources required.

Optical filters were designed using three different approaches (refinement, genetic algorithm, and needle synthesis), and compared with respect to their optical performance and effect in colour vision. While the needle synthesis method was able to produce the best results for high optical thicknesses, it was found that all three methods can produce similar results for thinner devices with a small number of layers. With respect to their performance for colour vision deficiency correction, minor differences were observed. The selection of a particular design for manufacturing should consider various factors, such as performance in the final application, material usage, robustness, *etc.*

Future work should consider modified versions of the genetic algorithm to improve performance and reduce computation times. Memetic optimization is an interesting alternative, consisting of refining individual solutions for each generation of the genetic algorithm, which can reduce convergence time and increase the performance of the final solution.

Optical multilayer systems were fabricated using plasma enhanced chemical vapour deposition (PECVD). The technique was selected for the high precision on the deposited layer thickness and geometry, and for being a well-established and accessible technique available for the purposes and resources of this investigation. Three different multilayer designs were considered and fabricated using PECVD, using silica and silicon nitride as the layer materials: a notch filter (quarter-wave stack with a half-wave cavity), a double quarter-wave stack with cavity, and a generic multilayer system designed using genetic algorithm. The spectral reflectance of the fabricated optical devices was measured for normal and oblique incidence, and are in good agreement by the predicted behaviour calculated using Rouard's recursion method. However, small differences can be observed, which can be attributed to differences between the real and expected refractive index values, potential errors in the layers thickness control during deposition, human or equipment errors during optical characterization, and other considerations not taken into account in the design and calculations, such as the frequency-dependent nature of the refractive index.

The multilayer systems designed and fabricated in this work were subject to the available fabrication methods and materials. Only systems composed of alternating layers of two different materials (silica and silicon nitride) were considered, however, the implemented numerical methods can be extended to consider systems with three or more constituent materials, while different fabrication techniques can change restrictions such as thickness and number of layers.

Multilayer optical filters are well studied, and high precision manufacturing methods are available, such as PECVD. However, the proliferation and improvement of new optical structures could allow for a new generation of optical filters. Colloidal and photonic crystals have attracted attention from researchers and industry over the past decades due to their unique optical properties. An exploratory study into the fabrication of colloidal crystals and inverse opals was presented in this work. While successful in fabricating opal and inverse opal structures *via* vertical evaporative deposition, the resulting devices presented very poor optical characteristics. Current manufacturing methods for these types of optical materials are still far from becoming a practical replacement for multilayer systems, both from the perspective of equipment cost, and performance of the fabricated devices.

CHAPTER 5: CONCLUSIONS AND FUTURE WORK

This section summarizes and highlight the essential elements that make up this work, from motivation and objectives to the main results and discussions. The objective is to put these elements into perspective from one another and discuss the conclusions that can be made from these results, including the challenges and potential improvements upon the employed methods or assumptions. The chapter is divided according to the main ideas or elements that make up this dissertation.

5.1 SUMMANRY, AND GENERAL REMARKS

The main objective of this work is to assess the potential use of frequency selective optical filters as wearable devices for chromatic enhancement and colour correction in human visual perception, establishing computational design methods based on numerical optimization for the design of these devices, and fabricating some of these using well-established deposition techniques.

Understanding the underlying biological, electrochemical, and physical mechanisms and phenomena involved in the perception of colour is the first step towards creating solutions aimed to improve colour discrimination in colour vision deficient individuals. Light is absorbed by three different cone photoreceptors in the retina, each of which is sensitive to different regions of the visible spectrum. The relative intensity of the electrochemical signals resulting from the activation of the different photoreceptors is what defines the perception of colour.

Colour vision deficiency (CVD) is a family of different conditions related to the perception of colour. Dichromacy occurs when one of the cone receptors is missing, and the chromatic information is given by the remaining two photoreceptors. In trichromatic theory, colour is described in a three-dimensional space, but this space is reduced to a two-dimensional space in dichromatic vision.

In anomalous trichromacy, all three photoreceptors are present but the sensitivity of one of these receptors is altered, having a maximum absorbance that is shifted with respect to the normal trichromat response. While in normal trichromacy the cone sensitivity curves have some degree of overlap, it is increased in the case of anomalous trichromacy, reducing the limits of the three-dimensional colour space that can be interpreted by the nervous system.

To date, there exists no definite solution for colour vision deficiency, however, some tools, devices, and experimental therapies have been used in the past and are the subject of investigation currently. Gene therapy is possibly the most promising solution and, while it has been successfully tested in mice and some non-human primates, it is unlikely to be applied in humans in the near future. Tools and devices aimed towards colour discrimination for colour vision deficient individuals include active tools, such as digital re-mapping of colour spaces, high contrast overlays, image re-colouring, *etc*., and passive devices such as wearable tinted spectacles and frequency selective filters. The effectiveness of these devices, however, is a contentious topic, and there is scarce scientific evidence for the effectiveness of these.

5.2 SIMULATION OF COLOUR VISION AND COLOUR VISION DEFICIENCY

Red-green colour vision deficiencies are the most common conditions, and up to 8% of males (0.4% in females) have some form of this condition. The cone replacement model was used for the estimation of colour matching functions in anomalous trichromats, as a linear combination of the normal cone sensitivity functions, defined by the CIE-LMS cone fundamentals, and the replacement factor, α, representing the severity of the condition ($\alpha = 0$, for normal trichromats; $\alpha = 1$, for dichromats). The model can predict the shift in the spectral sensitivity maximum of retinal and achromatic channels, observed in psychophysical experiments, while keeping consistent with dichromatic and normal trichromatic behaviour. However, the methodology relies on colour matching data from unilateral dichromats, which is assumed to be representative for both dichromatic and anomalous trichromatic perception, under the ‘reduction’ (König assumption) and ‘cone replacement’ hypotheses, respectively. While these assumptions are hard to justify rigorously due to the difficulty in comparing visual perception across individuals, they provide one of the very few working and consistent methods to model colour vision deficiency, which has been extensively used for CVD simulation in academic literature and commercial applications. The methods which derive from these assumptions, albeit their limitations, are supported by their consistency and build-up from the physiological and genetic aspects of colour vision, and further reinforced by experimental studies on the absorbance of retinal pigments.

With respect to neural image processing and interpretation, the main assumption is that while CVD affects the retinal photopigment sensitivities, the electrochemical signal output is processed by retinal and higher stages of the neural system, in the same way as normal trichromatic vision. The use of standard colorimetric methods in colour vision deficiency is debatable, and researchers generally agree that a set of individual-specific transformations and functions (opponent-space transformations, colour difference formulae, chromatic adaptation transforms, *etc.*) would be more precise and rigorous. However, deriving and calculating such transformations requires complex mathematics, intensive computations, and psychophysical testing, and thus it remains an open-ended problem. The use of standard colorimetry, while limited, allows for a direct comparison to similar studies available in the literature, is compatible with current colour displays devices and image processing software, and is in good agreement with the general expected behaviour. Besides the issues on the generalization of standard colorimetry to CVD simulation, the intrinsic limitations and error sources associated to any colorimetric standard system must be considered, such as the non-uniformity of the CIELUV and CIELAB colour spaces. A generalized colorimetric system and colour appearance models, capable of consistently and precisely predict all forms of trichromatic and dichromatic vision, represents the apex in the field of colour vision.

5.3 NUMERICAL DESIGN OF OPTICAL FILTERS AS COLOUR ENHANCING DEVICES IN ANOMALOUS TRICHROMACY

The effectiveness of colour correction optical devices for red-green anomalous trichromacy was evaluated according to the formulations of total colour difference, chroma difference, and chromaticity diversity. A numerical optimization method was implemented to find an optimum set of spectral properties for an optical filter, evaluated according to various fitness functions based on the differential perception between anomalous and normal trichromats. In particular, the method minimizes the average colour and/or chroma differences for a particular spectral reflectance database (MacBeth colour chart, Farnsworth-Munsell 100, *etc.*).

To compare the normal and anomalous perceptions, the choice of a metric is required to measure the 'similarity' of colour perception by both individuals. Visual comparison from simulated images, as well as quantifiable colour (ΔE_{uv}) and chroma difference (ΔC_{uv}) were used in this work to compare normal and anomalous trichromatic vision. While visual comparison can be useful at drawing quick conclusions, there are hard to quantify, are subjective in nature, and are influenced by external factors such as illumination, or the nature of the media in which the images are presented (*e.g.,* brand and settings of a computer monitor, or the type of paper and ink in a printed version). On the other hand, colour difference metrics have the advantage of having simple formulation, and are intended to produce a uniform chromaticity space (see Sections 3.4.3 and 3.7). This metric, however, is applicable to small colour differences, and are unable to reliably predict results from psychophysical experiments when dealing with large differences in colour perception. When comparing normal and anomalous trichromatic vision, the values calculated by the ΔE_{uv} are large, and increase for higher replacement factor values, α.

The topic of distance metrics for large colour differences is still a topic of research. Abasi, Tehran, and Fairchild published a study comparing predictions for large colour differences in psychophysical experiments, using CIELAB, CIEDE2000, and non-Euclidean metrics [84]. They concluded that both CIELAB and CIEDE2000 were unreliable to predict the expected results from visual observations, and the best results were obtained metrics which considered lightness as a separated element. They concluded that the best performing metric for large colour differences is a hybrid metric, consisting of the sum between the chroma Euclidean distance, and the absolute value for lightness difference ($|\Delta L| + \sqrt{(\Delta a^*)^2 + (\Delta b^*)^2}$). While the issue of large colour differences was not formally addressed in this work, the combined use of Euclidean colour and chroma differences allowed for a better understanding in the differences between normal and anomalous trichromatic vision. In addition, the proposed methodology for filter design was based on chroma differences, which is independent of lightness. Future work should include a more in-depth analysis and testing for the selection of an adequate metric for colour differences between normal and anomalous colour vision.

It was found that, in general, stop-bands in the overlap regions between the cone sensitivity functions (~475 and 560 nm, depending on type and severity of the condition) can help to reduce the difference between the normal and anomalous trichromat by filtering out the redundant information captured by both cone photoreceptors. This improvement is small, and imperceptible to most observers. It is possible, however, to create filters that selectively improve colour perception, in a magnitude that is perceptible to the average observer, by optimizing the square (or higher powers) of the colour and chroma differences. This will improve colours which are further away from the normal trichromat value, but can be detrimental for other colours, and for the global average. With respect to the chromatic diversity, it was found that while the total number of discernible colours cannot be increased for the full spectrum, these optical filters are able to significantly increase the average saturation value, and the relative area in the chromaticity diagram, for a subspace defined by a given set of spectral reflective samples. Considering that the spectrum profiles of most natural, or artificial, scenes are not composed of monochromatic stimuli, but rather by smooth-continuous spectrums, these results support the idea that optical filters can positively influence colour perception and discrimination for red-green CVD observers in natural scenes. In particular, the design of optical filters for specific applications where there is a reduced number of relevant colours, for example, improving discrimination between red and green, which can be useful in applications such as fruit selection by visual inspection, or improving visual acuity in outdoors activities by enhancing contrast of natural foliage.

5.4 NUMERICAL DESIGN OF MULTILAYER OPTICAL FILTERS

Optical filter design methods were implemented and utilized to generate multilayer optical systems that present spectral profiles in accordance with the results from the CVD correction optimization. Three different numerical design approaches were taken into consideration: refinement of an initial candidate solution, needle synthesis, and genetic algorithm synthesis. These seek to minimize a merit function, given by the average square differences between the objective filter, given by the CVD correction optimization results, and the actual spectral profile of the multilayer system, estimated by the methods and equations of optics and electromagnetic theory. The choice of materials and boundary conditions used in the design of optical filters are strictly limited by the availability and technical capabilities of manufacturing technologies. Binary silica/silicon nitride systems were designed, and later fabricated *via* plasma-enhanced chemical vapour deposition (PECVD). The objective spectral profile was selected from the optimization of the fourth power chroma difference ($\overline{\Delta C_{uv}^{*}}^{4}$), for a deuteranomalous observer ($\alpha = 0.9$), in D65 illumination. The transmission spectra of this objective is made-up two stopband regions centred at approximately 475 and 560 nm, and a band-pass centred at 525 nm.

With respect to the numerical design methods, similar results were obtained for a reduced number of layer and optical thicknesses in all three design strategies. The refinement strategy, while it is a straightforward and simple approach, it can generate high precision optic components from an adequate initial solution, but the sensitivity to the choice in this initial solution makes the method impractical for complex design problems. In this study, the similarity of the objective profile to a conventional band-pass filter makes the choice of an initial candidate solution a relatively simple task. Optical filters were designed by numerical refinement from a quarter-wave reflector, band-pass notch filter, and a double-stack of quarter wave reflectors.

Using needle synthesis, the highest performing designs were produced. This is the most prevalent method in the field of optical filter design, consequence of its computational efficiency, and generation of very accurate spectral profiles. The optical power of a filter, represented by its total optical thickness, is a limiting variable to the merit function's value, and the required optical thickness increases exponentially in order to achieve a higher performance.

The genetic algorithm (GA) is a random heuristic search method based on the concepts of natural selection, genetic heritage, and mutation. It is used as a global optimisation method due to its capability of handling non-continuous, non-differentiable functions, avoiding local minimums. Optical filter design by GA synthesis was implemented to minimize the merit function in terms of the filter's optical thickness vector. The number of independent variables in the optimisation problem is determined by the number of layers, which is a user-determined set value. The function's domain is given by the upper and lower boundaries, which are determined by manufacturing considerations. The total optical thickness is mainly determined by the total number of layers, and it's correlated to the merit value in the form of a power law. Similar to needle synthesis, the decrease of the merit value requires an exponential increase in the total optical thickness. While results from GA and needle synthesis similar at a small number of layers (~20 layers), needle synthesis largely outperforms GA when producing high optical power devices. The computational costs of GA significantly increase with number of variables, affecting the precision of the solution. These costs can be partially compensated reducing the size of the search space, using a small, but representative, set of boundary conditions. The main advantage of the GA approach is its flexibility, which can be used in optical filter design to alter the way in which performance is evaluated, through the merit function. This flexibility can allow to design optical devices according to various design requirements and expectations, such as robustness, in terms of layer thickness or angle of incidence, or to directly design for colour perception attributes.

It is important to note that the final design of a multilayer system for colour correction in anomalous trichromats is the result of two consecutive numerical optimization processes, first calculating the ideal spectral properties for a filter minimizing the average difference between normal and anomalous trichromacy, and subsequently designing a multilayer system with spectral properties as close as possible to the objective spectral properties set previously. It can be possible to integrate both sections of the design in a single optimization process, finding a multilayer system that optimizes colour perception attributes. However, the computational resources and computation times required increase significantly, as every candidate solution in each iteration of the genetic algorithm is evaluated according to the objective function, and each iteration in the colour perception optimization is evaluated for every sample in the selected spectral database. One advantage to considering a single optimization step is the possibility of evaluating certain aspects of the multilayer system that can alter colour perception. For example, this work considers a state of adaptation generated by the optical filter defined in terms of the normal incidence spectral properties, when it could be considered that the tristimulus values for the reference white is some form of integral function of the filter spectral transmittance with respect to the angle of incidence, or estimated as the chromaticity of a perfect reflecting diffuser observed at specific angle of incidence.

5.5 OPTICAL FILTER FABRICATION

Optical filters were fabricated using plasma enhanced chemical vapour deposition (PECVD) of silica and silicon nitride. The resulting spectral properties are in good agreement with the expected behaviour, with small differences that can be attributed to differences between the real and reference values for refractive index and layer thickness, as well as possible human and equipment errors in the characterization methods, and considerations not taken into account such as the frequency dependence of the refractive index. The fabricated multilayer is contrasted to a notch filter, and a double quarter-wave with a half-wave cavity, which are well known periodic or semi-periodic structures used commonly as narrow band-pass filters.

Other optical structures were explored as blue-sky alternatives to multilayer systems. Three-dimensional photonic and colloidal structures were studied for the potential use as frequency selective devices. Synthetic polystyrene opals and silica inverse opals were fabricated by colloidal self-assembly in a vertical deposition setup. The resulting structures, while displaying iridescent behaviour, had very poor optical power and performance. Although some of the deposited areas showed a high degree of arrangement, the macroscopic quality of the depositions was affected by gain boundaries and crack formation, making these unsuitable for the application of wearable colour correction devices. The main appeal for colloidal crystals produced by self-assembly is that it is an inexpensive and simple process for producing optical systems. Further investigation and testing on the methods, materials, and conditions for colloidal self-assembly is recommended, with the objective to produce high optical-power, and macroscopic quality in colloidal crystals.

REFERENCES

[1] EnChroma, “How EnChroma glasses work,” 2018. https://enchroma.com/ (accessed May 15, 2019).

[2] Wikimedia Commons, “Free media repository,” 2018. https://commons.wikimedia.org/ (accessed May 19, 2019).

[3] Eupedia, “Social & economic maps of Europe,” 2019. https://www.eupedia.com/europe/economic_maps_of_europe.shtml (accessed May 15, 2019).

[4] Colblindor, “Coblis- Color blindness simulator,” 2018. https://www.color-blindness.com/coblis-color-blindness-simulator/ (accessed May 15, 2019).

[5] M. Fairchild, *Color appearance models*, Third Edit. John Wiley & Sons, Ltd, 2013.

[6] Charles Retina Institute, “Eye anatomy- The retina,” 2019. https://charlesretina.com/eye-anatomy-retina/ (accessed Oct. 28, 2019).

[7] X. G. Troncoso, S. L. Macknik, and S. Martinez-Conde, “Vision’s first steps: Anatomy, physiology, and perception in the retina, lateral geniculate nucleus, and early visual cortical areas,” in *Visual Prosthetics*, Boston, MA: Springer US, 2011, pp. 23–57.

[8] B. B. Boycott and J. E. Downling, “Organization of the primate retina: Light microscopy, with an appendix: A second type of midget bipolar cell in the primate retina,” *Philos. Trans. R. Soc. Lond. B. Biol. Sci.*, vol. 255, no. 799, pp. 109–184, Mar. 1969, doi: 10.1098/rstb.1969.0004.

[9] L. Hofmann and K. Palczewski, “Advances in understanding the molecular basis of the first steps in color vision,” *Prog. Retin. Eye Res.*, vol. 49, pp. 46–66, Nov. 2015, doi: 10.1016/j.preteyeres.2015.07.004.

[10] R. K. Crouch, “The visual cycle: Generation of 11-cis retinal for photoreceptors,” *American Society for Photobiology*, 2009. http://photobiology.info/Crouch.html (accessed Nov. 05, 2019).

[11] S. Miyazono, Y. Shimauchi-Matsukawa, S. Tachibanaki, and S. Kawamura, “Highly efficient retinal metabolism in cones.,” *Proc. Natl. Acad. Sci. U. S. A.*, vol. 105, no. 41, pp. 16051–6, 2008, doi: 10.1073/pnas.0806593105.

[12] M. Neitz, “Molecular genetics of color vision and color vision defects,” *Arch. Ophthalmol.*, vol. 118, no. 5, p. 691, 2012, doi: 10.1001/archopht.118.5.691.

[13] S. S. Deeb, “Molecular genetics of color-vision deficiencies,” *Vis. Neurosci.*, vol. 21, no. 3, pp. 191–196, May 2004, doi: 10.1017/S0952523804213244.

[14] S. S. Deeb and A. G. Motulsky, “Color vision defects,” *Emery Rimoin’s Princ. Pract. Med. Genet.*, pp. 1–17, 2013, doi: 10.1016/B978-0-12-383834-6.00142-7.

[15] J. Neitz and M. Neitz, “The genetics of normal and defective color vision,” *Vision Res.*, vol. 51, no. 7, pp. 633–651, Apr. 2011, doi: 10.1016/j.visres.2010.12.002.

[16] L. T. Sharpe, A. Stockman, H. Jägle, H. Knau, G. Klausen, A. Reitner, and J. Nathans,, “Red, green, and red-green hybrid pigments in the human retina: correlations between deduced protein sequences and psychophysically measured spectral sensitivities.,” *J. Neurosci.*, vol. 18, no. 23, pp. 10053–10069, 1998.

[17] M. P. Simunovic, “Colour vision deficiency,” *Eye*, vol. 24, no. 5, pp. 747–755, 2010, doi: 10.1038/eye.2009.251.

[18] G. Machado, “A model for simulation of color vision deficiency and a color contrast enhancement technique for dichromats,” Universidade Federal do Rio Grande do Sul, 2010.

[19] A. Popleteev, N. Louveton, and R. McCall, “Colorizer: Smart glasses aid for the colorblind,” *Proc. 2015 Work. Wearable Syst. Appl.*, pp. 7–8, 2015, doi: 10.1145/2753509.2753516.

[20] J. C. Maxwell, “XVIII.—Experiments on colour, as perceived by the eye, with remarks on colour-blindness,” *Trans. R. Soc. Edinburgh*, vol. 21, no. 02, pp. 275–298, Jan. 1857, doi: 10.1017/S0080456800032117.

[21] S. Deeb and A. Motulsky, “Red-green color vision defects,” pp. 1–33, 2015, Accessed: Feb. 20, 2017. [Online]. Available: https://www.ncbi.nlm.nih.gov/books/NBK1301/?report=reader.

[22] L. Gómez-Robledo, E. M. Valero, R. Huertas, M. A. Martínez-Domingo, and J. Hernández-Andrés, “Do EnChroma glasses improve color vision for colorblind subjects?,” *Opt. Express*, vol. 26, no. 22, p. 28693, Oct. 2018, doi: 10.1364/OE.26.028693.

[23] K. Mancuso, W. W. Hauswirth, Q. Li, T. B. Connor, J. A. Kuchenbecker, M. C. Mauck, J. Neitz, and M. Neitz, “Gene therapy for red-green colour blindness in adult primates,” *Nature*, vol. 461, no. 7265, pp. 784–787, 2009, doi: 10.1038/nature08401.

[24] M. Neitz and J. Neitz, “Curing color blindness-mice and nonhuman primates,” *Cold Spring Harb. Perspect. Med.*, vol. 4, no. 11, pp. a017418–a017418, Nov. 2014, doi: 10.1101/cshperspect.a017418.

[25] J. Bennett, “Gene therapy for color blindness,” *N. Engl. J. Med.*, vol. 361, no. 25, pp. 2483–2484, Dec. 2009, doi: 10.1056/NEJMcibr0908643.

[26] D. W. Prather, S. Shi, A. Sharkawy, J. Murakowski, and G. J. Schneider, “Photonic crystal technologies: From theories to practice,” in *Photonic Bandgap Structures Novel Technological Platforms for Physical, Chemical and Biological Sensing*, M. Pisco, A. Cusano, and A. Cutolo, Eds. Bentham Science Publishers, 2012, pp. 49–83.

[27] C. I. Aguirre, E. Reguera, and A. Stein, “Tunable colors in ppals and inverse opal photonic crystals,” *Adv. Funct. Mater.*, vol. 20, no. 16, pp. 2565–2578, Aug. 2010, doi: 10.1002/adfm.201000143.

[28] H. Wang and K.-Q. Zhang, "Photonic crystal structures with tunable structure color as colorimetric sensors.," *Sensors (Basel).*, vol. 13, no. 4, pp. 4192–213, Jan. 2013, doi: 10.3390/s130404192.

[29] D. P. Josephson, M. Miller, and A. Stein, "Inverse opal SiO_2 photonic crystals as structurally-colored pigments with additive primary colors," *Zeitschrift für Anorg. und Allg. Chemie*, vol. 640, no. 3–4, pp. 655–662, Mar. 2014, doi: 10.1002/zaac.201300578.

[30] C. López, "Materials aspects of photonic crystals," *Adv. Mater.*, vol. 15, no. 20, pp. 1679–1704, Oct. 2003, doi: 10.1002/adma.200300386.

[31] J. Ge and Y. Yin, "Responsive photonic crystals.," *Angew. Chem. Int. Ed. Engl.*, vol. 50, no. 7, pp. 1492–522, Feb. 2011, doi: 10.1002/anie.200907091.

[32] C. Ciminelli, "Theoretical background of photonic cystals: Bandgap and dispersion properties," in *Photonic Bandgap Structures: Novel Technological Platforms for Physical, Chemical and Biological Sensing*, M. Pisco, A. Cusano, and A. Cutolo, Eds. BENTHAM SCIENCE PUBLISHERS, 2012, pp. 2–22.

[33] S. John, "Strong localization of photons in certain disordered dielectric superlattices," *Phys. Rev. Lett.*, vol. 58, no. 23, pp. 2486–2489, Jun. 1987, doi: 10.1103/PhysRevLett.58.2486.

[34] E. Yablonovitch, "Inhibited spontaneous emission in solid-State physics and electronics," *Phys. Rev. Lett.*, vol. 58, no. 20, pp. 2059–2062, May 1987, doi: 10.1103/PhysRevLett.58.2059.

[35] J. D. Joannopoulos, P. R. Villeneuve, and S. Fan, "Photonic crystals: putting a new twist on light," *Nature*, vol. 386, no. 6621, pp. 143–149, Mar. 1997, doi: 10.1038/386143a0.

[36] J. D. Joannopoulos, S. G. Johnson, J. N. Winn, and R. D. Meade, *Photonic crystals: Molding the flow of light*, Second Edi. Princeton, NJ: Princeton University Press, 2008.

[37] G. Guan, "Preferential CO oxidation over catalysts with well-defined inverse opal structure in microchannels," *Int. J. Hydrogen Energy*, vol. 33, no. 2, pp. 797–801, Jan. 2008, doi: 10.1016/j.ijhydene.2007.10.054.

[38] M. Ren, R. Ravikrishna, and K. T. Valsaraj, "Photocatalytic degradation of gaseous organic species on photonic band-gap titania," *Environ. Sci. Technol.*, vol. 40, no. 22, pp. 7029–7033, Nov. 2006, doi: 10.1021/es061045o.

[39] Y.-J. Lee and P. V. Braun, "Tunable inverse opal hydrogel pH sensors," *Adv. Mater.*, vol. 15, no. 78, pp. 563–566, Apr. 2003, doi: 10.1002/adma.200304588.

[40] I. Burgess, M. Lončar, and J. Aizenberg, "Structural colour in colourimetric sensors and indicators," *J. Mater. Chem. C*, vol. 1, no. 38, p. 6075-6086, 2013, doi: 10.1039/c3tc30919c.

[41] S. A. Asher, V. L. Alexeev, A. V. Goponenko, A. C. Sharma, I. K. Lednev, C. S. Wilcox, and D. N. Finegold, "Photonic crystal carbohydrate sensors: low ionic strength sugar sensing.," *J. Am. Chem. Soc.*, vol. 125, no. 11, pp. 3322–9, Mar. 2003, doi:

10.1021/ja021037h.

[42] M. Kamenjicki and S. A. Asher, “Epoxide functionalized polymerized crystalline colloidal arrays,” *Sensors Actuators B Chem.*, vol. 106, no. 1, pp. 373–377, Apr. 2005, doi: 10.1016/j.snb.2004.08.018.

[43] Y. Nishijima, K. Ueno, S. Juodkazis, V. Mizeikis, H. Misawa, T. Tanimura, and K. Maeda,, “Inverse silica opal photonic crystals for optical sensing applications,” *Opt. Express*, vol. 15, no. 20, p. 12979, 2007, doi: 10.1364/OE.15.012979.

[44] S. F. Leung, M. Yu, Q. Lin, K. Kwon, K. L. Ching, L. Gu, K. Yu, and Z. Fan,, “Efficient photon capturing with ordered three-dimensional nanowell arrays,” *Nano Lett.*, vol. 12, no. 7, pp. 3682–3689, 2012, doi: 10.1021/nl3014567.

[45] Y. Yu, L. Wen, S. Song, and Q. Chen, “Transmissive/reflective structural color filters: Theory and applications,” *J. Nanomater.*, vol. 2014, pp. 1–17, 2014, doi: 10.1155/2014/212637.

[46] M. E. Calvo, S. Colodrero, T. C. Rojas, J. A. Anta, M. Ocaña, and H. Míguez, “Photoconducting Bragg mirrors based on TiO_2 nanoparticle multilayers,” *Adv. Funct. Mater.*, vol. 18, no. 18, pp. 2708–2715, Sep. 2008, doi: 10.1002/adfm.200800039.

[47] K. Kordás, S. Beke, A. E. Pap, A. Uusimäki, and S. Leppävuori, “Optical properties of porous silicon.,” *Opt. Mater. (Amst).*, vol. 25, no. 3, pp. 257–260, Apr. 2004, doi: 10.1016/S0925-3467(03)00254-4.

[48] D. B. Judd, “Fundamental studies of color vision from 1860 to 1960,” *Proc. Natl. Acad. Sci. U. S. A.*, vol. 55, no. 6, pp. 1313–1330, 1966, doi: 10.1073/pnas.55.6.1313.

[49] B. B. Lee, “The evolution of concepts of color vision.,” *Neurociências*, vol. 4, no. 4, pp. 209–224, Jul. 2008, [Online]. Available: http://www.ncbi.nlm.nih.gov/pubmed/21593994.

[50] R. M. Boynton, “History and current status of a physiologically based system of photometry and colorimetry,” *J. Opt. Soc. Am. A*, vol. 13, no. 8, p. 1609, Aug. 1996, doi: 10.1364/JOSAA.13.001609.

[51] R. W. G. Hunt and M. R. Pointer, *Measuring colour*. Chichester, UK: John Wiley & Sons, Ltd, 2011.

[52] D. H. Brainard and A. Stockman, “Colorimetry,” *Opt. Soc. Am. Handb. Opt. 3rd Ed. Vol. III Vis. Vis. Opt.*, pp. 10.1-10.56, 2010.

[53] H. Grassmann, “Zur theorie der farbenmischung,” *Ann. der Phys. und Chemie*, vol. 165, no. 5, pp. 69–84, 1853, doi: 10.1002/andp.18531650505.

[54] W. D. W. Abney and E. R. Festing, “XII. The Bakerian lecture.—Colour photometry,” *Philos. Trans. R. Soc. London*, vol. 177, pp. 423–456, Jan. 1886, doi: 10.1098/rstl.1886.0013.

[55] T. Young, “II. The Bakerian lecture. On the theory of light and colours,” *Philos. Trans. R. Soc. London*, vol. 92, pp. 12–48, Jan. 1802, doi: 10.1098/rstl.1802.0004.

[56] ASTM International, "ASTM E308, Standard practice for computing the colors of objects by using the CIE system," West Conshohocken, PA, 2015. doi: 10.1520/E0308-15.

[57] E. F. Schubert, "Colorimetry," in *Light-Emiting Diodes*, Second Edi., Cambridge, UK: Cambridge University Press, 2006, pp. 292–305.

[58] M. Wojciech and T. Maciej, "Color difference Delta E - A survey," *Mach. Graph. Vis.*, vol. 20, no. 4, pp. 383–411, 2011, [Online]. Available: http://www.researchgate.net/publication/236023905_Color_difference_Delta_E_-_A_survey.

[59] Comission Internationale de L'Eclairage (CIE), "Fundamental chromaticity diagram with physiological axes- Part 1 (CIE 16x:2005)," 2005.

[60] A. Stockman and L. T. Sharpe, "The spectral sensitivities of the middle- and long-wavelength-sensitive cones derived from measurements in observers of known genotype," *Vision Res.*, vol. 40, no. 13, pp. 1711–1737, 2000, doi: 10.1016/S0042-6989(00)00021-3.

[61] Comission Internationale de L'Eclairage (CIE), "Fundamental chromaticity diagram with physiological axes - Part 2: Spectral luminous efficiency functions and chromaticity diagrams (CIE 170-2:2015)," Apr. 2015.

[62] Y. Hsia and C. H. Graham, "Spectral luminosity curves for protanopic, deuteranopic, and normal subjects," *Proc. Natl. Acad. Sci. U. S. A.*, vol. 43, no. 11, pp. 1011–1019, 1957, [Online]. Available: http://www.ncbi.nlm.nih.gov/pmc/articles/PMC528574/pdf/pnas00702-0073.pdf.

[63] A. Stockman, "Luminous efficiency, cone fundamentals and chromatic adaptation," *Light Eng.*, vol. 17, no. 4, pp. 34–42, 2009.

[64] M. D. Fairchild, "Testing colour-appearance models: Guidelines for coordinated research," *Color Res. Appl.*, vol. 20, no. 4, pp. 262–267, Aug. 1995, doi: 10.1002/col.5080200410.

[65] S. Brodsky, *Encyclopedia of Color Science and Technology*, no. 1763. New York, NY: Springer New York, 2016.

[66] Comission Internationale de L'Eclairage (CIE), "A review of chromatic adaptation transforms (160:2004)," 2004. doi: 978 3 901906 30 5.

[67] M. R. Luo, "A review of chromatic adaptation transforms," *Rev. Prog. Color. Relat. Top.*, vol. 30, no. 1, pp. 77–92, Oct. 2008, doi: 10.1111/j.1478-4408.2000.tb03784.x.

[68] C. F. Andersen, G. D. Finlayson, and D. Connah, "Estimating individual cone fundamentals from their color-matching functions.," *J. Opt. Soc. Am. A. Opt. Image Sci. Vis.*, vol. 33, no. 8, pp. 1579–88, 2016, doi: 10.1364/JOSAA.33.001579.

[69] G. M. Machado, M. M. Oliveira, and L. Fernandes, "A physiologically-based model for simulation of color vision deficiency," *IEEE Trans. Vis. Comput. Graph.*, vol. 15, no. 6,

pp. 1291–1298, Nov. 2009, doi: 10.1109/TVCG.2009.113.

[70] M. F. Wesner, J. Pokorny, S. K. Shevell, and V. C. Smith, “Foveal cone detection statistics in color-normals and dichromats,” *Vision Res.*, vol. 31, no. 6, pp. 1021–1037, Jan. 1991, doi: 10.1016/0042-6989(91)90207-L.

[71] R. Shrestha, “Simulating colour vision deficiency from a spectral image,” *Stud. Health Technol. Inform.*, vol. 229, no. August 2016, pp. 392–401, 2016, doi: 10.3233/978-1-61499-684-2-392.

[72] Y. M. Ro and S. Yang, “Color adaptation for anomalous trichromats,” *Int. J. Imaging Syst. Technol.*, vol. 14, no. 1, pp. 16–20, 2004, doi: 10.1002/ima.20002.

[73] S. S. Deeb and A. G. Motulsky, “Red - green color vision defects,” in *GeneReviews® [Internet]*, A. H. Pagon RA, Adam MP and Et.al., Eds. Seattle (WA), 2005, pp. 1–19.

[74] C. E. Rodriguez-Pardo and G. Sharma, “Dichromatic color perception in a two stage model: Testing for cone replacement and cone loss models,” in *2011 IEEE 10th IVMSP Workshop: Perception and Visual Signal Analysis*, Jun. 2011, pp. 12–17, doi: 10.1109/IVMSPW.2011.5970347.

[75] M. Lucassen, J. Alferdinck, and T. N. O. H. Factors, “Dynamic simulation of color blindness for studying color vision requirements in practice,” in *Conference on Colour in Graphics, Imaging, and Vision, CGIV*, 2006, no. 1, pp. 355–358, [Online]. Available: https://www.ingentaconnect.com/content/ist/cgiv/2006/00002006/00000001/art00073.

[76] H. Brettel, F. Viénot, and J. D. Mollon, “Computerized simulation of color appearance for dichromats,” *J. Opt. Soc. Am. A*, vol. 14, no. 10, p. 2647, 1997, doi: 10.1364/josaa.14.002647.

[77] P. B. M. Thomas and J. D. Mollon, “Modelling the Rayleigh match,” *Vis. Neurosci.*, vol. 21, no. 3, pp. 477–482, 2004, doi: 10.1017/S095252380421344X.

[78] D. Rezeanu, R. Barborek, M. Neitz, and J. Neitz, “Potential value of color vision aids for varying degrees of color vision deficiency,” *Opt. Express*, vol. 30, no. 6, p. 8857, 2022, doi: 10.1364/oe.451331.

[79] R. Trukša, S. Fomins, and M. Ozolinš, “Rayleigh equation anomaloscope from commercially available LEDs,” *Medziagotyra*, vol. 18, no. 2, pp. 202–205, 2012, doi: 10.5755/j01.ms.18.2.1928.

[80] C. S. McCamy, H. Marcus, and J. G. Davidson, “Color-rendition chart.,” *J Appl Photogr Eng*, vol. 2, no. 3. pp. 95–99, 1976.

[81] X-Rite, “MacBeth Lighting history,” 2009. https://www.xritephoto.com/Documents/Literature/EN/L10-399_Macbeth_Lighting_History.pdf (accessed Aug. 20, 2023).

[82] D. Pascale, “‘ColorChecker_RGB_and_spectra.xls,’ Microsoft Excel format spreadsheet containing average spectral data, RGB values based on reference and user-measured data,” *The BabelColor Company*, 2016.

http://www.babelcolor.com/main_level/ColorChecker.htm (accessed Aug. 27, 2019).

[83] D. Pascale, "RGB coordinates of the Macbeth ColorChecker," *The BabelColor Company*, 2006. http://www.babelcolor.com/download/RGB Coordinates of the Macbeth ColorChecker.pdf.

[84] S. Abasi, M. Amani Tehran, and M. D. Fairchild, "Distance metrics for very large color differences," *Color Res. Appl.*, vol. 45, no. 2, pp. 208–223, 2020, doi: 10.1002/col.22451.

[85] J. Hiltunen, "University of Eastern Finland, spectral color research group: Computational spectral imaging. Spectral Database." http://www.uef.fi/web/spectral/-spectral-database (accessed Sep. 05, 2019).

[86] Color Imaging Laboratory. University of Granada, "UGR hyperspectral image database." http://colorimaginglab.ugr.es/pages/Data.

[87] M. A. Martínez-Domingo, L. Gómez-Robledo, E. M. Valero, R. Huertas, J. Hernández-Andrés, S. Ezpeleta, and E. Hita,, "Assessment of VINO filters for correcting red-green Color Vision Deficiency," *Opt. Express*, vol. 27, no. 13, p. 17954, 2019, doi: 10.1364/oe.27.017954.

[88] S. Hecht, "The development of Thomas Young's theory of color vision" *J. Opt. Soc. Am.*, vol. 20, no. 5, p. 231, May 1930, doi: 10.1364/JOSA.20.000231.

[89] L. T. Sharpe and H. Jägle, "I used to be color blind," *Color Res. Appl.*, vol. 26, no. SUPPL., pp. 6–9, 2001, doi: 10.1002/1520-6378(2001)26:1.

[90] A. Seebeck, "Ueber den bei manchen Personen vorkommenden Mangel an Farbensinn," *Ann. der Phys. und Chemie*, vol. 118, no. 10, pp. 177–233, 1837, doi: 10.1002/andp.18371181002.

[91] J. C. Maxwell, "Experiments on colour, as perceived by the eye, with remarks on colour-blindness," *Trans. R. Soc. Edinburgh*, vol. 21, no. 2, pp. 275–298, Jan. 1857, doi: 10.1017/S0080456800032117.

[92] M. Á. Martínez-Domingo, E. M. Valero, L. Gómez-Robledo, R. Huertas, and J. Hernández-Andrés, "Spectral filter selection for increasing chromatic diversity in CVD subjects," *Sensors*, vol. 20, no. 7, p. 2023, Apr. 2020, doi: 10.3390/s20072023.

[93] A. E. Salih, M. Elsherif, M. Ali, N. Vahdati, A. K. Yetisen, and H. Butt, "Ophthalmic wearable devices for color blindness management," *Adv. Mater. Technol.*, vol. 5, no. 8, 2020, doi: 10.1002/admt.201901134.

[94] M. F. A. Otlowski and R. Williamson, "Ethical and legal issues and the 'new genetics,'" *Med. J. Aust.*, vol. 178, no. 11, pp. 582–585, Jun. 2003, doi: 10.5694/j.1326-5377.2003.tb05365.x.

[95] C. Tapia, A. Sánchez de Miguel, and J. Zamorano, "LICA-UCM lamps spectral database," 2015. Accessed: Oct. 14, 2021. [Online]. Available: https://eprints.ucm.es/id/eprint/40930/.

[96] C. Tapia, A. Sánchez de Miguel, and J. Zamorano, “Spectra of lamps,” *Database*, 2015. https://guaix.fis.ucm.es/lamps_spectra (accessed Oct. 14, 2021).

[97] N. Almutairi, J. Kundart, N. Muthuramalingam, J. Hayes, and K. Citek, “Assessment of Enchroma filter for correcting color vision deficiency,” *Coll. Optom.*, vol. 21, pp. 1–48, 2017, [Online]. Available: http://commons.pacificu.edu/opt/21.

[98] J. Schanda, *Colorimetry- Understanding the CIE system*. 2007.

[99] Comission Internationale de L’Eclairage (CIE), “Colorimetry Third Edition (CIE 15.3:2004),” 2004.

[100] National Centers for Enviromental Information, “Laboratory Spectra,” *National Oceanic and Atmospheric Adminiatration (NOAA)*, 2021. https://ngdc.noaa.gov/eog/night_sat/spectra.html (accessed Jan. 15, 2022).

[101] J. Roby and M. Aubé, “LSPDD: Lamp spectral power distribution database.” https://lspdd.org/app/en/lamps (accessed Jan. 15, 2022).

[102] G. Sharma and H. J. Trussell, “Figures of merit for color scanners,” *IEEE Trans. Image Process.*, vol. 6, no. 7, pp. 990–1001, 1997, doi: 10.1109/83.597274.

[103] The MathWorks Inc., “fmincon- Documentation,” 2023. https://uk.mathworks.com/help/optim/ug/fmincon.html?s_tid=srchtitle_fmincon_1 (accessed Apr. 02, 2023).

[104] M. Novac, E. Vladu, O. Novac, and A. Grava, “Aspects regarding the optimization of the induction heating process using differential evolution,” *J. Electr. Electron. Eng.*, vol. 5, no. 1, pp. 145–150, 2012.

[105] M. D. Vose, “Random heuristic search,” *Theor. Comput. Sci.*, vol. 229, no. 1–2, pp. 103–142, 1999, doi: 10.1016/S0304-3975(99)00120-6.

[106] J. M. M. Linhares, P. D. Pinto, and S. M. C. Nascimento, “The number of discernible colors perceived by dichromats in natural scenes and the effects of colored lenses,” *Vis. Neurosci.*, vol. 25, no. 03, pp. 493–499, May 2008, doi: 10.1017/S0952523808080620.

[107] J. M. M. Linhares, P. D. Pinto, and S. M. C. Nascimento, “The number of discernible colors in natural scenes,” *J. Opt. Soc. Am. A*, vol. 25, no. 12, p. 2918, 2008, doi: 10.1364/josaa.25.002918.

[108] J. D. Moreland, S. Westland, V. Cheung, and S. J. Dain, “Quantitative assessment of commercial filter ‘aids’ for red-green colour defectives,” *Ophthalmic Physiol. Opt.*, vol. 30, no. 5, pp. 685–692, 2010, doi: 10.1111/j.1475-1313.2010.00761.x.

[109] T. P. Barber and M. Changizi, “Apparatus and method for orthogonalizing signals detecting blood oxygenation and blood volume,” US 20120277558A1, 2012.

[110] S. S. Guan and M. R. Luo, “A colour-difference formula for assessing large colour differences,” *Color Res. Appl.*, vol. 24, no. 5, pp. 344–355, 1999, doi: 10.1002/(SICI)1520-6378(199910)24:5<344::AID-COL6>3.0.CO;2-X.

[111] A. Schmeder and D. McPherson, “Multi-band color vision filters and method by lp-optimization,” *US Pat. App. 14/014,991*, vol. 1, no. 61, 2013, Accessed: Feb. 20, 2017. [Online]. Available: http://www.google.com/patents/US20140233105.

[112] V. L. Kalyani and V. Sharma, “Different types of optical filters and their realistic application,” *J. Manag. Eng. Inf. Technol.*, vol. 3, no. 3, pp. 2394–8124, 2016.

[113] O. Pust, “Optical filters – Technology and applications,” in *Portable Spectroscopy and Spectrometry*, Wiley, 2021, pp. 147–177.

[114] Jay Reichman, “Handbook of optical filters for fluorescence microscopy,” *Chroma Technol. Corp.*, 2000, [Online]. Available: www.chroma.com.

[115] K.-H. Stephan, H. Bräuninger, C. Reppin, H. J. Maier, D. Frischke, M. Krumrey, and P. Müller, “Optical filter for X-ray astronomy CCDs,” *Nucl. Instruments Methods Phys. Res. Sect. A Accel. Spectrometers, Detect. Assoc. Equip.*, vol. 334, no. 1, pp. 229–233, Sep. 1993, doi: 10.1016/0168-9002(93)90557-X.

[116] K. Lenhardt, “Optics for digital photography,” Nov. 2007, p. 68340W, doi: 10.1117/12.785073.

[117] S. Ray, “Optical Filters,” in *Manual of Photography: Photographic and Digital Imaging*, 9th Editio., R. Jacobson, S. Ray, G. G. Attridge, and N. Axford, Eds. New York, NY: Routledge, 2000.

[118] S. V. Boriskina, “Optics on the Go,” *Opt. Photonics News*, vol. 28, no. 9, p. p.34-41, 2017.

[119] J. E. Shelby, “Optical materials | Color filter and absorption Glasses,” in *Encyclopedia of Modern Optics*, Elsevier, 2005, pp. 440–446.

[120] N. Base, *Photonic Crystals and Light Localization in the 21st Century*. Dordrecht: Springer Netherlands, 2001.

[121] S. J. Orfanidis, *Electromagnetic Waves and Antennas*. 2016.

[122] C. K. Madsen and J. H. Zhao, *Optical Filter Design and Analysis*, vol. 3. 1999.

[123] F. Rainer, W. H. Lowdermilk, D. Milam, C. K. Carniglia, T. T. Hart, and T. L. Lichtenstein, “Materials for optical coatings in the ultraviolet,” *Appl. Opt.*, vol. 24, no. 4, p. 496, Feb. 1985, doi: 10.1364/AO.24.000496.

[124] A. Piegari and F. Flory, Eds., *Optical thin films and coatings: From materials to applications*, 2nd Editio. Duxford, UK: Woodhead Publishing, 2018.

[125] A. V. Tikhonravov, M. K. Trubetskov, and G. W. DeBell, “Application of the needle optimization technique to the design of optical coatings,” *Appl. Opt.*, vol. 35, no. 28, p. 5493, 1996, doi: 10.1364/ao.35.005493.

[126] K. A. Winick, “Effective-index method and coupled-mode theory for almost-periodic waveguide gratings: a comparison,” *Appl. Opt.*, vol. 31, no. 6, p. 757, Feb. 1992, doi: 10.1364/AO.31.000757.

[127] L. G. Parratt, “Surface studies of solids by total reflection of x-rays,” *Phys. Rev.*, vol. 95, no. 2, pp. 359–369, 1954, doi: 10.1103/PhysRev.95.359.

[128] L. A. Weller-Brophy and D. G. Hall, “Analysis of waveguide gratings: application of Rouard’s method,” *J. Opt. Soc. Am. A*, vol. 2, no. 6, p. 863, Jun. 1985, doi: 10.1364/JOSAA.2.000863.

[129] P. G. Verly and D. Poitras, “Design of complex optical coatings,” in *Optical Thin Films and Coatings*, Elsevier, 2018, pp. 25–64.

[130] A. Thelen, “Design strategies for thin film optical coatings,” in *Thin Films on Glass*, H. Bach and D. Krause, Eds. Berlin, Heidelberg: Springer Berlin Heidelberg, 2003, pp. 23–50.

[131] A. Thelen, *Design of Optical Interference Coatings*. Mc Graw Hill, 1989.

[132] R. R. Willey, *Practical Design and Production of Optical Thin Films*, 2nd Editio. New York, NY: Marcel Dekker, Inc, 2002.

[133] P. Baumeister, *Optical coating technology*. Bellingham, WA: SPIE Optical Engineering Press, 2004.

[134] M. J. Vrhel and H. J. Trussell, “Filter considerations in color correction,” *IEEE Trans. Image Process.*, vol. 3, no. 2, pp. 147–161, 1994, doi: 10.1109/83.277897.

[135] A. V. Tikhonravov, “Needle optimization technique: the history and the future,” *Opt. Thin Film. V New Dev.*, vol. 3133, p. 2, 1997, doi: 10.1117/12.290180.

[136] S. A. Furman and A. V. Tikhonravov, “Basics of optics of multilayer systems,” p. 104, 1992, [Online]. Available: https://books.google.cl/books?id=7LTjjUSAu9EC.

[137] A. V. Tikhonravov and M. K. Trubetskov, “Modern status and prospects of the development of methods of designing multilayer optical coatings,” *J. Opt. Technol.*, vol. 74, no. 12, p. 845, 2007, doi: 10.1364/jot.74.000845.

[138] A. V. Tikhonravov, M. K. Trubetskov, and G. W. DeBell, “Optical coating design approaches based on the needle optimization technique,” *Appl. Opt.*, vol. 46, no. 5, pp. 704–710, 2007, doi: 10.1364/AO.46.000704.

[139] M. D. Vose, *The simple genetic algorithm: foundations and theory*. MIT press, 1999.

[140] D. Whitley, “A genetic algorithm tutorial,” *Stat. Comput.*, vol. 4, no. 2, pp. 65–85, Jun. 1994, doi: 10.1007/BF00175354.

[141] D. Wiesmann, U. Hammel, and T. Back, “Robust design of multilayer optical coatings by means of evolutionary algorithms,” *IEEE Trans. Evol. Comput.*, vol. 2, no. 4, pp. 162–167, 1998, doi: 10.1109/4235.738986.

[142] H. Greiner, “Robust optical coating design with evolutionary strategies,” *Appl. Opt.*, vol. 35, no. 28, p. 5477, 1996, doi: 10.1364/ao.35.005477.

[143] J. M. Yang and C. Y. Kao, “An evolutionary algorithm for the synthesis of oblique

incidence optical coatings," *IECON Proc. (Industrial Electron. Conf.*, vol. 1, no. 4, pp. 2780–2785, 2000, doi: 10.1109/IECON.2000.972438.

[144] M. A. Barry, V. Berthier, B. D. Wilts, M. C. Cambourieux, P. Bennet, R. Pollès, O. Teytaud, E. Centeno, N. Biais, and A. Moreau,, "Evolutionary algorithms converge towards evolved biological photonic structures," *Sci. Rep.*, vol. 10, no. 1, pp. 1–10, 2020, doi: 10.1038/s41598-020-68719-3.

[145] S. Orfanidis, "Electromagnetic waves & antennas toolbox," *MATLAB Central File Exchange*, 2021. https://uk.mathworks.com/matlabcentral/fileexchange/4456-electromagnetic-waves-antennas-toolbox (accessed Mar. 15, 2021).

[146] S. Larouche and L. Martinu, "OpenFilters: Open-source software for the design, optimization, and synthesis of optical filters," *Appl. Opt.*, vol. 47, no. 13, pp. 219–230, 2008, doi: 10.1364/AO.47.00C219.

[147] S. Larouche and L. Martinu, "Functional coating and surface engineering laboratory (FCSEL)." https://www.polymtl.ca/larfis/en/links (accessed Feb. 23, 2022).

[148] The MathWorks Inc., "MATLAB Global Optimization Toolbox Release R2021a." https://uk.mathworks.com/products/global-optimization.html (accessed Mar. 15, 2021).

[149] L. Martinu and D. Poitras, "Plasma deposition of optical films and coatings: A review," *J. Vac. Sci. Technol. A Vacuum, Surfaces, Film.*, vol. 18, no. 6, pp. 2619–2645, 2000, doi: 10.1116/1.1314395.

[150] S. Raoux, D. Cheung, M. Fodor, W. N. Taylor, and K. Fairbairn, "Growth, trapping and abatement of dielectric particles in PECVD systems," *Plasma Sources Sci. Technol.*, vol. 6, no. 3, pp. 405–414, 1997, doi: 10.1088/0963-0252/6/3/018.

[151] B. R. Rajakumar and A. George, "APOGA: An adaptive population pool size based genetic algorithm," *AASRI Procedia*, vol. 4, pp. 288–296, 2013, doi: 10.1016/j.aasri.2013.10.043.

[152] S. Martin, J. Rivory, and M. Schoenauer, "Synthesis of optical multilayer systems using genetic algorithms," *Appl. Opt.*, vol. 34, no. 13, p. 2247, 1995, doi: 10.1364/ao.34.002247.

[153] V. Yakovlev and G. Tempea, "Optimization of chirped mirrors," *Appl. Opt.*, vol. 41, no. 30, p. 6514, Oct. 2002, doi: 10.1364/AO.41.006514.

[154] "International Iberian Nanotechnology Laboratory (INL)," 2019. https://inl.int/ (accessed May 17, 2019).

[155] R. Oulton, H. M. Whitney, G. Atkinson, M. J. Cryan, M. Lopez-Garcia, H. E. O'Brien, J. Lennon, and N. Masters, "Light-induced dynamic structural color by intracellular 3D photonic crystals in brown algae," *Sci. Adv.*, vol. 4, no. 4, p. eaan8917, 2018, doi: 10.1126/sciadv.aan8917.

[156] M. Polyanskiy, "Refractive index database," 2019. https://refractiveindex.info/ (accessed May 23, 2019).

[157] B. Hatton, L. Mishchenko, S. Davis, K. H. Sandhage, and J. Aizenberg, "Assembly of large-area, highly ordered, crack-free inverse opal films.," *Proc. Natl. Acad. Sci. U. S. A.*, vol. 107, no. 23, pp. 10354–9, Jun. 2010, doi: 10.1073/pnas.1000954107.

[158] J. Zhang, Z. Sun, and B. Yang, "Self-assembly of photonic crystals from polymer colloids," *Curr. Opin. Colloid Interface Sci.*, vol. 14, no. 2, pp. 103–114, 2009, doi: 10.1016/j.cocis.2008.09.001.

[159] D. J. Norris, E. G. Arlinghaus, L. Meng, R. Heiny, and L. E. Scriven, "Opaline photonic crystals: How does self-assembly work?," *Adv. Mater.*, vol. 16, no. 16, pp. 1393–1399, Aug. 2004, doi: 10.1002/adma.200400455.

[160] S. H. Im, M. H. Kim, and O. O. Park, "Thickness control of colloidal crystals with a substrate dipped at a tilted angle into a colloidal suspension," *Chem. Mater.*, vol. 15, no. 9, pp. 1797–1802, May 2003, doi: 10.1021/cm021793m.

[161] B. V Lotsch, C. B. Knobbe, and G. a Ozin, "A step towards optically encoded silver release in 1D photonic crystals.," *Small*, vol. 5, no. 13, pp. 1498–503, Jul. 2009, doi: 10.1002/smll.200801925.

ANNEXES

Annex 1. MACULA AND OCULAR OPTICAL DENSITY

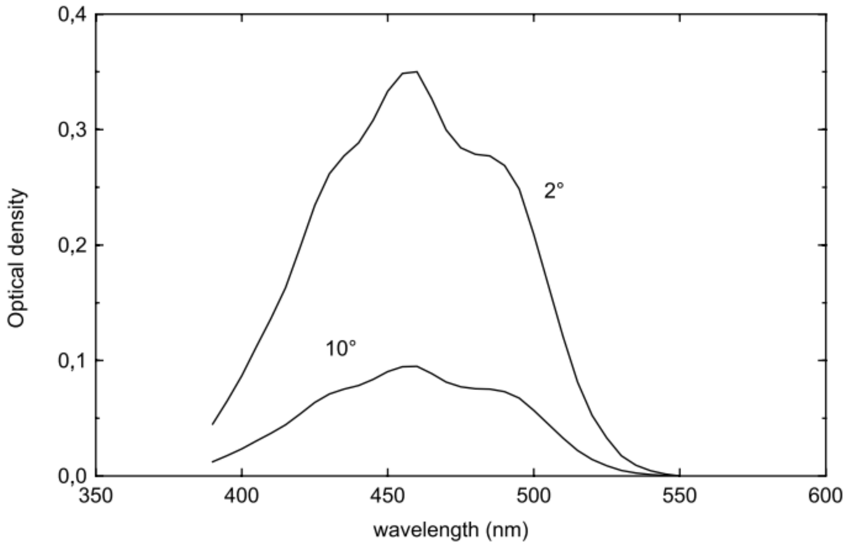

Figure 0-1: Optical density of macular pigment, $D_{\tau,macula}(\lambda)$, for 2° and 10° field size

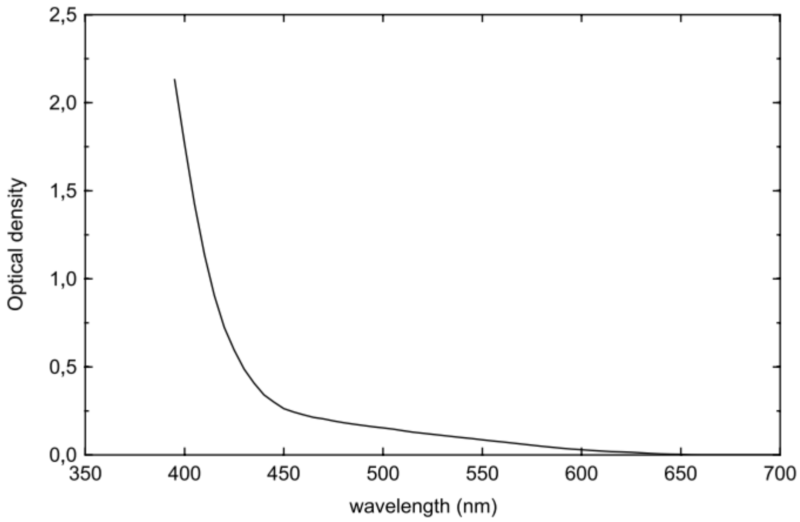

Figure 0-2: Optical density of the lens and other ocular media, $D_{\tau,ocul}(\lambda)$.

Annex 2. CAT02

a) Starting data:

Chromaticity coordinates of a sample in first illuminant A: X_A, Y_A, Z_A

Reference white in illuminant A: X_{WA}, Y_{WA}, Z_{WA}

Reference white in illuminant B: X_{WB}, Y_{WB}, Z_{WB}

Luminance of adapting field $\left[\frac{cd}{m^2}\right]$: L_A

b) Degree of adaptation D:

$$D = \alpha_D F \left[1 - \left(\frac{1}{3.6}\right) e^{\left(\frac{-L_A - 42}{92}\right)}\right] \qquad \text{Eq. 0-1}$$

L_A is required for calculating the degree of adaptation, D, however L_A can usually be taken as:

$$L_A = \frac{L_W Y_b}{100} \qquad \text{Eq. 0-2}$$

where L_W is the luminance of a white in the illuminant (in cd/m^2), and Y_b is the Y value of the background. The value for L_A is not critical, and a value of $D = 0.95$ can be set to represent typical viewing conditions for reflecting colours.

c) **Calculate RGB values for sample under first illuminant ($\boldsymbol{R_A, B_A, G_A}$), and reference white under reference and adapting illuminants ($\boldsymbol{R_{WA}, G_{WA}, B_{WA}}$, and $\boldsymbol{R_{WB}, G_{WB}, B_{WB}}$ respectively):**

$$[R_i\ G_i\ B_i\ ] = M_{CAT02}[X_i\ Y_i\ Z_i\ ] \qquad \text{Eq. 0-3}$$

Where $i = A, B, WA, WB$

$$M_{CAT02} = \begin{bmatrix} 0.7328 & 0.4296 & -0.1624 \\ -0.7036 & 1.6975 & 0.0061 \\ 0.0030 & 0.0136 & 0.9834 \end{bmatrix} \qquad \text{Eq. 0-4}$$

d) **Calculate factors $\boldsymbol{D_r, D_g, D_b}$:**

$$D_r = (Y_{WA}/Y_{WB})D(R_{WB}/R_{WA}) + 1 - D \qquad \text{Eq. 0-5}$$

$$D_g = (Y_{WA}/Y_{WB})D(G_{WB}/G_{WA}) + 1 - D \qquad \text{Eq. 0-6}$$

$$D_b = (Y_{WA}/Y_{WB})D(B_{WB}/B_{WA}) + 1 - D \qquad \text{Eq. 0-7}$$

e) **Calculate corresponding RGB colours for sample in second illuminant:**

$$R_{AC} = D_r * R_A \qquad \text{Eq. 0-8}$$

$$G_{AC} = D_g * G_A \qquad \text{Eq. 0-9}$$

$$B_{AC} = D_b * B_A \qquad \text{Eq. 0-10}$$

f) Calculate XYZ tristimulus for the sample (X_{AC}, Y_{AC}, Z_{AC}) and test white under the second illuminant ($X_{WAC}, Y_{WAC}, Z_{WAC}$):

$$[X_i\ Y_i\ Z_i\ ] = (M_{CAT02})^{-1}[R_i\ G_i\ B_i\ ] \qquad \text{Eq. 0-11}$$

$$(M_{CAT02})^{-1} = \begin{bmatrix} 0.7328 & 0.4296 & -0.1624 \\ -0.7036 & 1.6975 & 0.0061 \\ 0.0030 & 0.0136 & 0.9834 \end{bmatrix}^{-1} = \begin{bmatrix} 1.0961 & -0.2789 & 0.1827 \\ 0.4544 & 0.4735 & 0.0721 \\ -0.0096 & -0.0096 & 1.0153 \end{bmatrix} \qquad \text{Eq. 0-12}$$

Annex 3. CIECAM02

Published in 2002, the CIECAM02 is the latest colour appearance model proposed by the CIE. It builds upon the basic structure and form of its predecessor, the CIECAM97.

$$[\rho\ \gamma\ \beta] = M_{CIECAM02}[X\ Y\ Z] \qquad \text{Eq. 0-13}$$

$$M_{CIECAM02} = \begin{bmatrix} 0.38971 & 0.68898 & 0.07868 \\ -0.22981 & 1.18340 & 0.04641 \\ 0 & 0 & 1 \end{bmatrix} \qquad \text{Eq. 0-14}$$

a) Cone dynamic response:

$$f_n(\rho) + 0.1 = \frac{[400(\rho/100)^{0.42}]}{[27.13 + (\rho/100)^{0.42}]} + 0.1 \qquad \text{Eq. 0-15}$$

The +0.1 term represents the noise.

b) Luminance adaptation:

$$\rho_a = f_n(F_L\rho) + 0.1 = \frac{[400(F_L\rho/100)^{0.42}]}{[27.13 + (F_L\rho/100)^{0.42}]} + 0.1 \qquad \text{Eq. 0-16}$$

$$F_L = 0.2k^4(5L_A) + 0.1(1-k^4)(5L_A)^{1/3} \quad \text{Eq. 0-17}$$

$$k = \frac{1}{5L_A + 1} \quad \text{Eq. 0-18}$$

$$F = \begin{cases} 1.0\ (average\ surround) \\ 0.9\ (\mathrm{dim}\ surround) \\ 0.8\ (dark\ surround) \end{cases} \quad \text{Eq. 0-19}$$

c) Criteria for achromacy and for constant hue:

$$C_1 = \rho_a - \gamma_a \quad \text{Eq. 0-20}$$

$$C_2 = \gamma_a - \beta_a \quad \text{Eq. 0-21}$$

$$C_3 = \beta_a - \rho_a \quad \text{Eq. 0-22}$$

Achromacy:

$$\rho_a = \beta_a = \gamma_a \quad \text{Eq. 0-23}$$

in other words,

$$C_1 = C_2 = C_3 = 0 \quad \text{Eq. 0-24}$$

Constant hue:

Ratios,

$$C_1 : C_2 : C_3 = constant \quad \text{Eq. 0-25}$$

d) Redness-greenness, a, and yellowness-blueness, b:

$$a = C_1 - \frac{C_2}{11} = (\rho_a - \gamma_a) - \left(\frac{\gamma_a - \beta_a}{11}\right) = \rho_a - \frac{12}{11}\gamma_a + \frac{\beta_a}{11} \qquad \text{Eq. 0-26}$$

$$b = \frac{C_2 - C_3}{9} = \frac{(\gamma_a - \beta_a) - (\beta_a - \rho_a)}{9} = \frac{\gamma_a + \rho_a - 2\,\beta_a}{9} \qquad \text{Eq. 0-27}$$

e) Hue angle, h:

$$h = \arctan(b/a) \qquad \text{Eq. 0-28}$$

f) Eccentricity factor, e:

$$e_t = \frac{1}{4}\left[\cos\left(\frac{h\pi}{180} + 2\right) + 3.8\right] \qquad \text{Eq. 0-29}$$

g) Achromatic response:

$$A = \left[2\rho_a + \gamma_a + \frac{\beta_a}{20} - 0.305\right] N_{bb} \qquad \text{Eq. 0-30}$$

$$N_{bb} = 0.725(Y_w/Y_b)^{0.2} \qquad \text{Eq. 0-31}$$

h) Lightness, J:

$$J = 100(A/A_w)^{cz} \qquad \text{Eq. 0-32}$$

$$c = \left\{ \begin{array}{c} 0.69\ (average\ surround) \\ 0.59\ (\dim surround) \\ 0.525\ (dark\ surround) \end{array} \right\} \quad \text{Eq. 0-33}$$

$$z = 1.48 + (Y_b/Y_w)^{0.5} \quad \text{Eq. 0-34}$$

i) Brightness, Q:

$$Q = \frac{4}{c}\left(\frac{J}{100}\right)^{0.5} (A_w + 4)F_L^{0.25} \quad \text{Eq. 0-35}$$

j) Chroma, C:

$$C = t^{0.9}\left(\frac{J}{100}\right)^{0.5} \left(1.64 - 0.29^{(Y_b/Y_w)}\right)^{0.73} \quad \text{Eq. 0-36}$$

$$t = \frac{\left[5000\left(\frac{10}{13}\right) N_c N_{cb} e_t (a^2 + b^2)^{0.5}\right]}{\left[\rho_a + \gamma_a + \frac{21}{20}\beta_a\right]} \quad \text{Eq. 0-37}$$

$$N_c = \{ \begin{array}{c} 1.0\ (average\ surround) \\ 0.9\ (\dim surround) \\ 0.8\ (dark\ surround) \end{array} \quad \text{Eq. 0-38}$$

k) Colourfulness, M:

$$M = C\ F_L^{0.25} \quad \text{Eq. 0-39}$$

l) Saturation, s:

$$s = 100(M/Q)^{0.5} \quad \text{Eq. 0-40}$$

m) Uniform colour spaces, and colour difference formulae:

$$a'_M = M' \cos(h) \qquad \text{Eq. 0-41}$$

$$b'_M = M' \sin(h) \qquad \text{Eq. 0-42}$$

$$J' = \frac{(1.7)J}{1 + (0.007)\,J} \qquad \text{Eq. 0-43}$$

$$M' = \left(\frac{1}{0.0228}\right)\log_{10}(1 + 0.0228\,M) \qquad \text{Eq. 0-44}$$

$$\Delta E' = \left(\Delta \mathrm{J}'^2 + \Delta \mathrm{a}'_{\mathrm{M}}{}^2 + \Delta \mathrm{b}'_M{}^2\right)^{0.5} \qquad \text{Eq. 0-45}$$

Annex 4. JACOBIAN MATRIX FOR CIELUV TRANSFORMATION

Given the 3-by-3 non-linear transformation, from XYZ to CIELUV space:

$\mathcal{F}$ represents the 3-by-3 non-linear transformation, from CIE XYZ to CIE L*u*v*

$$\mathcal{F}(XYZ) = \begin{bmatrix} L^*(Y) \\ u^*(X,Y,Z) \\ v^*(X,Y,Z) \end{bmatrix} \qquad \text{Eq. 0-46}$$

$$L^* = \begin{Bmatrix} \left(\frac{29}{3}\right)^3 \frac{Y}{Y_n}, & \frac{Y}{Y_n} \leq \left(\frac{6}{29}\right)^3 \\ 116\left(\frac{Y}{Y_n}\right)^{\frac{1}{3}} - 16, & \frac{Y}{Y_n} > \left(\frac{6}{29}\right)^3 \end{Bmatrix} \qquad \text{Eq. 0-47}$$

$$u^* = 13L^*(u' - u'_n) \qquad \text{Eq. 0-48}$$

$$v^* = 13L^*(v' - v_n') \qquad \text{Eq. 0-49}$$

The Jacobian matrix for the transformation is:

Jacobian Matrix for the XYZ→L*u*v* transformation:

$$J_{\mathcal{F}}(X,Y,Z) = \begin{bmatrix} \frac{\partial L^*}{\partial X} & \frac{\partial L^*}{\partial Y} & \frac{\partial L^*}{\partial Z} \\ \frac{\partial u^*}{\partial X} & \frac{\partial u^*}{\partial Y} & \frac{\partial u^*}{\partial Z} \\ \frac{\partial v^*}{\partial X} & \frac{\partial v^*}{\partial Z} & \frac{\partial v^*}{\partial Z} \end{bmatrix} \qquad \text{Eq. 0-50}$$

$$\frac{\partial L^*}{\partial X} = 0 \qquad \text{Eq. 0-51}$$

$$\frac{\partial L^*}{\partial Y} = \begin{Bmatrix} \left(\frac{29}{3}\right)^3 Y_n^{-1}, & \frac{Y}{Y_n} \leq \left(\frac{6}{29}\right)^3 \\ \frac{116}{3} Y^{-\frac{2}{3}} Y_n^{-\frac{1}{3}}, & \frac{Y}{Y_n} > \left(\frac{6}{29}\right)^3 \end{Bmatrix} \qquad \text{Eq. 0-52}$$

$$\frac{\partial L^*}{\partial Z} = 0 \qquad \text{Eq. 0-53}$$

$$\frac{\partial u^*}{\partial X} = 13\left[\frac{60Y + 12Z}{(X + 15Y + 3Z)^2}\right] L^* \qquad \text{Eq. 0-54}$$

$$\frac{\partial u^*}{\partial Y} = 13\left[\frac{-60X}{(X+15Y+3Z)^2}\right]L^* + 13\left[\frac{4X}{(X+15Y+3Z)}\right]\left(\frac{\partial L^*}{\partial Y}\right) - 13\left(\frac{4X_w}{(X_w+15Y_w+3Z_w)}\right)\left(\frac{\partial L^*}{\partial Y}\right) \quad \text{Eq. 0-55}$$

$$\frac{\partial u^*}{\partial Z} = 13 * \left[\frac{-12X}{(X+15Y+3Z)^2}\right]L^* \quad \text{Eq. 0-56}$$

$$\frac{\partial v^*}{\partial X} = 13\left[\frac{-9Y}{(X+15Y+3Z)^2}\right]L^* \quad \text{Eq. 0-57}$$

$$\frac{\partial v^*}{\partial Y} = 13\left[\frac{9X+27Z}{(X+15Y+3Z)^2}\right]L^* + 13\left[\frac{9Y}{(X+15Y+3Z)}\right]\left(\frac{\partial L^*}{\partial Y}\right) - 13\left[\frac{9Y_w}{(X_w+15Y_w+3Z_w)}\right]\left(\frac{\partial L^*}{\partial Y}\right) \quad \text{Eq. 0-58}$$

$$\frac{\partial v^*}{\partial Z} = 13\left[\frac{-27Y}{(X+15Y+3Z)^2}\right]L^* \quad \text{Eq. 0-59}$$